NAVAL POSTGRADUATE SCHOOL

MONTEREY, CALIFORNIA

DISSERTATION

AUTONOMOUS SPACECRAFT RENDEZVOUS WITH A TUMBLING OBJECT: APPLIED REACHABILITY ANALYSIS AND GUIDANCE AND CONTROL STRATEGIES

by

Costantinos Zagaris

September 2018

Dissertation Supervisor: Marcello Romano

THIS PAGE INTENTIONALLY LEFT BLANK

REPORT DOCUMENTATION PAGE			*Form Approved OMB No. 0704-0188*

1. AGENCY USE ONLY *(Leave blank)*	**2. REPORT DATE** September 2018	**3. REPORT TYPE AND DATES COVERED** Dissertation

4. TITLE AND SUBTITLE
AUTONOMOUS SPACECRAFT RENDEZVOUS WITH A TUMBLING OBJECT: APPLIED REACHABILITY ANALYSIS AND GUIDANCE AND CONTROL STRATEGIES

5. FUNDING NUMBERS

6. AUTHOR(S) Costantinos Zagaris

7. PERFORMING ORGANIZATION NAME(S) AND ADDRESS(ES)
Naval Postgraduate School
Monterey, CA 93943-5000

8. PERFORMING ORGANIZATION REPORT NUMBER

9. SPONSORING / MONITORING AGENCY NAME(S) AND ADDRESS(ES)
N/A

10. SPONSORING / MONITORING AGENCY REPORT NUMBER

11. SUPPLEMENTARY NOTES The views expressed in this thesis are those of the author and do not reflect the official policy or position of the Department of Defense or the U.S. Government.

12a. DISTRIBUTION / AVAILABILITY STATEMENT
Approved for public release. Distribution is unlimited.

12b. DISTRIBUTION CODE
A

13. ABSTRACT (maximum 200 words)

Rendezvous and proximity operations are an essential component of both military and commercial space missions and are rising in complexity. This dissertation presents an applied reachability analysis and develops a computationally feasible autonomous guidance algorithm for the purpose of spacecraft rendezvous and proximity maneuvers around a tumbling object. Recent advancements enable the use of more sophisticated, computation-based algorithms, instead of traditional control methods. These algorithms are desirable for autonomous applications due to their ability to optimize performance and explicitly handle constraints (e.g., safety, control limits). In an autonomous setting, however, some important questions must be answered before an algorithm implementation can be realized. First, the feasibility of a maneuver is addressed by analyzing the fundamental spacecraft relative dynamics. Particularly, a set of initial relative states is computed and visualized from which the desired rendezvous state can be reached (i.e., backward reachability analysis). Second, with the knowledge that a maneuver is feasible, the Model Predictive Control (MPC) framework is utilized to design a stabilizing feedback control law that optimizes performance and incorporates constraints such as control saturation limits and collision avoidance. The MPC algorithm offers a computationally efficient guidance strategy that could potentially be implemented in real-time on-board a spacecraft.

14. SUBJECT TERMS
reachability, optimal control, model predictive control, autonomous guidance, spacecraft guidance and control, spacecraft relative motion, rendezvous and proximity operations

15. NUMBER OF PAGES
289

16. PRICE CODE

17. SECURITY CLASSIFICATION OF REPORT	**18. SECURITY CLASSIFICATION OF THIS PAGE**	**19. SECURITY CLASSIFICATION OF ABSTRACT**	**20. LIMITATION OF ABSTRACT**
Unclassified	Unclassified	Unclassified	UU

NSN 7540-01-280-5500

Standard Form 298 (Rev. 2-89)
Prescribed by ANSI Std. 239-18

THIS PAGE INTENTIONALLY LEFT BLANK

Approved for public release. Distribution is unlimited.

AUTONOMOUS SPACECRAFT RENDEZVOUS WITH A TUMBLING OBJECT: APPLIED REACHABILITY ANALYSIS AND GUIDANCE AND CONTROL STRATEGIES

Costantinos Zagaris
Major, United States Air Force
BSE, Virginia Tech, 2007
MSE, Air Force Institute of Technology, 2012

Submitted in partial fulfillment of the
requirements for the degree of

DOCTOR OF PHILOSOPHY IN ASTRONAUTICAL ENGINEERING

from the

NAVAL POSTGRADUATE SCHOOL
September 2018

Approved by:

Marcello Romano
Department of Mechanical and Aerospace Engineering
Dissertation Supervisor

Jae Jun Kim
Department of Mechanical and Aerospace Engineering

Oleg A. Yakimenko
Department of Systems Engineering

Xiaoping Yun
Department of Electrical and Computer Engineering

Richard Cobb
Department of Aeronautics and Astronautics
AFIT

Approved by:

Garth V. Hobson,
Chair, Department of Mechanical and Aerospace Engineering

Douglas Moses, Vice Provost of Academic Affairs

THIS PAGE INTENTIONALLY LEFT BLANK

ABSTRACT

Rendezvous and proximity operations are an essential component of both military and commercial space missions and are rising in complexity. This dissertation presents an applied reachability analysis and develops a computationally feasible autonomous guidance algorithm for the purpose of spacecraft rendezvous and proximity maneuvers around a tumbling object. Recent advancements enable the use of more sophisticated, computation-based algorithms, instead of traditional control methods. These algorithms are desirable for autonomous applications due to their ability to optimize performance and explicitly handle constraints (e.g., safety, control limits). In an autonomous setting, however, some important questions must be answered before an algorithm implementation can be realized. First, the feasibility of a maneuver is addressed by analyzing the fundamental spacecraft relative dynamics. Particularly, a set of initial relative states is computed and visualized from which the desired rendezvous state can be reached (i.e., backward reachability analysis). Second, with the knowledge that a maneuver is feasible, the Model Predictive Control (MPC) framework is utilized to design a stabilizing feedback control law that optimizes performance and incorporates constraints such as control saturation limits and collision avoidance. The MPC algorithm offers a computationally efficient guidance strategy that could potentially be implemented in real-time on-board a spacecraft.

THIS PAGE INTENTIONALLY LEFT BLANK

Table of Contents

THIS PAGE INTENTIONALLY LEFT BLANK

List of Figures

THIS PAGE INTENTIONALLY LEFT BLANK

List of Tables

List of Acronyms and Abbreviations

ATV	Automated Transfer Vehicle
APF	Artificial Potential Function
CCS	Cartesian Coordinate System
CG&C	Computational Guidance & Control
CLF	Control Lyapunov Function
CMG	Control Moment Gyroscope
CW	Clohessy-Wiltshire
DARE	Discrete Algebraic Riccati Equation
DART	Demonstration of Autonomous Rendezvous Technology
DCM	Direction Cosine Matrix
DOF	Degrees of Freedom
ECI	Earth Centered Inertial
GNC	Guidance, Navigation & Control
GPOPS	General Purpose OPtimal control Software
HJ	Hamilton-Jacobi
HPC	High Performance Computing
IDVD	Inverse Dynamics in the Virtual Domain
IPOPT	Interior Point OPTimizer
ISS	International Space Station

KOZ	Keep-Out-Zone
LEO	Low Earth Orbit
LQ	Linear Quadratic
LQR	Linear Quadratic Regulator
LTI	Linear Time-Invariant
LTV	Linear Time-Varying
LVLH	Local Vertical Local Horizontal
MPC	Model Predictive Control
MPT	Multi-Parametric Toolbox
MRP	Modified Rodrigues Parameters
MT-OCP	Minimum Time Optimal Control Problem
NASA	National Aeronautics and Space Administration
NLP	Nonlinear Programming
NMC	Natural Motion Circumnavigation
NMPC	Nonlinear Model Predictive Control
NMPC-OCP	NMPC Optimal Control Problem
NPS	Naval Postgraduate School
PD	Proportional-Derivative
PDE	Partial Differential Equation
POSEIDYN	Proximity Operations of Spacecraft: Experimental hardware-In-the-loop DYNamic test bed
QP	Quadratic Programming

RPO	Rendezvous and Proximity Operations
SPHERES	Synchronized Position Hold Engage and Reorient Experimental Satellites
SQP	Sequential Quadratic Programming
STLC	Small Time Locally Controllable

THIS PAGE INTENTIONALLY LEFT BLANK

List of Symbols and Variables

General Nomenclature

$\vec{a}$	an unresolved vector
${}^{\mathsf{A}}\dot{\vec{a}}$	time derivative of vector $\vec{a}$ with respect to A Cartesian coordinate system
$\boldsymbol{a}^{\mathsf{A}}$	vector $\vec{a}$ resolved in the A Cartesian coordinate system
$\boldsymbol{a}^{\times}$	skew-symmetric matrix representing the vector cross product operator
a^*	optimal value of variable a
A^{-1}	inverse of matrix A
A^+	Moore-Penrose pseudoinverse of matrix A
C	chief body-fixed Cartesian coordinate system
D	deputy body-fixed Cartesian coordinate system
I	Earth-centered inertial Cartesian coordinate system
L	chief local vertical local horizontal Cartesian coordinate system
$\mathbb{N}$	set of integers
$\mathbb{R}$	set of real numbers
$\mathbb{R}^n$	set of n-dimensional vectors
$\mathrm{SE}(n)$	special Euclidean group of dimension n
$\mathrm{SO}(n)$	special orthogonal group of dimension n

Variables

$0_{n\times m}$	n by m matrix of zeros
A	continuous-time state space plant matrix
A_d	discrete-time state space plant matrix
A_T	continuous-time translational subsystem state space plant matrix
a	orbit semi-major axis
B	continuous-time state space input matrix
B_d	discrete-time state space input matrix
B_T	continuous-time translational subsystem state space input matrix
$\tilde{B}$	matrix used in Modified Rodrigues Parameter kinematic expression
b	moment arm length

$C_{\mathsf{A/B}}$	Direction Cosine Matrix of coordinate system A with respect to B
ce	control effort
e	orbit eccentricity
$\hat{e}$	Euler axis of rotation
$\vec{F}_d$	control force applied to the deputy
$\mathbf{F}_d$	control force vector applied to the deputy resolved in C
$F_{x,y,z}$	x, y, or z component of control force vector
f	drift vector field
f_0	true anomaly
f_d	discretized drift vector field
f_R	drift vector field of rotational subsystem
f_T	drift vector field of translational subsystem
G	constant control vector field
G_d	discretized constant control vector field
G_R	constant control vector field of rotational subsystem
G_T	constant control vector field of translational subsystem
g	control vector field
g_d	discretized control vector field
H	system Hamiltonian
I_n	n by n identity matrix
i	orbit inclination
J	optimization performance index
$J_{c,d}$	inertia matrix of the chief and deputy, respectively
$J_{c,d_{x,y,z}}$	chief or deputy inertia along x, y, or z principal axes
K	constant state feedback gain matrix
l	stage (or running) cost in optimization cost functional
$L_f g$	Lie derivative of f with respect to g
$\vec{M}_d$	control torque applied to the deputy
$\mathbf{M}_d^{\mathsf{D}}$	control torque applied to the deputy resolved in D
$M_{x,y,z}$	x, y, or z component of control torque vector
m_d	deputy's mass
N	prediction horizon
n	chief orbital mean motion

Q	state weighting matrix
$\tilde{Q}$	matrix used in quaternion kinematic expression
$q_{\mathsf{A/B}}$	unit quaternion representing the orientation of A with respect to B
q	relative attitude unit quaternion
q_i	i-th element of quaternion
R	control weighting matrix
$\mathcal{R}_B(T)$	backward T-reachable set
$\mathcal{R}_F(T)$	forward T-reachable set
$\vec{r}_c$	inertial position vector of chief
$\vec{r}_d$	inertial position vector of deputy
s	slack variable for relaxed constraints
t	time
t_f	final time
t_s	sampling time
$\mathcal{U}$	set of admissible controls
U_k^*	optimal control sequence computed at time step k
u	control input vector
$u_{i\|k}$	i-th element of optimal control sequence predicted at time step k
u_{max}	maximum allowable control input
u_R	rotational control component (i.e., torque)
u_s	steady-state control required to maintain desired condition
u_T	translational control component (i.e., force)
V	implicit value function in Hamilton-Jacobi optimal control formulation
V_f	terminal value function
$\mathbf{v}$	relative velocity vector resolved in C
$v_{x,y,z}$	x, y, or z component of relative velocity vector
$\mathcal{X}$	set of admissible states
$\mathcal{X}_f$	terminal set
X_k	predicted trajectory at time step k
x	state vector
x_0	initial condition (i.e, state at $t = 0$)
x_d	desired state
x_e	linearization expansion point

x_f	final condition (i.e., state at $t = t_f$)
$x_{i\|k}$	i-th element of predicted state trajectory predicted at time step k
x_R	relative rotational state vector
x_T	relative translational state vector

Greek Symbols

α	weighting parameter on state variables
β	weighting parameter on control variables
$\gamma_\Sigma(a, b)$	admissible trajectory of system Σ in time span $t = [a, b]$
δt_f	variation of final time variable
ϵ	weighting parameter on slack variables
η	weighting parameter on terminal cost
$\kappa(t)$	feedback control law
μ	Earth's gravitational constant
$\vec{\rho}$	relative position vector
$\boldsymbol{\rho}$	relative position vector resolved in C
$\rho_{x,y,z}$	x, y, or z component of relative position vector
Σ	general dynamical system
$\boldsymbol{\sigma}$	Modified Rodrigues Parameter (MRP) vector
σ_i	i-th element of MRP vector
σ^2	magnitude of MRP vector
τ	independent variable of integration
ϕ	Euler rotation angle
Ω	constant rotation rate of the chief
$\vec{\omega}_{\mathsf{A/B}}$	angular velocity of A with respect to B
$\boldsymbol{\omega}^{\mathsf{D}}$	relative angular velocity vector resolved in D
$\boldsymbol{\omega}_c$	chief angular velocity vector resolved in C
ω_{ra}	right ascension of the ascending node
ω_p	argument of perigee
$\omega_{x,y,x}$	x, y, or z component of relative angular velocity vector

Acknowledgments

Many will say that completing a doctoral degree in three years is crazy. I would say that it is only possible with the support of our professors, peers, and families. Without that foundation, I would not have been able to complete this program, at least not with my sanity intact.

First, I would like to thank my advisor, Professor Marcello Romano, for taking me under his wing and mentoring me. Also to Professors Cobb, Kim, Yakimenko, and Yun, thank you for being valuable members of my committee. Thank you for pushing me academically and for providing me with the tools I needed to complete my research. Lastly, thank you for your advice and direction throughout my studies.

Second, I would like to thank my labmates in the Spacecraft Robotics Lab (SRL). To Dr. Richard Zappulla II, Dr. Josep Virgili-Llop, and Dr. Hyeongjun Park, thank you for instantly making me feel like a part of the SRL team and for sharing your knowledge on the test bed and spacecraft guidance. To all past and current members of the SRL team, thank you for giving me an outlet to discuss research ideas and for taking my mind off of my work when I needed a break.

Third, to my biggest fans, coming home to you is something I look forward to every day; you give me the motivation I need to keep going. Of course, I would be lost in this life journey without my amazing wife and best friend. Thank you for always supporting me and my career choices, and for taking care of our family. Thank you for listening to me vent and work through research problems, even after a day of arguing with toddlers. You and the kids are my purpose, and without you, none of this would have been possible.

THIS PAGE INTENTIONALLY LEFT BLANK

Part I

Introductory Material

THIS PAGE INTENTIONALLY LEFT BLANK

CHAPTER 1:
Introduction

Spacecraft Rendezvous and Proximity Operations (RPO) have become a critical component across the spectrum of space activities. Applications of RPO range from the nowadays routine docking to the International Space Station (ISS), to spacecraft formation flying, servicing and inspection, on-orbit assembly, and even asteroid missions. Specifically, the problem of conducting RPO around an object that is tumbling, or uncontrolled, has been gaining research interest over the past two decades, primarily for applications of servicing and inspecting non-functioning satellites. In previous literature, the problem is addressed from a guidance and control perspective, with the focus of devising algorithms to conduct such maneuvers. However, a more fundamental analysis, not specific to a certain algorithm, is lacking.

Generally, spacecraft relative translational and rotational dynamics are treated separately. Traditional equations of motion for relative translation treat the spacecraft as a point mass, while a rigid body assumption is imposed for rotational motion. It has been shown, however, that when considering relative motion between two rigid bodies coupling of translational and rotational motions exists [1], [2]. In the problem of docking with, or maneuvering close to, a tumbling object where both position and attitude requirements are imposed simultaneously, the inherent coupling would affect maneuver execution. Therefore, it is important to accurately represent the relative motion between the two spacecraft in order to account for the tumbling motion in a guidance and control scheme. This spacecraft relative motion dynamical framework has not been fully analyzed in literature.

There is a rich history of spacecraft rendezvous and docking missions starting as early as 1966 with the Gemini program, and continuing with the Apollo program, Russian modules, Space Shuttle missions to the ISS, and the European Automated Transfer Vehicle (ATV) [3]. The earliest U.S. on-orbit rendezvous and repair missions occurred in 1973 when Skylab was repaired by the crew during a series of space walks [4] and in 1984, when astronauts on-board the Space Shuttle retrieved, repaired, and redeployed the Solar Maximum satellite [5]. In these early missions, crew involvement in the rendezvous and docking phases was necessary. Technology developments in autonomous rendezvous and docking capabilities have been

demonstrated in a series of experimental missions over the last decade, nicely summarized by Nolet [6] as well as Boyarko [7]. These experimental missions have greatly contributed to the technological advancements required for autonomous rendezvous and docking; however, from a guidance and control aspect, trajectory generation still required the involvement of mission planners [8].

In 2011, the results of a decadal study completed by the National Research Council urged the National Aeronautics and Space Administration (NASA) to assess the technology needs in order to meet the requirements of future planetary missions [9], [10]. Within those studies, NASA reported that the Guidance, Navigation & Control (GNC) area is one of the highest technical priorities, given the rising complexity of space missions. Specifically, the need for autonomous trajectory generation was highlighted. The on-board algorithms to perform this task must offer optimality when possible, robustness, and most importantly, safety [9], [10]. The need for safety in autonomous spacecraft operations is also highlighted by the rare, but detrimental, mishaps that have occurred. The prime example is the collision between the Iridium and Cosmos satellites, in 2009, which resulted in a significant debris cloud threatening many Low Earth Orbit (LEO) spacecraft [11]. Although the Iridium-Cosmos incident is not related to rendezvous operations, it highlights the severity of the consequences resulting from a collision. NASA's Demonstration of Autonomous Rendezvous Technology (DART) mission also experienced a collision during close proximity maneuvers [12], although not as severe as the Iridium-Cosmos incident. As space missions become more complex, and the environment more congested, constraint handling must be one of the main characteristics of an on-board GNC algorithm. A recent survey of spacecraft formation-flying missions highlights the need for autonomous GNC to meet future challenges [13].

With this mindset, the aerospace research community is experiencing a trend toward iterative-based on-board guidance methods, a term coined Computational Guidance & Control (CG&C) [14]. Advancements in computing technology enable application of such algorithms to systems for on-board computation of reliable, and safe, control actions [14], [15].

1.1 Research Questions

Implementation of an autonomous GNC algorithm raises some important questions. First, before even trying to iteratively solve a control problem, can one be certain that the maneuver is feasible (i.e., does a solution exist)? Second, if the problem is feasible, does the algorithm ensure convergence to a solution and can one know a priori if the problem can be solved within the allotted time? Finally, assuming the problem can be repeatedly solved in a feedback control framework, is the resulting system response stable? These questions were the motivating elements for this research.

Research Objectives

With inspiration from recent advancements in CG&C, this research analyzed the problem of conducting autonomous RPO maneuvers around a tumbling satellite. A spacecraft in an arbitrary Earth orbit, referred to as the chief, in a tumbling state of motion is considered. A controlled spacecraft, referred to as the deputy, is tasked with approaching the tumbling chief and reaching a desired relative state (e.g., docking), as depicted in Figure 1.1. The focus of this research was to analyze the 6-Degrees of Freedom (DOF) relative dynamics of this scenario and assess its reachability characteristics. Before any control method was applied, a fundamental question was answered to determine if a maneuver is feasible within predefined constraints. Among the many control methods that can be used in scenario, Model Predictive Control (MPC) stands out due to its inherent ability to enforce constraints while optimizing performance. In this research, MPC methods were leveraged to design and implement an algorithm to conduct these RPO maneuvers, taking into account control and collision avoidance constraints. More specifically, the following research questions were answered:

1. Reachability Analysis Objective: Given a desired final relative state, and bounded control input, what are the possible initial conditions from which a maneuver can be successfully completed in a given amount of time?
2. Guidance and Control Objective: Assuming the desired relative state is reachable, how can the MPC framework be used to generate a stabilizing feedback control law in the presence of constraints, and how does this solution compare to an optimal solution?

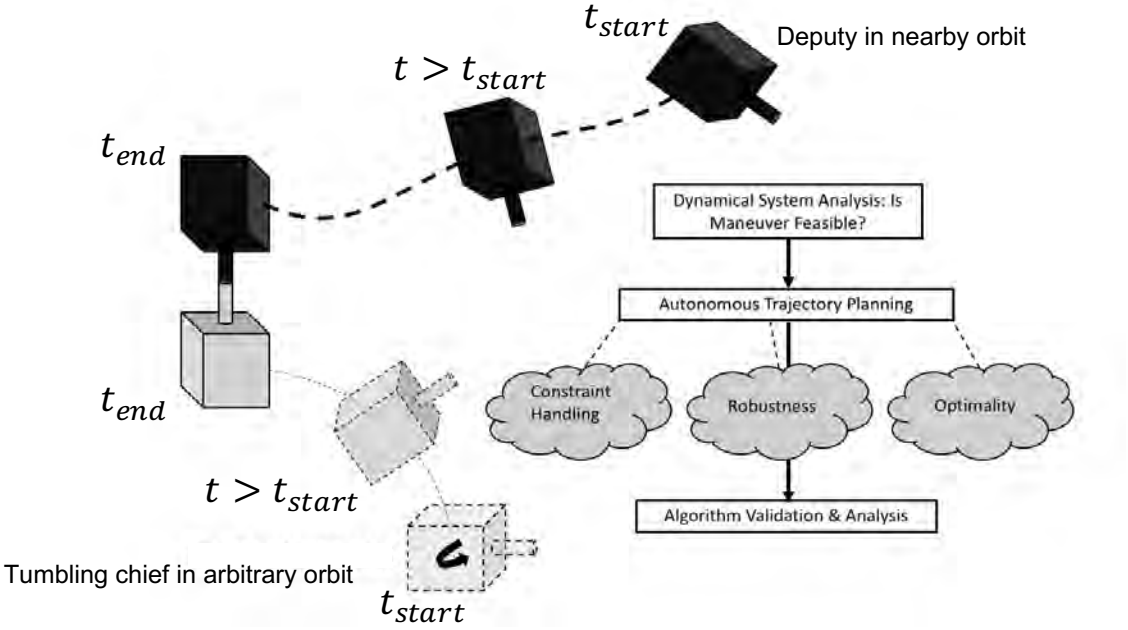

Figure 1.1. Depiction of research objective.

1.2 Research Scope and Assumptions

In order to accomplish the research objective, the following research tasks were defined:

1. Formulation of spacecraft relative roto-translational kinematics and dynamics.
2. Reachability analysis of relative roto-translational motion.
3. Autonomous guidance algorithm development for relative roto-translational control.

The focus of the first task was on modeling of spacecraft relative roto-translational motion, leveraging existing models and methods published in literature. In particular, this task aimed to formulate simplified models, well-suited for reachability analysis. The second task applied reachability analysis techniques to the resulting dynamic models to answer the first research objective. Using results and insights gained from the first two tasks, an autonomous guidance algorithm was developed for constrained roto-translational maneuvers. Following the recent trends in CG&C algorithms, the focus of this task was on MPC-based approaches.

In accomplishing the research objectives, the following main assumptions were made:

1. The chief and deputy spacecraft are rigid bodies in Keplerian restricted two-body orbital motion; perturbing forces and torques are neglected.

2. The chief spacecraft is uncontrolled, while the deputy is fully actuated with the ability to create a force and torque vector in any direction.
3. There is no interaction between control forces and torques.
4. The deputy has full knowledge of the relative state and the chief's orbital and tumbling motion; i.e., the relative navigation problem is considered a priori solved and is not treated in this research.

In addition to the assumptions above, some parts of the dissertation required further assumptions, which are detailed in the appropriate sections.

1.3 Dissertation Outline

The dissertation comprises four parts, and eight chapters. The contents of each part and chapter are summarized below.

- Part I: Introductory Material
  - Chapter 1: Introduces and motivates the research topic.
  - Chapter 2: Reviews relevant literature and presents the 6-DOF spacecraft relative motion model that is used for this research.
- Part II: Applied Reachability Analysis
  - Chapter 3: Introduces the reachability concepts used herein and describes the methodology used to conduct the analysis and visualize results.
  - Chapter 4: Presents analysis for the case of the chief in circular orbit, rotating on the orbit plane about its z body axis at a constant rate. First, simplified kinematic and dynamic models for this case are introduced through appropriate assumptions. Reachability analysis of the simplified models is then conducted and results are presented.
  - Chapter 5: Extends the analysis from Chapter 4 to study the reachability characteristics of the full 6-DOF relative dynamics for cases where the chief, in circular orbit, is rotating on the plane about its z body axis at a constant rate or is rotating about an off-principal axis (i.e., tumbling).
- Part III: Autonomous Guidance and Control Algorithm Development
  - Chapter 6: Introduces the MPC framework, and presents an autonomous guidance algorithm for rendezvous with a tumbling object. An applied reachability

concept is defined to analyze reachability characteristics of a closed-loop system, culminating in the closed-loop reachability analysis of the developed MPC algorithm.

  - Chapter 7: Presents numerical simulation results from specific test scenarios comparing the performance of the developed MPC algorithm to minimum time optimal solutions.

- Part IV: Concluding Material
  - Chapter 8: Summarizes the contributions and results of this research and offers recommendations for future work in this field.

1.4 Summary

This chapter introduced the topic that was studied in this dissertation. After identifying the research gap, the research objectives were defined in terms of questions that were answered by the work herein. The scope of this research and the underlying assumptions were stated. The chapter closed with an outline of the dissertation. A complete list of the different rendezvous scenarios studied during this research is included in Chapter 8.

CHAPTER 2:
Derivation of 6-DOF Relative Roto-Translational Dynamics

This chapter lays the foundation for this research. Relevant literature on the topic of RPO with a tumbling object is discussed, and the gaps addressed by this dissertation are illustrated. The specific problem at hand is defined in detail, and different ways that have been used in literature to represent roto-translational motion are discussed. Finally, the derivation of the spacecraft relative motion model used in this research is provided.

2.1 Previous Literature

The problem of autonomous rendezvous and docking with a tumbling object has only been the subject of publications over the past two decades. The earliest work on this topic was published in 2003 by Henshaw [16], who studies optimal trajectory planning approaches for docking with an uncontrolled spacecraft. In 2006, Ma et al. [17] approach the problem from an optimal control perspective, and show numerical results for a planar case study. Nolet [6] presents an overarching GNC framework for docking with a tumbling object, along with experimental demonstrations through the Synchronized Position Hold Engage and Reorient Experimental Satellites (SPHERES) facility on the ISS. In this work, the coupling between translational and rotational dynamics is not considered. Additionally, the path-planning and control tasks are separated, and a glideslope approach is used for on-board trajectory generation. Similarly, Fejzić [18] develops a spline-based path planning method to handle obstacle avoidance, which is also validated on the SPHERES testbed. This algorithm is limited to a single stationary spherical obstacle. As in Nolet's work, the control task is separated from the path planning task. In parallel to Nolet and Fejzić, McCamish [19] presents a Linear Quadratic Regulator (LQR)/Artificial Potential Function (APF)-based algorithm for translational control of multiple spacecraft in close proximity, which is experimentally validated through hardware-in-the loop facilities at Naval Postgraduate School (NPS), and through the SPHERES testbed. A few years later, Boyarko [7], [20] extends the work in [17] by presenting the optimal control formulation, and numerical solution, for close-range rendezvous and docking with a tumbling satellite in a 6-DOF

environment. The proposed dynamic model includes 20 states, and the rotational motion is not formulated as a relative state. Additionally, a rapid trajectory generation method is proposed based on an Inverse Dynamics in the Virtual Domain (IDVD) approach, which requires the off-line solution to a Nonlinear Programming (NLP) problem. The IDVD algorithm solves for both attitude and translational trajectories [7]. The dimensionality of the problem considered makes the IDVD algorithm computationally expensive, and since a NLP solver is required, there is no convergence guarantee. A closed-loop implementation of the IDVD algorithm for docking to a tumbling target is later implemented by Ventura et al. [21] and experimentally characterized by Wilde et al. [22] on an air-bearing testbed at NPS. The experimental validation of the IDVD algorithm demonstrates the applicability of a computation-based guidance and control method on a real system. Michael et al. [23] follow a similar dynamic modeling approach to Boyarko's in order to formulate and solve an optimal control problem for docking with an uncontrolled spacecraft, but without discussing the feasibility of on-board computation. Notably, both Boyarko and Michael use linearized relative translation models, restricting their work to a chief spacecraft in circular orbit. More recently, Sternberg and Miller [24] present a parametrization technique to generate fuel-optimal trajectories for a spacecraft to rendezvous with a tumbling object, but only consider the translational aspect of the maneuver.

The work summarized above shows an extensive interest in the development of autonomous computational guidance methods for RPO with a tumbling spacecraft, but without studying or exploiting the inherent coupling between translational and rotational motions. Literature on the coupled control problem, specifically for RPO with a tumbling object, is not nearly as expansive and focuses mainly on feedback control approaches. Lu et al. [25] present an integrated coupled dynamics formulation, through the assumption that body-fixed thrusters provide coupled control forces and torques. Within this integrated dynamics scheme, they develop a robust sliding mode control method, based on two sliding surfaces. A related publication shows a robust sliding mode control approach applied only to the attitude synchronization aspect for docking with a tumbling satellite [26]. These applications of sliding mode control, however, do not incorporate control or state constraints. Sun and Huo [27] present a similar coupled motion model, but using Modified Rodrigues Parameters (MRP) for attitude parametrization instead of quaternions. They then develop a nonlinear adaptive controller for the coupled dynamics, but without incorporating control

or state constraints.

Previous literature in this subject area does not offer any insights on the relative roto-translational dynamics, and this is one of the gaps addressed by this research. Additionally, coupled control methods that have been previously developed are classical feedback controllers, which offer robustness to uncertainties but do not directly handle constraints. Constraint handling capability is an important consideration for autonomous systems with implementations of CG&C algorithms.

2.2 Problem Definition

Consider a chief spacecraft in arbitrary Earth orbit, in a tumbling state of motion, and a deputy spacecraft in a nearby orbit, as depicted in Figure 2.1. The deputy is tasked with approaching the chief, and achieving a desired relative state. An Earth Centered Inertial (ECI) Cartesian Coordinate System (CCS), I, is defined with its origin at the center of the Earth, x-axis pointing towards the vernal equinox, z-axis pointing towards the North Pole, and y-axis completing the right-handed coordinate system. Although the Earth's equatorial plane changes slightly over time, the ECI CCS is commonly treated as a Newtonian inertial reference frame by referring to the equator and equinox at a particular point in time [28]. The vectors $\vec{r}_c$ and $\vec{r}_d$ define the inertial positions of the chief and deputy spacecraft, respectively. Note that an unresolved geometric vector is denoted by an arrow over the variable ($\vec{a}$), while a resolved vector in a specified CCS is denoted by a bold symbol with the CCS indicated as a superscript on the right side ($\mathbf{a}^{\mathsf{C}}$). A superscript on the left side of a variable accompanies a time derivative, indicating the reference frame with respect to which the differentiation is performed (${}^{\mathsf{C}}\dot{\vec{a}}$). As perturbing forces are neglected, the orbital motion of the chief and deputy can be expressed by the Keplerian restricted two-body equations [28],

$$ {}^{\mathsf{I}}\ddot{\vec{r}}_c = -\frac{\mu}{R_c^3}\vec{r}_c, \tag{2.1} $$

$$ {}^{\mathsf{I}}\ddot{\vec{r}}_d = -\frac{\mu}{R_d^3}\vec{r}_d + \frac{1}{m_d}\vec{F}_d, \tag{2.2} $$

where μ is the Earth's gravitational constant, $R_c = ||\vec{r}_c||$, $R_d = ||\vec{r}_d||$, $\vec{F}_d$ is the control force acting on the deputy, and m_d is the deputy's mass.

The relative motion between the two spacecraft is derived by defining the relative position vector, $\vec{\rho} = \vec{r}_d - \vec{r}_c$, and taking its time derivative with respect to I twice,

$$\begin{aligned} {}^{\mathsf{I}}\ddot{\vec{\rho}} &= {}^{\mathsf{I}}\ddot{\vec{r}}_d - {}^{\mathsf{I}}\ddot{\vec{r}}_c, \\ {}^{\mathsf{I}}\ddot{\vec{\rho}} &= -\frac{\mu}{R_d^3}\vec{\rho} + \frac{\mu\left(R_d^3 - R_c^3\right)}{R_c^3 R_d^3}\vec{r}_c + \frac{1}{m_d}\vec{F}_d. \end{aligned} \tag{2.3}$$

Traditionally, the relative motion is written with respect to a chief orbit-fixed Local Vertical Local Horizontal (LVLH) CCS, L, with origin at the chief's center of mass, its x-axis pointing radially outward, z-axis perpendicular to the orbit plane, and y-axis completing the right-handed coordinate system. Expressing derivatives and resolving (2.3) in L leads to the well-known nonlinear relative motion models, as well as approximate linearized models after making appropriate assumptions (e.g., the Clohessy-Wiltshire (CW) model) [2]. A body-fixed CCS is defined for the chief and deputy spacecraft, with origin at the respective center of mass, denoted by C and D, respectively.

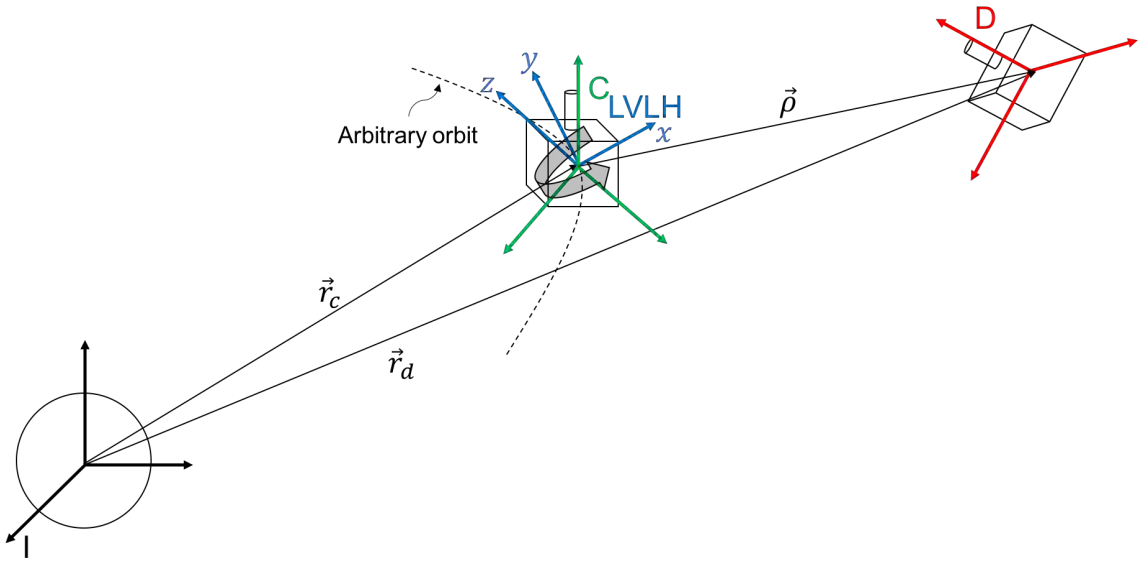

Figure 2.1. Depiction of coordinate systems and vectors for the problem of rendezvous with a tumbling object.

Traditional relative motion models only account for relative translation between the two spacecraft's centers of mass. With the chief in a tumbling state, the relative attitude between the two spacecraft must also be incorporated. As a result, this research considers

relative roto-translational motion models, combining relative translation and rotation states, that incorporate the chief's tumbling motion into the equations of motion.

2.3 Representations of Roto-Translational Motion

In classical mechanics, the translational and rotational equations of motion for a rigid body are decoupled and derived independently. The translational equations describe the motion of the rigid body center of mass, while rotational motions describe the orientation of a body-fixed CCS with respect to an inertial CCS. In this manner, the full 6-DOF motion model is reduced to two 3-DOF models. Much of the previous literature presented roto-translational dynamic models by combining the two 3-DOF models (see for example [20], [29]), or by introducing dynamic coupling between translational and rotational motions due to thrust alignment or gravity gradient considerations (see for example [25], [27], [30]–[32]). These types of models are effective and use intuitive states (e.g., position, velocity), but they are often derived with respect to the chief's LVLH CCS. As a result, when the chief is tumbling, the desired relative state becomes time-varying.

Another approach for deriving coupled relative motion models is presented by Segal and Gurfil [1], where a kinematic coupling between translational and rotational states is introduced by considering the relative motion between off-center of mass points on the chief and deputy rigid bodies (i.e., relative motion between the two docking ports) . Their results show that the kinematically coupled model is a more accurate representation of relative motion between two rigid spacecraft, than the widely used CW model [1], [2]. It is assumed that the deputy body-fixed coordinate system is always aligned with the chief orbital frame, and relative attitude control is not considered. This assumption is later removed to allow for a relative motion model that can be used for precise rendezvous maneuvers with a tumbling chief [33], [34]. The kinematically coupled model is useful for precision close-range maneuvers, but is not widely applicable in the context of RPO maneuvers.

Arguably the most elegant way to express roto-translational motion is to represent the relative state as a general rigid body screw displacement (translation + rotation). Similar to the way rigid body rotational kinematics can be expressed through a variety of representations (Direction Cosine Matrix (DCM), Euler Angles, Quaternions, etc.) [35], there exist different schemes to express general screw displacements. In this manner, translational and rotational

kinematics can be combined into one state variable, leading to a compact expression of the 6-DOF dynamics.

The topic of general screw displacement representation has been popular in literature from the early 1970s, especially in the computer graphics and robotics communities. Rooney [36] presents a comprehensive comparison between two classes of screw displacement representations: point transformations and line transformations. The former defines 3-dimensional space as a collection of points and screw representations operate on those points through homogeneous coordinates. The latter defines 3-dimensional space as a collection of lines and screw representations involve dual numbers. Amongst the three different representations of point transformations considered in this paper, Rooney claims that the real 4-by-4 homogeneous transformation matrix is the best and most widely used [36]. Amongst four different representations of line transformations, Rooney claims that the unit dual quaternion is the best [36]. A direct comparison between the two "winners" is not included, however. A similar comparison is presented by Funda and Paul [37]. The authors compare four different representations in terms of compactness and computational efficiency, also offering a comparison between the homogeneous transformation matrix and the unit dual quaternion. Their concluding remarks indicate that the unit dual quaternion is the most compact and efficient representation of general rigid body screw displacements [37].

Compact representations of rigid body motion have been used in literature for spacecraft applications. Holguin et al. [38] present a geometric mechanics-based guidance approach for spacecraft rendezvous, by formulating the spacecraft dynamics in the special Euclidean configuration space SE(3) . In this work, the guidance and control schemes are treated separately by first solving for a reference trajectory and using a tracking controller to follow the prescribed trajectory. However, no considerations on constraints are included in the formulation. Similarly, Lee and Vukovich [39] present a robust adaptive sliding mode controller on SE(3) for spacecraft rendezvous, including higher-order gravitational perturbations and a rigorous Lyapunov stability analysis. Geometric mechanics offers a compact representation of the 6-DOF relative dynamics, through the configuration manifold SE(3); however, special considerations must be taken in order to perform integrations on the geometric manifold, as well as in the formulation of optimal control problems [40], [41]. Another application of an SE(3)-based control scheme is presented by Misra et al. [42], for the problem of soft landing on an asteroid.

Literature on the theoretical aspects of dual quaternions dates back to the late 1800s, but their use for spacecraft applications is fairly recent. A good overview of the mathematical preliminaries behind modeling of rigid body motion using dual quaternions is included in [43], [44]. Wang et al. [45] present the coupled 6-DOF dynamics for spacecraft relative motion in terms of dual quaternions, and a Proportional-Derivative (PD)-type coupled control law along with a rigorous stability analysis. More generally, Price [43] presents the problem of nonlinear dual quaternion-based tracking of rigid body motion using a sliding mode control method. Filipe [44] studies the problem of spacecraft relative pose control and estimation using dual quaternions. Specifically, a dual quaternion-based adaptive control approach, along with stability analysis, is presented for coupled attitude and position tracking which requires no prior knowledge of the spacecraft's mass and inertia properties [44], [46]. Additionally, a pose estimation approach is presented through a dual quaternion-based multiplicative Extended Kalman Filter [44]. Finally, Lee and Mesbahi [47], [48] present a dual quaternion-based MPC approach for constrained precision landing, showing a capability for on-board, optimization-based, 6-DOF guidance and control.

Although compact representations of rigid body screw displacements offer elegant ways to write the roto-translational dynamic equations, these states are not necessarily intuitive. The dual quaternion, for example, is quite difficult to visualize. Since the main goal of this dissertation is to analyze the roto-translational dynamics, the relative motion equations are derived using the traditional states (e.g., position, velocity) while taking into account the chief's tumbling motion. As mentioned at the beginning of Section 2.3, traditional models are derived with respect to the LVLH CCS. In the following section, a derivation of the 6-DOF relative roto-translational dynamics is presented with respect to the chief's body-fixed CCS, in order to incorporate its tumbling motion into the equations of motion.

2.4 Chief Perspective Model

The content of this section was published at the 2018 Science and Technology Forum (American Astronautical Society Spaceflight Mechanics Meeting) [49].

2.4.1 Relative Translational Motion

The general relative translation dynamic equation was shown in (2.3). The transport theorem allows for time derivatives to be taken with respect to non-inertial reference frames [50]. Invoking the transport theorem and taking the time derivative of the relative position vector twice with respect to C yields,

$$ {}^{\mathsf{I}}\ddot{\vec{\rho}} = {}^{\mathsf{C}}\ddot{\vec{\rho}} + \dot{\vec{\omega}}_{\mathsf{C/I}} \times \vec{\rho} + 2\vec{\omega}_{\mathsf{C/I}} \times {}^{\mathsf{C}}\dot{\vec{\rho}} + \vec{\omega}_{\mathsf{C}/\mathcal{I}} \times (\vec{\omega}_{\mathsf{C/I}} \times \vec{\rho}) , \tag{2.4} $$

where $\vec{\omega}_{\mathsf{C/I}}$ is the angular velocity of C with respect to I, and $\dot{\vec{\omega}}_{\mathsf{C/I}} = {}^{\mathsf{I}}\dot{\vec{\omega}}_{\mathsf{C/I}} = {}^{\mathsf{C}}\dot{\vec{\omega}}_{\mathsf{C/I}}$.

Combining (2.3) and (2.4) results in the following expression,

$$ \begin{aligned} {}^{\mathsf{C}}\ddot{\vec{\rho}} &= -\frac{\mu}{R_d^3}\vec{\rho} + \frac{\mu\left(R_d^3 - R_c^3\right)}{R_c^3 R_d^3}\vec{r}_c + \frac{1}{m_d}\vec{F}_d - \dot{\vec{\omega}}_{\mathsf{C/I}} \times \vec{\rho} \\ &\quad -2\vec{\omega}_{\mathsf{C/I}} \times {}^{\mathsf{C}}\dot{\vec{\rho}} - \vec{\omega}_{\mathsf{C}/\mathcal{I}} \times (\vec{\omega}_{\mathsf{C/I}} \times \vec{\rho}) . \end{aligned} \tag{2.5} $$

Finally, resolving (2.5) in C gives the following translational equation of motion,

$$ \begin{aligned} \ddot{\boldsymbol{\rho}}^{\mathsf{C}} &= -\frac{\mu}{R_d^3}\boldsymbol{\rho}^{\mathsf{C}} + \frac{\mu\left(R_d^3 - R_c^3\right)}{R_c^3 R_d^3}\mathbf{r}_c^{\mathsf{C}} + \frac{1}{m_d}\mathbf{F}_d^{\mathsf{C}} - [\dot{\boldsymbol{\omega}}_{\mathsf{C/I}}^{\mathsf{C}}]^{\times}\boldsymbol{\rho}^{\mathsf{C}} \\ &\quad -2[\boldsymbol{\omega}_{\mathsf{C/I}}^{\mathsf{C}}]^{\times}\dot{\boldsymbol{\rho}}^{\mathsf{C}} - [\boldsymbol{\omega}_{\mathsf{C}/\mathcal{I}}^{\mathsf{C}}]^{\times}\left([\boldsymbol{\omega}_{\mathsf{C/I}}^{\mathsf{C}}]^{\times}\boldsymbol{\rho}^{\mathsf{C}}\right), \end{aligned} \tag{2.6} $$

where $[]^{\times}$ is the skew-symmetric matrix representing the vector cross-product operator. It is evident that the translational relative equation in (2.6) is coupled to the chief's tumbling motion, governed by the rotational equation of motion (Euler's equation) [35],

$$ \dot{\boldsymbol{\omega}}_{\mathsf{C/I}}^{\mathsf{C}} = J_c^{-1}\left(-[\boldsymbol{\omega}_{\mathsf{C/I}}^{\mathsf{C}}]^{\times} J_c \boldsymbol{\omega}_{\mathsf{C/I}}^{\mathsf{C}}\right), \tag{2.7} $$

where J_c is the chief's inertia matrix. Equation (2.6) is also a function of the chief's orbital motion (R_c, $\mathbf{r}_c^{\mathsf{C}}$). It is important to note that for an arbitrary chief orbit, the variable R_c is not constant.

2.4.2 Relative Rotational Motion

In order to describe the orientation of the deputy with respect to the chief, an attitude parametrization scheme must be selected. Unit quaternions are often preferred, from a numerical perspective, as a singularity-free representation of attitude. The unit quaternion, $q_{\mathsf{D/C}}$ describes the orientation of the deputy with respect to the chief and is comprised of a vector part and a scalar part, $q_{\mathsf{D/C}} = [\bar{q}\ q_4]^T = [q_1\ q_2\ q_3\ q_4]^T$, and satisfies $||q_{\mathsf{D/C}}|| = 1$. The quaternion kinematic equation is [35],

$$\dot{q}_{\mathsf{D/C}} = \frac{1}{2}\tilde{Q}\boldsymbol{\omega}^{\mathsf{D}}_{\mathsf{D/C}}, \tag{2.8}$$

where

$$\tilde{Q} = \begin{bmatrix} q_4 & -q_3 & q_2 \\ q_3 & q_4 & -q_1 \\ -q_2 & q_1 & q_4 \\ -q_1 & -q_2 & -q_3 \end{bmatrix}. \tag{2.9}$$

Although the unit quaternion offers a singularity-free representation, it requires four parameters to describe the 3-DOF orientation. As a result, the four parameters must adhere to the unit constraint: $q_1^2 + q_2^2 + q_3^2 + q_4^2 = 1$. It may be desirable to use a minimal attitude representation (i.e., orientation represented by three parameters). MRPs are often used as an alternative to quaternions as they allow representation of large attitude maneuvers that are less than a full 360 degree rotation. The MRP vector, $\boldsymbol{\sigma} = [\sigma_1,\ \sigma_2,\ \sigma_3]^T$, is a stereographic projection of the set of unit quaternions (four-dimensional unit sphere) onto a particular hyperplane [50]. The three parameters are given by,

$$\sigma_i = \frac{q_i}{1 + q_4},\ i = 1,\ 2,\ 3. \tag{2.10}$$

The MRP can also be expressed in terms of the principal rotation by,

$$\boldsymbol{\sigma} = \hat{e} \tan\frac{\phi}{4}, \tag{2.11}$$

where $\hat{e}$ is the Euler axis of rotation, and ϕ is the rotation angle. It is evident in (2.11) that the singularity occurs at $\phi = \pm 2\pi$. Additionally, the "shadow" MRP, $\boldsymbol{\sigma}^S$, corresponding to the orientation given by $-q$ (which is equivalent to the orientation given by q), is a distinct

set of parameters representing the same orientation. This characteristic allows to switch between $\boldsymbol{\sigma}$ and $\boldsymbol{\sigma}^S$ at $\phi = \pi$ (i.e., orientations with $\phi \leq \pi$ are represented by $\boldsymbol{\sigma}$, while orientations with $\phi > \pi$ are represented by $\boldsymbol{\sigma}^S$). As a result, the magnitude of the MRP vector is bounded, $0 \leq \boldsymbol{\sigma}^T\boldsymbol{\sigma} \leq 1$ [50].

Let $\boldsymbol{\sigma}$ represent the relative attitude of the deputy with respect to the chief, and let $\sigma^2 = \boldsymbol{\sigma}^T\boldsymbol{\sigma}$. The MRP kinematic equation is [50],

$$\dot{\boldsymbol{\sigma}} = \frac{1}{4}\tilde{B}\boldsymbol{\omega}^{\mathsf{D}}_{\mathsf{D/C}}, \tag{2.12}$$

where

$$\tilde{B} = (1 - \sigma^2)I_3 + 2[\boldsymbol{\sigma}]^{\times} + 2\boldsymbol{\sigma}\boldsymbol{\sigma}^T \tag{2.13}$$

and I_3 is the 3-by-3 identity matrix.

The relative angular velocity is defined by the following equation,

$$\vec{\omega}_{\mathsf{D/C}} = \vec{\omega}_{\mathsf{D/I}} - \vec{\omega}_{\mathsf{C/I}}. \tag{2.14}$$

The relative dynamic equation can then be derived by taking the time derivative of (2.14),

$${}^{\mathsf{I}}\dot{\vec{\omega}}_{\mathsf{D/C}} = {}^{\mathsf{I}}\dot{\vec{\omega}}_{\mathsf{D/I}} - {}^{\mathsf{I}}\dot{\vec{\omega}}_{\mathsf{C/I}} = {}^{\mathsf{D}}\dot{\vec{\omega}}_{\mathsf{D/I}} - {}^{\mathsf{C}}\dot{\vec{\omega}}_{\mathsf{C/I}}. \tag{2.15}$$

The attitude dynamic motion of the deputy and chief with respect to the inertial frame (${}^{\mathsf{D}}\dot{\vec{\omega}}_{\mathsf{D/I}}$ and ${}^{\mathsf{C}}\dot{\vec{\omega}}_{\mathsf{C/I}}$ respectively) are defined by Euler's equation [35]. Using the transport theorem, the following equation can be written,

$${}^{\mathsf{I}}\dot{\vec{\omega}}_{\mathsf{D/C}} = {}^{\mathsf{D}}\dot{\vec{\omega}}_{\mathsf{D/C}} + \vec{\omega}_{\mathsf{D/I}} \times \vec{\omega}_{\mathsf{D/C}}. \tag{2.16}$$

Combining (2.15) and (2.16), and plugging in Euler's equation for the deputy rotational motion provides the following equation for the relative rotational motion,

$$\begin{aligned} {}^{\mathsf{D}}\dot{\vec{\omega}}_{\mathsf{D/C}} &= J_d^{-1}\left[\vec{M}_d - (\vec{\omega}_{\mathsf{D/C}} + \vec{\omega}_{\mathsf{C/I}}) \times J_d(\vec{\omega}_{\mathsf{D/C}} + \vec{\omega}_{\mathsf{C/I}})\right] \\ &\quad - {}^{\mathsf{C}}\dot{\vec{\omega}}_{\mathsf{C/I}} - \vec{\omega}_{\mathsf{C/I}} \times \vec{\omega}_{\mathsf{D/C}}, \end{aligned} \tag{2.17}$$

where $\vec{M}_d$ is the control torque applied to the deputy, and J_d is the deputy's inertia matrix.

Let $C_{\mathsf{D/C}}$ be the DCM corresponding to the unit quaternion $q_{\mathsf{D/C}}$, which transforms a resolved vector from the C CCS to the D CCS. As a proper DCM, $C_{\mathsf{D/C}}$ belongs to the group, SO(3), of three by three orthogonal matrices with determinant equal to one. The mapping from a unit quaternion to the corresponding DCM is shown in (2.18) [35], [50],

$$C_{\mathsf{D/C}} = \begin{bmatrix} 1-2(q_2^2+q_3^2) & 2(q_1q_2+q_3q_4) & 2(q_1q_3-q_2q_4) \\ 2(q_2q_1-q_3q_4) & 1-2(q_1^2+q_3^2) & 2(q_2q_3+q_1q_4) \\ 2(q_3q_1+q_2q_4) & 2(q_3q_2-q_1q_4) & 1-2(q_1^2+q_2^2) \end{bmatrix}. \tag{2.18}$$

Finally, (2.17) can be resolved in D,

$$\begin{aligned} \dot{\boldsymbol{\omega}}^{\mathsf{D}}_{\mathsf{D/C}} &= J_d^{-1}\left[\mathbf{M}_d^{\mathsf{D}} - [\boldsymbol{\omega}^{\mathsf{D}}_{\mathsf{D/C}} + C_{\mathsf{D/C}}\boldsymbol{\omega}^{\mathsf{C}}_{\mathsf{C/I}}]^{\times} J_d(\boldsymbol{\omega}^{\mathsf{D}}_{\mathsf{D/C}} + C_{\mathsf{D/C}}\boldsymbol{\omega}^{\mathsf{C}}_{\mathsf{C/I}})\right] \\ &\quad -C_{\mathsf{D/C}}\dot{\boldsymbol{\omega}}^{\mathsf{C}}_{\mathsf{C/I}} - [C_{\mathsf{D/C}}\boldsymbol{\omega}^{\mathsf{C}}_{\mathsf{C/I}}]^{\times}\boldsymbol{\omega}^{\mathsf{D}}_{\mathsf{D/C}}. \end{aligned} \tag{2.19}$$

As with the translational equation, the attitude equation is a function of the chief's tumbling motion defined in (2.7).

2.4.3 6-DOF Relative Roto-Translation Model

For notational compactness, the following variables are defined:

- $\boldsymbol{\rho} = \boldsymbol{\rho}^{\mathsf{C}}$; relative position vector resolved in C
- $\mathbf{v} = \dot{\boldsymbol{\rho}}^{\mathsf{C}}$; relative velocity vector resolved in C
- $q = q_{\mathsf{D/C}}$; relative attitude unit quaternion
- $\boldsymbol{\sigma}$; relative attitude MRP vector
- $\boldsymbol{\omega}^{\mathsf{D}} = \boldsymbol{\omega}^{\mathsf{D}}_{\mathsf{D/C}}$; relative angular velocity vector resolved in D
- $\mathbf{F}_d = \mathbf{F}_d^{\mathsf{C}}$; control force vector acting on the deputy resolved in C
- $\mathbf{M}_d^{\mathsf{D}}$; control torque vector acting on the deputy resolved in D
- $\boldsymbol{\omega}_c = \boldsymbol{\omega}^{\mathsf{C}}_{\mathsf{C/I}}$; chief angular velocity vector resolved in C

The full 6-DOF model describing the relative roto-translational motion of the deputy with respect to the chief is written by (2.6), (2.8) or (2.12), and (2.19), and shown for completeness

in (2.20):

$$\dot{\boldsymbol{\rho}} = \mathbf{v} \tag{2.20a}$$

$$\dot{\mathbf{v}} = -\frac{\mu}{R_d^3}\boldsymbol{\rho} + \frac{\mu\left(R_d^3 - R_c^3\right)}{R_c^3 R_d^3}\mathbf{r}_c^{\mathsf{C}} + \frac{1}{m_d}\mathbf{F}_d - \left[J_c^{-1}\left(-[\boldsymbol{\omega}_c]^{\times} J_c \boldsymbol{\omega}_c\right)\right]^{\times}\boldsymbol{\rho} - 2[\boldsymbol{\omega}_c]^{\times}\mathbf{v} - [\boldsymbol{\omega}_c]^{\times}\left([\boldsymbol{\omega}_c]^{\times}\boldsymbol{\rho}\right) \tag{2.20b}$$

$$\dot{q} = \frac{1}{2}\tilde{Q}\boldsymbol{\omega}^{\mathsf{D}} \text{ or } \dot{\boldsymbol{\sigma}} = \frac{1}{4}\tilde{B}\boldsymbol{\omega}^{\mathsf{D}} \tag{2.20c}$$

$$\dot{\boldsymbol{\omega}}^{\mathsf{D}} = J_d^{-1}\left[\mathbf{M}_d^{\mathsf{D}} - [\boldsymbol{\omega}^{\mathsf{D}} + C_{\mathsf{D/C}}\boldsymbol{\omega}_c]^{\times} J_d(\boldsymbol{\omega}^{\mathsf{D}} + C_{\mathsf{D/C}}\boldsymbol{\omega}_c)\right] - C_{\mathsf{D/C}}\left[J_c^{-1}\left(-[\boldsymbol{\omega}_c]^{\times} J_c\boldsymbol{\omega}_c\right)\right] - [C_{\mathsf{D/C}}\boldsymbol{\omega}_c]^{\times}\boldsymbol{\omega}^{\mathsf{D}}. \tag{2.20d}$$

The above 6-DOF model is advantageous because the chief's tumbling motion is explicitly incorporated, a consequence of the original choice in this research of resolving all vectors in the chief's body CCS. The dynamic system in (2.20) is quite complex. The system is comprised of 13 (or 12) states and the equations of motion are nonlinear, coupled, and time-varying. By defining the state vector $x = [\boldsymbol{\rho},\ \mathbf{v},\ q \text{ (or } \boldsymbol{\sigma}),\ \boldsymbol{\omega}^{\mathsf{D}}]^T \in \mathbb{R}^{13(12)}$ and control vector $u = [\mathbf{F}_d,\ \mathbf{M}_d^{\mathsf{D}}]^T \in \mathbb{R}^6$, the system can be written in control-affine form,

$$\dot{x} = f(x,t) + Gu, \tag{2.21}$$

where $f \in \mathbb{R}^{13(12)\times 1}$ is the drift vector field from equations (2.20a) - (2.20d),

$$f = \begin{bmatrix} \mathbf{v} \\ -\frac{\mu}{R_d^3}\boldsymbol{\rho} + \frac{\mu\left(R_d^3 - R_c^3\right)}{R_c^3 R_d^3}\mathbf{r}_c^{\mathsf{C}} - \left[J_c^{-1}\left(-[\boldsymbol{\omega}_c]^{\times} J_c\boldsymbol{\omega}_c\right)\right]^{\times}\boldsymbol{\rho} - 2[\boldsymbol{\omega}_c]^{\times}\mathbf{v} - [\boldsymbol{\omega}_c]^{\times}\left([\boldsymbol{\omega}_c]^{\times}\boldsymbol{\rho}\right) \\ \frac{1}{2}\tilde{Q}\boldsymbol{\omega}^{\mathsf{D}} \ \left(\text{or } \frac{1}{4}\tilde{B}\boldsymbol{\omega}^{\mathsf{D}}\right) \\ -J_d^{-1}[\boldsymbol{\omega}^{\mathsf{D}} + C_{\mathsf{D/C}}\boldsymbol{\omega}_c]^{\times} J_d(\boldsymbol{\omega}^{\mathsf{D}} + C_{\mathsf{D/C}}\boldsymbol{\omega}_c) - C_{\mathsf{D/C}}\left[J_c^{-1}\left(-[\boldsymbol{\omega}_c]^{\times} J_c\boldsymbol{\omega}_c\right)\right] - [C_{\mathsf{D/C}}\boldsymbol{\omega}_c]^{\times}\boldsymbol{\omega}^{\mathsf{D}} \end{bmatrix} \tag{2.22}$$

and $G \in \mathbb{R}^{13(12)\times 6}$ is the constant control vector field,

$$G = \begin{bmatrix} 0_{3\times 3} & 0_{3\times 3} \\ \frac{1}{m_d} I_3 & 0_{3\times 3} \\ 0_{4(3)\times 3} & 0_{4(3)\times 3} \\ 0_{3\times 3} & J_d^{-1} \end{bmatrix}. \tag{2.23}$$

Although time does not explicitly appear in these equations, it is implicitly incorporated into the chief's parameters (R_c, $\mathbf{r}_c^{\mathsf{C}}$, $\boldsymbol{\omega}_c$). In some cases, closed form solutions for these parameters are known, and a simplified model can be derived. For the most general cases, values for these parameters can be obtained via numerical integration. This dissertation treats both of these instances. In Chapter 4, simplified models are derived, and used for reachability analysis, under specific assumptions on the chief's orbital and tumbling motions. In Chapter 5, reachability analysis is presented for the more general cases, where the dynamics remain in its unsimplified form.

2.4.4 Maintaining an Arbitrary Desired State

Generally, the goal of the rendezvous problem is to reach a desired relative state, x_d. In some applications, it may be required that the deputy spacecraft be able to maintain this state (e.g., for inspection or servicing purposes). By inspecting the 6-DOF relative roto-translational dynamics for rendezvous with a tumbling object in (2.20), it is clear than an arbitrary desired state is not an equilibrium state of this system (i.e., a control input would be required to maintain this condition). Assume that the desired condition x_d is reached at time t_f. In order to maintain the rendezvous condition, the following must hold,

$$0 = f(x_d, t) + G u_s, \text{ for } t = [t_f, \infty) \tag{2.24}$$

where u_s is the steady-state control input required to maintain rendezvous. From (2.24), the required control input is then,

$$u_s = -G^{+} f(x_d, t), \text{ for } t = [t_f, \infty), \tag{2.25}$$

where G^+ is the Moore-Penrose pseudoinverse of G given by,

$$G^+ = \begin{bmatrix} 0_{3\times3} & m_d I_3 & 0_{4(3)\times3} & 0_{3\times3} \\ 0_{3\times3} & 0_{3\times3} & 0_{4(3)\times3} & J_d \end{bmatrix}. \tag{2.26}$$

Given a specific scenario, this analysis allows for a quick assessment of the deputy spacecraft's capability to maintain a rendezvous condition within its control authority limits.

2.5 Summary

This chapter discussed relevant literature on the topic of RPO around a tumbling chief spacecraft, and laid the foundation for building a mathematical model for the 6-DOF relative motion. The original contribution presented in this chapter was the derivation of the roto-translational relative motion model, using the chief's body CCS as the frame of reference. This model is similar to traditional relative motion models but explicitly accounts for the chief's tumbling motion, which is important in this work. The resulting model enables further analysis, specifically for the reachability question posed in this dissertation. The research contributions offered in this chapter are shown in Table 2.1, mapped to the corresponding research objectives.

Table 2.1. Research contributions in Chapter 2.

Contribution	**Objective**
Derivation of chief perspective 6-DOF relative dynamics model	1, 2

Part II

Applied Reachability Analysis: Rendezvous with a Tumbling Object

THIS PAGE INTENTIONALLY LEFT BLANK

CHAPTER 3:
Reachability Theory

This chapter introduces the topic of reachability. First, some key terms are defined and relevant literature is discussed. Then, the relationship between reachability, controllability, and optimal control is explained, culminating in the methodology proposed in this research to conduct the reachability analysis for the problem of rendezvous with a tumbling spacecraft. Parts of this chapter were published in [49], [51], [52].

3.1 Reachability Notions

If one were asked to define reachability, without knowing the precise mathematical meaning of this term, the answer would likely be more or less correct by intuition: Can a particular state be reached? In the context of dynamical systems, answering this seemingly simple question can be quite complicated. The topic of reachability is motivated by the need to verify control system behavior and safety. As such, the main question posed by a reachability problem is one of control verification, rather than synthesis [53]. Consider a general control-affine system, Σ,

$$\Sigma : \dot{x}(t) = f(x(t), t) + g(x(t), t)u(t), \tag{3.1}$$

where $x \in \mathbb{R}^n$ is the n-dimensional state vector, $u \in \mathbb{R}^m$ is the m-dimensional control input, f is the drift vector field and g is the control vector field. The control input is constrained to lie within a set, $u(t) \in \mathcal{U} \subset \mathbb{R}^m$. The set $\mathcal{U}$ is referred to as the set of admissible controls and is assumed to be proper, compact, and convex. The control input, $u(t)$, is assumed to be a measurable function. Finally, the functions f and g are assumed to be Lipschitz, in order for the dynamics to have a unique solution. The time span of interest is defined as $t \in [0, T]$. Let $x_0 = x(0)$ and $x_f = x(T)$. The following definitions are written (adapted from [54], [55]).

Definition 3.1 *An **admissible trajectory**, $\gamma_\Sigma(0, T)$, is a trajectory of the system, Σ, starting from initial condition x_0, ending at x_f, under admissible control actions $u(t) \in \mathcal{U}$.*

Now, given a particular initial state, x_0, the following reachable set is defined.

Definition 3.2 *The **forward T-reachable set**, $\mathcal{R}_F(T)$, from the initial condition x_0 is the set of states, $x(t)$, that can be reached by admissible trajectories $\gamma_\Sigma(0,T)$ in time $T > 0$ or less:*

$$\mathcal{R}_F(T) = \{x(t) | \exists\, u(t) \in \mathcal{U} \text{ and } \gamma_\Sigma(0,t),\ x(0) = x_0,\ 0 < t \leq T\} \tag{3.2}$$

Conversely, given a particular final state, x_f, the following reachable set is defined.

Definition 3.3 *The **backward T-reachable set**, $\mathcal{R}_B(T)$, from the final condition x_f is the set of states, $x(0)$, from which admissible trajectories $\gamma_\Sigma(0,T)$ reach x_f in time $T > 0$ or less:*

$$\mathcal{R}_B(T) = \{x(0) | \exists\, u(t) \in \mathcal{U} \text{ and } \gamma_\Sigma(0,t),\ x(t) = x_f,\ 0 < t \leq T\} \tag{3.3}$$

Definitions 3.2 and 3.3 are illustrated in Figure 3.1.

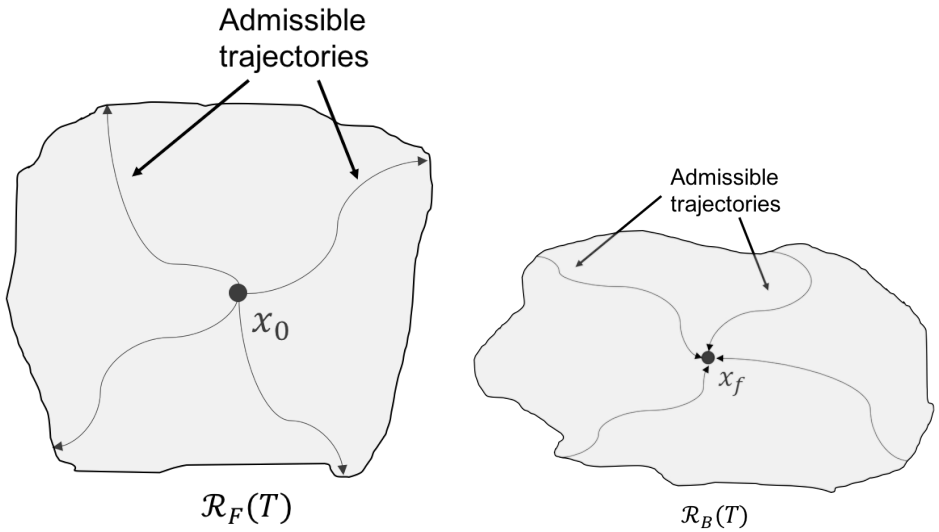

(a) Forward T-reachable set (b) Backward T-reachable set

Figure 3.1. Illustration of forward and backward T-reachable sets.

Although the definitions above do not explicitly include state constraints, they could in theory be incorporated by enforcing an admissible set of states $x(t) \in \mathcal{X}$ in addition to the set of admissible controls. The focus of this dissertation is on backward reachability, since the research question aims to find a set of feasible initial conditions, but the methodology herein is also applicable to a forward reachability analysis.

Computing these reachable sets is a complicated matter and still an active research topic. The reachability problem can be posed as an optimal control problem through a Hamilton-Jacobi (HJ) formulation [56], [57]. By Definition 3.3, an admissible control input $u(t)$ to the system 3.1 exists on the interval $[t, T]$. Assume that this control input minimizes the value function,

$$V(x,t) = \int_t^T l(x,u,\tau)d\tau + V_f(x(T)), \tag{3.4}$$

where $l(x,u,t)$ is the stage cost (or running cost) and $V_f(x(T))$ is the terminal cost related to the target state. Since the reachability problem is only concerned with reaching the target state, the running cost is omitted, $l(x,u,t) = 0$. The optimal value function is,

$$V^*(x,t) = \min_{u(t)\in\mathcal{U}} \left\{ V_f(x(T)) \right\}. \tag{3.5}$$

The principle of optimality states that since the control $u(t)$ is optimal on the interval $[t, T]$, it is necessarily optimal over any subinterval $[t, t + \Delta t]$ [58]. As a result,

$$V^*(x,t) = \min_{u(t)\in\mathcal{U}} \left\{ V^*(x(t+\Delta t), t+\Delta t) \right\}. \tag{3.6}$$

Expanding 3.6 in a Taylor series about (x,t) yields,

$$\begin{aligned} V^*(x,t) &= \min_{u(t)\in\mathcal{U}} \left\{ V^*(x,t) + \frac{\partial V^*}{\partial t}(t+\Delta t - t) + \frac{\partial V^*}{\partial t}^T (x(t+\Delta t) - x) + o(\Delta t) \right\}, \\ &= \min_{u(t)\in\mathcal{U}} \left\{ V^*(x,t) + \frac{\partial V^*}{\partial t}\Delta t + \frac{\partial V^*}{\partial t}^T [f(x,t) + g(x,t)u(t)] + o(\Delta t) \right\}, \end{aligned} \tag{3.7}$$

where $o(\Delta t)$ are higher order terms in Δt. Removing from the minimization the terms that do not depend on $u(t)$, dividing by Δt, and then letting $\Delta t \to 0$ yields the HJ Partial

Differential Equation (PDE) [58],

$$\frac{\partial V^*(x,t)}{\partial t} + \min_{u(t)\in\mathcal{U}} \left\{ \frac{\partial V^*(x,t)}{\partial x}^T [f(x,t) + g(x,t)u(t)] \right\} = 0, \tag{3.8}$$

with boundary condition $V^*(x,T) = V_f(x(T))$. Solving the HJ PDE above yields the function $V(x,t)$. By defining a terminal set as the zero level set of the implicit function V_f,

$$\mathcal{X}_f = \left\{ x | V_f(x) \leq 0 \right\}, \tag{3.9}$$

the HJ PDE can be solved using the terminal set as the boundary condition. As proven in [57], the zero level set of the solution represents the backward reachable set,

$$\mathcal{R}_B(T) = \{ x | V(x,t) \leq 0 \} . \tag{3.10}$$

The question then remains, how does one compute these sets?

3.1.1 Methods and Tools for Computing Reachable Sets

As mentioned earlier, computing reachable sets is a complex process. Simulation of trajectories is a commonly used approach for system verification, but the main drawback is that only a single point within a set can be simulated, and computing the entire reachable set would require an exhaustive search of the state space [53]. The desired result is the computation of *all* possible cases within the set. A variety of methods have been presented in literature to compute reachable sets that can be divided in two major categories: numerical computation of the exact reachable set, and approximate geometric methods. Related work from each category is briefly discussed below. In addition to computational complexity, visualization of the set becomes challenging especially for systems of more than three dimensions. This problem is common among all methods for computing reachable sets. In these cases, only specific projections (or slices) of the set can be meaningfully depicted.

Numerical Computation of Exact Reachable Sets

Exact computation of a reachable set requires solving the HJ PDE, shown in (3.8). Although classical solutions to the HJ PDE are not generally attainable, unique viscosity solutions are

available and have been well studied [59]. A toolbox of algorithms, referred to as Level-Set methods, was designed to numerically compute viscosity solutions of the HJ PDE [57], [59]. The toolbox is MATLAB-based and publicly available [60], and has been used for a variety of applications. Although accuracy of the results obtained through Level-Set methods is high, the computational complexity of the algorithms limits their applicability only to low-dimensional systems [59]. Specifically, the computational complexity of the HJ reachability problem is known to be exponential in relation to dimensionality, and is intractable for systems of more than five dimensions [61].

Mitchell et al. [57] apply the HJ formulation to compute the reachable set for a two-player differential game, representing an aircraft collision avoidance scenario. Oishi et al. [62] use a reachability computation, through the HJ PDE framework, to synthesize a controller that simultaneously satisfies state constraints, and stabilizes the system under input saturation. They present results of their technique applied to two different scenarios. Ding et al. [63] use HJ PDE reachability calculations to design switching conditions for a hybrid system representing maneuvers of unmanned aerial vehicles under human supervision. In overcoming the dimensional limitations of Level-Set methods, Stipanović et al. [64] present a method of decomposing the problem into computing reachable sets for a series of lower-dimensional subspaces, providing over-approximations of subsystem level-set functions. Another approach to alleviate the curse of dimensionality for reachability computations is presented by Chen et al. [65], where the authors propose using decoupled dynamic subsystems to compute conservative approximations of full reachable sets. Although these methods of decomposing the system are innovative, the problem of 6-DOF spacecraft rendezvous is difficult to decompose into subsystems of low dimensions, especially when the chief spacecraft is tumbling.

Approximate Geometric Methods

More popular methods for computing reachable sets in literature involve approximating a convex set by a geometric shape (i.e., ellipsoid, polytope), and propagating the set according to the system dynamics. These approaches require set-based computations, which can be computationally expensive depending on the geometry of the approximate sets [53], [66]. One of the drawbacks of these methods is that as the set grows at each iteration of the algorithm, computations such as the Minkowski sum become more expensive. Additionally,

depending on the geometry chosen to represent the sets, the Minkowski sum results in an over-approximation at each step, and the propagation of those errors could cause a dramatic over-approximation of the complete set (known as the wrapping effect) [67]. Girard et al. [67] present an algorithm for computing reachable sets of Linear Time-Invariant (LTI) systems based on zonotopes (centrally symmetric polytopes), which is not subject to the wrapping effect.

An application to nonlinear systems is presented by Greenstreet and Mitchell [68], where a reachability analysis tool (Coho) is developed for reachability computations using projection of high-dimensional objects onto planes. Kurzhanskiy and Varaiya [69] present a technique based on ellipsoidal approximation of convex sets, for discrete-time linear systems. The main advantage of ellipsoidal approximations is lower computational complexity, compared to polytopes. Makhouf et al. [66] present a comparison of reachability calculation methods using zonotopes, support functions, and invariant sets as approximations, applied to LTI systems. Reachability analysis for LTI systems through polytopic approximation is implemented in the MATLAB-based Multi-Parametric Toolbox (MPT), which is publicly available [70].

Some blends of exact and approximate methods have also been presented in literature. Varaiya [71] presents a method for computing reachable sets through an optimal control formulation. The method involves approximating the true set using a set of support hyperplanes, which provide an inner and outer approximation. The normal vectors of the support hyperplanes are then used to initialize the costates. This results in a polytopic approximation of the reachable set. Hwang et al. [72] use polytopic approximations combined with dynamic optimization to compute reachable sets for linear systems and a class of nonlinear systems.

The reachability problem for spacecraft applications has been investigated but is limited to translational reachability analysis. Holzinger and Scheeres [73] present a HJ PDE based reachability analysis to study safety in spacecraft proximity operations. Dueri et al. [74] use a convex optimization technique to generate reachable sets through a simplex growth method, applied to a spacecraft docking problem with a line-of-sight constraint. A similar method is used by Eren et al. [75] applied to a precision planetary landing problem. HomChaudhuri et al. [76] use a polytopic approximation method, combined with HJ theory to propagate

only the usable faces of the polytope in order to compute reach-avoid sets for a spacecraft docking scenario with a line-of-sight constraint.

3.1.2 Limitations and Challenges for Spacecraft Rendezvous with Tumbling Object

The reachability problem posed in this dissertation is a challenging one due to the dimensionality and nonlinearity of the roto-translational dynamics shown in (2.20). Application of numerical methods, such as the Level-Set toolbox, is not possible due to the dimensionality of the problem. Geometric methods, such as polytopic approximation via MPT, pose limitations due to the nonlinearity of the dynamics. Visualization alone is a challenge, assuming one could compute a set. However, a common denominator seen across much of the relevant literature is the relationship between reachability and optimal control. In this research, this relationship is examined and exploited in order to devise a method for the reachability analysis of this complex dynamic system.

The relationship between reachability and optimal control is further explained in the next subsection, followed by a discussion on the relationship between reachability and controllability concepts.

3.1.3 Relating Reachability and Optimal Control Concepts

Per Definition 3.2, reachability analysis shows that if a particular state, x_f, is reachable from x_0, then at least one admissible trajectory exists between the two states. In fact, it is likely that multiple trajectories exist. It follows, then, that one of these trajectories minimizes a particular performance index. In other words, an optimal trajectory must also exist. The Minimum Time Optimal Control Problem (MT-OCP) is of particular importance. Assume that the set of admissible controls, $\mathcal{U}$, is an m-dimensional cube of semi-side u_{max}. For the

control-affine system, Σ, the MT-OCP is formulated as,

$$\begin{aligned}
\text{minimize} \quad &: \quad J = \int_0^{t_f} 1 \, dt && \text{(3.11a)}\\
\text{subject to} \quad &: \quad \dot{x}(t) = f(x(t), t) + g(x(t), t)u(t) && \text{(3.11b)}\\
&\quad\;\; u(t) \in \mathcal{U} \implies ||u(t)||_\infty \leq u_{max} && \text{(3.11c)}\\
&\quad\;\; x(0) = x_0 && \text{(3.11d)}\\
&\quad\;\; x(t_f) = x_f. && \text{(3.11e)}
\end{aligned}$$

Equation (3.11a) is the optimization performance index, minimizing the value of t_f. Equation (3.11b) enforces the dynamic constraints, (3.11c) is the cubic control constraint, and equations (3.11d) and (3.11e) enforce the initial and final states.

Using the classical variational approach [58], the system Hamiltonian is written as,

$$H(x, \lambda, u, t) = 1 + \lambda^T(t)[f(x, t) + g(x, t)u(t)], \tag{3.12}$$

where λ is the n-dimensional costate. Through Pontryagin's minimum principle it is known that an optimal control, $u^*(t)$, will satisfy the following necessary conditions [58]:

$$\begin{aligned}
\dot{x}(t) &= \frac{\partial H}{\partial \lambda}(x^*, \lambda^*, u^*, t) && \text{(3.13a)}\\
\dot{\lambda}(t) &= -\frac{\partial H}{\partial x}(x^*, \lambda^*, u^*, t) && \text{(3.13b)}\\
H(x^*, \lambda^*, u^*, t) &\leq H(x^*, \lambda^*, u, t), \; \forall u(t) \in \mathcal{U} && \text{(3.13c)}\\
0 &= H(x^*(t_f), \lambda^*(t_f), u^*(t_f), t_f)\delta t_f && \text{(3.13d)}
\end{aligned}$$

The Hamiltonian minimization condition implies that,

$$\begin{aligned}
1 + \lambda^{*T}(t)[f(x^*, t) + g(x^*, t)u^*(t)] &\leq 1 + \lambda^{*T}(t)[f(x^*, t) + g(x^*, t)u(t)]\\
\lambda^{*T}(t)g(x^*, t)u^*(t) &\leq \lambda^{*T}(t)g(x^*, t)u(t), && \text{(3.14)}
\end{aligned}$$

which highlights that the optimal controls will be determined by the sign of the costate vector [58].

Comparing the minimized function of the HJ reachability problem in (3.8) with the Hamiltonian in (3.12), it is clear that the costate solution of the MT-OCP is related to the reachable set.

$$\frac{\partial V^*(x,t)}{\partial x}^T [f(x,t) + g(x,t)u(t)] \leftrightarrow \lambda^T(t)[f(x,t) + g(x,t)u(t)]$$
$$\lambda(t) = \frac{\partial V^*(x,t)}{\partial x} \tag{3.15}$$

With this insight, it becomes evident that the reachable set is related to the existence of a time optimal control solution.

Before trying to solve the MT-OCP formulated in (3.11), one could try to visualize the time optimal solution through reachability notions, as shown in some optimal control textbooks (e.g., [58], [77]). First, assume that the following conditions hold [77]:

- x_f is reachable from x_0 in finite time; otherwise, the problem is infeasible.
- $\mathcal{R}_F(T)$ is a closed and bounded set for any $T > 0$.
- $0 < T_1 < T_2 < \cdots < T_k$, for some finite k.
- $x_0 \in \text{int}(\mathcal{R}_F(T_1))$, i.e., the system is locally controllable.
- Forward reachable sets for increasing time values grow outward, such that $\mathcal{R}_F(T_1) \subset \mathcal{R}_F(T_2) \subset \cdots \subset \mathcal{R}_F(T_k)$.

As the reachable sets grow with increasing time, the desired state will eventually be included in a set. As illustrated in Figure 3.2, the time optimal solution can be visualized as the earliest time instant, T^*, at which the reachable set includes x_f [58], [77]. More precisely, one can assert that x_f will lie on the boundary of $\mathcal{R}_F(T^*)$,

$$x_f \in \partial\mathcal{R}_F(T^*) \tag{3.16}$$

Now, using the backward reachability notion (Definition 3.3), the time optimal solution can be visualized in a similar fashion. Assume that the following conditions hold:

- x_f is reachable from x_0 in finite time; otherwise, the problem is infeasible.
- $\mathcal{R}_B(T)$ is a closed and bounded set for any $T > 0$.
- $0 < T_1 < T_2 < \cdots < T_k$, for some finite k.
- $x_f \in \text{int}(\mathcal{R}_B(T_1))$, i.e., the system is locally controllable.

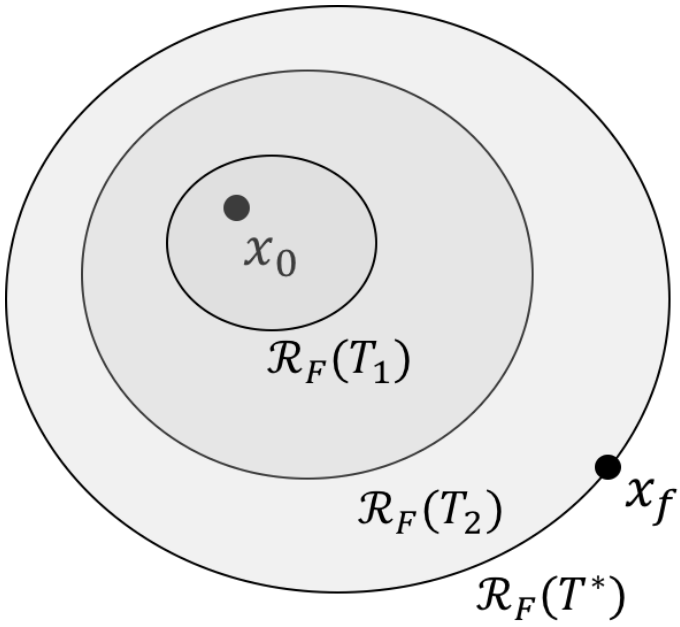

Figure 3.2. Visualization of time optimal solution through notions of forward reachable sets.

- Backward reachable sets for increasing time values grow outward, such that $\mathcal{R}_B(T_1) \subset \mathcal{R}_B(T_2) \subset \cdots \subset \mathcal{R}_B(T_k)$.

As illustrated in Figure 3.3, the time optimal solution can be visualized as the earliest time instant, T^*, at which the backward reachable set includes x_0. More precisely, one can assert that x_0 will lie one the boundary of $\mathcal{R}_B(T^*)$,

$$x_0 \in \partial\mathcal{R}_B(T^*) \tag{3.17}$$

With this insight in mind, the following remarks are offered.

Remark 3.1 *The boundary of $\mathcal{R}_F(T)$ is made up of all final states that can be reached by time optimal admissible trajectories in time T,*

$$\partial\mathcal{R}_F(T) = \{x_f |\ \gamma_\Sigma(0,T),\ x(0) = x_0,\ T = \textit{minimum time to reach } x_f\}. \tag{3.18}$$

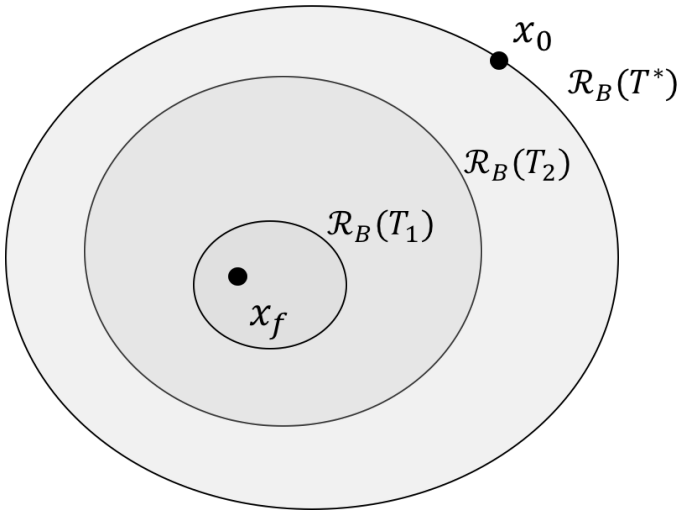

Figure 3.3. Visualization of time optimal solution through notions of backward reachable sets.

Remark 3.2 *The boundary of $\mathcal{R}_B(T)$ is made up of all initial conditions from which time optimal admissible trajectories reach the desired state in time T,*

$$\partial\mathcal{R}_B(T) = \{x_0 |\ \gamma_\Sigma(0,T),\ x(T) = x_f,\ T = \textit{minimum time to reach } x_f\}. \tag{3.19}$$

The concept in Remarks 3.1 and 3.2 is also referred to as a minimum isochrone [77], and can be useful in cases where computing reachable sets may be difficult or impossible.

Singular Extremals in Minimum Time Optimal Control Problems

As previously discussed, the minimum time optimal controls shown in (3.11c) for a general control-affine problem are dictated by the sign of the costate. Specifically, each control element $u_i(t)$, for $i = 1, \ldots, m$, is determined by the sign of the switching function $\lambda^{*T}(t)g_i(x^*, t)$, where g_i is the i-th column of the control vector field. A singular extremal exists if for a finite period of time, $[t_1,\ t_2]$, the switching function is equal to zero (i.e., $\lambda^{*T}(t)g_i(x^*, t) = 0$) [58]. In these cases, the Hamiltonian minimization condition does not provide any information about the optimal control value.

The existence of completely singular extremals for a control-affine system can be investigated

by evaluating the following Lie bracket conditions [78]:

1. $L_{g_i} g_j = 0$, for $i, j = 1, \ldots, m$,
2. $\{g_1, \ldots, g_m,\ L_f g_1, \ldots, L_f g_m\}$ are linearly independent,

where the Lie brackets are computed by $L_f g = \frac{\partial g}{\partial x} f - \frac{\partial f}{\partial x} g$. The above conditions are applied to the problem of rendezvous with a tumbling chief, with dynamics shown in (2.21). Since the control vector field in this case is constant, the first condition is automatically met. The second condition is evaluated by computing the appropriate Lie brackets through the MATLAB Symbolic Toolbox, and computing the rank of the distribution.

Remark 3.3 *The minimum time optimal control solution for the problem of rendezvous with a tumbling chief does not exhibit any completely singular extremals (i.e., at least one of the six control variables will be bang-bang), since,*

$$L_{g_i} g_j = 0, \text{ for } i, j = 1, \ldots, 6, \tag{3.20}$$

$$\text{rank}[g_1, \ldots, g_m,\ L_f g_1, \ldots, L_f g_m] = 12. \tag{3.21}$$

3.1.4 Relating Reachability and Controllability Concepts

The research question posed in this research is a backward reachability question. In some literature, backward reachable sets are referred to as controllable sets (e.g., [55], [74]), highlighting a relationship between the concepts of reachability and controllability. Generally, the controllability property answers whether a control input can drive the state x_0 to a specified location x_f in finite time [54]. This question is similar to the reachability question. It is clear that if the state x_f is reachable (i.e., there exists an admissible trajectory from x_0 to x_f) then the system must be controllable at x_0. The following definitions are offered to show the connection between reachability and controllability, adapted from Bullo and Lewis [54]. Consider, again, the general control-affine system Σ in (3.1).

Definition 3.4 *The system Σ is **accessible** from x_0 if there exists $T > 0$ such that* $\text{int}(\mathcal{R}_F(\tau)) \neq \emptyset$ *for* $\tau = (0, T]$.

The concept of accessibility essentially means that from a particular initial condition x_0, the system can move in more than a single direction. Thus, the forward reachable set for some finite time (τ) will have a nonempty interior. Accessibility, however, does not imply controllability.

Definition 3.5 *The system Σ is **locally controllable** from x_0 is there exists $\tau > 0$ such that $x_0 \in \text{int}(\mathcal{R}_F(\tau))$.*

In contrast to the concept of accessibility, local controllability means that from an initial condition x_0 the system can move in any direction. Clearly, local controllability also implies accessibility. These notions are depicted in Figure 3.4. Since the value of τ can be arbitrarily small, a system meeting the local controllability condition is often referred to as a Small Time Locally Controllable (STLC) system [54].

Finally, the strongest controllability notion is defined as follows.

Definition 3.6 *The system Σ is **controllable** from x_0 if, for every $x \in \mathbb{R}^n$, there exists $T > 0$ and $\gamma_\Sigma(0, T)$ such that $x(T) = x$.*

Definition 3.6 implies that if Σ is controllable, then for any x_0 there must exist a time T such that $\mathcal{R}_F(T) = \mathbb{R}^n$ [55] (i.e., the entire state space is reachable). For general nonlinear systems, it may be quite difficult to establish this property. Traditionally, controllability analysis of nonlinear systems is performed by examining the Lie structure of the vector fields f and g. The controllability condition boils down to checking the linear independence of the system's Lie brackets [79],

$$\text{rank}\{g,\ L_f g,\ L_f^2 g, \ldots, L_f^{n-1} g\} = n. \tag{3.22}$$

This condition essentially checks the directions in which the system is allowed to move, thus establishing local controllability. For linear systems, in particular, since the vector fields are constant, and not state or time dependent, the concepts of local controllability and controllability coincide. In this case, (3.22) yields the well-known controllability matrix rank condition for linear systems [54], [80].

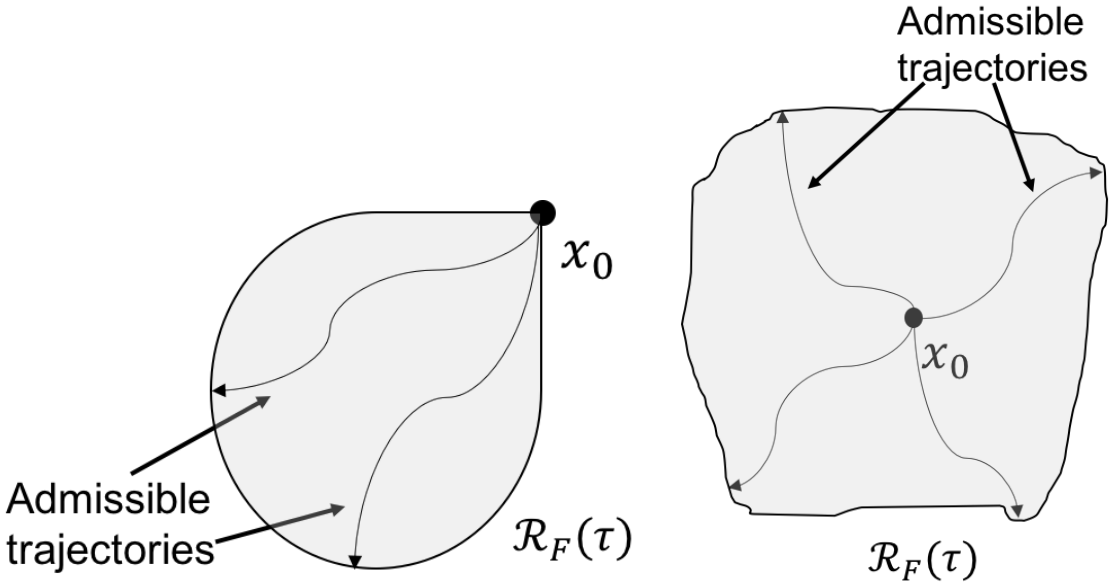

(a) Accessible but not controllable (b) Accessible and locally controllable

Figure 3.4. Depiction of controllability notions. Adapted from [54].

Controllability analysis can be a useful tool in analyzing how choice of actuators could affect the dynamics [81], how disturbances affect orbital and attitude motion [31], or investigating control of an underactuated system [82]. However, controllability analysis alone does not completely answer the research question posed in Section 1.1. To answer this question, a backward reachable set must be computed.

3.2 Proposed Methodology

The previous sections highlighted the important relationship between reachability and time optimal control. In order to analyze the backward reachability for the problem of rendezvous with a tumbling chief spacecraft, this relationship is exploited. Based on Remark 3.2, a family of time optimal solutions can be used to visualize the boundary of the reachable set. This family of MT-OCPs can be solved using existing techniques and tools, such as the MATLAB-based General Purpose OPtimal control Software (GPOPS)-II software package [83]. The GPOPS-II software can be used to solve a variety of optimal control problems using a Gaussian quadrature collocation method coupled with a NLP solver; the Interior Point OPTimizer (IPOPT) solver [84] is used in this research. Computing the

solutions to these MT-OCPs on a user-defined subspace (e.g., vary relative positions while holding other states constant), makes reachability analysis of this complex system tractable.

Backward reachability analysis is conducted in the following sequential steps.

1. Step 1: Generate a set of test points, x_0, on the subspace of interest.
2. Step 2: Given x_f, maximum allowable time (T_{max}), and control constraints, attempt to solve the MT-OCP for each test point.
3. Step 3: Plot contours of minimum time to reach x_f on the user-defined subspace. Note that MATLAB built-in commands for plotting contours include interpolation between grid points.

The proposed methodology provides an alternative to computing the full reachable set, which is advantageous for the problem of rendezvous with a tumbling chief. Since the roto-translational system (2.20) studied in this dissertation is comprised of at least 12 states, and nonlinear, available reachability analysis tools are not applicable. Additionally, computation and visualization of a 12-dimensional set is challenging, since maneuver times of interest for this problem could be large. Although the proposed method is computationally intensive, it provides a path to accomplish the research objectives. Although the concept of using minimum time contours to visualize a reachable set has been mentioned in literature (e.g., see [85], or the isochrone concept in [77]), it has not been exploited for analysis of a complex system as shown in this dissertation.

3.2.1 Validation of Proposed Method

The proposed method was validated by showing two example reachability computations: one for a linear system and one for a nonlinear system. The backward reachable sets were computed using available tools, as well as through the proposed method, and results are compared. These examples were selected to be simple enough so that analytical solutions to the MT-OCP could be found.

Double Integrator Example

The first example is the double integrator. The system is comprised of two states (x_1 and x_2) and one control variable (u), with the following dynamics.

$$\dot{x}_1 = x_2, \tag{3.23}$$

$$\dot{x}_2 = u. \tag{3.24}$$

The control variable is bounded, $-1 \leq u \leq 1$, and the desired final state is the origin, $x_f = [0,\ 0]^T$. The MT-OCP is formulated as follows:

$$\text{minimize} \quad : \quad J = \int_0^{t_f} 1 \, dt \tag{3.25a}$$

$$\text{subject to} \quad : \quad \dot{x}_1 = x_2 \tag{3.25b}$$

$$\dot{x}_2 = u \tag{3.25c}$$

$$|u| \leq 1 \tag{3.25d}$$

$$x(t_f) = x_f. \tag{3.25e}$$

The solution to the MT-OCP for the double integrator is well studied, as it is one of the few optimal control problems that yields an analytical solution. The optimization problem in 3.25 can be solved as shown in [58]. First the Hamiltonian is written as,

$$H = 1 + \lambda_1 x_2 + \lambda_2 u. \tag{3.26}$$

Applying the necessary conditions shown in (3.13), the costate solution is derived,

$$\dot{\lambda}_1 = -\frac{\partial H}{\partial x_1} = 0 \quad \Longrightarrow \quad \lambda_1 = c_1, \tag{3.27}$$

$$\dot{\lambda}_2 = -\frac{\partial H}{\partial x_2} = \lambda_1 = -c_1 \quad \Longrightarrow \quad \lambda_2 = -c_1 t + c_2, \tag{3.28}$$

where c_1 and c_2 are constants of integration. The Hamiltonian minimization is then used to

derive the optimal control,

$$\begin{aligned} 1 + \lambda_1^* x_2^* + \lambda_2^* u^* &\leq 1 + \lambda_1^* x_2^* + \lambda_2^* u, \\ \lambda_2^* u^* &\leq \lambda_2^* u, \\ u^* &= -\operatorname{sign}(\lambda_2^*). \end{aligned} \tag{3.29}$$

The optimal control solution in (3.29) reveals the well-known bang-bang structure, where the control will always take its maximum value with only one switching point in this case due to the linear nature of λ_2 in equation (3.28). Integrating the dynamic equations with the knowledge that $u = \pm 1$ yields segments of the optimal trajectories,

$$\dot{x}_2 = \pm 1 \implies x_2 = \pm t + c_3, \tag{3.30}$$

$$\dot{x}_1 = x_2 = \pm t + c_3 \implies x_1 = \pm \frac{1}{2} t^2 + c_3 t + c_4, \tag{3.31}$$

where c_3 and c_4 are constants of integration. Eliminating time from the above equations, and evaluating at the origin (x_f) yields the well-known switching curve for the double integrator system,

$$x_1 = -\frac{1}{2} x_2 |x_2|. \tag{3.32}$$

Backward reachable sets for this system were computed through a polytopic approximation method using the MPT software [70]. A grid of 900 test points was created in the subspace $-2\pi \leq x_1, x_2 \leq 2\pi$, and the corresponding MT-OCPs were solved through GPOPS-II [83]. For comparison, the backward T-reachable sets were plotted for $T = 3,\ 5,\ 7, 10,\ 13,\ 15$ seconds. Figure 3.5 shows the resulting plots, with the MPT result on the left (Figure 3.5a), and the minimum time contour visualization on the right (Figure 3.5b). The switching curve shown in 3.32 is also plotted on these plots as a dotted line.

It is evident that the minimum time contours resemble the shape of the backward reachable sets computed via MPT, thus representing an accurate approximation of the set boundaries.

Nonlinear System Example

For further validation, the proposed method is applied to a slightly more complicated example. This example was created specifically for this validation and does not have a

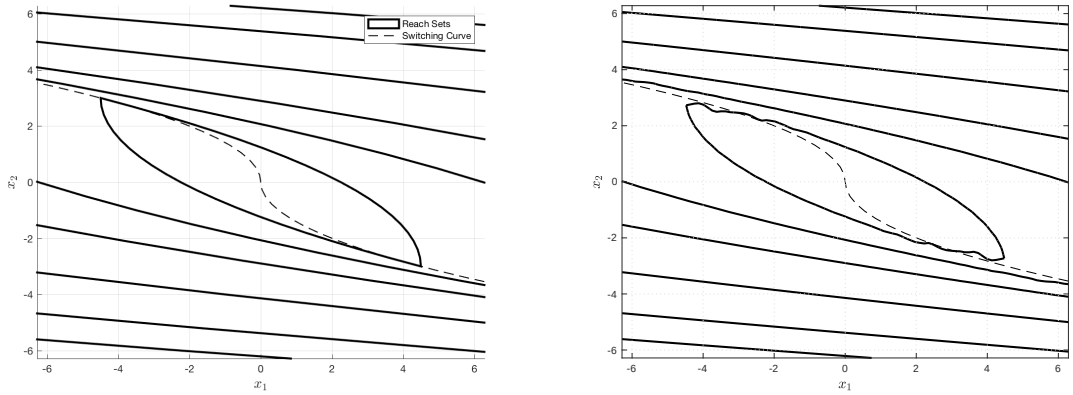

(a) MPT Backward Reachable Sets (b) Minimum Time Contours

Figure 3.5. Comparison of backward reachable sets computed via MPT to proposed minimum time contour approach for the double integrator example.

physical meaning. The system is comprised of two states (x_1 and x_2) and one control variable (u), with the following dynamics.

$$\dot{x}_1 = \sin x_2, \tag{3.33}$$

$$\dot{x}_2 = u. \tag{3.34}$$

The control variable is bounded, $-1 \leq u \leq 1$, and the desired final state is the origin, $x_f = [0,\ 0]^T$. The MT-OCP is formulated as follows.

$$\text{minimize} \quad : \quad J = \int_0^{t_f} 1\ dt \tag{3.35a}$$

$$\text{subject to} \quad : \quad \dot{x}_1 = \sin x_2 \tag{3.35b}$$

$$\dot{x}_2 = u \tag{3.35c}$$

$$|u| \leq 1 \tag{3.35d}$$

$$x(t_f) = x_f \tag{3.35e}$$

This MT-OCP also yields an analytical solution. The system Hamiltonian is written as,

$$H = 1 + \lambda_1 \sin x_2 + \lambda_2 u. \tag{3.36}$$

The costate solution is derived by applying the necessary conditions in (3.13),

$$\dot{\lambda}_1 = -\frac{\partial H}{\partial x_1} = 0 \implies \lambda_1 = c_1 \tag{3.37}$$

$$\dot{\lambda}_2 = -\frac{\partial H}{\partial x_2} = -\lambda_1 \cos x_2 = -c_1 \cos x_2, \tag{3.38}$$

where c_1 is a constant of integration. The Hamiltonian minimization is then used to derive the optimal control,

$$\begin{aligned} 1 + \lambda_1^* \sin x_2^* + \lambda_2^* u^* &\leq 1 + \lambda_1^* \sin x_2^* + \lambda_2^* u, \\ \lambda_2^* u^* &\leq \lambda_2^* u, \\ u^* &= -\operatorname{sign}(\lambda_2^*). \end{aligned} \tag{3.39}$$

As with the double integrator example, the optimal control in this case will also be bang-bang, but there is no certainty on the number of switches since λ_2 is a nonlinear function of the trajectory. Knowing that $u = \pm 1$, the dynamics can be integrated as follows,

$$\dot{x}_2 = \pm 1 \implies x_2 = \pm t + c_2, \tag{3.40}$$

$$\implies \lambda_2 = \mp c_1 \cos(\pm t + c_2) + c_3 \tag{3.41}$$

$$\dot{x}_1 = \sin x_2 = \sin(\pm t + c_2) \implies x_1 = \mp \cos(\pm t + c_2) + c_4, \tag{3.42}$$

with c_2, c_3, and c_4 being constants of integration. Eliminating time from the above equations and evaluating at x_f yields the switching curve for this system,

$$x_1 = \frac{|x_2|}{x_2}(\cos x_2 - 1). \tag{3.43}$$

Backward reachable sets for this system were computed through the Level-Set toolbox [60]. A grid of 900 test points was created in the subspace $-8 \leq x_1, x_2 \leq 8$, and the corresponding MT-OCPs were solved through GPOPS-II [83]. For comparison, the backward T-reachable sets were plotted for $T = 3,\ 6,\ 9,\ 12,\ 15$ seconds. Figure 3.6 shows the resulting plots, with the Level-Set result on the left (Figure 3.6a), and the minimum time contour visualization on the right (Figure 3.6b). The switching curve shown in (3.43) is also plotted on these plots as a dotted line.

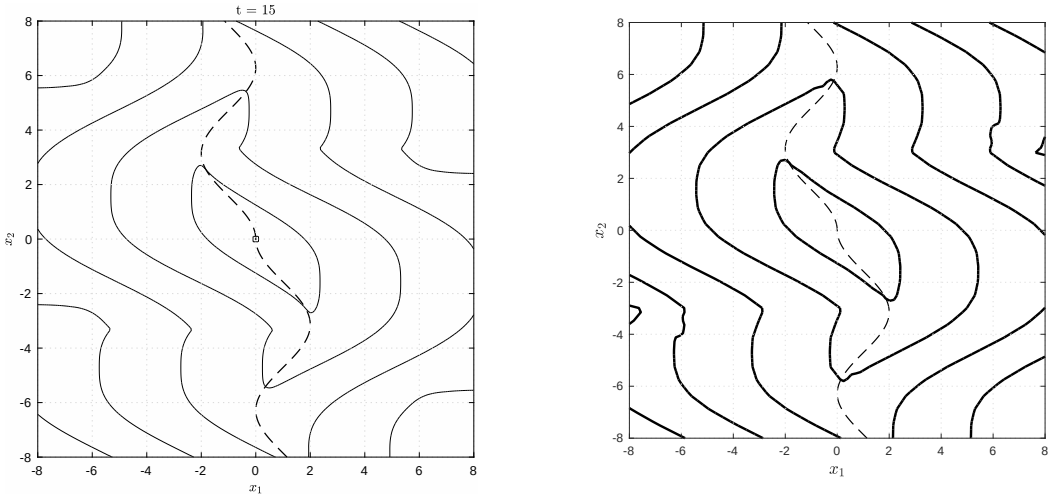

(a) Level-Set Backward Reachable Sets (b) Minimum Time Contours

Figure 3.6. Comparison of backward reachable sets computed via Level-Set methods to proposed minimum time contour approach for the nonlinear system example.

As with the double integrator example, Figure 3.6 shows that the proposed method provides an accurate approximation of the backward reachable sets.

3.2.2 Visualization of Relative Attitude Sets

Visualization of translational states is fairly intuitive. Attitude states are more challenging due to the non-Euclidean nature of the rigid body orientation parameters. To the best of the author's knowledge, visualization of a reachable set of attitude has not been discussed in literature. In this research, a method is proposed to visualize a set of attitudes using MRPs.

Recall that MRPs are a minimal representation of attitude, made up of three parameters, $\boldsymbol{\sigma} = [\sigma_1,\ \sigma_2,\ \sigma_3]^T$. As noted in Chapter 2 the magnitude of the MRP vector is bounded. The MRP magnitude (or norm) is given by,

$$\boldsymbol{\sigma}^T\boldsymbol{\sigma} = \sigma_1^2 + \sigma_2^2 + \sigma_3^2 = c^2, \tag{3.44}$$

where c is a variable representing the numerical result. Geometrically, (3.44) represents a sphere of radius c on the MRP subspace. The MRP vector definition in terms of a principal

rotation in (2.11) reveals that the magnitude is only a function of the rotation angle, ϕ,

$$\boldsymbol{\sigma}^T\boldsymbol{\sigma} = \tan^2\left(\frac{\phi}{4}\right). \tag{3.45}$$

It follows that all MRP vectors representing relative attitudes of equal rotation angle will have equal magnitudes.

Reachable relative attitudes can be visualized by using the MRP magnitude as a spherical projection surface. Minimum time data, computed by scattered test points within the subspace, can be projected onto the spherical surface for visualization. The spherical projection surface represents orientations of equal angular displacement. A particular point on this sphere represents the direction of the Euler axis, while the contour (or color) represents the minimum time to reach the desired attitude from this point.

An example is used to illustrate this method. Begin with two relative attitudes represented by principal rotations of $\phi = 90$ degrees about the Euler axes, $\hat{e}_1 = [0, 0, 1]^T$, and $\hat{e}_2 = [-1/\sqrt{3}, -1/\sqrt{3}, 1/\sqrt{3}]^T$. The corresponding MRPs are

$$\boldsymbol{\sigma}_1 = \begin{bmatrix} 0 \\ 0 \\ 0.4142 \end{bmatrix}, \quad \boldsymbol{\sigma}_2 = \begin{bmatrix} -0.2391 \\ -0.2391 \\ 0.2391 \end{bmatrix}. \tag{3.46}$$

Note that both of these MRP vectors have equal magnitude, $\boldsymbol{\sigma}_1^T\boldsymbol{\sigma}_1 = \boldsymbol{\sigma}_2^T\boldsymbol{\sigma}_2 = 0.4142$. Figure 3.7 illustrates the visualization of these two attitudes. The sphere represents the 90-degree angular displacement in this case. The two Euler axes are plotted to illustrate their direction. The two red dots, on the surface of the sphere, are the two sets of MRPs considered in this example.

3.2.3 Limitations of Proposed Method

As with any approximation, the proposed method exhibits some limitations that must be highlighted. The minimum time contour method is dependent on the ability to compute a minimum time solution. The majority of practical minimum time optimal control problems do not have analytical solutions, and numerical methods must be utilized. There exists a variety of numerical techniques that can be used; a comprehensive survey was published

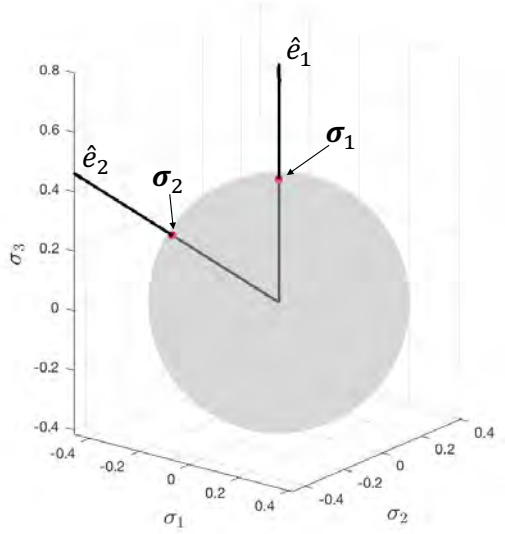

Figure 3.7. Illustration of visualization of attitudes on the MRP subspace; red dots represent the two sets of MRPs considered in this example.

in [86]. The GPOPS-II software package was selected in this research due to its user-friendly MATLAB interface, and applicability to a wide variety of problems.

All numerical methods, however, have some drawbacks. The solution will only be as accurate as the solver's tolerance. The GPOPS-II software has a number of user-defined parameters that will affect the accuracy of the solution, and depending on the problem, the solver may exhibit sensitivities to those parameters [83]. An investigation into the sensitivity of the GPOPS-II software to these parameters was outside the scope of this research. In this research, the GPOPS-II parameters were selected based on trials for a limited number of cases. The parameters used for specific scenarios will be specified where appropriate.

In addition to the solver parameters, the accuracy of the solution will also depend on the density of the selected test points on the subspace of interest. Clearly, there is a trade-off between number of test points and computational complexity. In this research, the number of test points was selected to be high enough to sample the desired subspace, while attempting to keep the amount of time required to run all cases to a reasonable limit.

An intensive computational effort is required to produce these results. The available computing architecture may be a limiting factor in applying the proposed method. For this research, the High Performance Computing (HPC) cluster, code named "Hamming," at

NPS was used to run the desired simulations.

3.3 Summary

This chapter focused on the theoretical concepts used throughout this research. The notions of reachability were formally defined and existing methods for solving reachability problems were discussed, while highlighting the challenges involved in solving the backward reachability problem posed in this dissertation. Specifically, the backward reachability problem answers the question of finding initial conditions from which the rendezvous maneuver is feasible. The relationships between reachability, time optimal control, and controllability were explained. By exploiting the relationship between reachability and time optimal control, a methodology was proposed for performing reachability analysis of complex dynamical systems and visualizing the sets through minimum time contours. This method was validated using two sample problems. Finally, a technique was proposed for visualizing backward reachable sets of relative attitudes using MRPs. The research contributions offered in this chapter are shown in Table 3.1, mapped to the corresponding research objective.

Table 3.1. Research contributions in Chapter 3.

Contribution	Objective
Methodology for applied reachability analysis via minimum time contours	2
Method for visualization of reachable attitudes on the MRP subspace	2

THIS PAGE INTENTIONALLY LEFT BLANK

CHAPTER 4:
Derivation and Reachability Analysis of Simplified Relative Motion Models

In this chapter, the general problem of RPO around a tumbling chief spacecraft is simplified. First, it is assumed that the chief spacecraft is in a circular orbit rotating on the orbit plane (about its z body axis) at a constant rate, and relative distances are small in comparison to the chief's orbit radius. These assumptions are traditionally made in deriving the well-known CW equations [2]. Secondly, it is assumed that the deputy is on the same orbit plane as the chief. Backward reachable sets are computed using the resulting simplified models. The results presented in this chapter were published in [49], [52].

4.1 Simplified Relative Motion Models

In Chapter 2, the relative roto-translational equations of motion were derived, using the chief's body frame as the frame of reference. The general 6-DOF model was shown in (2.20). Recall the problem setup from Chapter 2 depicted again in Figure 4.1. To simplify the roto-translational dynamics model, the following assumptions are made:

1. Chief is in a circular orbit with mean motion $n = \sqrt{\frac{\mu}{R_c^3}}$, and relative distances are small compared to the chief's orbit radius ($||\vec{\rho}|| << ||\vec{r}_c||$).
2. Chief and deputy body CCSs are aligned with their respective principal axes. This implies that J_c and J_d are diagonal matrices with the principal moments of inertia ($J_{c_{x,y,z}}$ and $J_{d_{x,y,z}}$) on the diagonals.
3. The chief and deputy spacecraft are spherically symmetric ($J_{c_x} = J_{c_y} = J_{c_z}$ and $J_{d_x} = J_{d_y} = J_{d_z}$).
4. The chief body CCS is initially aligned with the LVLH CCS.
5. The chief is rotating on the orbit plane, about its z body axis, at a constant rate (Ω).

With the above assumptions, the chief's orbital and attitude motion is known. The chief's

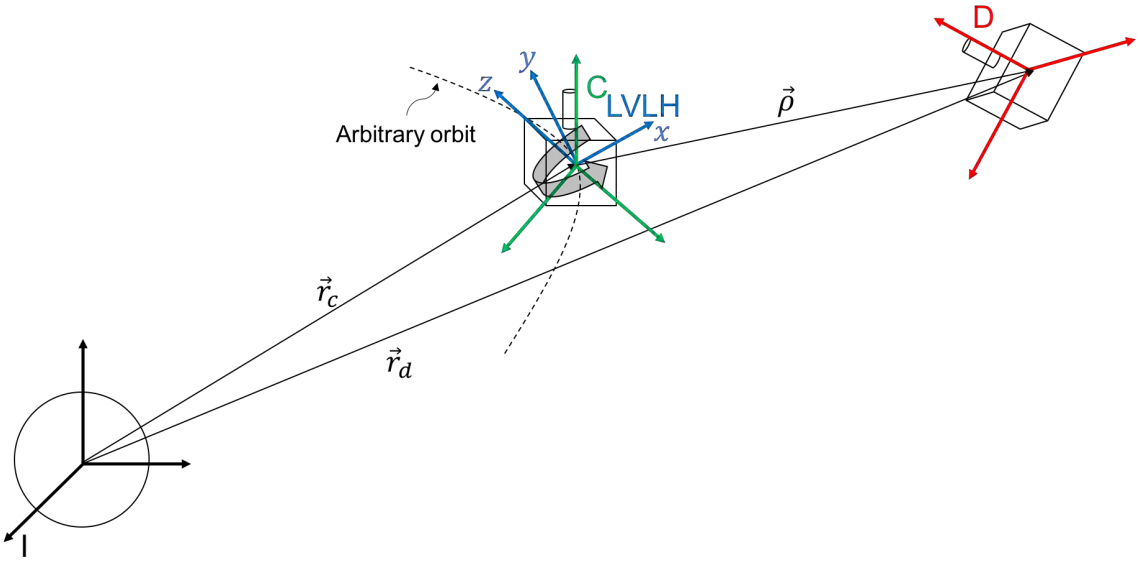

Figure 4.1. Depiction of general setup for the problem of rendezvous with a tumbling object.

position vector ($\vec{r}_c$) is constant when resolved in the LVLH CCS (L) and is written as

$$\boldsymbol{r}_c^{\mathsf{L}} = \begin{bmatrix} R_c \\ 0 \\ 0 \end{bmatrix}. \tag{4.1}$$

The chief's position vector can be resolved in the chief's body CCS (C) by

$$\boldsymbol{r}_c^{\mathsf{C}} = C_{\mathsf{C/L}}(t)\boldsymbol{r}_c^{\mathsf{L}}, \tag{4.2}$$

where $C_{\mathsf{C/L}}$ is the DCM representing the chief's attitude with respect to L. Since the chief's body CCS is initially aligned with L, and it is rotating about the z axis at a constant rate (Ω),

$$C_{\mathsf{C/L}}(t) = \begin{bmatrix} \cos(\Omega t) & \sin(\Omega t) & 0 \\ -\sin(\Omega t) & \cos(\Omega t) & 0 \\ 0 & 0 & 1 \end{bmatrix}. \tag{4.3}$$

The chief's position vector resolved in C is therefore written as

$$\boldsymbol{r}_c^{\mathsf{C}} = \begin{bmatrix} R_c \cos(\Omega t) \\ -R_c \sin(\Omega t) \\ 0 \end{bmatrix}. \tag{4.4}$$

The chief's angular velocity includes a component due to the motion of the chief with respect to L, and a component due to the orbital motion,

$$\vec{\omega}_{\mathsf{C/I}} = \vec{\omega}_{\mathsf{C/L}} + \vec{\omega}_{\mathsf{L/I}}. \tag{4.5}$$

Since it is assumed that the chief is rotating at constant rate about its z body axis, and is in a circular orbit the following equations hold:

$$\boldsymbol{\omega}_{\mathsf{C/L}}^{\mathsf{C}} = \begin{bmatrix} 0 \\ 0 \\ \Omega \end{bmatrix}, \text{ and } \boldsymbol{\omega}_{\mathsf{L/I}}^{\mathsf{L}} = \begin{bmatrix} 0 \\ 0 \\ n \end{bmatrix}. \tag{4.6}$$

The chief's angular velocity, resolved in C, is then

$$\boldsymbol{\omega}_c = \boldsymbol{\omega}_{\mathsf{C/L}}^{\mathsf{C}} + C_{\mathsf{C/L}}(t)\boldsymbol{\omega}_{\mathsf{L/I}}^{\mathsf{L}}. \tag{4.7}$$

Plugging in (4.3) into (4.7) yields the chief's constant angular velocity,

$$\boldsymbol{\omega}_c = \begin{bmatrix} 0 \\ 0 \\ \Omega + n \end{bmatrix} \tag{4.8}$$

It is simple to show that this angular velocity is constant by applying Euler's equation,

$$\dot{\boldsymbol{\omega}}_{\mathsf{C/I}}^{\mathsf{C}} = J_c^{-1}\left(-[\boldsymbol{\omega}_c]^{\times} J_c \boldsymbol{\omega}_c\right) = 0_{3\times 1}, \tag{4.9}$$

since it is assumed that the chief's body frame is aligned with its principal axes.

Defining the state components as $\boldsymbol{\rho} = [\rho_x,\ \rho_y,\ \rho_z]^T$, $\mathbf{v} = [v_x,\ v_y,\ v_z]^T$, $q = [q_1,\ q_2,\ q_3,\ q_4]^T$, $\boldsymbol{\omega}^{\mathsf{D}} = [\omega_x,\ \omega_y,\ \omega_z]^T$, control components $\mathbf{F}_d = [F_x,\ F_y,\ F_z]^T$, $\mathbf{M}_d^{\mathsf{D}} = [M_x,\ M_y,\ M_z]^T$, and

expanding (2.20a) - (2.20d), yields the simplified relative roto-translation model:

$$\dot{\rho}_x = v_x \tag{4.10a}$$

$$\dot{\rho}_y = v_y \tag{4.10b}$$

$$\dot{\rho}_z = v_z \tag{4.10c}$$

$$\begin{aligned}\dot{v}_x = &-\frac{\mu\rho_x}{[(R_c+\rho_x)^2+\rho_y^2+\rho_z^2]^{3/2}} + \frac{\mu}{R_c^2}\cos(\Omega t) - \frac{\mu R_c\cos(\Omega t)}{[(R_c+\rho_x)^2+\rho_y^2+\rho_z^2]^{3/2}} \\ &+\frac{1}{m_d}F_x + 2(\Omega+n)v_y + (\Omega+n)^2\rho_x\end{aligned} \tag{4.10d}$$

$$\begin{aligned}\dot{v}_y = &-\frac{\mu\rho_y}{[(R_c+\rho_x)^2+\rho_y^2+\rho_z^2]^{3/2}} - \frac{\mu}{R_c^2}\sin(\Omega t) + \frac{\mu R_c\sin(\Omega t)}{[(R_c+\rho_x)^2+\rho_y^2+\rho_z^2]^{3/2}} \\ &+\frac{1}{m_d}F_y - 2(\Omega+n)v_x + (\Omega+n)^2\rho_y\end{aligned} \tag{4.10e}$$

$$\dot{v}_z = -\frac{\mu\rho_z}{[(R_c+\rho_x)^2+\rho_y^2+\rho_z^2]^{3/2}} + \frac{1}{m_d}F_z \tag{4.10f}$$

$$\dot{q}_1 = \frac{1}{2}(q_4\omega_x - q_3\omega_y + q_2\omega_z) \tag{4.10g}$$

$$\dot{q}_2 = \frac{1}{2}(q_3\omega_x + q_4\omega_y - q_1\omega_z) \tag{4.10h}$$

$$\dot{q}_3 = \frac{1}{2}(-q_2\omega_x + q_1\omega_y + q_4\omega_z) \tag{4.10i}$$

$$\dot{q}_4 = \frac{1}{2}(-q_1\omega_x - q_2\omega_y - q_3\omega_z) \tag{4.10j}$$

$$\dot{\omega}_x = \frac{1}{J_{d_x}}M_x + (\Omega+n)[1-2(q_1^2+q_2^2)]\omega_y - 2(\Omega+n)(q_2q_3+q_1q_4)\omega_z \tag{4.10k}$$

$$\dot{\omega}_y = \frac{1}{J_{d_y}}M_y - (\Omega+n)[1-2(q_1^2+q_2^2)]\omega_x + 2(\Omega+n)(q_1q_3-q_2q_4)\omega_z \tag{4.10l}$$

$$\dot{\omega}_z = \frac{1}{J_{d_z}}M_z + 2(\Omega+n)(q_2q_3+q_1q_4)\omega_x - 2(\Omega+n)(q_1q_3-q_2q_4)\omega_y. \tag{4.10m}$$

Since the relative translational and relative rotational states are decoupled, the relative roto-translation model can be decomposed into two subsystems that can be studied independently.

4.1.1 Relative Translational Subsystem

The relative translational dynamics are shown in equations (4.10a)-(4.10f). Let the translational state vector be defined as $x_T = [\rho_x \ \rho_y \ \rho_z \ v_x \ v_y \ v_z]^T \in \mathbb{R}^6$, and the translational control vector as $u_T = [F_x \ F_y \ F_z]^T \in \mathbb{R}^3$. The translational subsystem can be written in control affine form as

$$\dot{x}_T = f_T(x_T, t) + G_T u_T, \tag{4.11}$$

where $f_T \in \mathbb{R}^6$ is the drift vector field from (4.10a)-(4.10f) and $G_T \in \mathbb{R}^{6\times 3}$ is

$$G_T = \begin{bmatrix} 0_{3\times 3} \\ \frac{1}{m_d} I_3 \end{bmatrix}. \tag{4.12}$$

The subsystem in (4.11) can be further simplified by applying the assumption that relative distances are small compared to the chief's orbit radius. The system can be linearized about the origin ($x_e = 0_{6\times 1}$), to yield the Linear Time-Varying (LTV) system

$$\dot{x}_T = A_T(t) x_T + B_T u_T, \tag{4.13}$$

where

$$A_T(t) = \left.\frac{\partial f_T}{\partial x_T}\right|_{x_e} = \begin{bmatrix} 0 & 0 & 0 & 1 & 0 & 0 \\ 0 & 0 & 0 & 0 & 1 & 0 \\ 0 & 0 & 0 & 0 & 0 & 1 \\ 3n^2\cos(\Omega t) + \Omega^2 + 2\Omega n & 0 & 0 & 0 & 2(\Omega + n) & 0 \\ 0 & \Omega^2 + 2\Omega n & 0 & -2(\Omega + n) & 0 & 0 \\ 0 & 0 & -n^2 & 0 & 0 & 0 \end{bmatrix},$$

and $B_T = G_T$.

Notably, the translational out-of-plane motion (ρ_z, v_z) is decoupled from the in-plane motion as seen in traditional relative motion models. The out-of-plane motion is not affected by the chief's rotation, since the rotation is occurring on the orbit plane. As a sanity check, it can be seen that when the chief is not rotating (i.e., $\Omega = 0$ degrees per second), (4.13) yields the well-known CW LTI model [2].

Relative Rotational Subsystem

The relative rotational dynamics are shown in equations (4.10g)-(4.10m). Let the rotational state vector be defined as $x_R = [q_1\ q_2\ q_3\ q_4\ \omega_x\ \omega_y\ \omega_z]^T \in \mathbb{R}^7$, and the rotational control vector as $u_R = [M_x\ M_y\ M_z]^T \in \mathbb{R}^3$. The rotational subsystem can be written in control affine form as

$$\dot{x}_R = f_R(x_R, t) + G_R u_R, \tag{4.14}$$

where $f_R \in \mathbb{R}^7$ is the drift vector field from (4.10g)-(4.10m) and $G_R \in \mathbb{R}^{7\times 3}$ is

$$G_R = \begin{bmatrix} 0_{4\times 3} \\ J_d^{-1} \end{bmatrix}. \tag{4.15}$$

Further simplification of the rotational subsystem is possible but would require restrictive assumptions (e.g., small angular maneuvers, or negligence of orbital motion). In the following section, a simplified system is presented for a close proximity planar scenario where these assumptions would be appropriate. In general, however, these assumptions would not be beneficial in reachability analysis since they would limit the operating region of the system.

Simplified Dynamics for Planar Docking in Close Proximity to Rotating Chief

In simplifying the problem further, a close proximity planar maneuver is examined. In addition to the previous assumptions, the following are assumed:

1. The chief and deputy are in close enough proximity, and maneuver times are short enough, that the relative orbital motion is negligible.
2. The deputy remains on the chief's orbit plane; reducing the translational motion to 2-DOF, and rotational motion to 1-DOF.

This scenario was previously examined by Ma et al. [17] from an optimal control perspective. This scenario is depicted in Figure 4.2. The angles θ_c and θ_d define the attitude of the chief and deputy spacecraft, respectively, with respect to the inertial CCS.

Since the chief is initially aligned with I and rotates about its z principal axis, it follows that $\ddot{\theta}_c = 0$, $\dot{\theta}_c = \Omega$, and $\theta_c(t) = \Omega t$. The deputy's rotational motion is also a principal rotation about its z principal axis, therefore $\ddot{\theta}_d = \frac{M_z}{J_{d_z}}$. The relative attitude is defined as $\theta_r = \theta_d - \theta_c$,

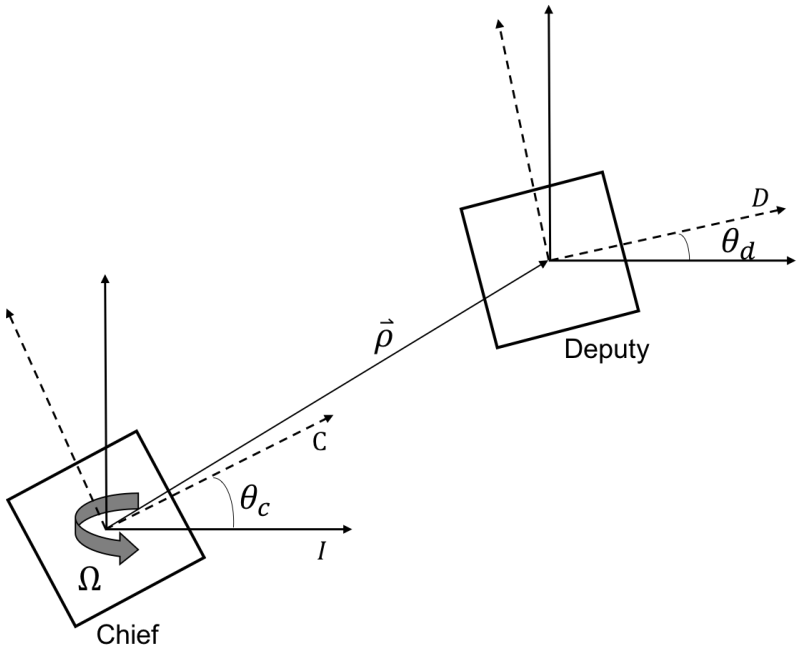

Figure 4.2. Depiction of planar spacecraft docking with chief rotating at a constant rate.

and relative angular velocity $\omega_r = \dot{\theta}_r$. The relative rotational dynamics are then written in double integrator form,

$$\dot{\theta}_r = \omega_r \tag{4.16}$$

$$\dot{\omega}_r = \frac{M_z}{J_{d_z}}. \tag{4.17}$$

The relative dynamics of this system were derived in [17], in nonlinear control-affine form. However, choosing the chief body CCS as the frame of reference results in an LTI system [51], [52].

Defining the rotational state vector $x_R = [\theta_r \ \omega_r]^T \in \mathbb{R}^2$ and rotational control vector $u_R = {}^{M_z}/_{J_{d_z}} \in \mathbb{R}$, the simplified rotational subsystem can be written as

$$\dot{x}_R = \begin{bmatrix} 0 & 1 \\ 0 & 0 \end{bmatrix} x_R + \begin{bmatrix} 0 \\ 1 \end{bmatrix} u_R. \tag{4.18}$$

The translational system can be simplified by modifying (4.13) to ignore the out-of-plane states (ρ_z, v_z), and by neglecting the orbital dynamics ($n = 0$). Defining the translational state vector $x_T = [\rho_x \; \rho_y \; v_x \; v_y]^T \in \mathbb{R}^4$, and translational control vector $u_T = [F_x/m_d \; F_y/m_d]^T \in \mathbb{R}^2$, the simplified translational subsystem can be written as,

$$\dot{x}_T = \begin{bmatrix} 0 & 0 & 1 & 0 \\ 0 & 0 & 0 & 1 \\ \Omega^2 & 0 & 0 & 2\Omega \\ 0 & \Omega^2 & -2\Omega & 0 \end{bmatrix} x_T + \begin{bmatrix} 0 & 0 \\ 0 & 0 \\ 1 & 0 \\ 0 & 1 \end{bmatrix} u_T. \tag{4.19}$$

The simplified dynamics for the planar docking scenario reduces the dimensionality of the problem and offers decoupled LTI subsystems describing the rotational and translational motions. This formulation is advantageous as it enables reachability computations via polytopic approximation methods (e.g., MPT [70]).

4.2 Reachability Analysis: Planar Docking in Close Proximity to Rotating Chief

The reachability analysis of the simplified planar docking scenario is presented in this section. The dynamics of the rotational and translational subsystems were shown in (4.18) and (4.19). Given control constraints of the form $-u_{max} \leq u_i \leq u_{max}$, backward reachable sets for the two subsystems were computed through a polytopic approximation method.

The MPT software [70] was used to perform the reachability computations of interest. MPT is an open source, MATLAB-based, toolbox that enables reachability computations for LTI systems through polytopic approximation methods. Following the example scenario presented in [17], the desired state (docking), was defined as $x_T = [1, \; 0, \; 0, \; 0]^T$, and $x_R = [0, \; 0]^T$. The parameters of interest in this case were the chief's rotation rate (Ω), the control bounds (u_{max}), and allotted time (T).

Backward reachable sets were computed for $\Omega = 0, \; 5, \; 10, \; 15,$ and $20 \; deg/sec$, $u_{max} = 1, \; 0.7, \; 0.5,$ and 0.1, and $T = 5, \; 10, \; 15,$ and $20 \; sec$. The control bounds, u_{max}, represent different levels of force-to-mass (translational acceleration in units $\frac{m}{s^2}$) and torque-to-inertia (angular acceleration in units $\frac{1}{s^2}$) ratios.

Figure 4.3 shows the backward reachable set for the rotational states. It can be seen clearly that the size of the reachabe set increases proportionally to the spacecraft's torque-to-inertia level. Additionally, as the allotted time is increased the size of the reachable set increases significantly.

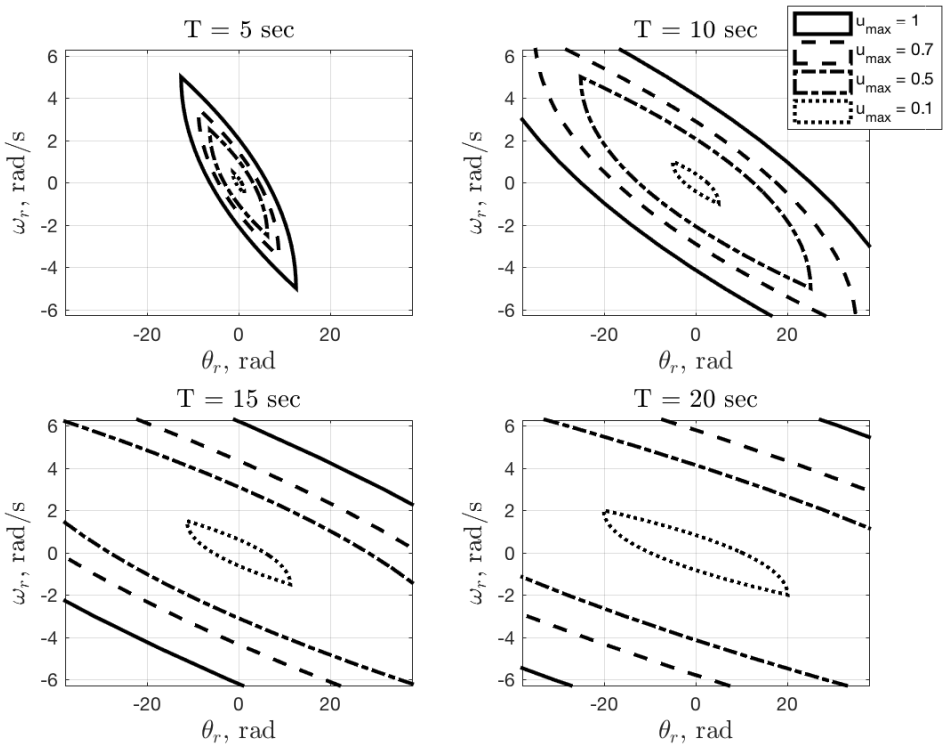

Figure 4.3. Backward reachable sets of rotational subsystem for simplified planar docking scenario.

In order to visualize the 4-dimensional translational sets, slices of the sets were plotted along the position variables at specific velocity values, and vice versa. The rows of Figures 4.4-4.7 show the slices of the backward reachable sets at different chief rotation rates, while the columns show different values of final time. When the chief is not rotating ($\Omega = 0$), the translational dynamics have a double-integrator form. Non-zero rotation rates, however, induce more complex behavior.

It can be clearly seen in Figures 4.4 and 4.5 that the translational backward reachable set decreases in size as the chief rotation rate is increased, and alloted time is decreased. As with the rotational sets, the size of the translational sets also increase proportionally to

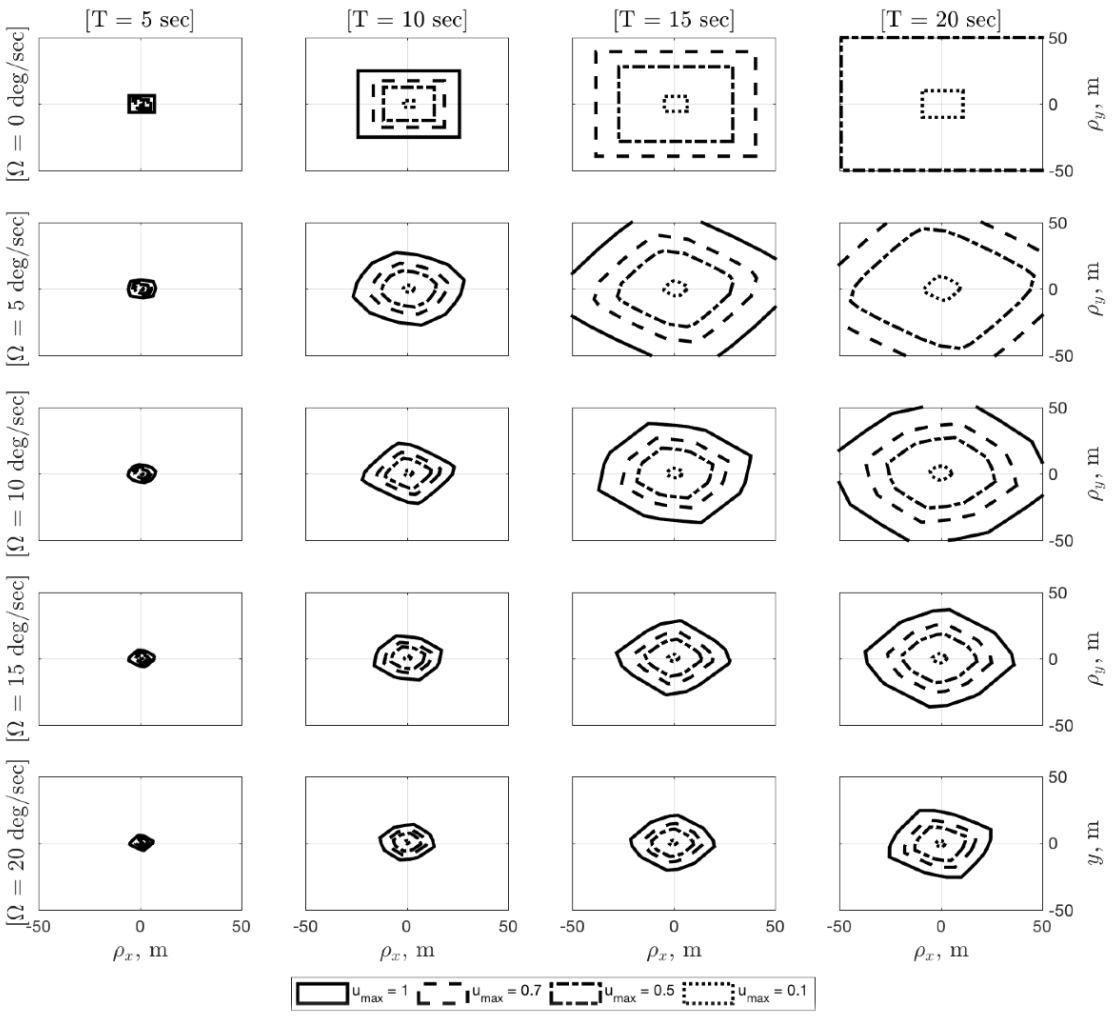

Figure 4.4. Slices of backward reachable sets of translational subsystem at $v_0 = [0, 0]\ m/s$.

the spacecraft's force-to-mass ratio. From the second plot in the top row of Figure 4.5, it is evident that when $u_{max} = 0.1$, and with initial relative velocity $[1, 1]\ m/s$, the set vanishes (i.e, the spacecraft does not have enough control authority to complete the docking maneuver). Examining the other plots in the second column of Figure 4.5 shows that the set corresponding to $u_{max} = 0.1$ becomes non-empty for faster chief rotation rates, which is somewhat unintuitive. In this case, the higher rotation rate serves to place the chief in a position where the deputy is able to reach it within the alloted time. Likewise, increasing the value of the final time can make the maneuver feasible with $u_{max} = 0.1$.

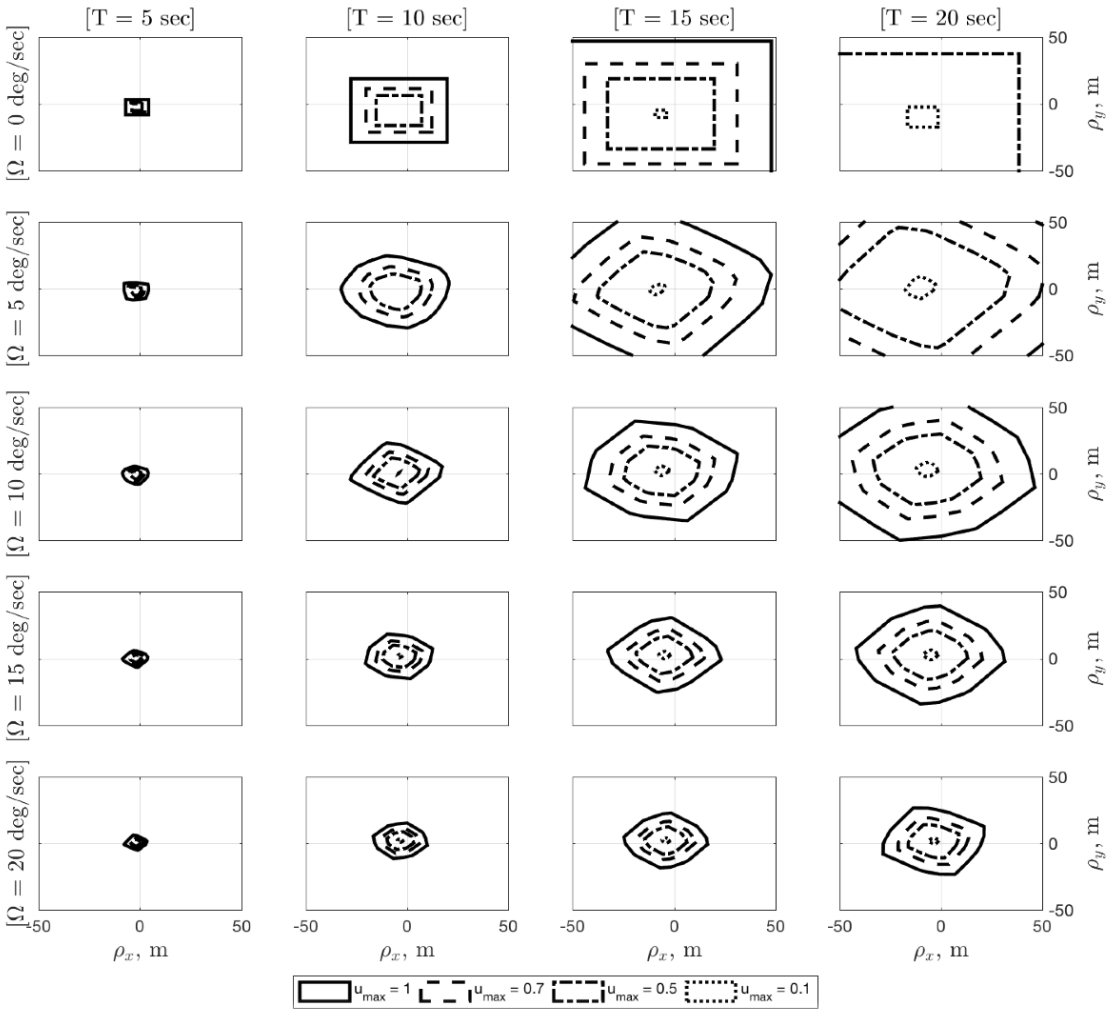

Figure 4.5. Slices of backward reachable sets of translational subsystem at $v_0 = [1, 1]\ m/s$.

Figures 4.6 and 4.7 show some additional characteristics of the considered maneuver. Particularly, it can be seen that when the deputy is further away from the origin, and the chief's rotation rate increases, a higher initial velocity is required to successfully dock with the rotating chief. For example, the sets depicted in the bottom right hand plot of Figure 4.7 are shifted in comparison to the same plot in Figure 4.6. It is also evident in Figure 4.7 that as the allotted time is decreased, lower values of u_{max} make the maneuver infeasible when the initial position is $[10, 10]\ m$. The first column of the figure shows that the only non-empty sets correspond to $u_{max} = 1$, and all other sets are empty. Conditions improve

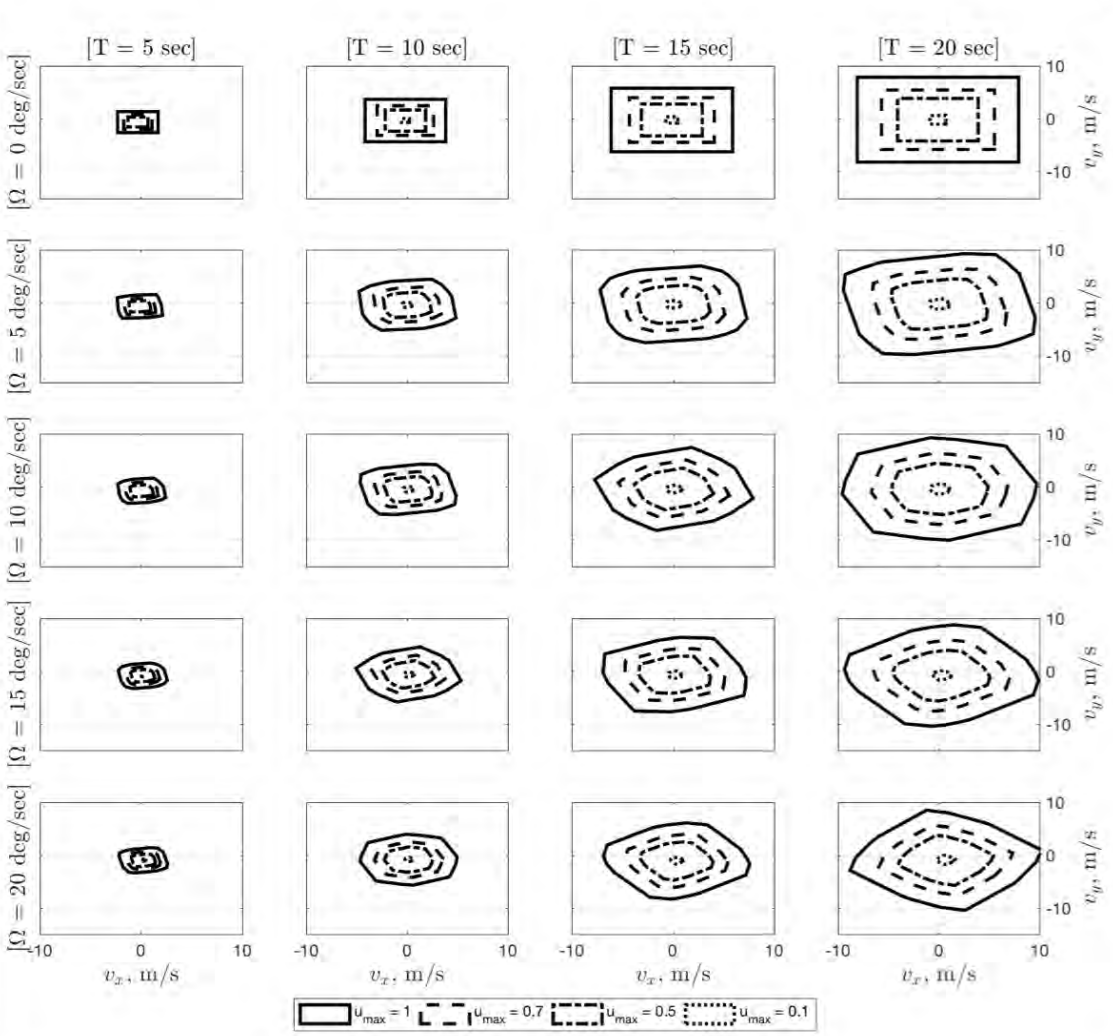

Figure 4.6. Slices of backward reachable sets of translational subsystem at $\rho_0 = [2, 2]$ m.

as the alloted time is increased, with the last column of the figure ($T = 20$ seconds) showing non-empty sets for all cases.

The insight gained through reachability analysis is valuable, even for the simplified example of planar docking. The results showed that as the chief's rotation rate increases and control authority decreases, docking becomes more difficult, if not infeasible. It was also shown that, in some cases, a higher rotation rate may help achieve a feasible condition.

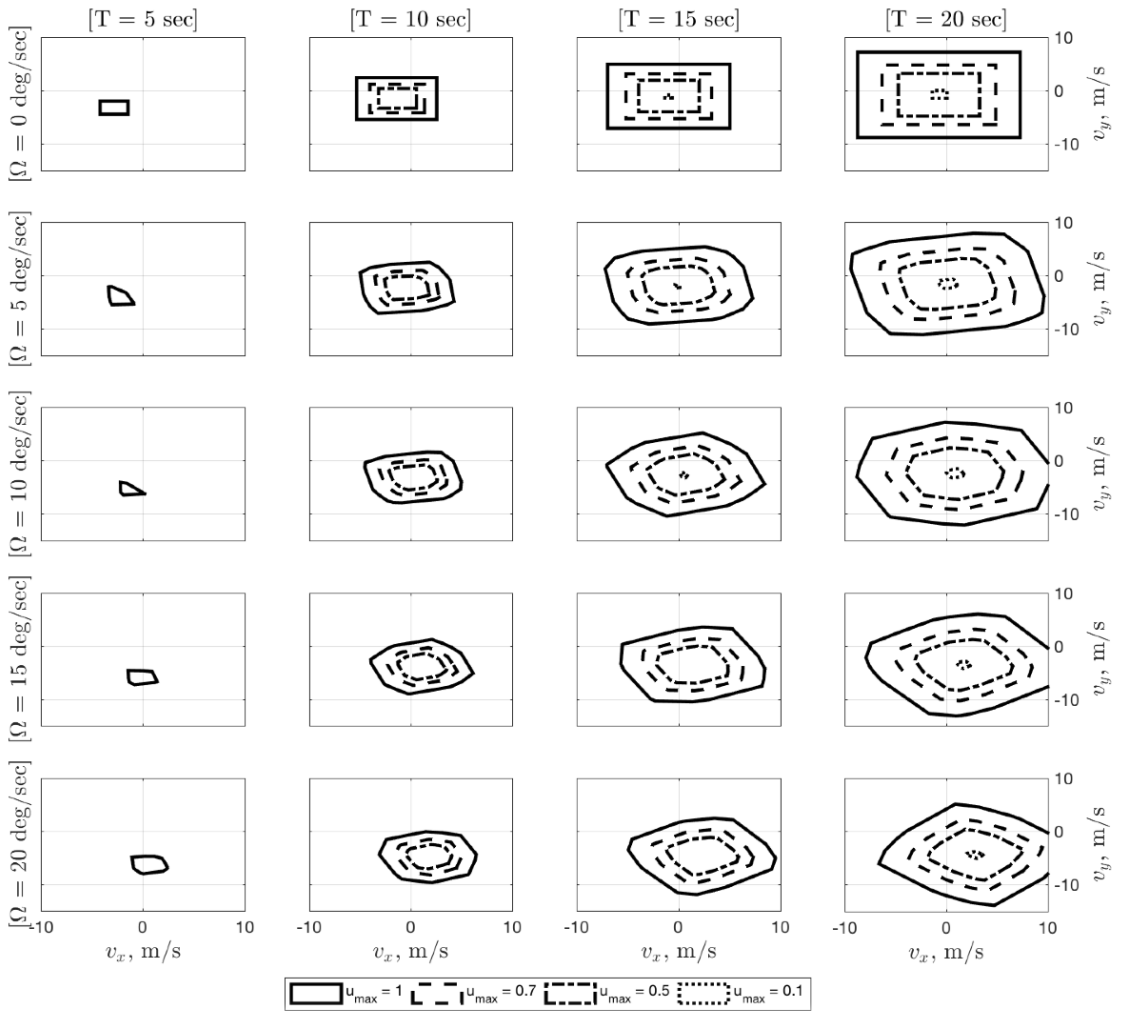

Figure 4.7. Slices of backward reachable sets of translational subsystem at $\rho_0 = [10, 10]$ m.

4.3 Reachability Analysis: 6-DOF Rendezvous with Rotating Chief

After studying the reachability characteristics of the simplified planar docking problem, the more complicated scenario of a 6-DOF rendezvous with a chief in circular orbit, rotating on the orbit plane, is considered. The chief and deputy are defined as one meter homogeneous cubes (i.e., dimensions of $1 \times 1 \times 1$ m), resulting in spherically symmetric inertia properties. The polytopic approximation method that was previously used is not tractable in this case

due to the dimensionality of the problem and complexity of the dynamics. The minimum time contour approach, described in Section 3.2, is used to analyze the backward reachability characteristics of this scenario. The parameters of the scenario studied during this phase of research are shown in Table 4.1. For the purpose of this analysis, a failure is defined as a simulation in which the GPOPS-II solver did not converge to a solution within the desired tolerance.

Table 4.1. Scenario parameters for 6-DOF rendezvous with chief in circular orbit, rotating on the orbit plane at a constant rate.

Chief Orbit Altitude (km)	400
Chief Mass (kg)	100
Deputy Mass (kg)	100
Chief Inertia (kg-m^2)	$diag(16.67,\ 16.67,\ 16.67)$
Deputy Inertia (kg-m^2)	$diag(16.67,\ 16.67,\ 16.67)$
F_{max} (N)	1
M_{max} (N-m)	1
T_{max} (s)	1000
Desired final condition	$\boldsymbol{\rho}_f = [1, 0, 0]^T\ m$
	$\mathbf{v}_f = [0, 0, 0]^T\ m/s$
	$q_f = [0, 0, 0, 1]^T$, or $\boldsymbol{\sigma}_f = [0, 0, 0]^T$
	$\boldsymbol{\omega}_f = [0, 0, 0]^T\ rad/s$

4.3.1 Analytical Limit of Chief Rotation Rate for Maintaining Rendezvous

Consider the simplified problem of rendezvous with a chief in circular orbit, rotating on the orbit plane at a constant rate, with simplified dynamics given in (4.10). It is clear that the rendezvous condition $\boldsymbol{\rho} = [1, 0, 0]^T$, $\mathbf{v} = [0, 0, 0]^T$, $q = [0, 0, 0, 1]^T$ (or $\boldsymbol{\sigma} = [0, 0, 0]^T$), and $\boldsymbol{\omega}^{\mathsf{D}} = [0, 0, 0]^T$, is not an equilibrium of this dynamic system. Applying (2.25), it can be seen that

$$u_s = \begin{bmatrix} -m_d \left(\frac{\mu}{(R_c+1)^3} + \frac{\mu}{R_c^2} \cos(\Omega t) - \frac{\mu R_c}{(R_c+1)^3} \cos(\Omega t) + (\Omega + n)^2 \right) \\ m_d \left(\frac{\mu}{R_c^2} \sin(\Omega t) - \frac{\mu R_c}{(R_c+1)^3} \sin(\Omega t) \right) \\ 0 \\ 0_{3\times 1} \end{bmatrix}. \tag{4.20}$$

Looking at the individual control components in (4.20), it is clear that the first component will dominate. In the second component, the two terms including $\sin(\Omega t)$ are almost equal, and that term will be very close to zero. In the first component, likewise, the $\cos(\Omega t)$ terms will be about equal and the first fractional term will be very small (on the order of 10^{-5}), leaving the dominant term $(\Omega + n)^2$. Therefore, it follows that

$$||u_s||_\infty \approx m_d(\Omega + n)^2 \tag{4.21}$$

Given a maximum available control input (u_{max}), the chief rotation rates for which the rendezvous condition can be maintained is then upper-bounded by

$$\Omega \leq \sqrt{\frac{u_{max}}{m_d}} - n. \tag{4.22}$$

Applying (4.22) to the scenario in Table 4.1, it can be seen that the highest chief rotation rate that can be maintained is about 5.67 degrees per second.

4.3.2 Analysis of Translational Backward Reachability

The translational subsystem is the 6-dimensional system shown in (4.13). The GPOPS-II parameters used for this scenario are shown in Table 4.2. In addition to computing the minimum time to achieve the desired relative state, the control effort required was also computed by

$$ce = \int_0^{t_f} ||u_T||_1 \, dt. \tag{4.23}$$

Table 4.2. GPOPS-II parameters used to solve the MT-OCP for the translational subsystem.

Parameter	Value
Mesh tolerance	$1e$-6
Max mesh refinements	10
Min collocation points	4
Max collocation points	10
Max NLP iterations	2000
Initial Guess	Endpoints (zero control)

Analysis of Out-of-Plane Subspace

Since the out-of-plane motion ($\rho_z,\ v_z$) is decoupled, it was analyzed independently from the planar motion. The two-dimensional out-of-plane motion is time-invariant and not dependent on the chief's rotation rate. A set of $1,000$ test initial conditions was created in the following subspace: $-100\ m\ \leq \rho_z \leq 100\ m$, and $-1\ m/s\ \leq v_z \leq 1\ m/s$. The control constraint on this subspace was $-1 \leq F_z \leq 1$. The MT-OCP was attempted from each of the conditions. Of the $1,000$ test cases, 6.1% failed to solve to within the desired tolerance. The resulting minimum time contours are shown in Figure 4.8. The approximate shape of the backward reachable sets becomes apparent, and it can be seen that the sets grow proportionally with time.

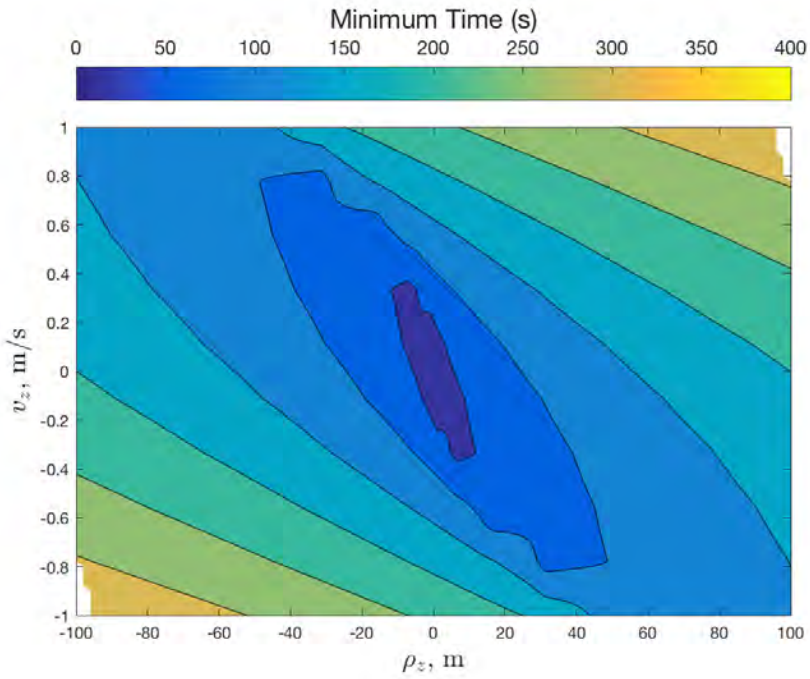

Figure 4.8. Out-of-plane slice of backward T-reachable set for chief planar rotation; color bar indicates minimum time values corresponding to the contours.

Figure 4.9 shows the correlation between the minimum time and control effort for the $1,000$ test cases. The plots on the diagonal show histograms of the minimum times and control effort, respectively. The off-diagonal plots show the two data sets plotted with respect to each other. From the histogram of minimum times, it is clear that the majority of the cases

completed the maneuver in 120 to 140 seconds, with the maximum time being around 340 seconds in this sample. The control effort histogram shows a very similar trend. The linear relationship between minimum time and control effort is expected since this is a bang-bang maneuver with one control variable (F_z). This expectation is depicted by the black line shown on the off-diagonal plots. The data follows the linear trend exactly in this case.

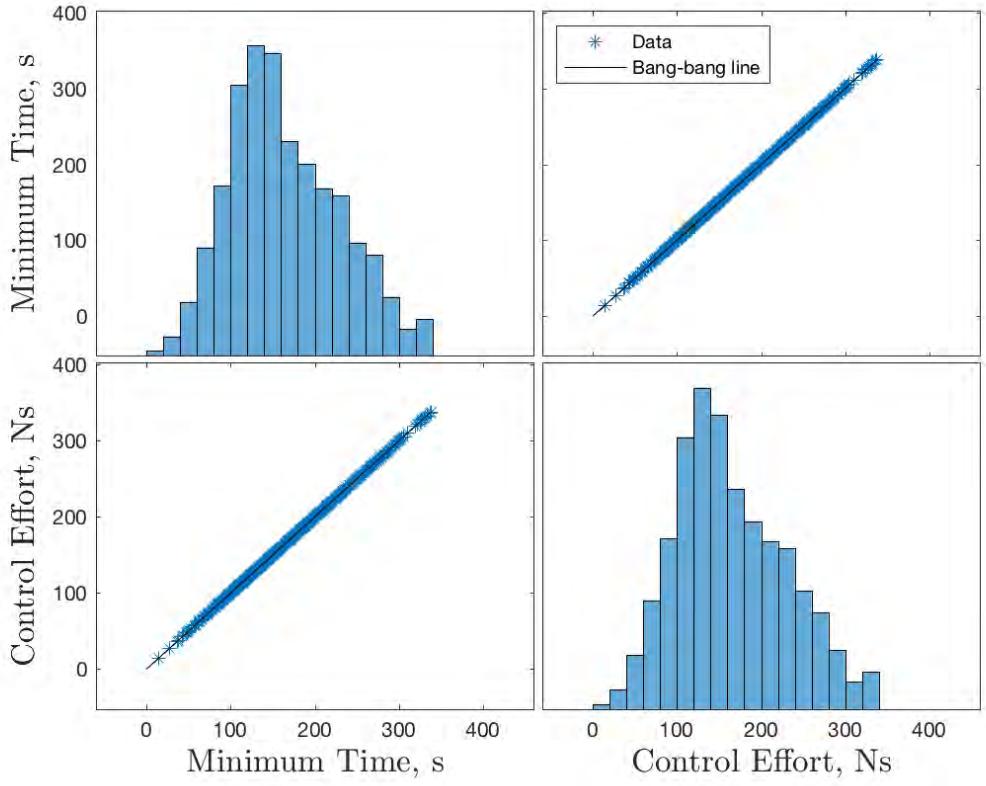

Figure 4.9. Minimum time and control effort histograms and correlation for out-of-plane subspace.

Three cases were selected in order to show a sampling of these minimum time trajectories. The first case was selected from the middle of the distribution (i.e., the largest bin in the minimum time histogram), the second one was selected from the low end of the distribution, and the third from the high end. For these samples, the optimal solution from GPOPS-II was applied to the out-of-plane dynamics independently, to serve as a validation of the optimal solution. Results from the three cases are shown in Figure 4.10. The circles on the

plots indicate the solution provided by GPOPS-II, while the lines indicate the integrated state trajectory after applying the optimal control. The first two cases (Figure 4.10a and 4.10b) seem accurate, however, the third case (Figure 4.10a) shows a deviation between the GPOPS-II and integrated trajectories toward the end of the maneuver. This is an indication that a higher tolerance, or larger number of collocation points, is needed to get a more accurate result.

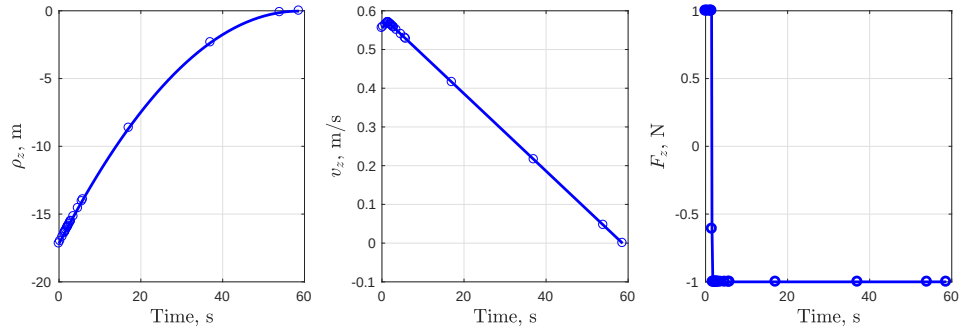

(a) Sample case # 1

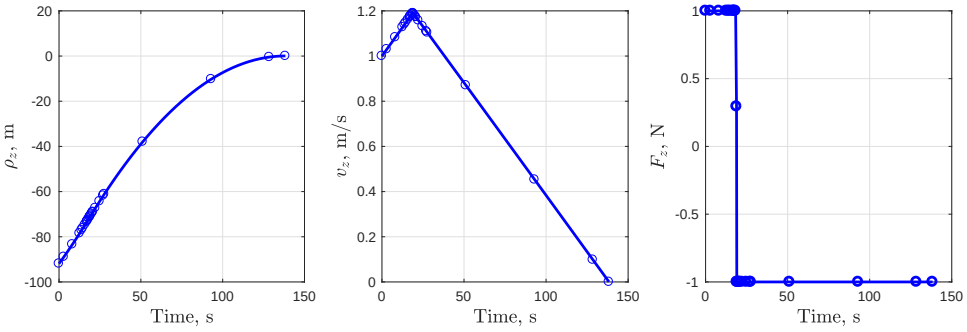

(b) Sample case # 2

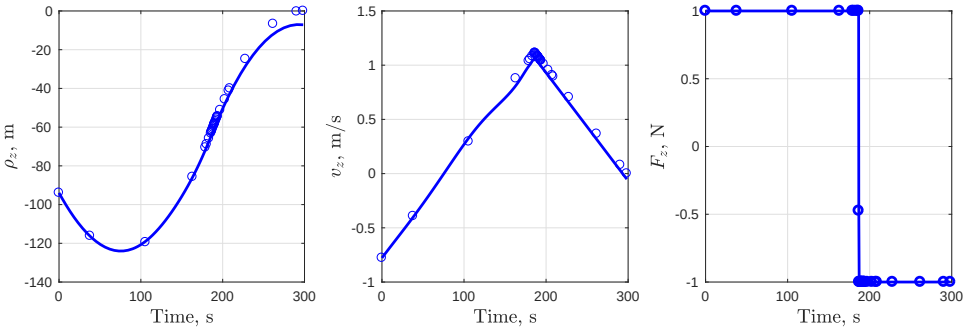

(c) Sample case # 3

Figure 4.10. Sample out-of-plane minimum time maneuvers.

Analysis of Planar Position Subspace

The four-dimensional planar motion poses a dimensionality problem for visualization. In this case, subspaces were created representing slices of the four-dimensional sets. The first subspace investigated reachability from different initial relative positions, at specific initial relative velocities. Two slices were created in this subspace. The first slice was defined by 2,500 test initial conditions in the following subspace: $-100\ m\ \leq (\rho_x,\ \rho_y) \leq 100\ m$, at $\mathbf{v} = [0, 0]^T$. Recall that the relative velocity is resolved in the chief's rotating body frame; as such, zero relative velocity imposes an initial inertial velocity on the deputy due to the chief's orbital and rotating motion. The control constraint on this subspace was $-1 \leq (F_x,\ F_y) \leq 1$. The MT-OCP was attempted for each test point with chief rotation rates of $\Omega = 0,\ 2,\ 4,$ and 6 degrees per second (total of 10,000 runs). Figure 4.11 shows the resulting minimum time contours. The contours increase proportionally with time and shrink as the target's rotation rate increases. As the chief's rotation rate is increased, the maneuver becomes more difficult. The percentage of failed cases is reported in Table 4.3. When the chief is not rotating, backward T-reachable sets have a rectangular shape as shown in Figure 4.11a. This is expected since the force constraint is cubic. As the chief's rotation rate is increased, the sets take an oval shape as shown in Figure 4.11b-Figure 4.11d. On this subspace, when the chief rotation rate is 2 deg/s, the minimum time to reach the desired rendezvous point from the edge of the subspace approaches the maximum $1,000$ seconds. At the higher rotation rates of 4 and 6 deg/s, the rendezvous point becomes unreachable from the edges of the subspace, in the alloted amount of time. Figure 4.12 shows a scatter plot of the test points and the corresponding minimum time solution. The minimum time contours plotted in Figure 4.11 were derived from this set of data and the resemblance is clear. The uncolored circles in these scatter plots indicate that the solver did not converge to a solution from that particular test point. In Figure 4.12b a small number of uncolored circles is visible (0.68% as reported in Table 4.3). These cases failed to converge due to the sensitivity of the solver, but are likely within the reachable set since the surrounding test points solved successfully. In Figure 4.12c a larger number of failures is seen (79.2% as reported in Table 4.3). These failed cases, especially toward the edges of the subspace, are truly not reachable within the allotted time.

Figure 4.13 shows the correlation between minimum time and control effort for the 2,500 cases, for each scenario. The histograms on the diagonals of each subfigure show the range

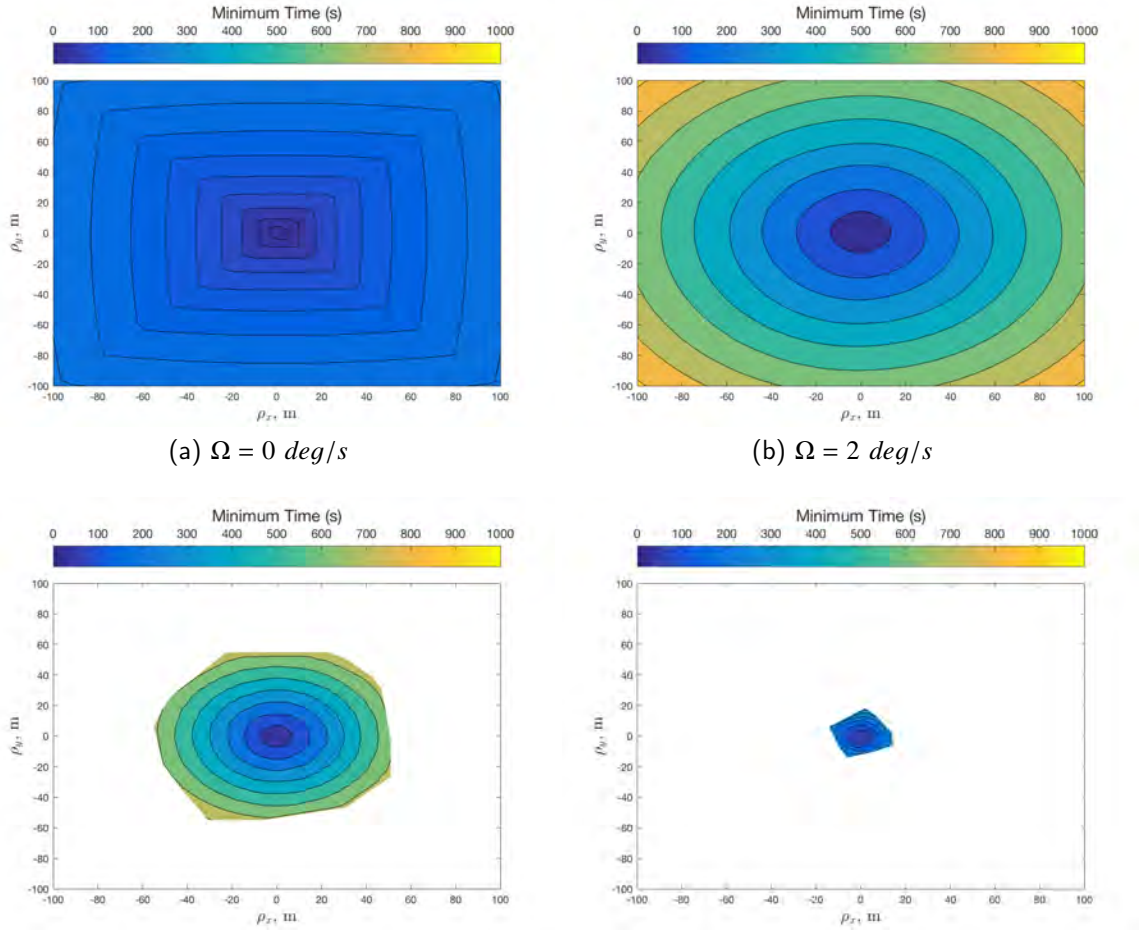

(a) $\Omega = 0\ deg/s$ (b) $\Omega = 2\ deg/s$

(c) $\Omega = 4\ deg/s$ (d) $\Omega = 6\ deg/s$

Figure 4.11. Translational backward T-reachable set slices at zero initial relative velocity at different chief rotation rates; color bar indicates minimum time values corresponding to the contours.

of minimum times and control effort from the sampled data, while the off-diagonals show the correlation between minimum time and control effort. For the case of $\Omega = 6\ deg/s$, the amount of data available is very limited since less than 2% of the cases were solved successfully. The linear correlation between minimum time and control effort, apparent in all of the four subfigures, is an indication that for these minimum time maneuvers both control variables (F_x and F_y) are bang-bang. The black lines plotted on the off-diagonal plots represent the expected linear relationship, assuming both control variables will exhibit bang-bang behavior. It can be seen that the data follows the bang-bang lines exactly.

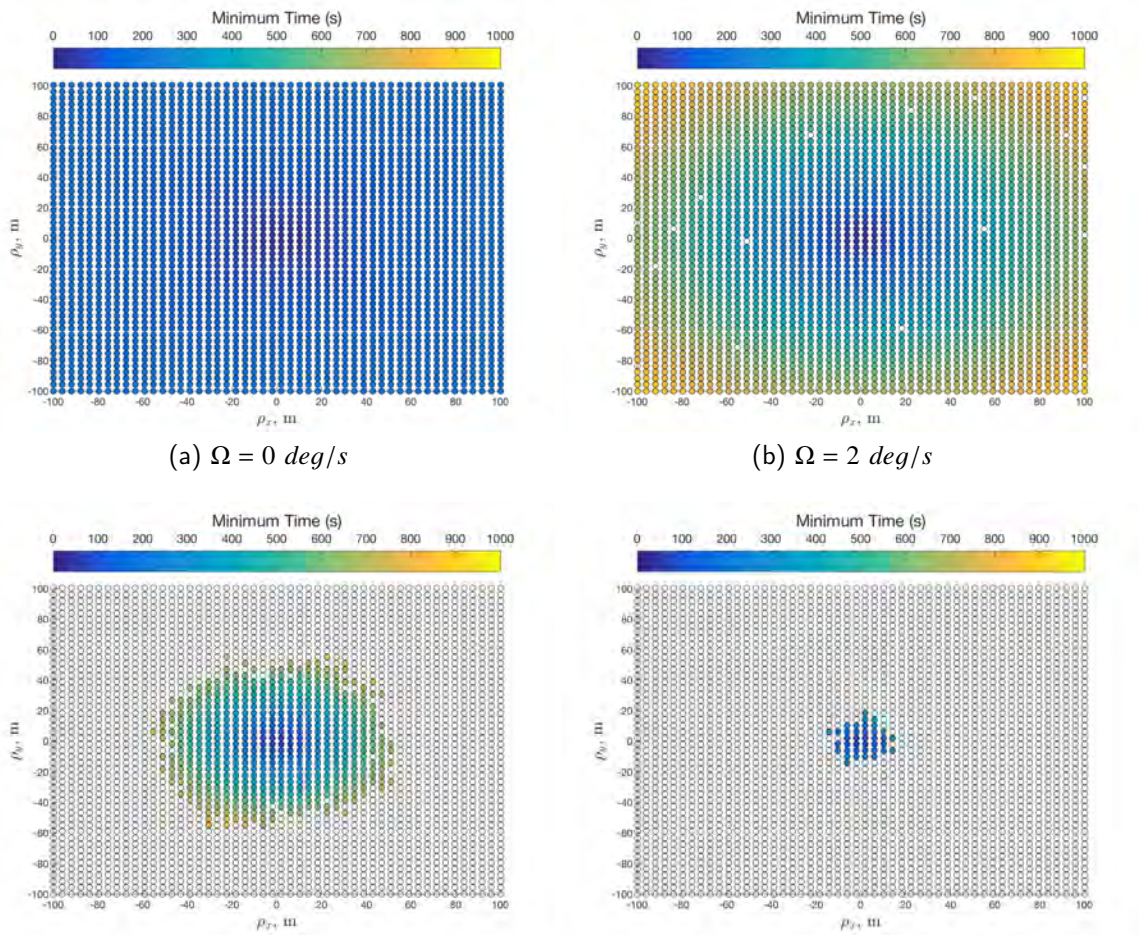

(a) $\Omega = 0\ deg/s$

(b) $\Omega = 2\ deg/s$

(c) $\Omega = 4\ deg/s$

(d) $\Omega = 6\ deg/s$

Figure 4.12. Relative position test points at zero initial relative velocity at different chief rotation rates; color indicates minimum time values for each test point. An uncolored test point indicates a failure (i.e., the solver did not converge).

Two sample test cases were selected to show an example of these minimum time trajectories. For comparison, the two selected samples were cases that were successfully completed for all chief rotation rates. Figures 4.14 and 4.15 show the two sample trajectories, for all chief rotation rates. In both figures, it can be seen that as the chief's rotation rate increases, the state trajectories become more nonlinear, and the controls show more frequent switches. The circles on the plots indicate the solution provided by GPOPS-II, while the lines indicate the integrated state trajectory after applying the optimal control. In Figure 4.15a it can

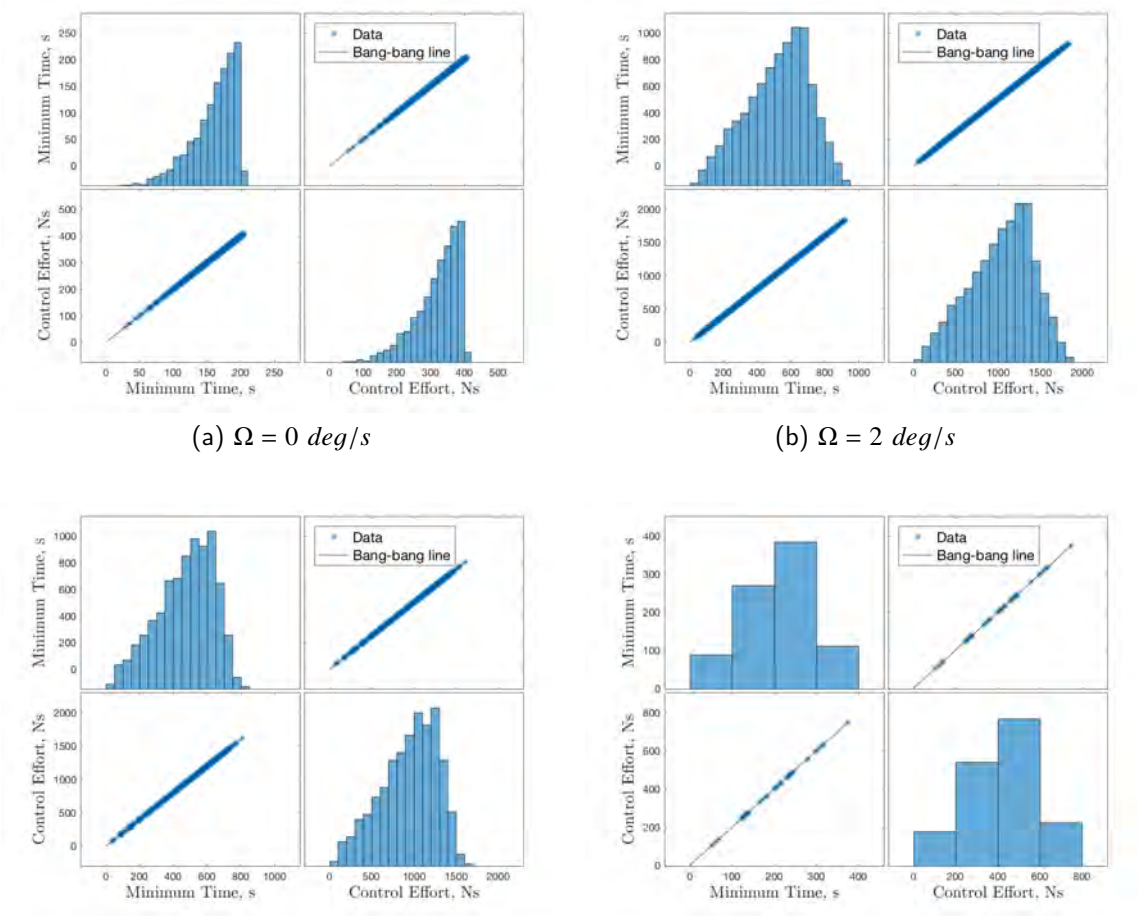

(a) $\Omega = 0\ deg/s$ (b) $\Omega = 2\ deg/s$

(c) $\Omega = 4\ deg/s$ (d) $\Omega = 6\ deg/s$

Figure 4.13. Minimum time and control effort histograms and correlation for position (zero velocity) subspace.

be seen that the integrated trajectory deviates from the optimal solution, indicating that the optimal solution is not accurate. GPOPS-II uses an adaptive method for placement of collocation points, allowing the algorithm to use as many points as needed to meet user-defined tolerances [83]. As a result, when the chief's rotation rate is higher, the solver uses more collocation points to capture the nonlinear behavior. The apparent error in the simpler case of $\Omega = 0\ deg/s$, seen in Figure 4.15a, can be corrected by using a larger number of collocation points, or a tighter solver tolerance.

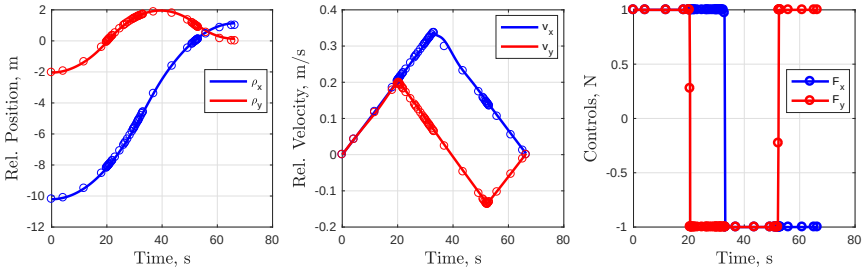

(a) $\Omega = 0\ deg/s$

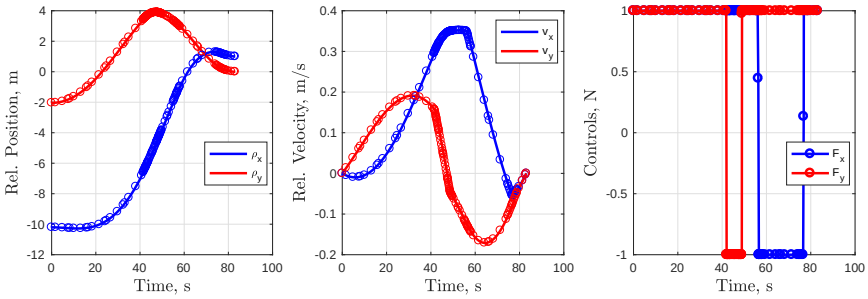

(b) $\Omega = 2\ deg/s$

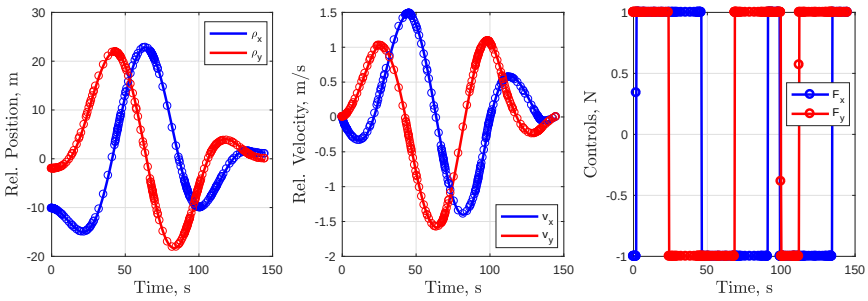

(c) $\Omega = 4\ deg/s$

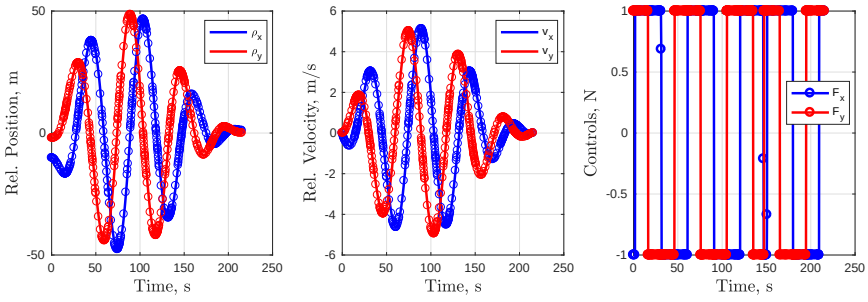

(d) $\Omega = 6\ deg/s$

Figure 4.14. Sample case #1 from position (zero velocity) subspace.

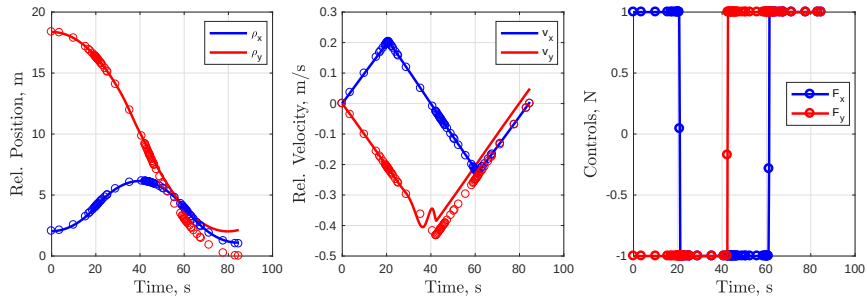

(a) $\Omega = 0\ deg/s$

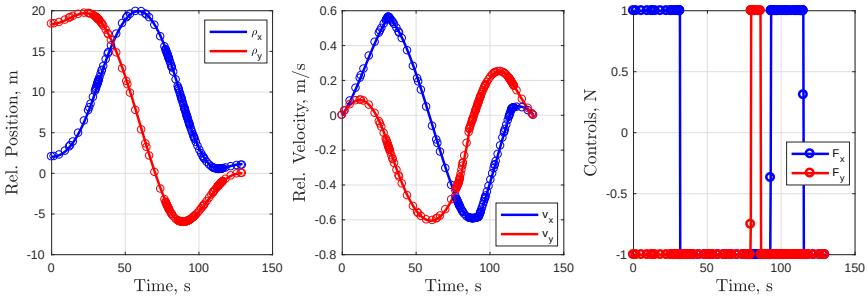

(b) $\Omega = 2\ deg/s$

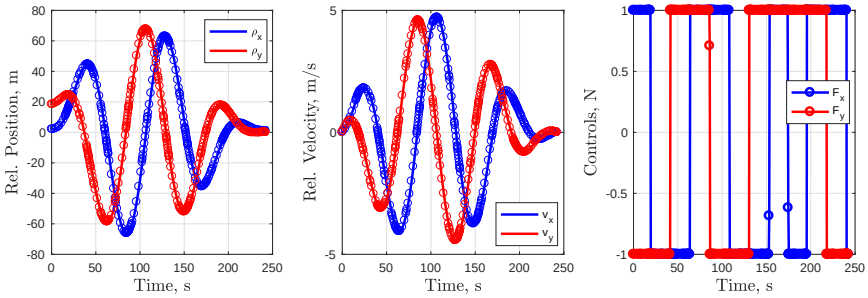

(c) $\Omega = 4\ deg/s$

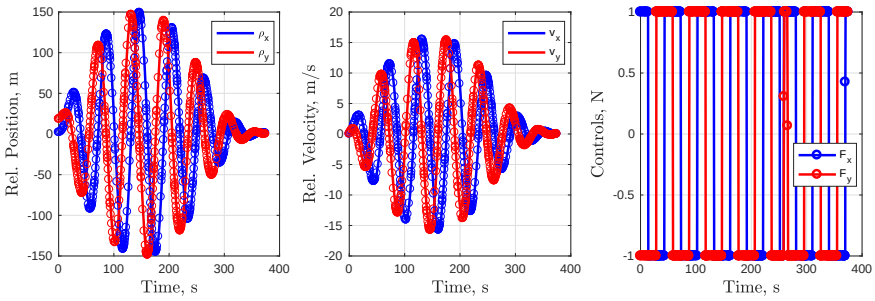

(d) $\Omega = 6\ deg/s$

Figure 4.15. Sample case #2 from position (zero velocity) subspace.

The second slice of the four-dimensional was defined by 2,500 test initial conditions in the following subspace: $-100\ m\ \leq (\rho_x,\ \rho_y) \leq 100\ m$, at an initial relative velocity corresponding to the deputy spacecraft being in a Natural Motion Circumnavigation (NMC) trajectory, transcribing a 2-by-1 ellipse around the chief. For each test point this initial relative velocity is given by

$$\mathbf{v}_0 = \begin{bmatrix} \frac{1}{2}n\rho_y \\ -2n\rho_x \\ 0 \end{bmatrix} - [\boldsymbol{\omega}_c]^{\times} \begin{bmatrix} \rho_x \\ \rho_y \\ 0 \end{bmatrix}, \tag{4.24}$$

where recall n is the chief's orbital mean motion, and $\boldsymbol{\omega}_c$ is the chief's angular velocity given in (4.8). Note that in (4.24) the chief's rotating motion is accounted for in order to express the NMC initial velocity in C. The control constraint on this subspace was $-1 \leq (F_x,\ F_y) \leq 1$. The MT-OCP was attempted for each test point with chief rotation rates of $\Omega = 0,\ 2,\ 4,$ and 6 degrees per second (total of 10,000 runs). Figure 4.16 shows the resulting minimum time contours. In this case, as the chief rotation rate increases the sizes of the contours do not change significantly, and the time values represented in Figure 4.16a - 4.16d remain the same. This is due to the fact that the initial velocity included the rotation of the chief. As opposed to the zero velocity subspace, depicted in Figure 4.11, there is no dramatic loss of maneuver feasibility in the NMC subspace, with chief rotation rate up to 6 deg/s. As reported in Table 4.3, all cases were completed successfully in this scenario and for all chief rotation rates.

Figure 4.17 shows the correlation between minimum time and control effort for the 2,500 cases, for each scenario. The histograms on the diagonals of each subfigure show the range of minimum times and control effort from the sampled data, while the off-diagonals show the correlation between minimum time and control effort. The histograms in Figure 4.17a - 4.17d show an almost identical distribution of minimum time and control effort, showing that the chief's rotation rate does not affect these parameters on this subspace. This result complies with the minimum time contours seen in Figure 4.16a - 4.16d. As seen in previous cases, the linear correlation between minimum time and control effort indicates that, for these maneuvers, both control variables (F_x and F_y) are bang-bang. Again, the data matches exactly with the line representing bang-bang behavior in both control variables.

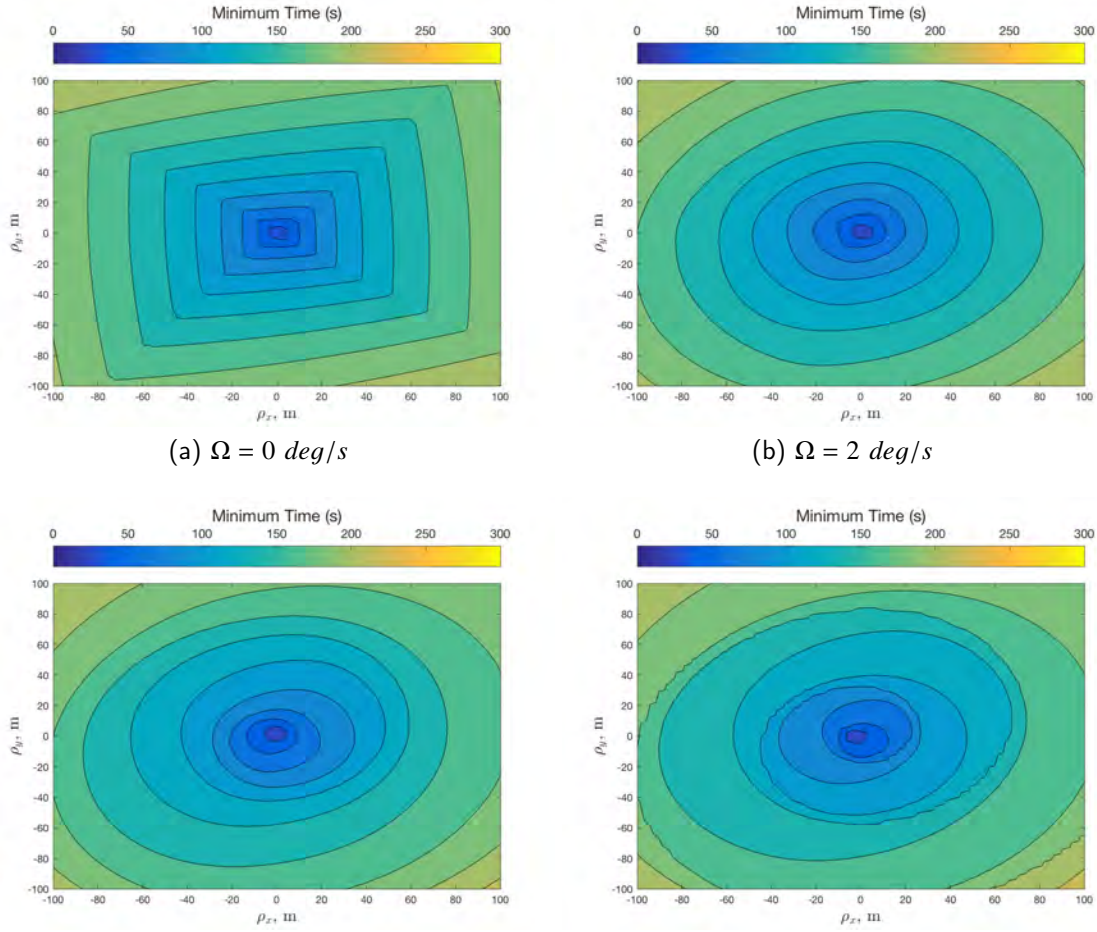

(a) $\Omega = 0\ deg/s$ (b) $\Omega = 2\ deg/s$

(c) $\Omega = 4\ deg/s$ (d) $\Omega = 6\ deg/s$

Figure 4.16. Translational backward T-reachable set slices at NMC initial relative velocity at different chief rotation rates; color bar indicates minimum time values corresponding to the contours.

Two sample test cases were selected to show an example of these minimum time trajectories. The two samples represent cases from the same initial position, however the initial velocities are different for each scenario as they are a function of the chief's rotation rate. Figures 4.18 and 4.19 show the two sample trajectories, for all chief rotation rates. As the chief rotation rate increases, it can be seen that the state trajectories become more nonlinear, and the controls switch more frequently (as also seen in the zero velocity subspace analysis). In this case, however, all maneuvers seen in Figures 4.18 and 4.19 took about the same amount of time.

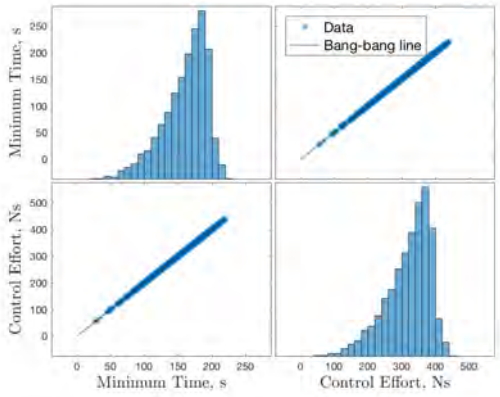

(a) $\Omega = 0\ deg/s$

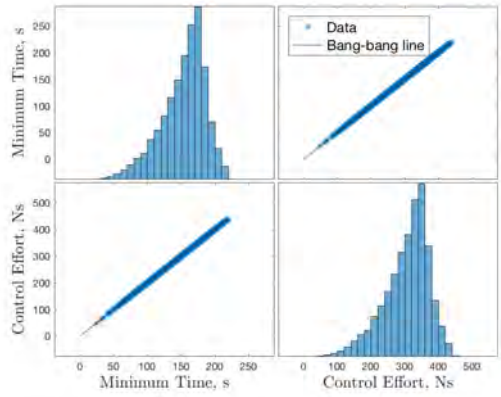

(b) $\Omega = 2\ deg/s$

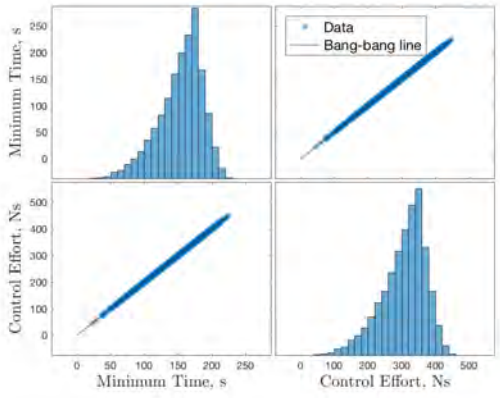

(c) $\Omega = 4\ deg/s$

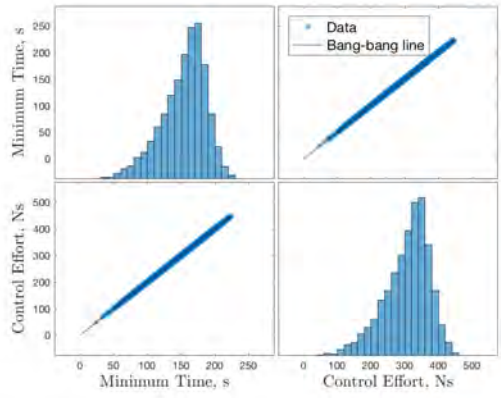

(d) $\Omega = 6\ deg/s$

Figure 4.17. Minimum time and control effort histograms and correlation for position (NMC velocity) subspace.

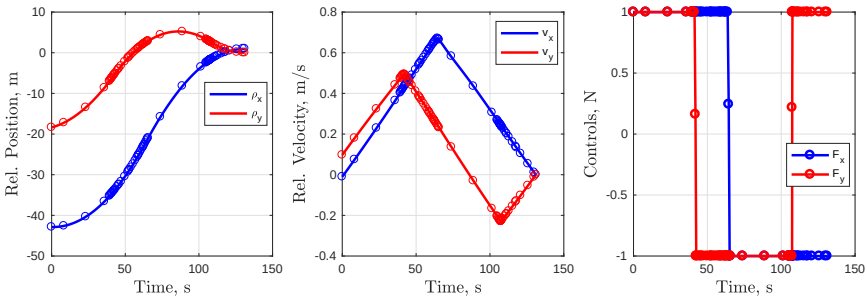

(a) $\Omega = 0\ deg/s$

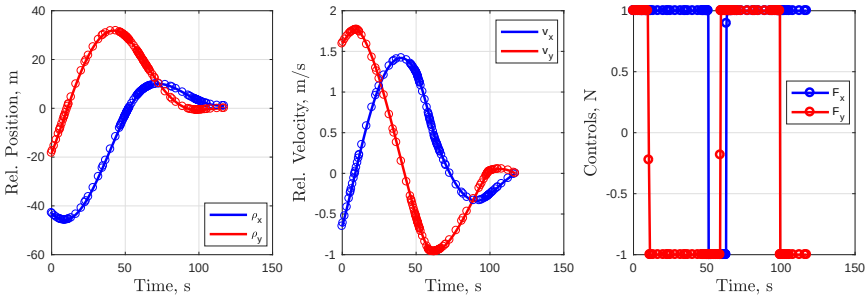

(b) $\Omega = 2\ deg/s$

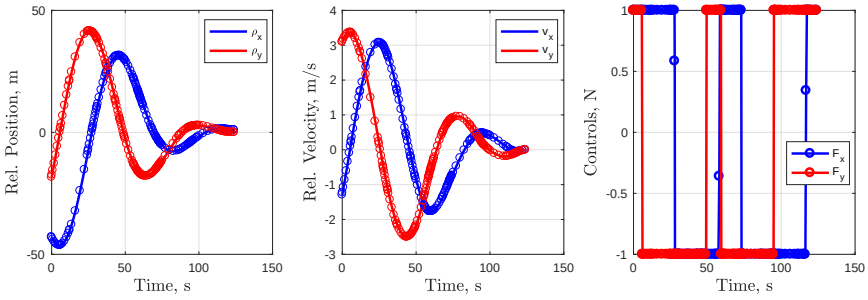

(c) $\Omega = 4\ deg/s$

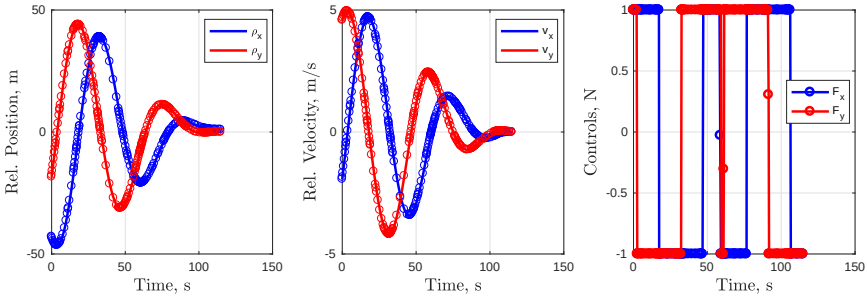

(d) $\Omega = 6\ deg/s$

Figure 4.18. Sample case #1 from position (NMC velocity) subspace.

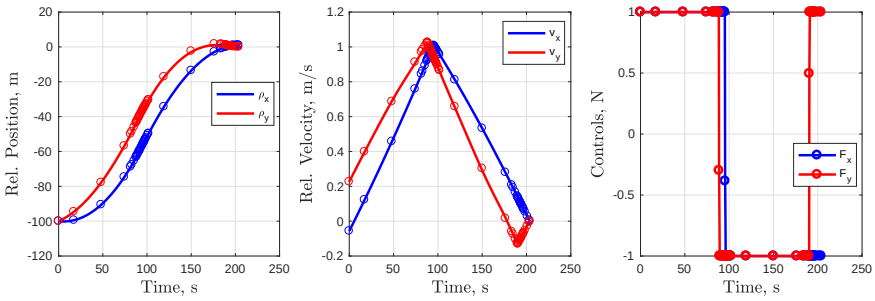

(a) $\Omega = 0\ deg/s$

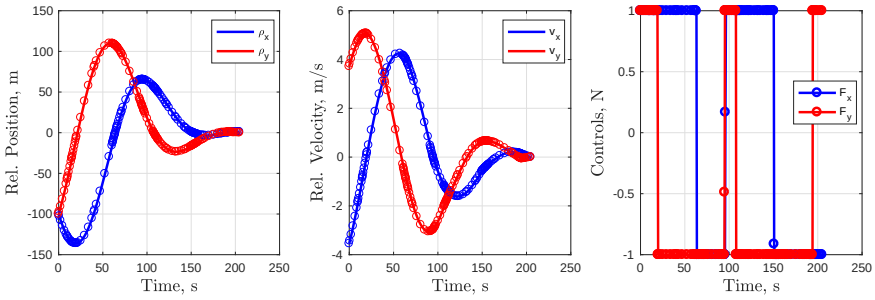

(b) $\Omega = 2\ deg/s$

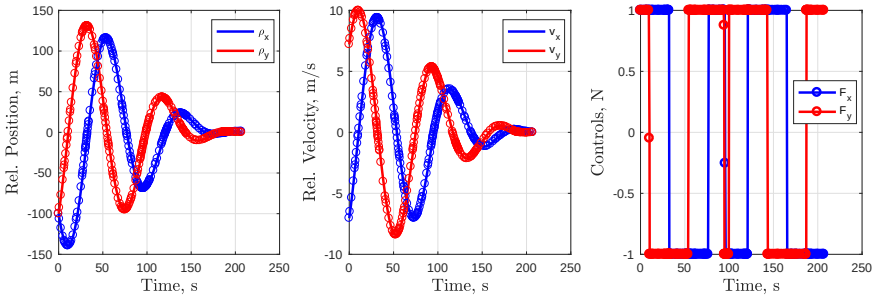

(c) $\Omega = 4\ deg/s$

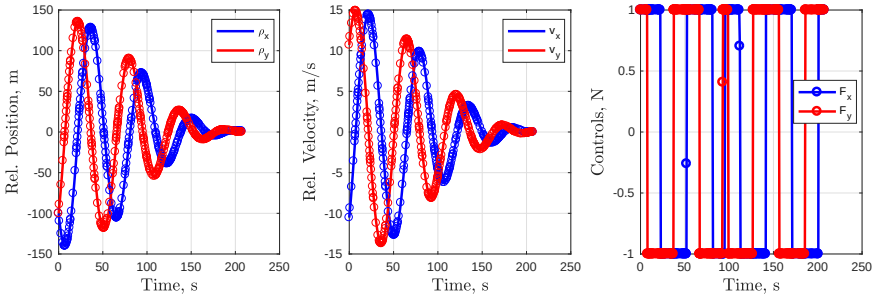

(d) $\Omega = 6\ deg/s$

Figure 4.19. Sample case #2 from position (NMC velocity) subspace.

Analysis of Planar Velocity Subspace

After investigating reachability of different relative positions, the relative velocity subspace was considered. Two slices were created in this subspace. The first slice of the four-dimensional backward reachable set was defined by 2,500 test initial conditions in the following subspace: $-10\ m/s \leq (v_x,\ v_y) \leq 10\ m/s$, at an initial relative position on the V-bar (y) axis, $\boldsymbol{\rho} = [0,\ 100]^T\ m$. The control constraint on this subspace was $-1 \leq (F_x,\ F_y) \leq 1$. The MT-OCP was attempted for each test point with chief rotation rates of $\Omega = 0,\ 2,\ 4,$ and 6 degrees per second (total of 10,000 runs). Figure 4.20 shows the resulting minimum time contours. It can be seen that as the chief's rotation rates increases, the contours move towards the right side of the plot, and are almost off the figure in Figure 4.20d. This behavior shows that at higher chief rotation rates, the deputy needs a larger initial relative velocity along the x direction in order to complete the maneuver successfully.

Figure 4.21 shows the correlation between minimum time and control effort for the 2,500 cases, for each scenario. The histograms on the diagonals of each subfigure show the range of minimum times and control effort from the sampled data, while the off-diagonals show the correlation between minimum time and control effort. For the case of $\Omega = 6\ deg/s$ the amount of data available is very limited since less than 2% of the cases were solved successfully. The linear correlation between minimum time and control effort, apparent in all of the four subfigures, is an indication that both control variables (F_x and F_y) are bang-bang. As in the previous analyses, the data matches exactly with the line representing bang-bang behavior in both control variables.

The second slice of the four-dimensional set was defined by 2,500 test initial conditions in the following subspace: $-10\ m/s \leq (v_x,\ v_y) \leq 10\ m/s$, at an initial relative position on the R-bar (x) axis, $\boldsymbol{\rho} = [100,\ 0]^T\ m$. The control constraint on this subspace was $-1 \leq (F_x,\ F_y) \leq 1$. The MT-OCP was attempted for each test point with chief rotation rates of $\Omega = 0,\ 2,\ 4,$ and 6 degrees per second (total of 10,000 runs). Figure 4.22 shows the resulting minimum time contours, showing a similar trend as the V-bar sets in Figure 4.20. In this case, the contours move towards the bottom of the plot showing that for higher chief rotation rates the deputy requires larger initial velocity in the y direction.

Figure 4.23 shows the correlation between minimum time and control effort for the 2,500

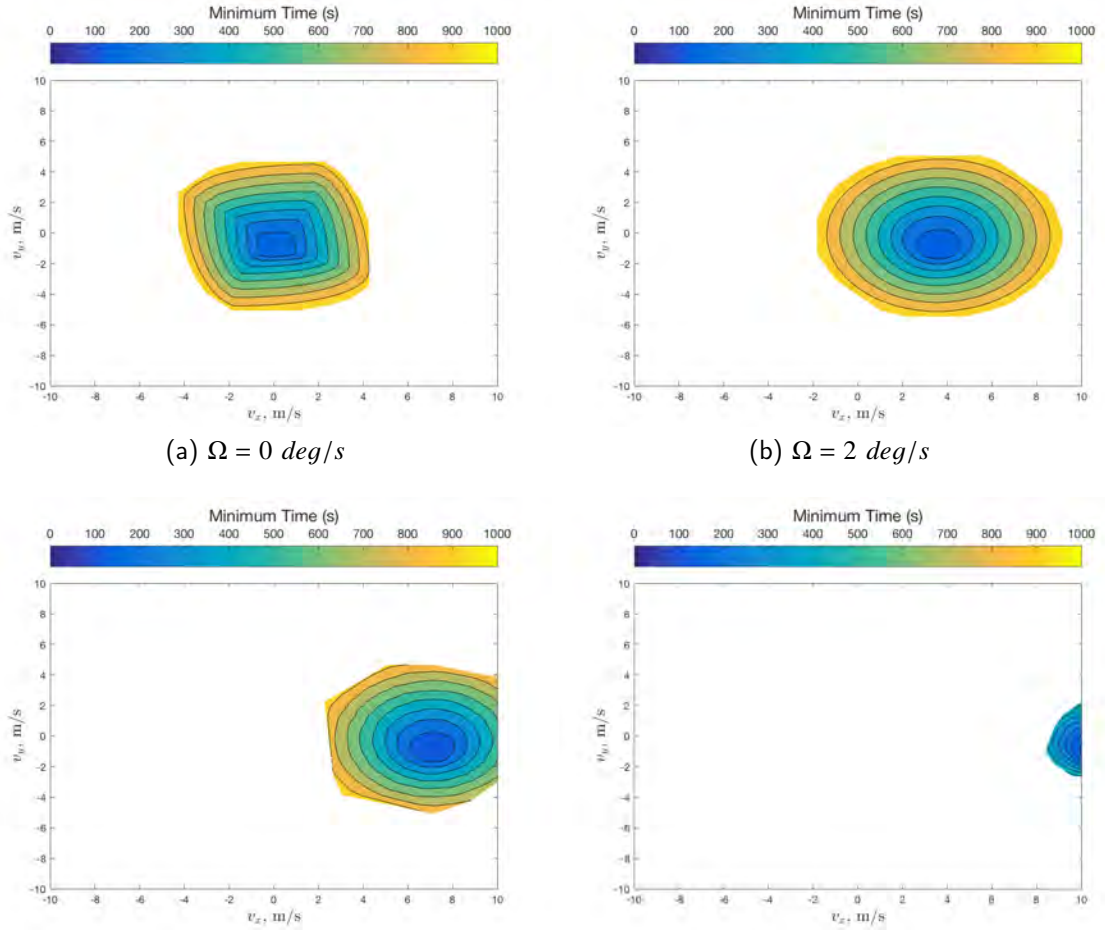

(a) $\Omega = 0\ deg/s$ (b) $\Omega = 2\ deg/s$

(c) $\Omega = 4\ deg/s$ (d) $\Omega = 6\ deg/s$

Figure 4.20. Translational backward T-reachable set slices at initial position on the V-bar axis at different chief rotation rates; color bar indicates minimum time values corresponding to the contours.

cases, for each scenario. These plots show very similar trends to what was observed in Figure 4.21.

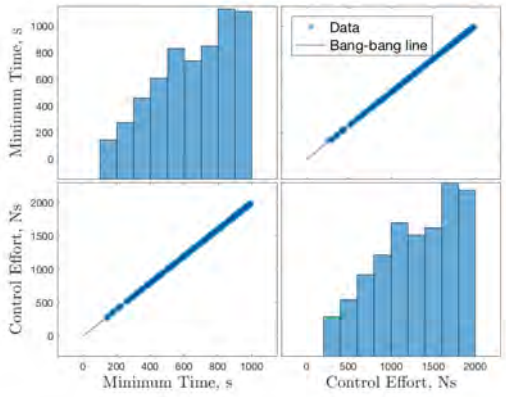

(a) $\Omega = 0\ deg/s$

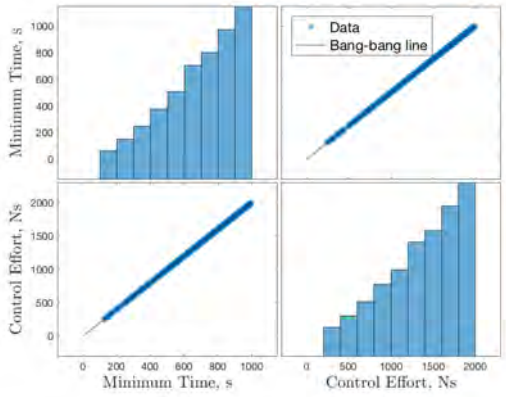

(b) $\Omega = 2\ deg/s$

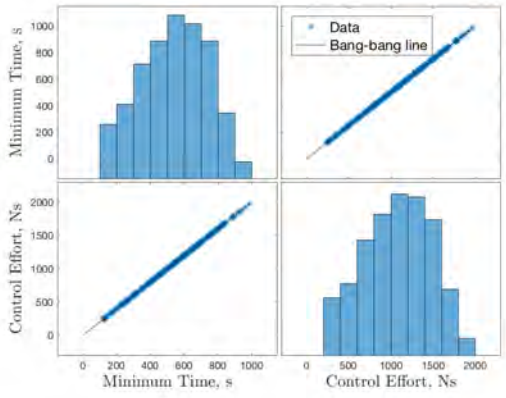

(c) $\Omega = 4\ deg/s$

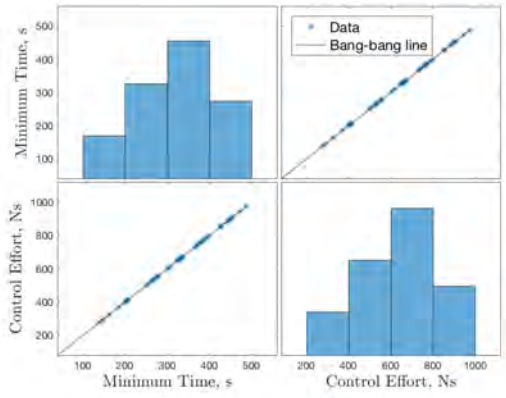

(d) $\Omega = 6\ deg/s$

Figure 4.21. Minimum time and control effort histograms and correlation for velocity (V-bar position) subspace.

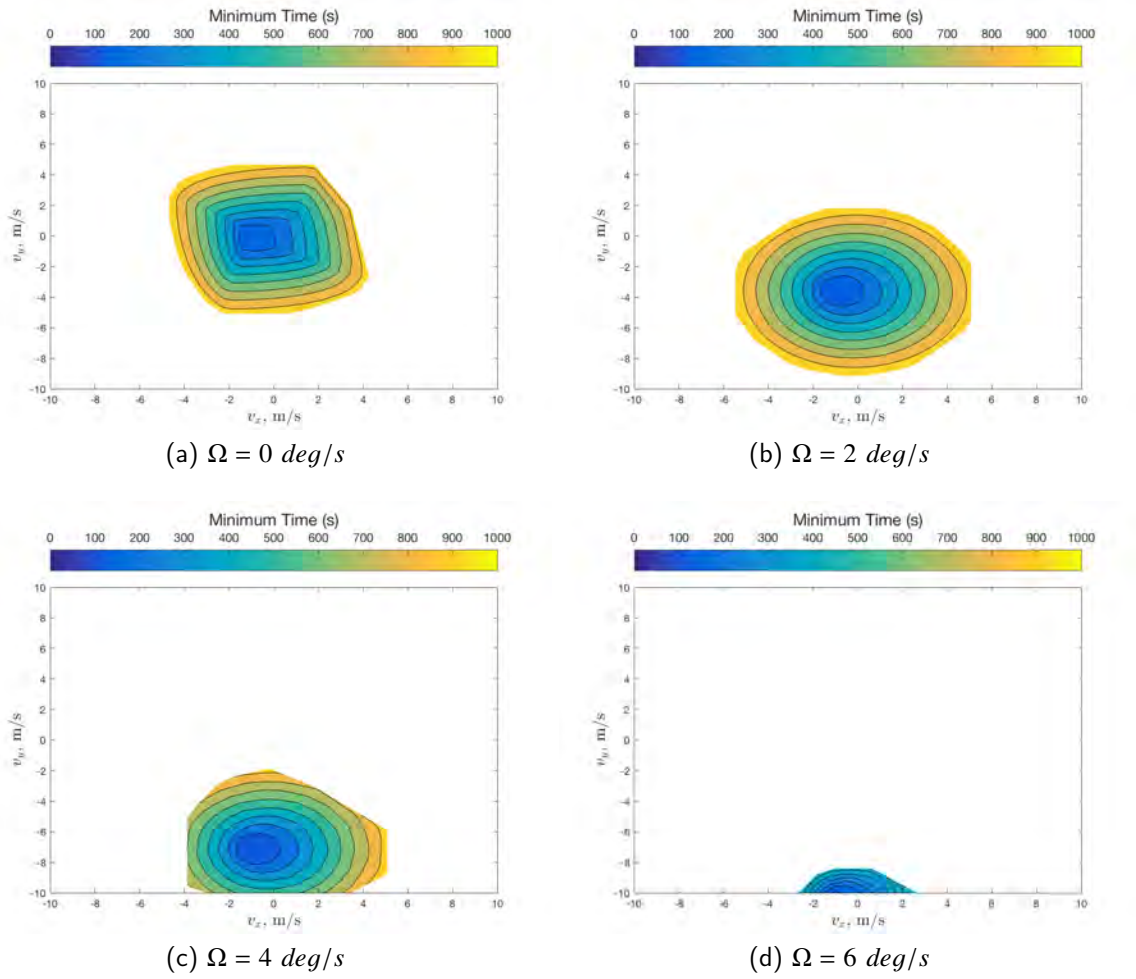

(a) $\Omega = 0\ deg/s$ (b) $\Omega = 2\ deg/s$

(c) $\Omega = 4\ deg/s$ (d) $\Omega = 6\ deg/s$

Figure 4.22. Translational backward T-reachable set slices at initial position on the R-bar axis at different chief rotation rates; color bar indicates minimum time values corresponding to the contours.

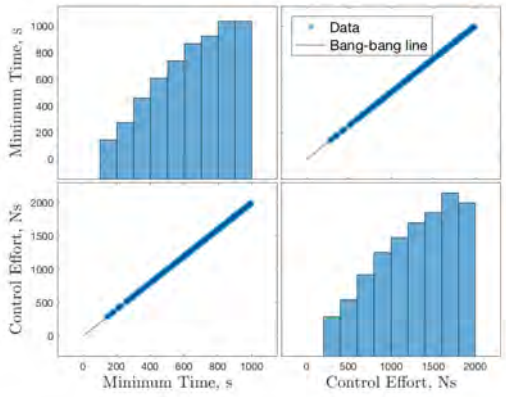

(a) $\Omega = 0\ deg/s$

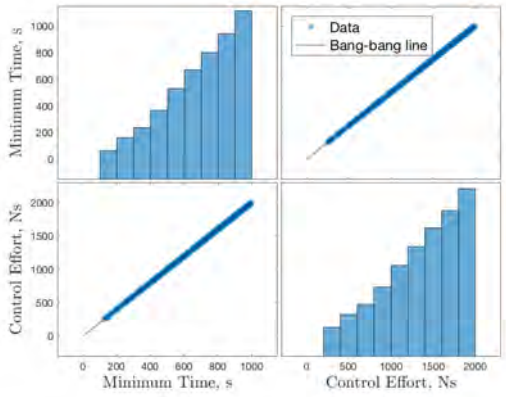

(b) $\Omega = 2\ deg/s$

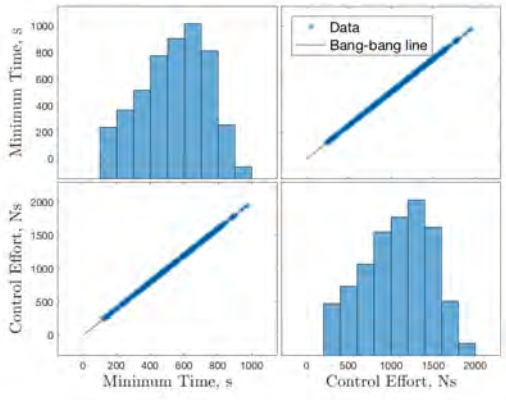

(c) $\Omega = 4\ deg/s$

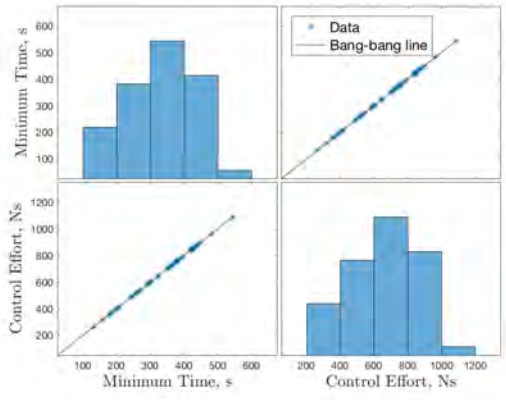

(d) $\Omega = 6\ deg/s$

Figure 4.23. Minimum time and control effort histograms and correlation for velocity (R-bar position) subspace.

The above analysis of the translational subsystem showed some characteristics and limitations of the rendezvous maneuver. The results showed expected behavior of sets growing proportionally with time, since the system is linear. It was evident that many of the test cases were not able to be solved. Many of the cases became infeasible, in the sense that the maneuver was not possible within the allowable 1,000 seconds. Some of the infeasibilities, however, could be due to sensitivity to user-defined parameters within GPOPS-II. Table 4.3 summarizes the percentage of cases that failed during computation of the reachable set slices described above.

Table 4.3. Case failures during translational reachability analysis.

Subspace (Slice)	Chief rotation rate, deg/s	Number of Cases	% failed
Out-of-plane	N/A	1000	6.1
Position; zero velocity	0	2500	0
Position; zero velocity	2	2500	0.68
Position; zero velocity	4	2500	79.2
Position; zero velocity	6	2500	98.48
Position; NMC velocity	0	2500	0
Position; NMC velocity	2	2500	0
Position; NMC velocity	4	2500	0
Position; NMC velocity	6	2500	0
Velocity; R-bar position	0	2500	83.92
Velocity; R-bar position	2	2500	76.88
Velocity; R-bar position	4	2500	86.64
Velocity; R-bar position	6	2500	98.16
Velocity; V-bar position	0	2500	83.8
Velocity; V-bar position	2	2500	76.56
Velocity; V-bar position	4	2500	87.16
Velocity; V-bar position	6	2500	98.36

4.3.3 Analysis of Rotational Backward Reachability

The rotational subsystem is the seven-dimensional system shown in (4.14). The GPOPS-II parameters used for this scenario are shown in Table 4.4. In addition to computing the minimum time to achieve the desired relative state, the control effort required was also computed by

$$ce = \int_0^{t_f} ||u_R||_1 \, dt. \tag{4.25}$$

Table 4.4. GPOPS-II parameters used to solve the MT-OCP for the rotational subsystem.

Parameter	Value
Mesh tolerance	$1e$-6
Max mesh refinements	10
Min collocation points	4
Max collocation points	10
Max NLP iterations	500
Initial Guess	Quaternion feedback control [35]

Analysis of Relative Attitude Subspace

First, the subspace of initial relative attitudes was considered, at specific values of relative angular velocity. Computing and visualizing a reachable set of attitudes is a complicated matter, and there is not much literature on this topic. A four-dimensional subspace of the seven-dimensional state space was created by selecting a random uniform distribution of 1,000 initial unit quaternions, using the procedure outlined in [87], while keeping a constant initial relative angular velocity, $\boldsymbol{\omega} = [0, 0, 0]^T$. The control constraint on this subspace was $-1 \leq (M_x,\ M_y,\ M_z) \leq 1$. The MT-OCP was attempted for each test point with chief rotation rates of $\Omega = 0,\ 2,\ 4,$ and 6 degrees per second (total of 4,000 runs). The MRPs were used as an alternative to quaternions for visualization of the backward reachable sets.

Each of the 1,000 test points has a corresponding $\boldsymbol{\sigma}$ (or $\boldsymbol{\sigma}^S$ depending on the rotation angle) and minimum time solution associated with it, resulting in a three-dimensional volume. As explained in Chapter 3, backward reachable sets of relative attitudes can be visualized by projecting slices of the three-dimensional volume onto spheres of a particular radius. This method provides an intuitive visualization technique.

Figure 4.24 shows the minimum time surfaces projected on a sphere representing $\boldsymbol{\sigma}^T\boldsymbol{\sigma} = 0.5$. The black arrows on the figures represent the principal axis directions (i.e., a rotation about these axes is a rotation about a principal axis). The minimum time surfaces for a slightly larger maneuver are shown in Figure 4.25, projected on a sphere representing $\boldsymbol{\sigma}^T\boldsymbol{\sigma} = 0.7$. Between these two figures, and their respective subfigures, the spheres do

not change very much. The minimum times represented by these spheres are all below 30 seconds, with the exception of some higher valued areas appearing in some spots, as seen for example in Figure 4.25b. The relative attitude dynamics are more complex than the relative translational dynamics, and the corresponding MT-OCP is more difficult to solve. As a result, the GPOPS-II solver is expected to be more sensitive in these cases. The bright spots appearing on these spheres are likely cases that were solved to the desired tolerance, but converged to an invalid solution. There was also a percentage of cases that failed to solve, as reported in Table 4.5.

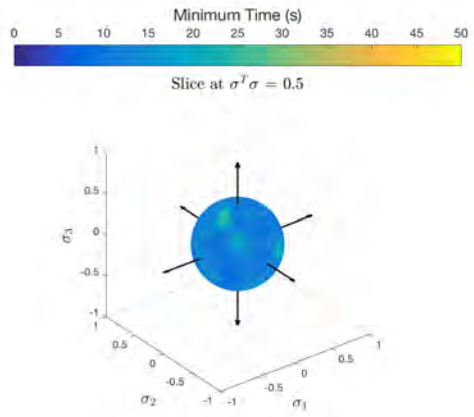

(a) $\Omega = 0\ deg/s$

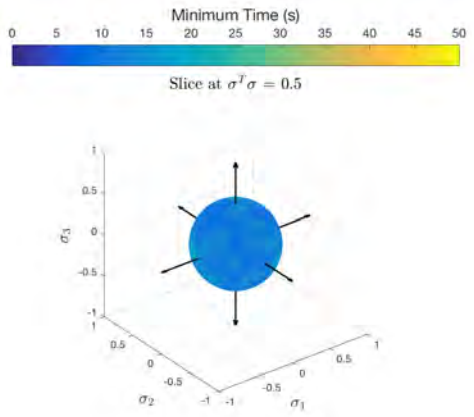

(b) $\Omega = 2\ deg/s$

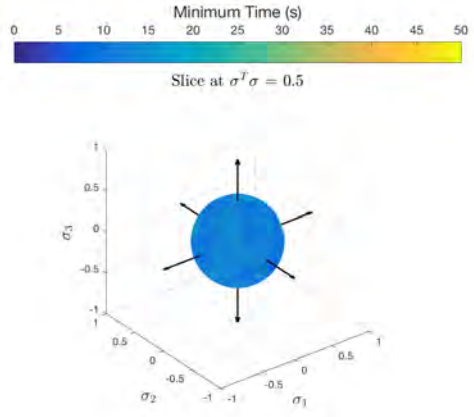

(c) $\Omega = 4\ deg/s$

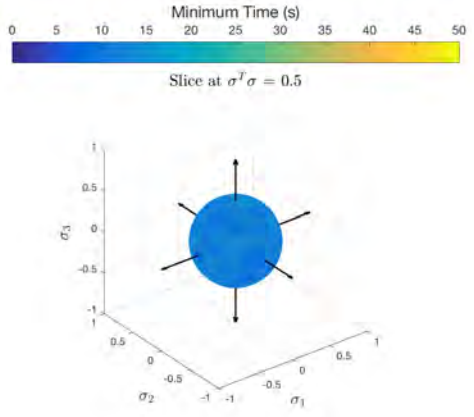

(d) $\Omega = 6\ deg/s$

Figure 4.24. Rotational backward T-reachable set slices at zero initial relative angular velocity for $\boldsymbol{\sigma}^T\boldsymbol{\sigma} = 0.5$ at different chief rotation rates; color bar indicates minimum time values corresponding to the contours.

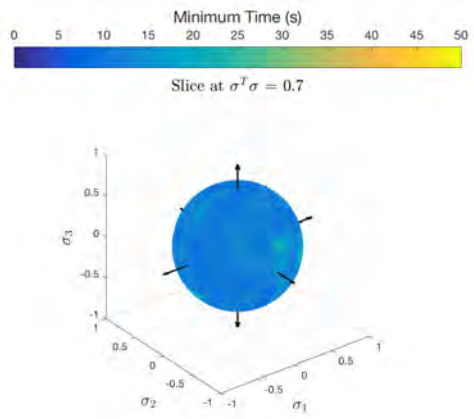

(a) $\Omega = 0\ deg/s$

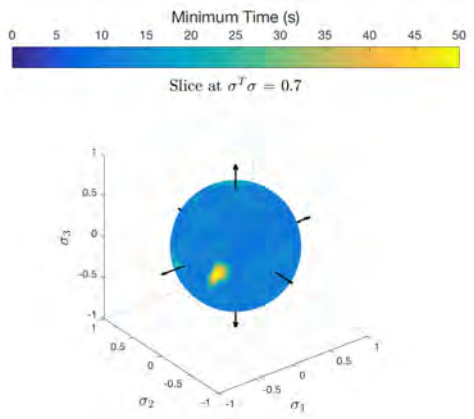

(b) $\Omega = 2\ deg/s$

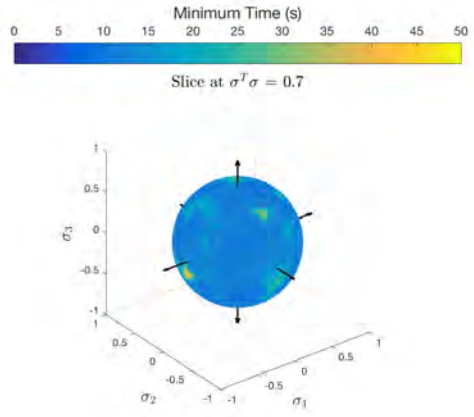

(c) $\Omega = 4\ deg/s$

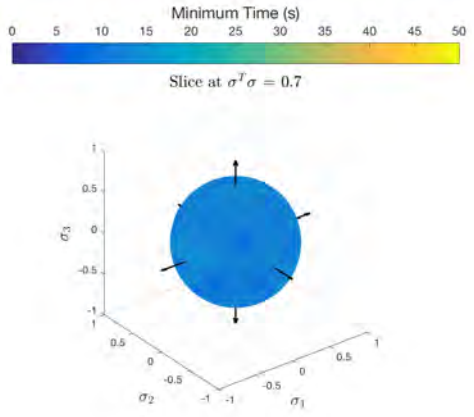

(d) $\Omega = 6\ deg/s$

Figure 4.25. Rotational backward T-reachable set slices at zero initial relative angular velocity for $\boldsymbol{\sigma}^T\boldsymbol{\sigma} = 0.7$ at different chief rotation rates; color bar indicates minimum time values corresponding to the contours.

The invalid solutions become more apparent by looking at the collection of data from these cases. Figure 4.26 shows the correlation between minimum time and control effort for the 1,000 cases, for each scenario. The histograms on the diagonals of each subfigure show the range of minimum times and control effort from the sampled data, while the off-diagonals show the correlation between minimum time and control effort. The majority of the cases have a minimum time around 10 to 15 seconds, but the minimum time distributions in Figure 4.26a - 4.26d have a pretty long right tail, indicating cases with much longer maneuver times. These outliers are clearly visible in the correlation plots. The correlation

trend shows a linear relationship between minimum time and control effort, indicating the expected bang-bang control behavior. The black lines represent the expected relationship, assuming all three control inputs exhibit bang-bang behavior. The outliers are cases that do not exhibit bang-bang behavior, although they were still solved successfully. These cases are not valid minimum time solutions, and are a good example of the solver sensitivities. By glancing at the four subfigures in Figure 4.26, the slopes of the linear trends seem different due to scaling of the axes. However, the slopes are actually the same in all subfigures, indicating that the minimum time maneuver should be bang-bang in all three control components, regardless of the chief's rotation rate.

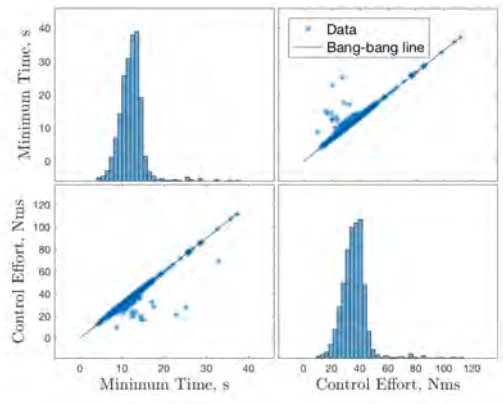

(a) $\Omega = 0\ deg/s$

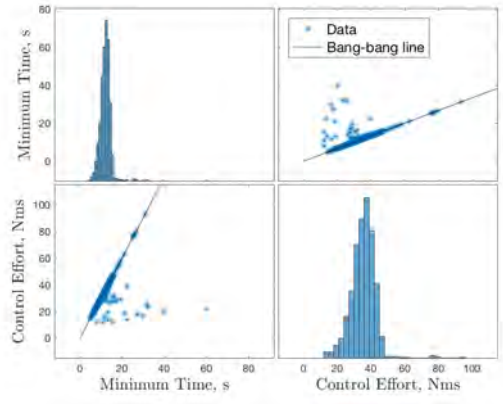

(b) $\Omega = 2\ deg/s$

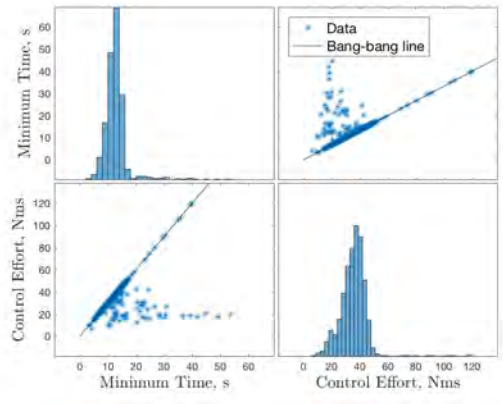

(c) $\Omega = 4\ deg/s$

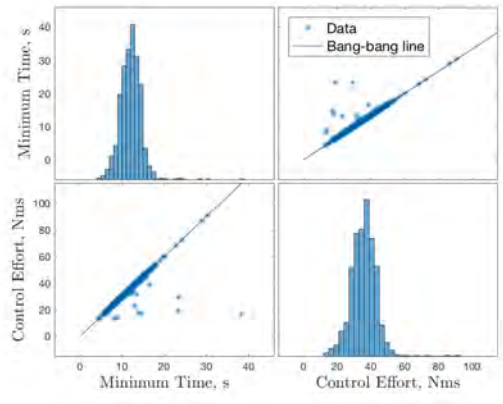

(d) $\Omega = 6\ deg/s$

Figure 4.26. Minimum time and control effort histograms and correlation for attitude (zero angular velocity) subspace.

Two sample cases were selected to show an example of these minimum time maneuvers. The first case was selected from the family of solutions that is within the trend, to show a "correct" bang-bang solution. The second case was chosen from the family of outliers. It is worthy to note that since the set of initial quaternions was randomly generated at the beginning of each simulation, the four scenarios did not run exactly the same initial conditions. Figure 4.27 shows the solutions for the first sample case. It is evident that for all chief rotation rates, the minimum time controls are bang-bang, as expected. Figure 4.28 shows the solutions for the second sample case. The optimal controls in these cases were not bang-bang, and exhibited chattering. This is an indication that these solutions are not valid. This issue could be alleviated by increasing the solver tolerance, number of collocation points, or providing a better initial guess.

Analysis of Angular Velocity Subspace

After investigating reachability from different relative attitudes, the angular velocity subspace was considered with the initial relative attitude of the deputy aligned with the chief. This subspace was defined by 1,000 test points with $-\pi/6\ rad/s \leq (\omega_x,\ \omega_y,\ \omega_z) \leq \pi/6\ rad/s$, at an initial relative quaternion $q = [0,\ 0,\ 0,\ 1]^T$. The control constraint on this subspace was $-1 \leq (M_x,\ M_y,\ M_z) \leq 1$. The MT-OCP was attempted for each test point with chief rotation rates of $\Omega = 0,\ 2,\ 4,$ and 6 degrees per second (total of 4,000 runs). In order to visualize the resulting three-dimensional volume, slice planes were used as projection surfaces. Minimum time contours were projected on these planes to visualize the reachability characteristics in this subspace. Figure 4.29 shows the resulting minimum time contour slices at values of $\omega_x = 0\ rad/s$ and $\omega_z = 0\ rad/s$. Figure 4.30 shows slices at $\omega_x = \pi/12\ rad/s$ and $\omega_z = -\pi/12\ rad/s$. An interesting characteristic that becomes evident in Figure 4.29 - 4.30 is that around the origin, the contours grow proportionally with time. This indicates that the behavior of the attitude dynamics around the origin is similar to that of a linear system. In regions further away from the origin, where a linear approximation would not be accurate, the contours show more complex behavior with multiple peaks. This linear region seems to be approximately contained within $\pm 0.2\ rad/s$.

Figure 4.31 shows the correlation between minimum time and control effort for the 1,000 cases, for each scenario. The histograms on the diagonals of each subfigure show the range of minimum times and control effort from the sampled data, while the off-diagonals

show the correlation between minimum time and control effort. As seen in the attitude subspace analysis, the correlation plots show some outliers that indicate invalid solutions. The percentage of failed cases is reported in Table 4.5.

Table 4.5. Case failures during rotational reachability analysis.

Subspace (Slice)	Chief rotation rate, deg/s	Number of Cases	% failed
Attitude; zero ang. velocity	0	1000	4.9
Attitude; zero ang. velocity	2	1000	7.5
Attitude; zero ang. velocity	4	1000	13
Attitude; zero ang. velocity	6	1000	2.6
Ang. Velocity; aligned attitude	0	1000	11.8
Ang. Velocity; aligned attitude	2	1000	6.8
Ang. Velocity; aligned attitude	4	1000	12.5
Ang. Velocity; aligned attitude	6	1000	16.1

The analysis of the rotational subsystem was limited by the small number of cases and sensitivity to the GPOPS-II solver. Analysis of this complex dynamical system has not been seen in literature before. The method proposed herein for visualization of rotational reachability characteristics provides an intuitive depiction of a complicated concept. Some interesting characteristics became apparent through this analysis; however, it became clear that more data is required to draw better conclusions.

4.4 Summary

This chapter simplified the complex problem of rendezvous with a tumbling chief by assuming that the chief spacecraft is in a circular orbit, and rotating on the orbit plane (about its z body axis) at a constant rate. The complex nonlinear system was decomposed into a translational subsystem and a rotational subsystem, which were studied independently. Applying the simplifying assumptions, the nonlinear translational subsystem was simplified to a LTV system. The rotational subsystem remained in its nonlinear form. The problem was simplified further by considering only planar motion, resulting in a LTI formulation of the planar roto-translational motion. The simplified models enabled backward reachability analysis using polytopic approximation methods, and the minimum time contour method proposed in Chapter 3. An analysis was presented to define the required control input to maintain the desired rendezvous condition. This analysis was applied to the scenario of the

chief in circular orbit, rotating on the orbit plane at a constant rate. An analytical upper bound was discovered in this case, defining the maximum chief rotation rate that can be maintained given the deputy's control constraints.

First, backward reachable sets were computed for the planar docking scenario, using a polytopic approximation method. The results showed that as the chief's rotation rate increases, and control authority decreases, docking becomes more difficult, if not infeasible. It was also shown that, in some cases, a higher rotation rate helps achieve a feasible condition. This work served as a foundation for further reachability analysis, for more complex scenarios.

Second, the 6-DOF rendezvous problem was examined, assuming the chief is in a circular orbit and rotating on its orbit plane at a constant rate. Backward reachable sets were visualized in predefined subspaces, by computing a sampling of minimum time solutions and plotting minimum time contours on the subspace of interest (as described in Chapter 3). Results presented the minimum time contour plots for both translational and rotational states, and a variety of cases, representing initial conditions from which the specified maneuver is feasible given control and time constraints. The translational subsystem results were fairly intuitive to visualize and showed expected behaviors. The rotational subsystem was more complex given the nonlinearity of the dynamics and dimensionality of the state space. Although the MRP visualization technique led to more intuitive visualization, more test points are necessary to gain further insight. Finally, analyzing the reachability characteristics on the angular velocity subspace provided valuable insight on the linear region of the state space, where a linear approximation may be appropriate.

The research contributions offered in this chapter are shown in Table 4.6.

Table 4.6. Research contributions in Chapter 4.

Contribution	**Objective**
Derivation of simplified models suitable for reachability analysis	1, 2
Analytical upper bound on chief rotation rate for maintaining rendezvous	1, 2
Reachability analysis of planar docking maneuver in close proximity	2
Reachability analysis of rendezvous with circular chief rotating on orbit plane	2

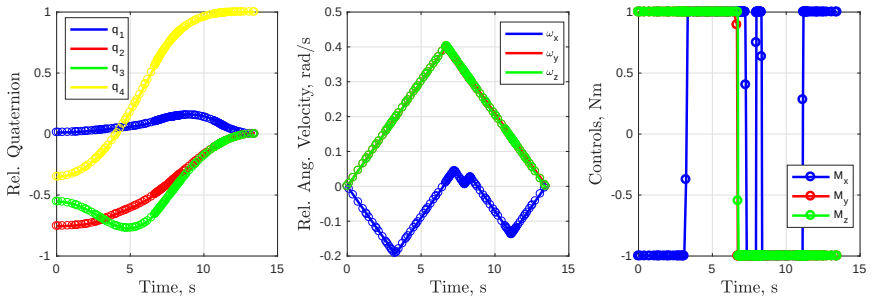

(a) $\Omega = 0\ deg/s$

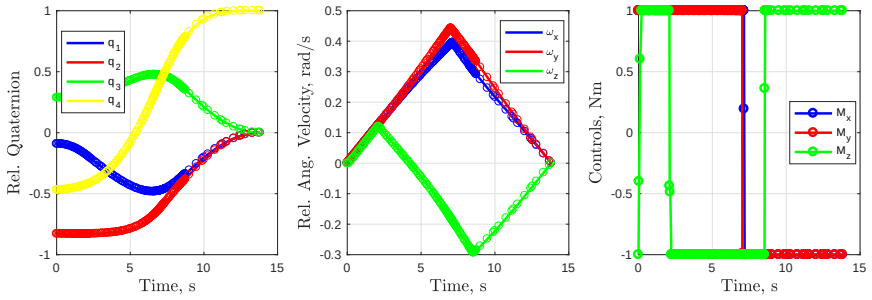

(b) $\Omega = 2\ deg/s$

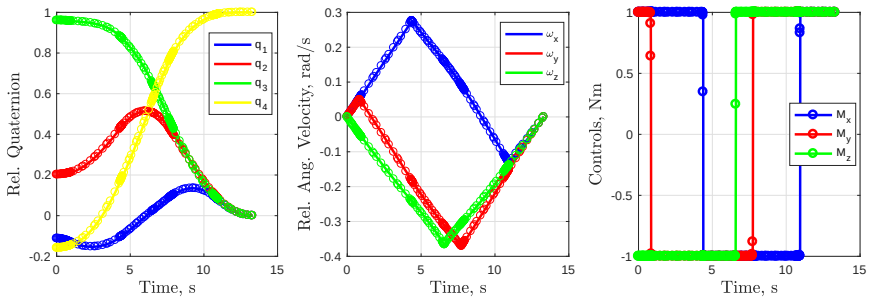

(c) $\Omega = 4\ deg/s$

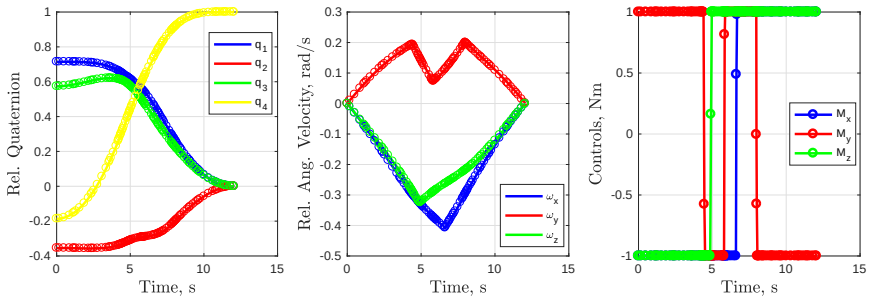

(d) $\Omega = 6\ deg/s$

Figure 4.27. Sample case #1 from attitude (zero angular velocity) subspace.

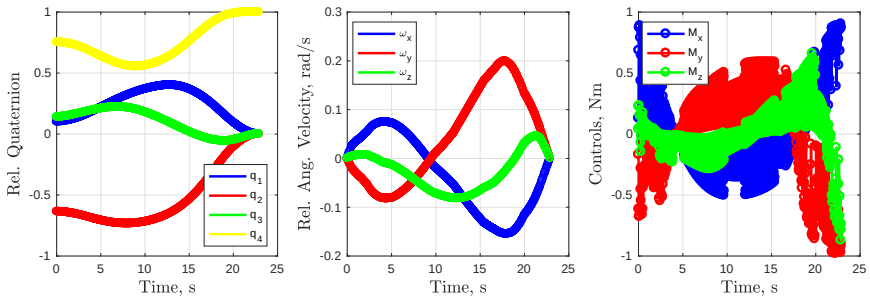

(a) $\Omega = 0\ deg/s$

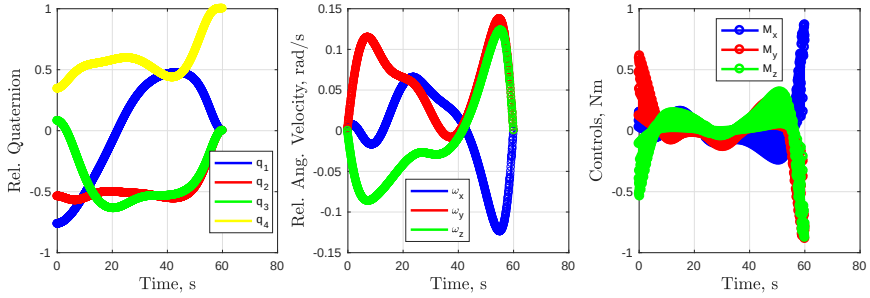

(b) $\Omega = 2\ deg/s$

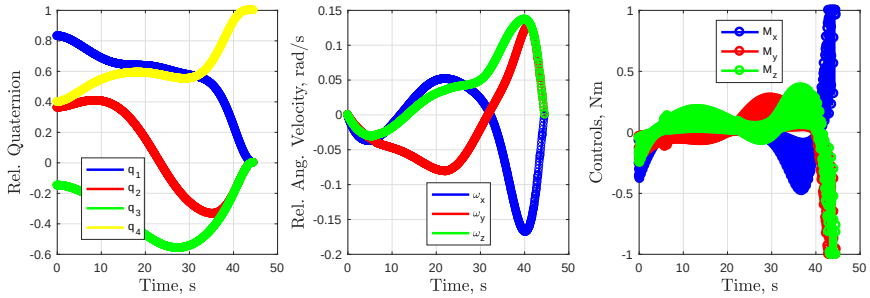

(c) $\Omega = 4\ deg/s$

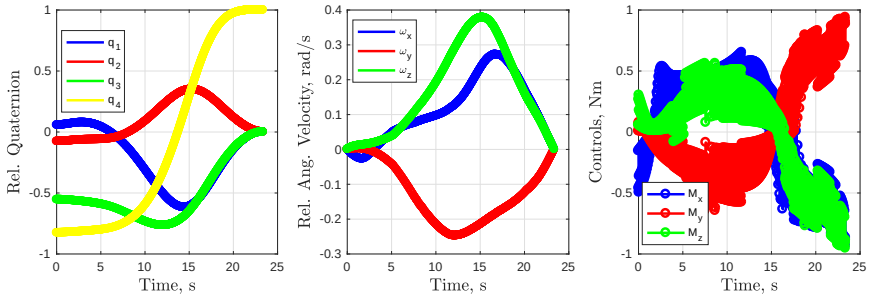

(d) $\Omega = 6\ deg/s$

Figure 4.28. Sample case #2 from attitude (zero angular velocity) subspace.

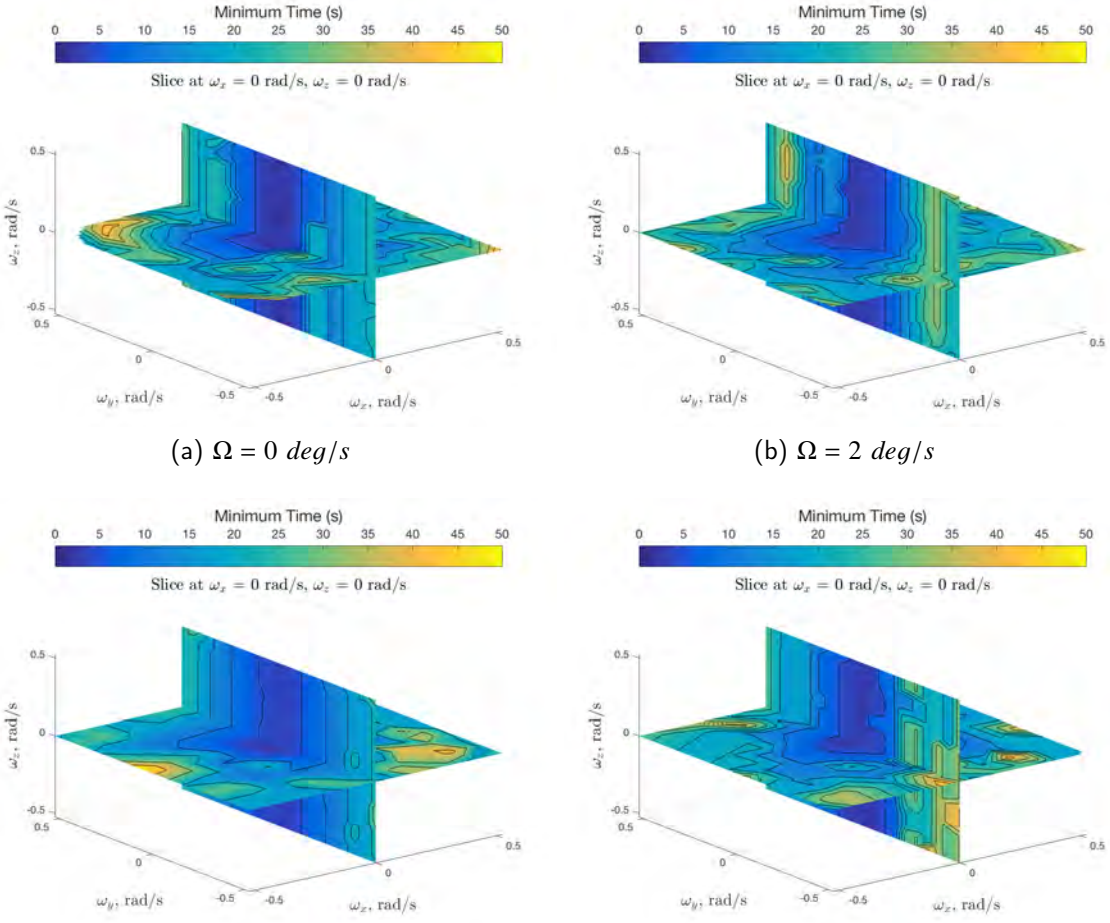

(a) $\Omega = 0\ deg/s$ (b) $\Omega = 2\ deg/s$

(c) $\Omega = 4\ deg/s$ (d) $\Omega = 6\ deg/s$

Figure 4.29. Rotational backward T-reachable set slices at aligned relative attitude for $\omega_x = 0\ rad/s$ and $\omega_z = 0\ rad/s$ at different chief rotation rates; color bar indicates minimum time values corresponding to the contours.

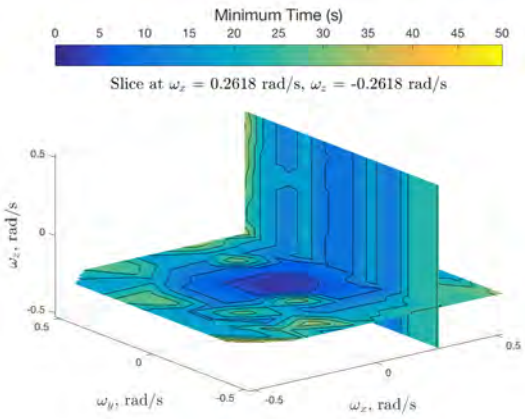

(a) $\Omega = 0\ deg/s$

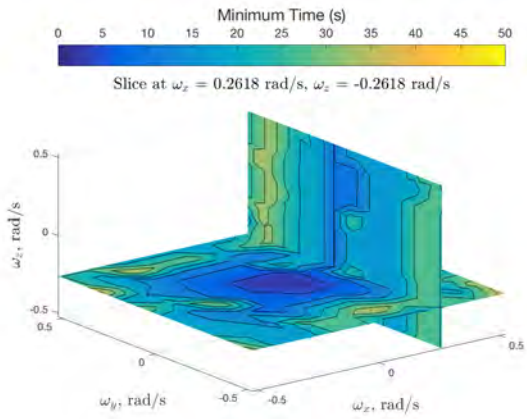

(b) $\Omega = 2\ deg/s$

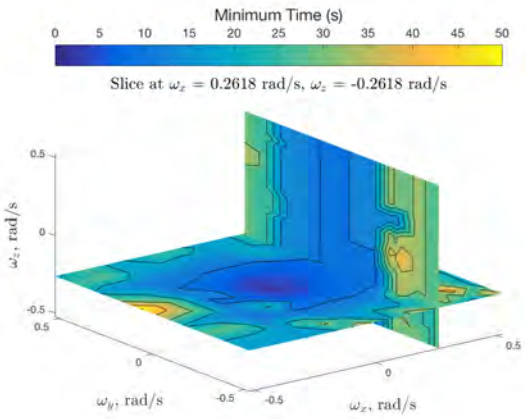

(c) $\Omega = 4\ deg/s$

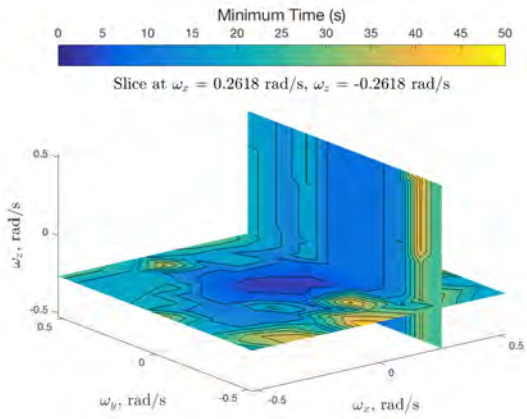

(d) $\Omega = 6\ deg/s$

Figure 4.30. Rotational backward T-reachable set slices at aligned relative attitude for $\omega_x = \pi/12\ rad/s$ and $\omega_z = -\pi/12\ rad/s$ at different chief rotation rates; color bar indicates minimum time values corresponding to the contours.

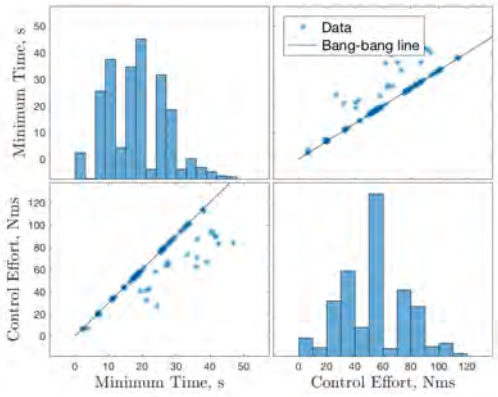

(a) $\Omega = 0\ deg/s$

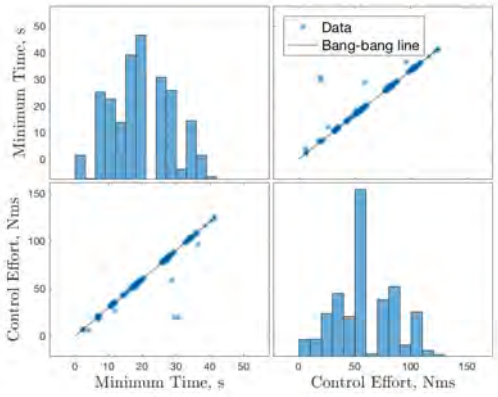

(b) $\Omega = 2\ deg/s$

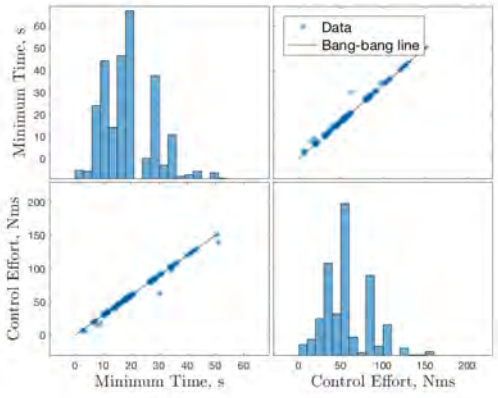

(c) $\Omega = 4\ deg/s$

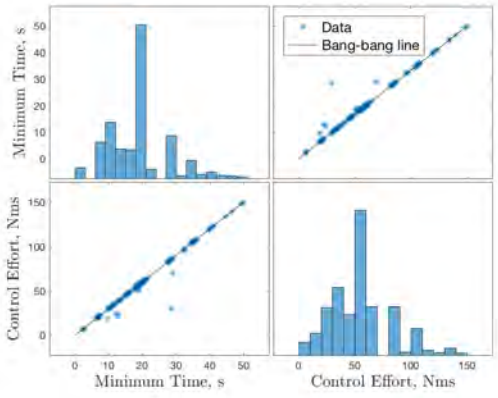

(d) $\Omega = 6\ deg/s$

Figure 4.31. Minimum time and control effort histograms and correlation for angular velocity (aligned attitude) subspace.

THIS PAGE INTENTIONALLY LEFT BLANK

CHAPTER 5:
Applied Reachability Analysis of Spacecraft Rendezvous with Tumbling Chief

In this chapter, the problem of RPO around a tumbling chief spacecraft is considered for the case where the chief is in a complex tumble. Applied reachability analysis is conducted for the full 6-DOF relative dynamics. The MRPs are used in this chapter to describe the relative attitude since the reachability analysis is conducted in the MRP subspace. As stated in Chapter 2, the 6-DOF relative dynamics utilized are shown in (5.1).

$$\dot{\boldsymbol{\rho}} = \mathbf{v} \tag{5.1a}$$

$$\begin{aligned}\dot{\mathbf{v}} = &-\frac{\mu}{R_d^3}\boldsymbol{\rho} + \frac{\mu\left(R_d^3 - R_c^3\right)}{R_c^3 R_d^3}\mathbf{r}_c^{\mathsf{C}} + \frac{1}{m_d}\mathbf{F}_d - \left[J_c^{-1}\left(-[\boldsymbol{\omega}_c]^{\times} J_c \boldsymbol{\omega}_c\right)\right]^{\times}\boldsymbol{\rho} \\ &-2[\boldsymbol{\omega}_c]^{\times}\mathbf{v} - [\boldsymbol{\omega}_c]^{\times}\left([\boldsymbol{\omega}_c]^{\times}\boldsymbol{\rho}\right)\end{aligned} \tag{5.1b}$$

$$\dot{\boldsymbol{\sigma}} = \frac{1}{4}\tilde{B}\boldsymbol{\omega}^{\mathsf{D}} \tag{5.1c}$$

$$\begin{aligned}\dot{\boldsymbol{\omega}}^{\mathsf{D}} = &J_d^{-1}\left[\mathbf{M}_d^{\mathsf{D}} - [\boldsymbol{\omega}^{\mathsf{D}} + C_{\mathsf{D/C}}\boldsymbol{\omega}_c]^{\times} J_d(\boldsymbol{\omega}^{\mathsf{D}} + C_{\mathsf{D/C}}\boldsymbol{\omega}_c)\right] \\ &-C_{\mathsf{D/C}}\left[J_c^{-1}\left(-[\boldsymbol{\omega}_c]^{\times} J_c \boldsymbol{\omega}_c\right)\right] - [C_{\mathsf{D/C}}\boldsymbol{\omega}_c]^{\times}\boldsymbol{\omega}^{\mathsf{D}}\end{aligned} \tag{5.1d}$$

From the simplifying assumptions made in Chapter 4, the following are kept for this research phase:

1. Chief and deputy body CCSs are aligned with their respective principal axes. This implies that J_c and J_d are diagonal matrices with principal moments of inertia ($J_{c_{x,y,z}}$ and $J_{d_{x,y,z}}$).
2. The chief body CCS is initially aligned with the LVLH CCS.

Using insight gained from the results in Chapter 4, the reachability analysis in this chapter is focused on two subspaces:

1. Relative position subspace; initial relative velocity set to corresponding NMC veloc-

ity, relative attitude initially aligned, and zero relative angular velocity.

2. Relative attitude subspace; initial relative position and velocity set to rendezvous condition, and zero relative angular velocity.

The state values used to define these subspaces are shown in Table 5.1.

Table 5.1. Definition of initial conditions for reachability analysis on relative position and relative attitude subspaces.

Relative Position Subspace:	
Relative position (m)	$-100 \leq (\rho_x,\ \rho_y,\ \rho_z) \leq 100$
Relative velocity (m/s)	corresponding NMC velocity
Relative attitude	$\boldsymbol{\sigma} = [0, 0, 0]^T$
Relative angular velocity (rad/s)	$\boldsymbol{\omega} = [0, 0, 0]^T$
Relative Attitude Subspace:	
Relative position (m)	$\boldsymbol{\rho} = [1, 0, 0]^T$
Relative velocity (m/s)	$\mathbf{v} = [0, 0, 0]^T$
Relative attitude	$-1 \leq (\sigma_1,\ \sigma_2,\ \sigma_3) \leq 1$
Relative angular velocity (rad/s)	$\boldsymbol{\omega} = [0, 0, 0]^T$

As in Chapter 4, the MT-OCP is solved for a family of test points on these subspaces and the reachable set boundaries are visualized as minimum time contours. The GPOPS-II parameters used for this analysis are shown in Table 5.2. For the purpose of this analysis, a failure is defined as a simulation in which the GPOPS-II solver did not converge to a solution within the desired tolerance. Since the translational and rotational components of the problem are treated simultaneously, the roto-translational control effort was computed by

$$ce = \int_0^{t_f} \left(||u_T||_1 + \frac{1}{b}||u_R||_1 \right) dt, \tag{5.2}$$

where b is a notional moment arm length used to translate a torque into an equivalent force [88]. In this work, $b = 1\ m$ was used as a benchmark, but this value is dependent on the actual spacecraft geometry.

Table 5.2. GPOPS-II parameters used to solve the MT-OCP for the full 6-DOF system.

Parameter	Value
Mesh tolerance	$1e$-6
Max mesh refinements	20
Min collocation points	25
Max collocation points	50
Max NLP iterations	1000
Initial Guess	Endpoints (zero control)

5.1 Reachability Analysis: 6-DOF Rendezvous with Rotating Chief

A scenario similar to what was studied in Chapter 4 was studied first. In this scenario, the chief is in a circular orbit, and rotating on the orbit plane about its z body axis. The chief and deputy are defined as one meter homogeneous cubes (i.e., dimensions of $1 \times 1 \times 1$ m), resulting in spherically symmetric inertia properties. The relative dynamics, however, was not simplified and the MT-OCP was solved for the full 6-DOF problem instead of considering the translational and rotational subsystems independently. These results enable reachability analysis of more complex scenarios. The parameters of the scenario studied during this phase of research are shown in Table 5.3.

Table 5.3. Scenario Parameters for 6-DOF rendezvous with chief in circular orbit, rotating on the orbit plane at a constant rate.

Chief Orbital Elements	a = 6878.137 km, $e = 0$, $i = 50$ deg, $\omega_{ra} = 0$ deg, $\omega_p = 0$ deg, $f_0 = 0$ deg
Chief Mass (kg)	100
Deputy Mass (kg)	100
Chief Inertia (kg-m^2)	$diag(16.67,\ 16.67,\ 16.67)$
Deputy Inertia (kg-m^2)	$diag(16.67,\ 16.67,\ 16.67)$
F_{max} (N)	1
M_{max} (N-m)	1
T_{max} (s)	1000
Desired final condition	$\boldsymbol{\rho}_f = [1, 0, 0]^T\ m$
	$\mathbf{v}_f = [0, 0, 0]^T\ m/s$
	$\boldsymbol{\sigma}_f = [0, 0, 0]^T$
	$\boldsymbol{\omega}_f = [0, 0, 0]^T\ rad/s$

5.1.1 Analysis of Relative Position Backward Reachability

The translational reachability was investigated by generating a subspace of relative positions at fixed values of initial relative velocity, initial relative attitude, and initial relative angular velocity, as shown in Table 5.1. The subspace was defined by 27,000 test points, with control constraints $-1 \leq (F_x,\ F_y,\ F_z) \leq 1$ and $-1 \leq (M_x,\ M_y,\ M_z) \leq 1$. The MT-OCP was attempted for each test point with chief rotation rates of $\Omega = 0,\ 2,$ and 4, degrees per second (total of 81,000 runs). Slice planes were used as projection surfaces in order to visualize the three-dimensional volume. Minimum time contours were projected on these surfaces to visualize the backward reachability characteristics in relative position. Figure 5.1 shows the resulting minimum time contours, at values of $\rho_x = 0\,m$ and $\rho_z = 0\,m$. Figure 5.2 shows the contours at $\rho_x = 40\,m$ and $\rho_z = -40\,m$. The contours grow proportionally with time. As the results in Chapter 4 showed, the contours on the x-y plane take an oval shape as the chief's rotation rate is increased. However, the contours on the y-z plane are not affected by the chief's rotation rate, as can be seen in Figures 5.1a - 5.1c. This result was explicitly shown in Chapter 4, where the simplified dynamics model showed that for the planar rotating chief scenario the out-of-plane motion is decoupled from the in-plane motion.

Figure 5.3 shows the correlation between minimum time and control effort for the 27,000 cases, for each scenario. The histograms on the diagonals of each subfigure show the range of minimum times and control effort from the sampled data, while the off-diagonals show the correlation between minimum time and control effort. As reported in Table 5.4, a small percentage of cases failed to converge. The correlation plots in Figure 5.3a - Figure 5.3c show a spread of results, instead of the linear trend shown in Chapter 4. This result is due to the fact that not all controls exhibit bang-bang behavior in these solutions. Since the MT-OCP was solved for the full 6-DOF dynamics, it was known, a priori, that at least one of the six control inputs would be bang-bang (see Chapter 3, Remark 3.3). Therefore, the spread of this data can be bounded, as shown in Figure 5.3a - Figure 5.3c. The correlation plots show two bang-bang lines: one assuming only one of the control variables is bang-bang, and another assuming all six control variables are bang-bang. It can be clearly seen in Figure 5.3a - Figure 5.3c that all data falls within these bounds, and there are no outliers.

Two sample test cases were selected to show an example of these minimum time trajectories.

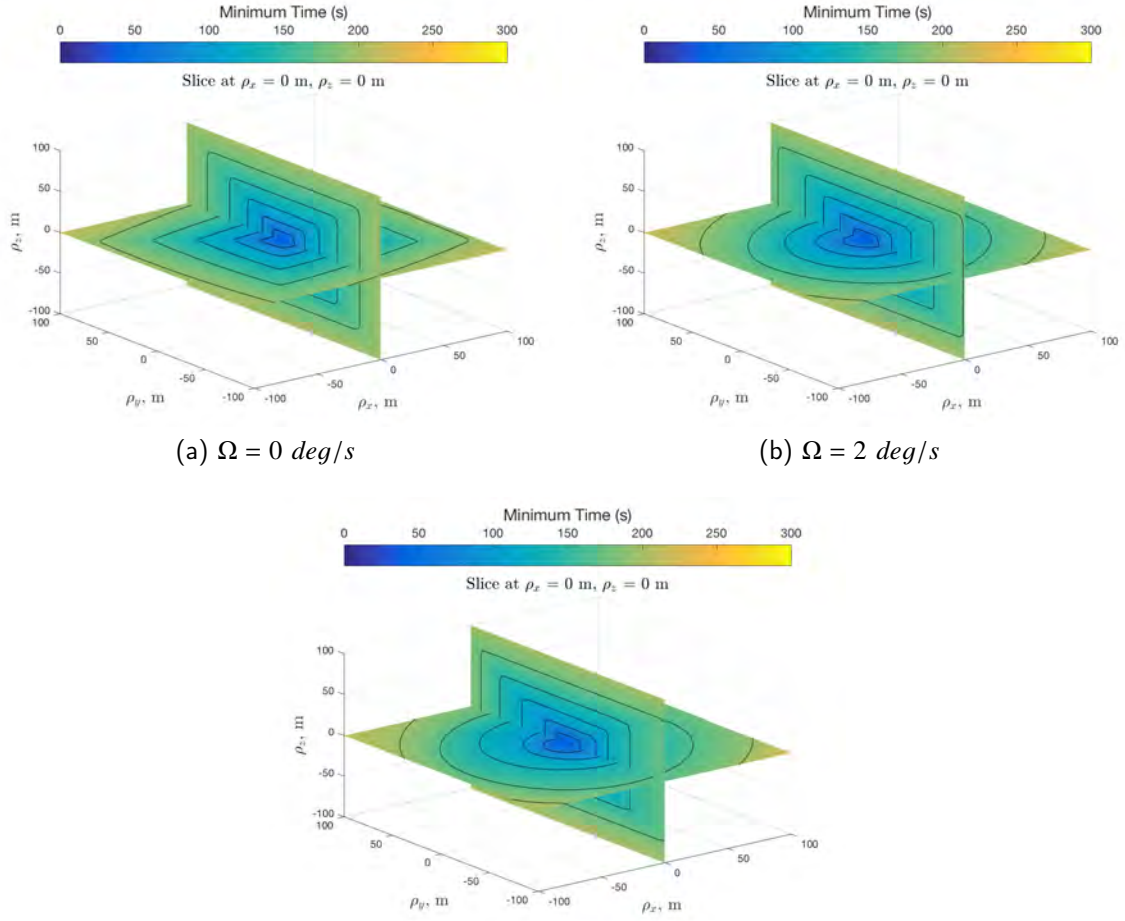

(a) $\Omega = 0\ deg/s$

(b) $\Omega = 2\ deg/s$

(c) $\Omega = 4\ deg/s$

Figure 5.1. Relative position backward T-reachable sets at NMC velocity, aligned attitude, and zero angular velocity at different chief rotation rates, sliced at $\rho_x = 0\ m$ and $\rho_z = 0\ m$; color bar indicates minimum time values corresponding to the contours.

The samples were selected to show two trajectories of very similar minimum time, but different control efforts. Figure 5.4 shows the state and control trajectories for the two samples when the chief rotation rate is $\Omega = 0\ deg/s$. In Figure 5.4a, it can be seen that for the first sample case, the three translational control inputs (forces) are bang-bang, and the rotational controls are not used since the relative attitude and angular velocity are aligned. The second sample case, which is essentially only a maneuver in the z direction, shows only one translational control input as bang-bang, as seen in Figure 5.4b. Figures 5.5 and

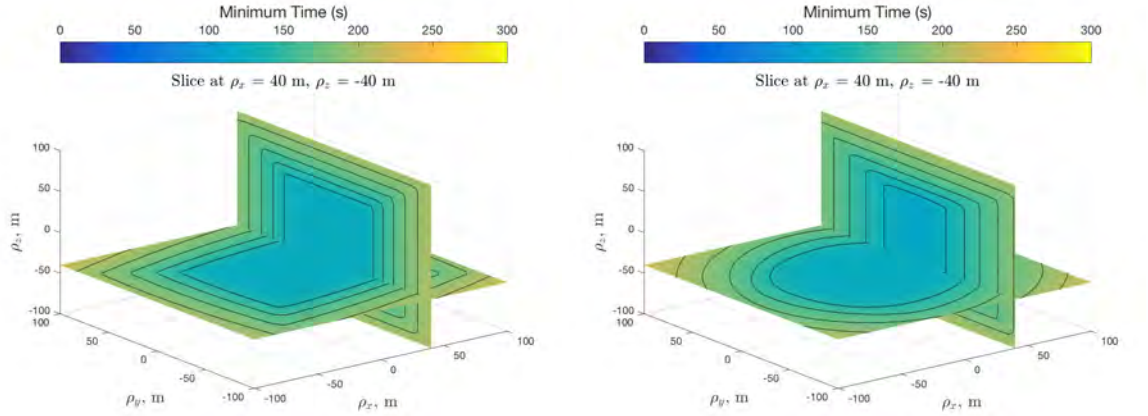

(a) $\Omega = 0\ deg/s$

(b) $\Omega = 2\ deg/s$

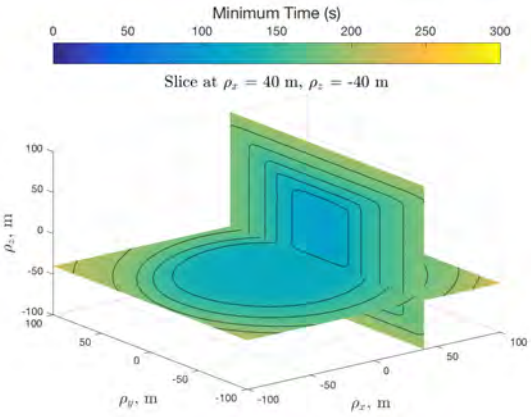

(c) $\Omega = 4\ deg/s$

Figure 5.2. Relative position backward T-reachable sets at NMC velocity, aligned attitude, and zero angular velocity at different chief rotation rates, sliced at $\rho_x = 40\ m$ and $\rho_z = -40\ m$; color bar indicates minimum time values corresponding to the contours.

5.6 show the same sample trajectories for the cases with chief rotation rate $\Omega = 2\ deg/s$ and $\Omega = 4\ deg/s$, respectively. In these figures, the forces in the x and y directions are not bang-bang, but exhibit some oscillatory behavior. Since they are not required to be bang-bang, the solver has no information on how to select these controls, other than they must meet the necessary conditions for optimality (see Chapter 3). Although these solutions are mathematically valid, they may not be practical due to the oscillations in the control inputs. The torques, for example, in Figures 5.4 - 5.6 do not exhibit such behavior because

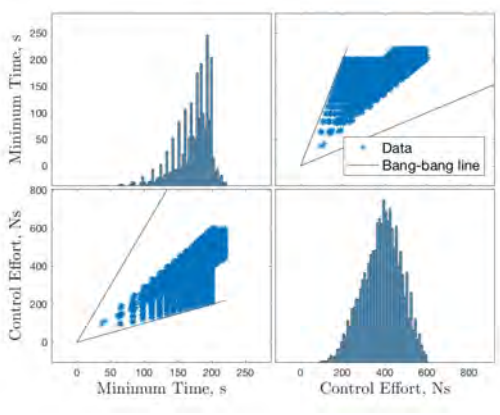

(a) $\Omega = 0\ deg/s$

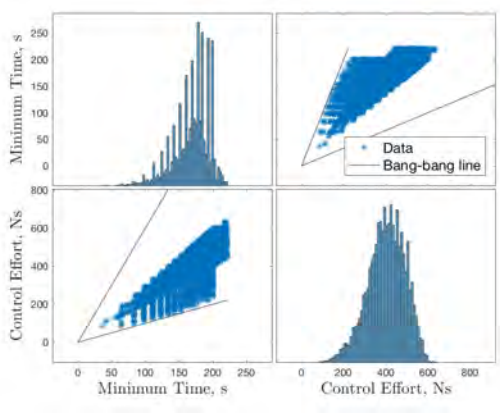

(b) $\Omega = 2\ deg/s$

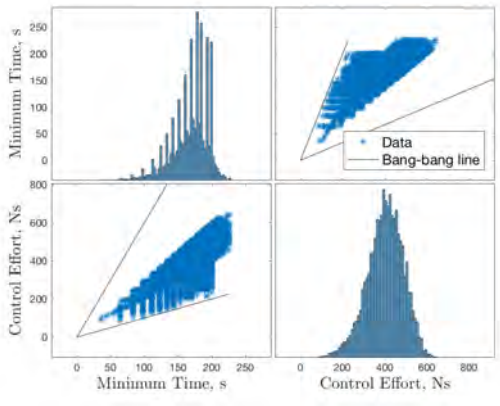

(c) $\Omega = 4\ deg/s$

Figure 5.3. Minimum time and control effort histograms and correlation for position (NMC velocity, aligned attitude) subspace.

the zero control initial guess, in this case, is a valid solution.

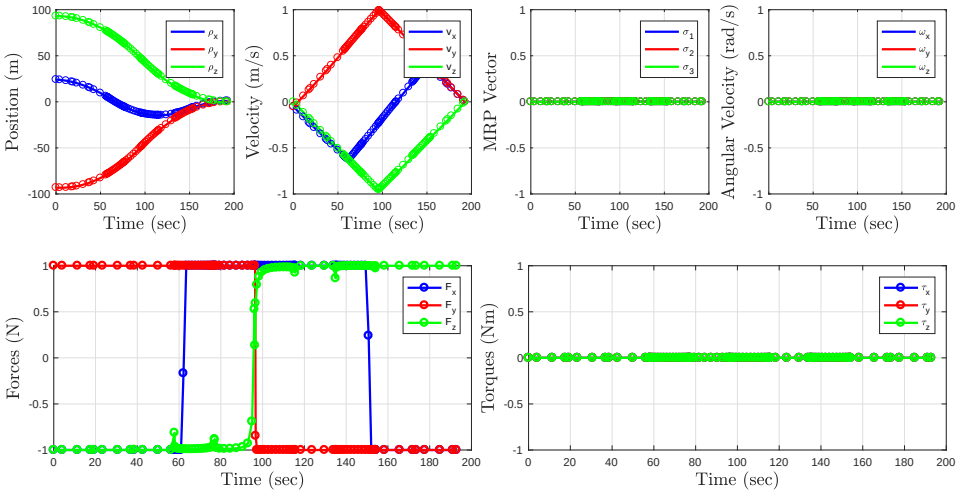

(a) Sample Case #1, $\Omega = 0\ deg/s$

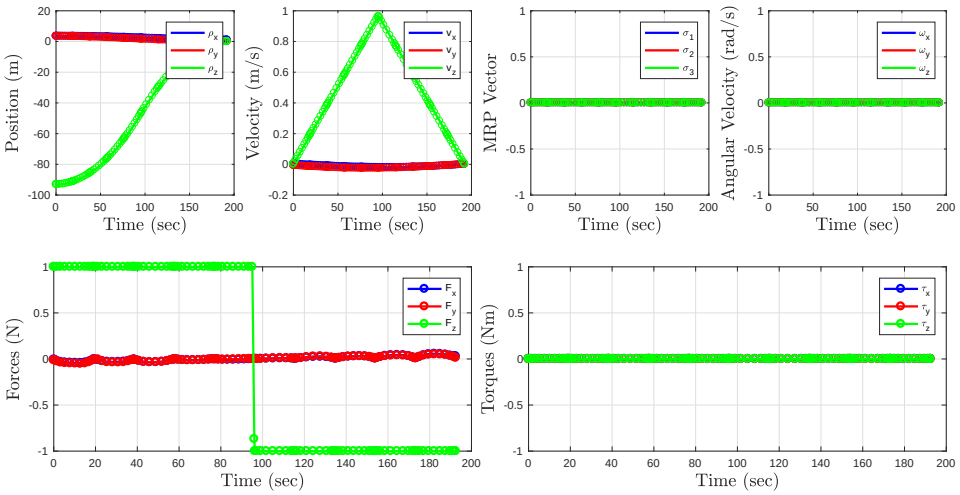

(b) Sample Case #2, $\Omega = 0\ deg/s$

Figure 5.4. Sample cases from position (NMC velocity, aligned attitude) for $\Omega = 0\ deg/s$.

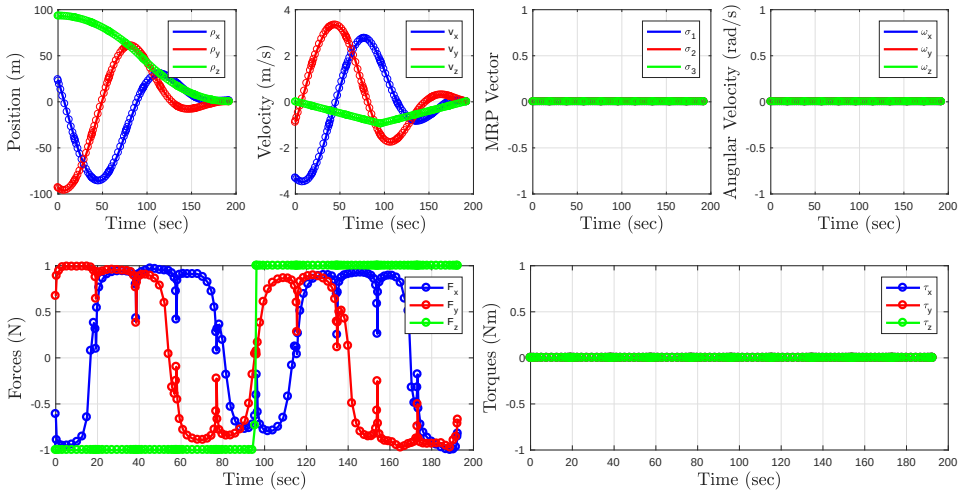

(a) Sample Case #1, $\Omega = 2\ deg/s$

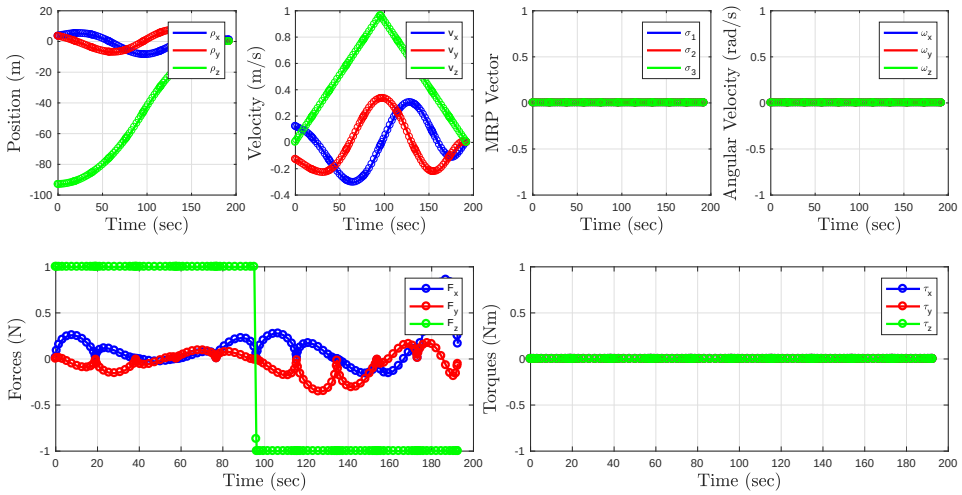

(b) Sample Case #2, $\Omega = 2\ deg/s$

Figure 5.5. Sample cases from position (NMC velocity, aligned attitude) subspace for $\Omega = 0\ deg/s$.

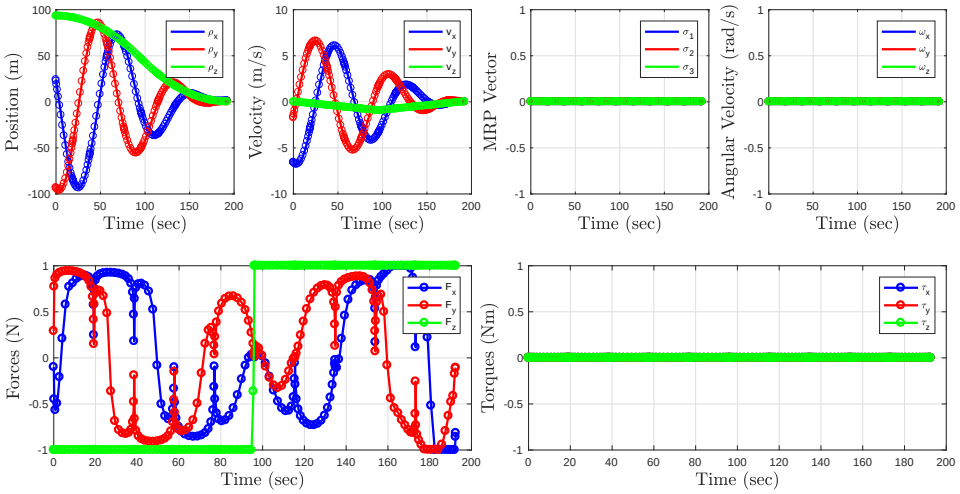

(a) Sample Case #1, $\Omega = 4\ deg/s$

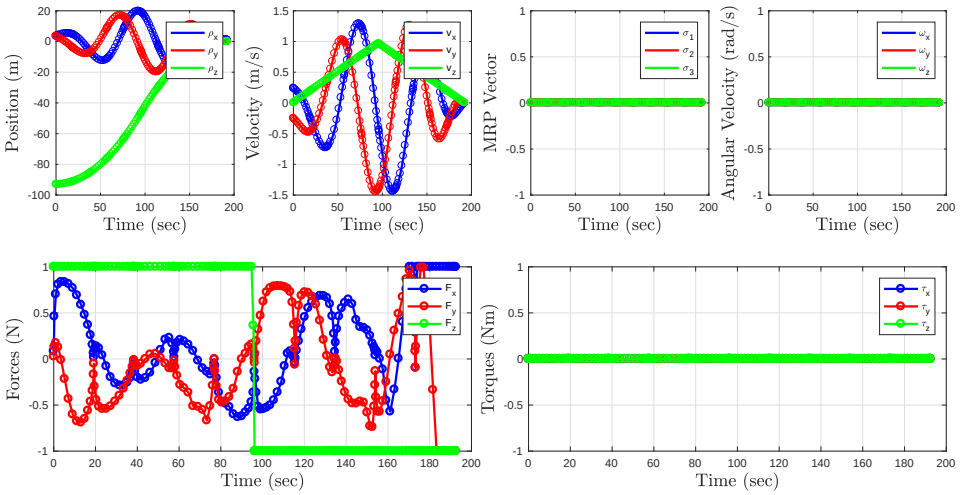

(b) Sample Case #2, $\Omega = 4\ deg/s$

Figure 5.6. Sample cases from position (NMC velocity, aligned attitude) subspace for $\Omega = 0\ deg/s$.

5.1.2 Analysis of Relative Attitude Backward Reachability

The rotational reachability was investigated by generating a subspace of relative attitudes at fixed values of initial relative angular velocity, initial relative position, and initial relative velocity, as shown in Table 5.1. The subspace was defined by 8,000 test points, with control constraints $-1 \leq (F_x,\ F_y,\ F_z) \leq 1$ and $-1 \leq (M_x,\ M_y,\ M_z) \leq 1$. The MT-OCP was attempted for each test point with chief rotation rates of $\Omega = 0,\ 2,$ and 4, degrees per second (total of 24,000 runs). As in Chapter 4, spheres of a particular radius, representing a particular value of the MRP norm, were used as projection surfaces in order to visualize this set of relative attitudes. Figure 5.7 shows the minimum time surfaces, projected on a sphere representing $\boldsymbol{\sigma}^T\boldsymbol{\sigma} = 0.4$. Figure 5.8 shows the resulting surfaces projected on a sphere representing $\boldsymbol{\sigma}^T\boldsymbol{\sigma} = 0.7$. These figures offer some intuitive results. Firstly, it is evident that the surfaces in Figure 5.8 are a lighter shade than the surfaces in Figure 5.7. This means that the set of relative attitudes with larger angular displacements (i.e., represented by larger spheres) will exhibit larger maneuver times. Secondly, a noticeable color difference is apparent on the spherical surfaces surrounding the black arrows representing the principal axes. Specifically, it can be concluded that an initial relative attitude represented by a rotation about one of the principal axes will have a slightly larger minimum time than an initial relative attitude represented by a rotation about an off-principal axis. This result is directly tied to the torque constraint. The maximum torque available in the direction of a principal axis is exactly 1 Nm. However, along the diagonal direction (i.e., $\hat{e} = [1/\sqrt{3},\ 1/\sqrt{3},\ 1/\sqrt{3}]^T$) the maximum torque available is larger at $\sqrt{3}\ Nm$, since the constraint is cubic. Since more torque is available in this direction, it makes sense that the minimum maneuver time is smaller. Lastly, it is evident that the chief's rotation rate does not have a visible effect on these surfaces with the exception of the yellow area seen on Figure 5.8c, which is due to sensitivities of the GPOPS-II solver. As reported in Table 5.4, the solver encountered a larger number of failures at increased chief rotation rates.

Figure 5.9 shows the correlation between minimum time and control effort for the 8,000 cases, for each scenario. The histograms on the diagonals of each subfigure show the range of minimum times and control effort from the sampled data, while the off-diagonals show the correlation between minimum time and control effort. The histograms show a tight grouping of minimum times; a large number of cases had minimum time values between 10 and 15 seconds. Some cases show larger minimum time values, as seen in the correlation

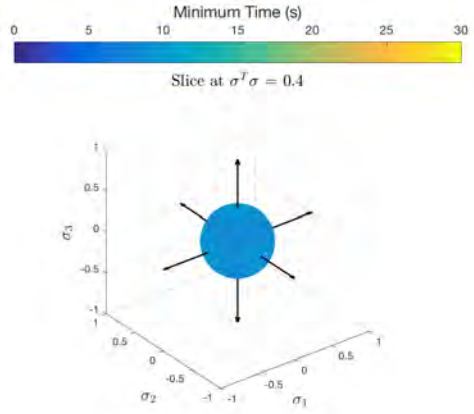

(a) $\Omega = 0\ deg/s$

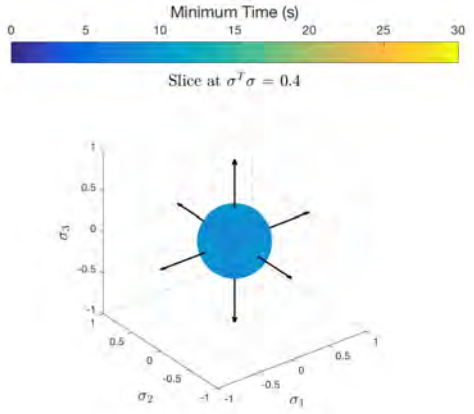

(b) $\Omega = 2\ deg/s$

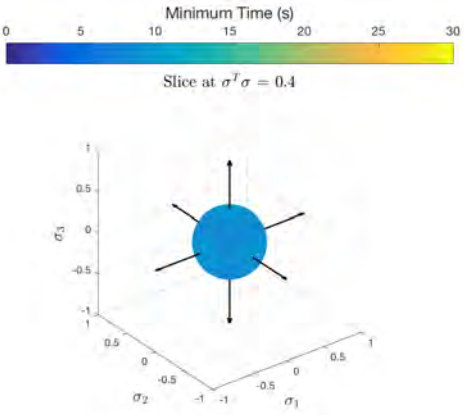

(c) $\Omega = 4\ deg/s$

Figure 5.7. Relative attitude backward T-reachable sets at zero angular velocity and rendezvous relative position and velocity at different chief rotation rates, sliced at $\boldsymbol{\sigma}^T\boldsymbol{\sigma} = 0.4$; color bar indicates minimum time values corresponding to the contours.

plots. The data on these plots, however, falls within the expected bang-bang control bounds.

Two sample cases were selected from this family of results to show an example of these minimum time trajectories. The first sample case was chosen to be within the majority of minimum time groupings, while the second sample shows the solution that exhibited the largest minimum time for each scenario. Figure 5.10 shows the two sample trajectories for $\Omega = 0\ deg/s$. In Figure 5.10a, Figure 5.11a, and Figure 5.12a, the torques show

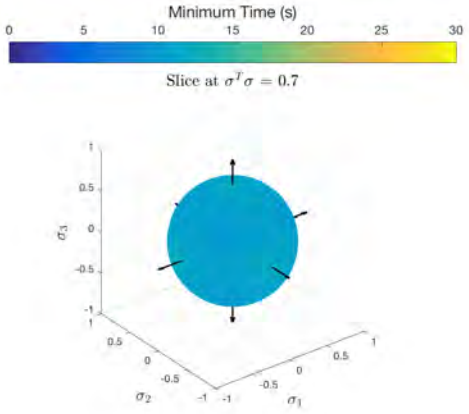

(a) $\Omega = 0\ deg/s$

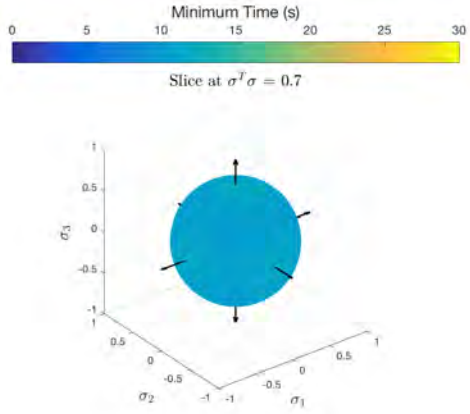

(b) $\Omega = 2\ deg/s$

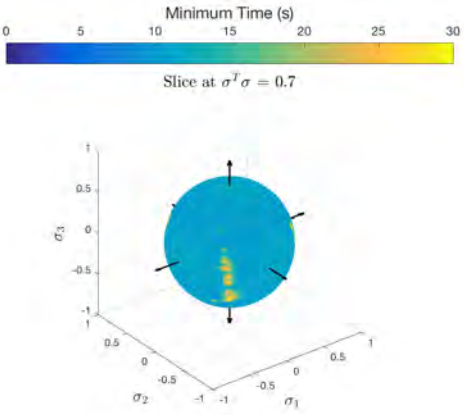

(c) $\Omega = 4\ deg/s$

Figure 5.8. Relative attitude backward T-reachable sets at zero angular velocity and rendezvous relative position and velocity at different chief rotation rates, sliced at $\boldsymbol{\sigma}^T\boldsymbol{\sigma} = 0.4$; color bar indicates minimum time values corresponding to the contours.

mostly bang-bang behavior. The translational forces show that a force in the x direction is required to maintain the rendezvous position, but this force is not bang-bang. Figure 5.10b, Figure 5.11b, and Figure 5.12b, show the GPOPS-II solutions for the case with the largest minimum time. It is evident that singularities are encountered by looking at the MRP state histories. As a result, the spacecraft goes through complete revolutions before converging to the desired relative attitude; these solutions are not truly minimum time maneuvers.

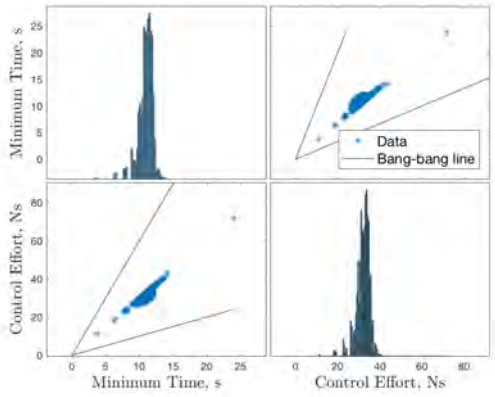

(a) $\Omega = 0\ deg/s$

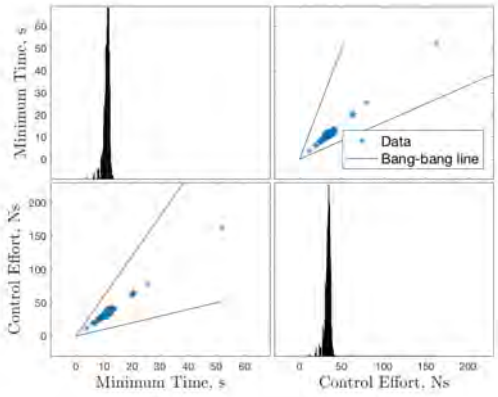

(b) $\Omega = 2\ deg/s$

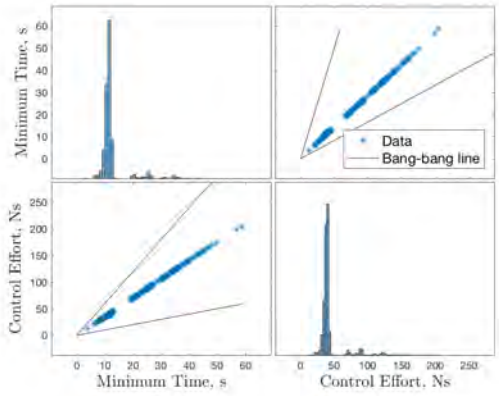

(c) $\Omega = 4\ deg/s$

Figure 5.9. Minimum time and control effort histograms and correlation for attitude (zero angular velocity, rendezvous position) subspace.

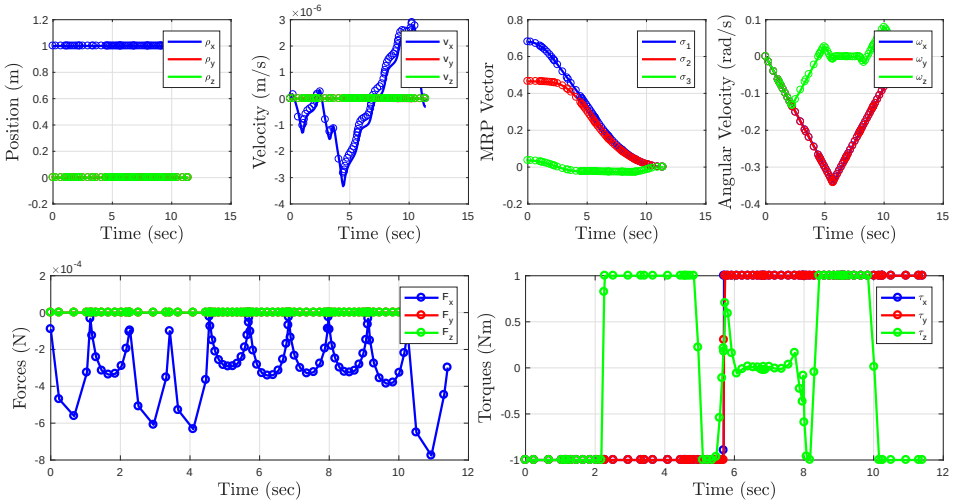

(a) Sample Case #1, $\Omega = 0\ deg/s$

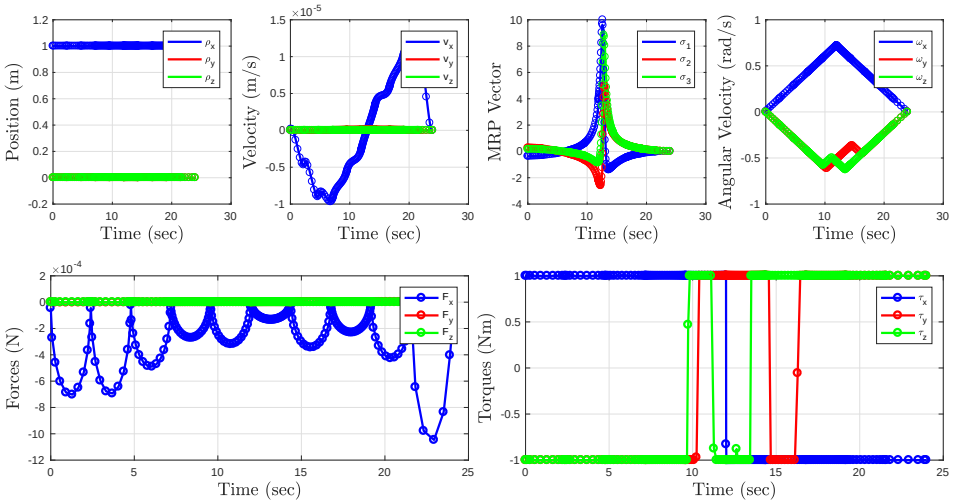

(b) Sample Case #2, $\Omega = 0\ deg/s$

Figure 5.10. Sample cases from attitude (zero angular velocity, rendezvous position) subspace for $\Omega = 0\ deg/s$.

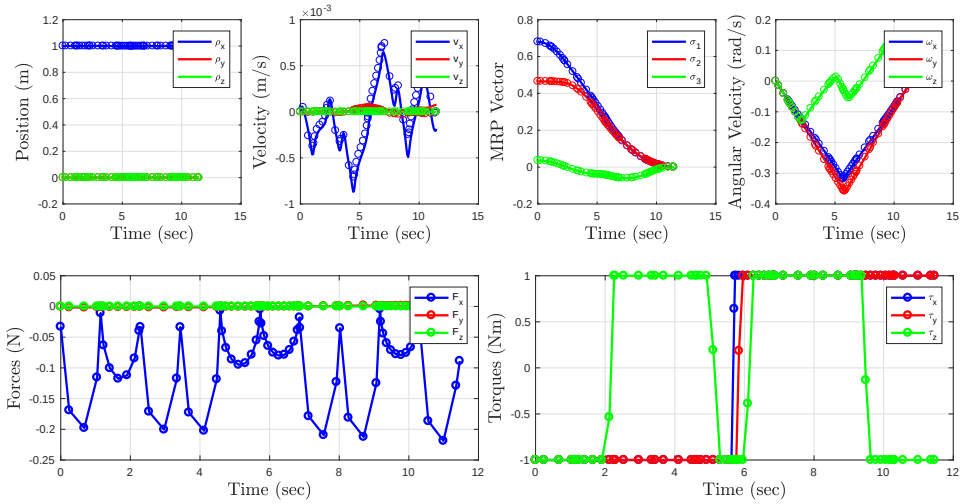

(a) Sample Case #1, $\Omega = 2\ deg/s$

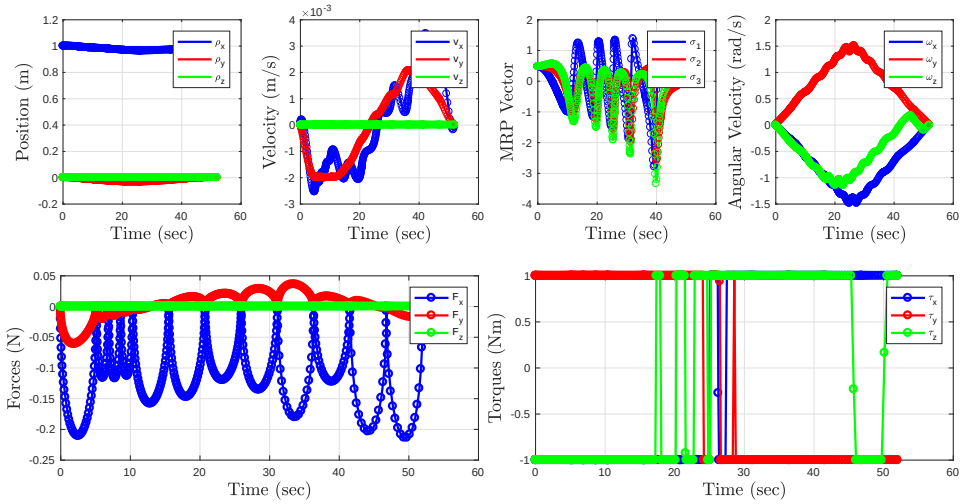

(b) Sample Case #2, $\Omega = 2\ deg/s$

Figure 5.11. Sample cases from attitude (zero angular velocity, rendezvous position) subspace for $\Omega = 2\ deg/s$.

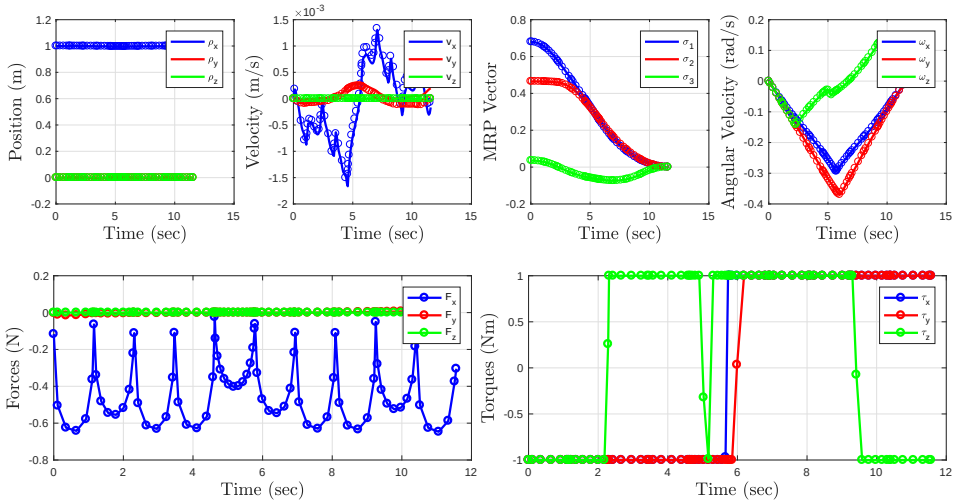

(a) Sample Case #1, $\Omega = 4\ deg/s$

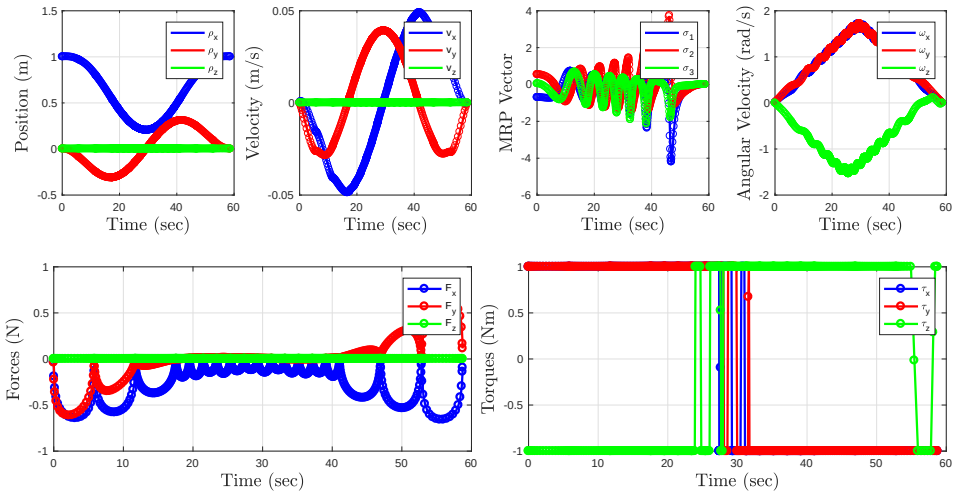

(b) Sample Case #2, $\Omega = 4\ deg/s$

Figure 5.12. Sample cases from attitude (zero angular velocity, rendezvous position) subspace for $\Omega = 4\ deg/s$.

Table 5.4. Case failures during 6-DOF reachability analysis.

Subspace (Slice)	Chief Rotation Rate, deg/s	Number of Cases	% failed
Position; NMC velocity	0	27000	0.1
Position; NMC velocity	2	27000	0.87
Position; NMC velocity	4	27000	2.51
Attitude; zero ang. velocity	0	8000	3.21
Attitude; zero ang. velocity	2	8000	4.94
Attitude; zero ang. velocity	4	8000	6.31

The above analysis of backward reachability in terms of relative position and relative attitude built on the results presented in Chapter 4. The framework created for solving a family of MT-OCPs for the 6-DOF dynamical system enables reachability analysis of more complex scenarios, such as an off-principal axis tumble.

5.2 Reachability Analysis: 6-DOF Rendezvous with Tumbling Chief

The next scenario that was investigated considers a chief spacecraft that is tumbling (i.e., has an initial angular velocity component in all three body axes). Additionally, the chief and deputy are defined as rectangular parallelepipeds with dimensions $1 \times 2 \times 3$ m, resulting in triaxial inertia properties (i.e., $J_{c_x} \neq J_{c_y} \neq J_{c_z}$ and $J_{d_x} \neq J_{d_y} \neq J_{d_z}$), thus relaxing the previous spherically symmetric assumption. The parameters of the scenario studied during this phase of research are shown in Table 5.5.

5.2.1 Analysis of Relative Position Backward Reachability

The translational reachability was investigated by generating a subspace of relative positions at fixed values of initial relative velocity, initial relative attitude, and initial relative angular velocity, as shown in Table 5.1. The subspace was defined by 27,000 test points, with control constraints $-1 \leq (F_x,\ F_y,\ F_z) \leq 1$ and $-1 \leq (M_x,\ M_y,\ M_z) \leq 1$. The MT-OCP was attempted for each test point with chief tumble rates of $\boldsymbol{\omega}_c = [0, 0, 0]^T$ and $\boldsymbol{\omega}_c = [-2, 1, 1]^T$ degrees per second (total of 54,000 runs). Figure 5.13 shows the resulting minimum time contours, at values of $\rho_x = 0$ m and $\rho_z = 0$ m and $\rho_x = 40$ m and $\rho_z = -40$ m. An expectation is that when the chief is not tumbling (i.e., $\boldsymbol{\omega}_{\mathsf{C/L}} = [0, 0, 0]^T$ deg/s) the results should be very similar to the previous results when the chief is not rotating (i.e., $\Omega = 0$ deg);

Table 5.5. Scenario parameters for 6-DOF rendezvous with a tumbling chief in circular orbit.

Chief Orbital Elements	$a = 6878.137$ km, $e = 0$, $i = 50$ deg, $\omega_{ra} = 0$ deg, $\omega_p = 0$ deg, $f_0 = 0$ deg
Chief Mass (kg)	100
Deputy Mass (kg)	100
Chief Inertia (kg-m^2)	$diag(108.33,\ 83.33,\ 41.67)$
Deputy Inertia (kg-m^2)	$diag(108.33,\ 83.33,\ 41.67)$
F_{max} (N)	1
M_{max} (N-m)	1
T_{max} (s)	1000
Desired final condition	$\boldsymbol{\rho}_f = [1, 0, 0]^T\ m$
	$\mathbf{v}_f = [0, 0, 0]^T\ m/s$
	$\boldsymbol{\sigma}_f = [0, 0, 0]^T$
	$\boldsymbol{\omega}_f = [0, 0, 0]^T\ rad/s$

the only difference between these scenarios is the chief and deputy inertia values. Clearly, Figures 5.13a and 5.13c look identical to Figures 5.1a and 5.2a, respectively. When the chief is tumbling at $\boldsymbol{\omega}_{\mathsf{C/L}} = [-2, 1, 1]^T$, the contours on both the x-y plane and y-z plane take an oval shape, indicating that the out-of-plane motion is no longer decoupled.

Figure 5.14 shows the correlation between minimum time and control effort for the 27,000 cases, for each scenario. The histograms on the diagonals of each subfigure show the range of minimum times and control effort from the sampled data, while the off-diagonals show the correlation between minimum time and control effort. As reported in Table 5.6, a small percentage of cases failed to converge. The correlation plots in Figure 5.14a show the spread of data indicating solutions with different numbers of bang-bang controls but all falling within the expected bounds (as previously seen in Figure 5.3). In Figure 5.14b, the correlation plots show a clear linear trend; in this case, it can be deduced that all solutions exhibit bang-bang control behavior for three of the six control inputs (i.e., all translational forces are bang-bang).

Two sample test cases were selected to show an example of these minimum time trajectories. Figure 5.15 shows the state and control trajectories for the two samples when the chief is not tumbling; results look very much like the trajectories in Figure 5.4. Figure 5.16 shows the resulting trajectories for the same sample cases when the chief is tumbling. It is evident

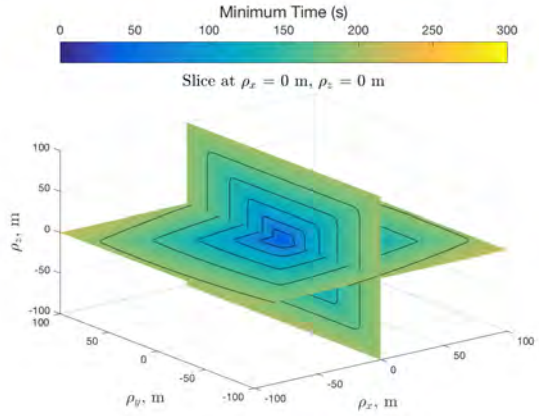

(a) Chief not tumbling

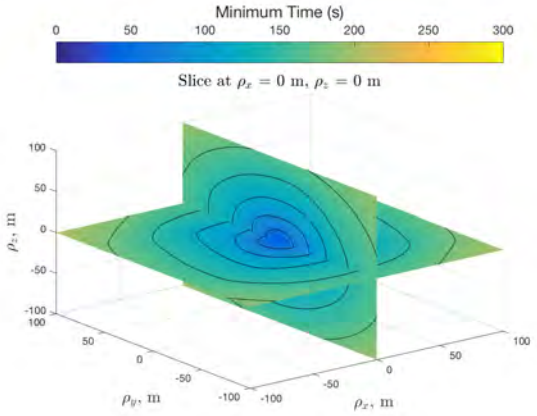

(b) Chief tumbling

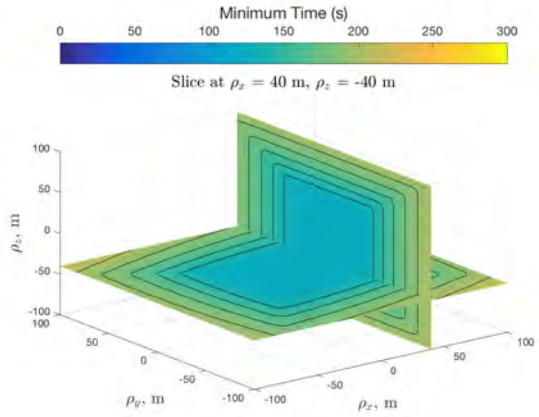

(c) Chief not tumbling

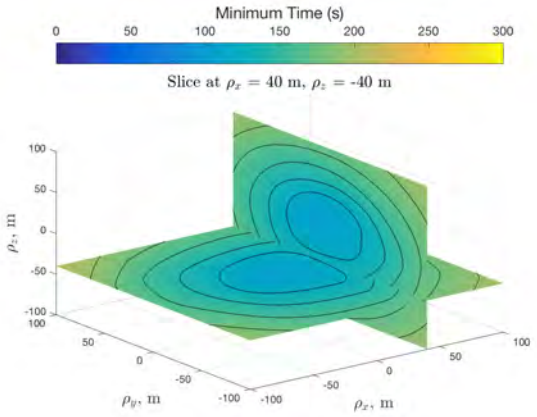

(d) Chief tumbling

Figure 5.13. Relative position backward T-reachable sets at NMC velocity, aligned attitude, and zero angular velocity with tumbling chief, sliced at $\rho_x = 0\ m$ and $\rho_z = 0\ m$ and $\rho_x = 40\ m$ and $\rho_z = -40\ m$; color bar indicates minimum time values corresponding to the contours.

that for both cases, when the chief is tumbling, all three translational forces are bang-bang.

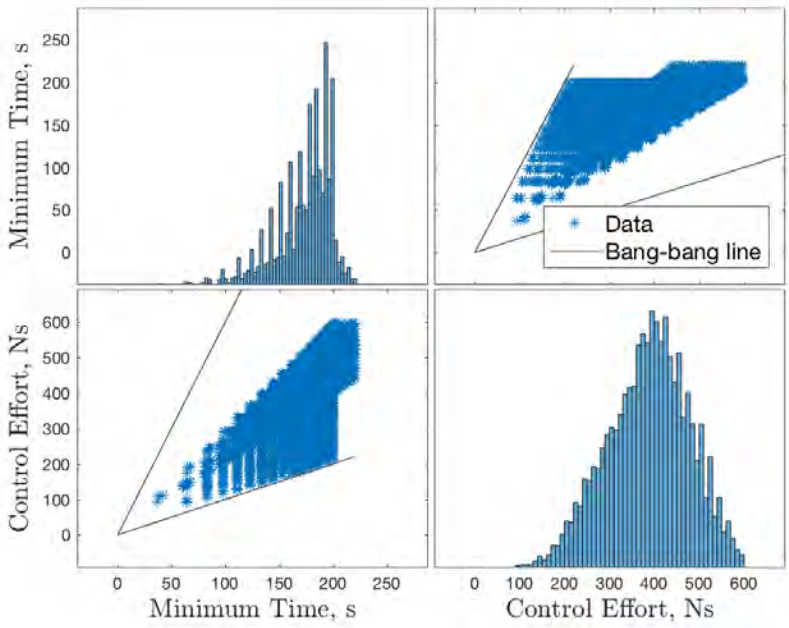

(a) Chief not tumbling

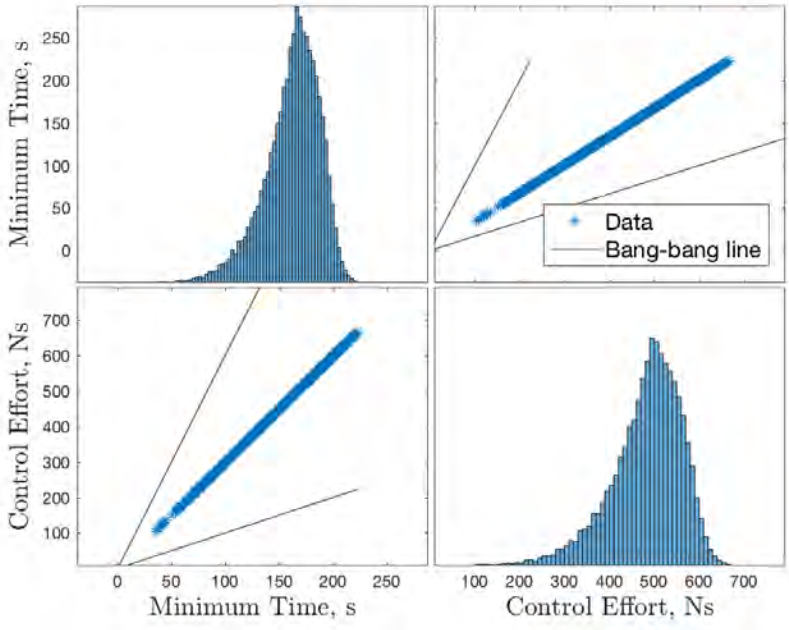

(b) Chief tumbling

Figure 5.14. Minimum time and control effort histograms and correlation for position (NMC velocity, aligned attitude) subspace.

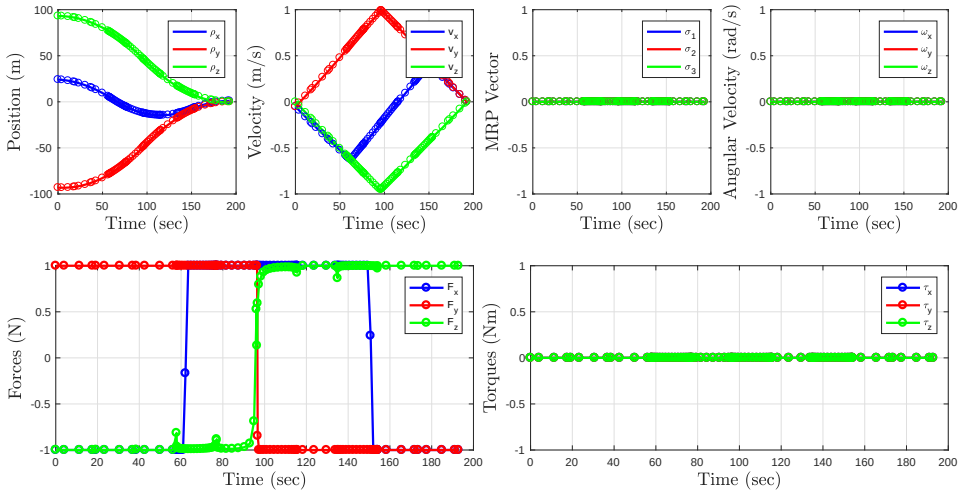

(a) Sample Case #1, Chief not tumbling

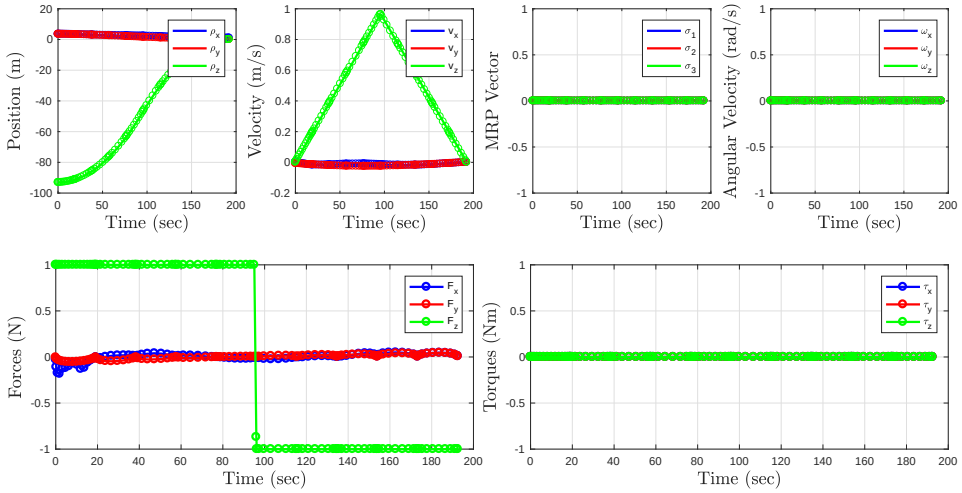

(b) Sample Case #2, Chief not tumbling

Figure 5.15. Sample cases from position (NMC velocity, aligned attitude) subspace with non-tumbling chief.

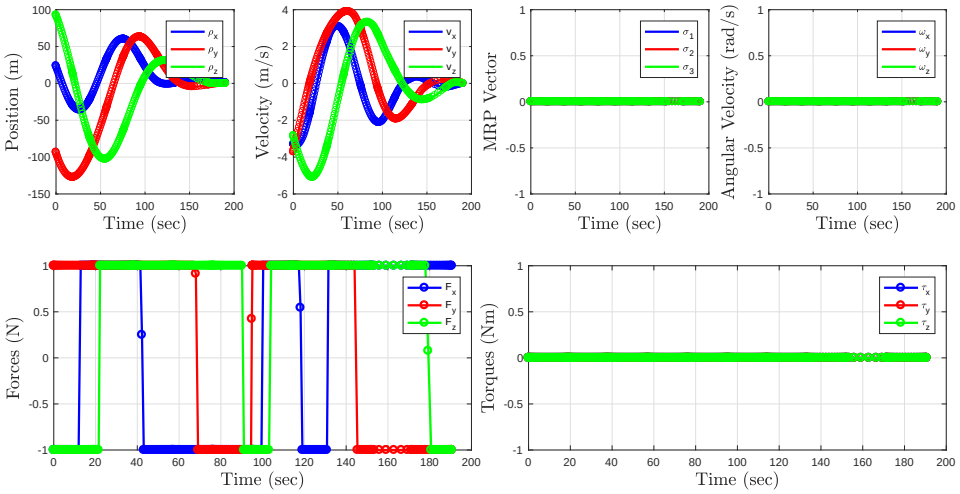

(a) Sample Case #1, Chief tumbling

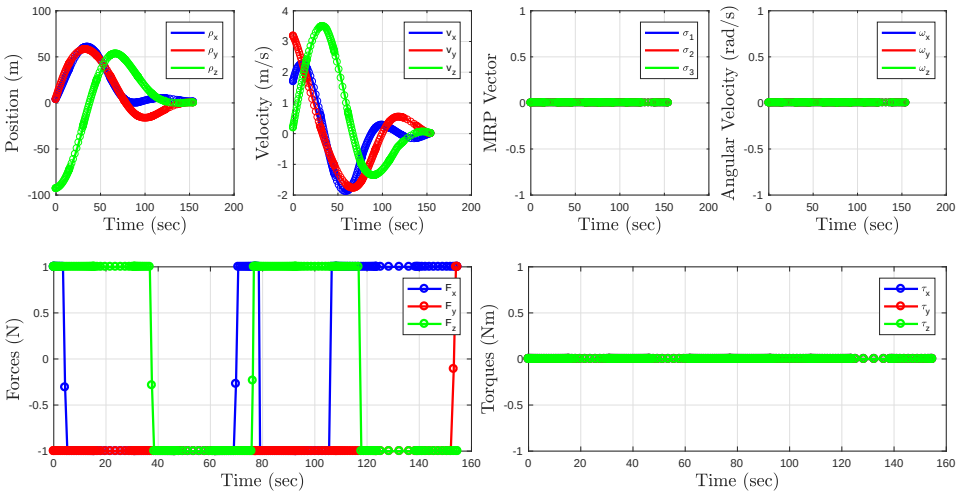

(b) Sample Case #2, Chief tumbling

Figure 5.16. Sample cases from position (NMC velocity, aligned attitude) subspace with tumbling chief.

5.2.2 Analysis of Relative Attitude Backward Reachability

The rotational reachability was investigated by generating a subspace of relative attitudes at fixed values of initial relative angular velocity, initial relative position, and initial relative velocity, as shown in Table 5.1. The subspace was defined by 8,000 test points, with control constraints $-1 \leq (F_x,\ F_y,\ F_z) \leq 1$ and $-1 \leq (M_x,\ M_y,\ M_z) \leq 1$. The MT-OCP was attempted for each test point with tumble rates of $\boldsymbol{\omega}_{\mathsf{C/L}} = [0, 0, 0]^T$ and $\boldsymbol{\omega}_{\mathsf{C/L}} = [-2, 1, 1]^T$ degrees per second (total of 16,000 runs). Figure 5.17 shows the minimum time surfaces, projected on spheres representing $\boldsymbol{\sigma}^T\boldsymbol{\sigma} = 0.4$ and $\boldsymbol{\sigma}^T\boldsymbol{\sigma} = 0.7$. Note that the minimum principal moment of inertia of the deputy is along the z axis. This can be seen in Figure 5.17a and 5.17c. The color of the spheres along the z principal axis (i.e., the vertical black arrow) is a darker shade, indicating that a rotation about that axis will have a smaller minimum time. This result is intuitive since the torque to inertia ratio along the minimum inertia direction is larger than in other directions. The bright yellow spots seen on the spheres are likely solutions that encountered singularities, as seen in previous results. These situations seem to be more prevalent when the chief is tumbling, as seen in Figure 5.17b and 5.17d.

Figure 5.18 shows the correlation between minimum time and control effort for the 8,000 cases, for each scenario. The histograms on the diagonals of each subfigure show the range of minimum times and control effort from the sampled data, while the off-diagonals show the correlation between minimum time and control effort. The histograms show that for the majority of cases, in both the non-tumbling and tumbling scenarios, the minimum times are between 20 to 30 seconds. The correlation plots clearly show the cases that exhibit larger maneuver times, which created the yellow spots on the spheres seen in Figure 5.17. With the exception of the one outlier data point in Figure 5.18b, there is no clear indication that the cases with larger maneuver times are invalid from these results. A closer look at the trajectories produced in these cases is necessary to assess the validity of the solution.

Two sample cases were selected to show an example of these minimum time trajectories. The first sample case was chosen to be within the majority of minimum time groupings, while the second sample exhibited a larger minimum time for each scenario. In Figure 5.19a, it can be seen that the torques show the expected bang-bang behavior, and a force is required in the x direction to maintain the rendezvous position. With the chief tumbling, the torque behavior is similar, but forces are required in all three directions to maintain the rendezvous position, as seen in Figure 5.20a. The second sample cases, with larger maneuver times,

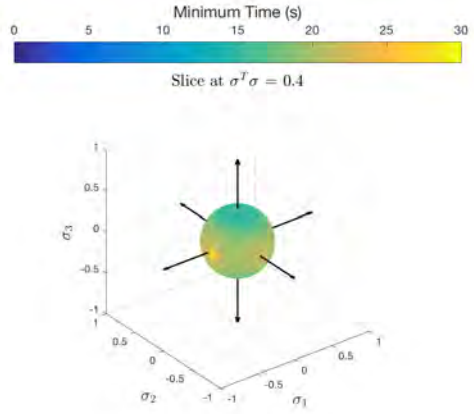

(a) Chief not tumbling

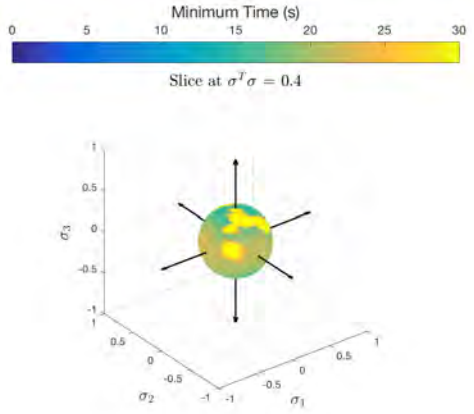

(b) Chief tumbling

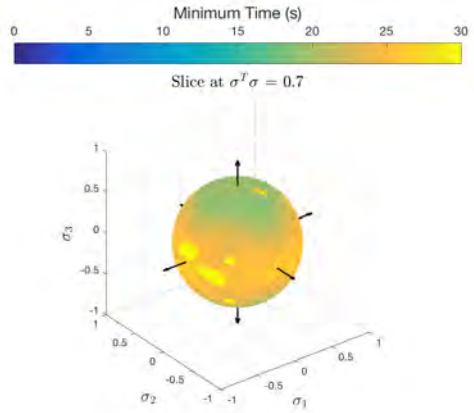

(c) Chief not tumbling

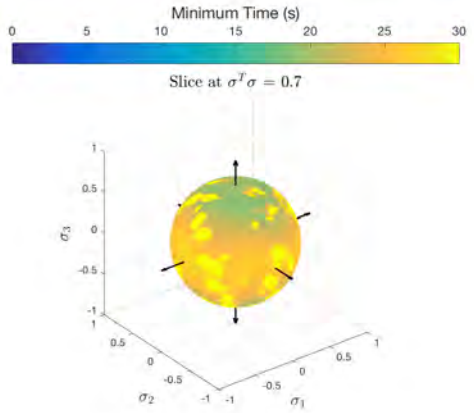

(d) Chief tumbling

Figure 5.17. Relative attitude backward T-reachable sets at zero angular velocity and rendezvous relative position and velocity with tumbling chief, sliced at $\boldsymbol{\sigma}^T\boldsymbol{\sigma} = 0.4$ and $\boldsymbol{\sigma}^T\boldsymbol{\sigma} = 0.7$; color bar indicates minimum time values corresponding to the contours.

clearly encounter singularities as evidenced by the MRP trajectories in Figures 5.19b and 5.20b. As a result, these are not truly minimum time maneuvers.

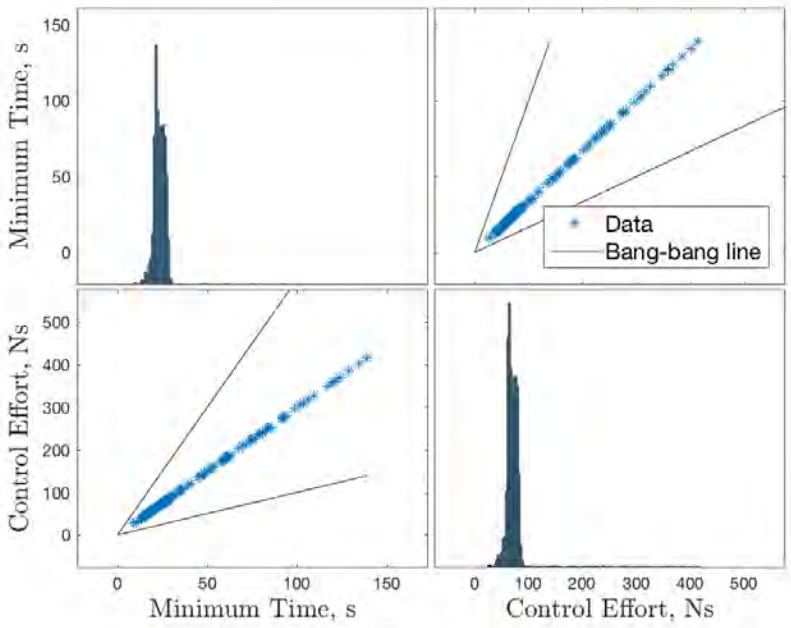

(a) Chief not tumbling

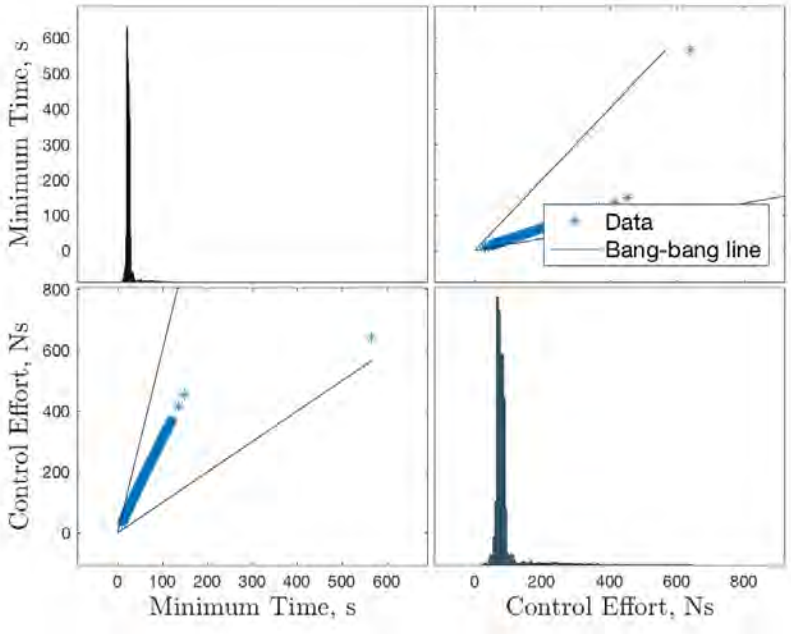

(b) Chief tumbling

Figure 5.18. Minimum time and control effort histograms, and correlation, for attitude (zero angular velocity, rendezvous position) subspace.

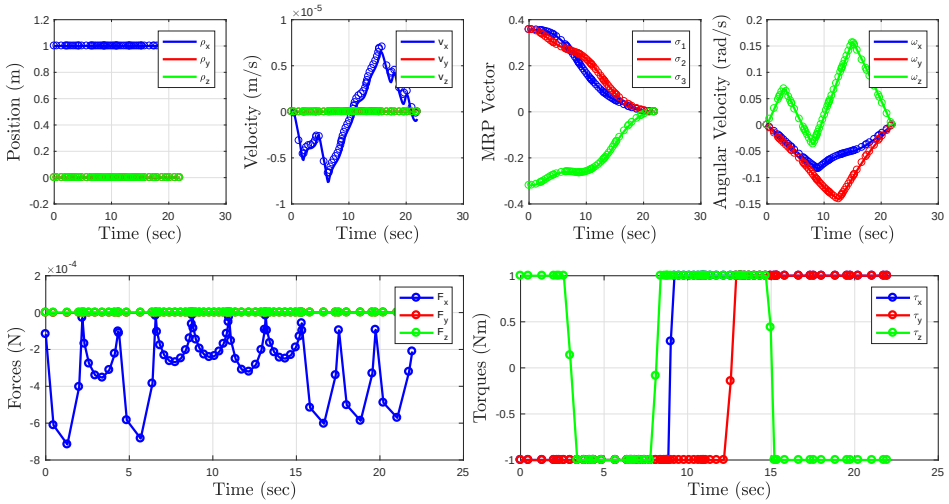

(a) Sample Case #1, Chief not tumbling

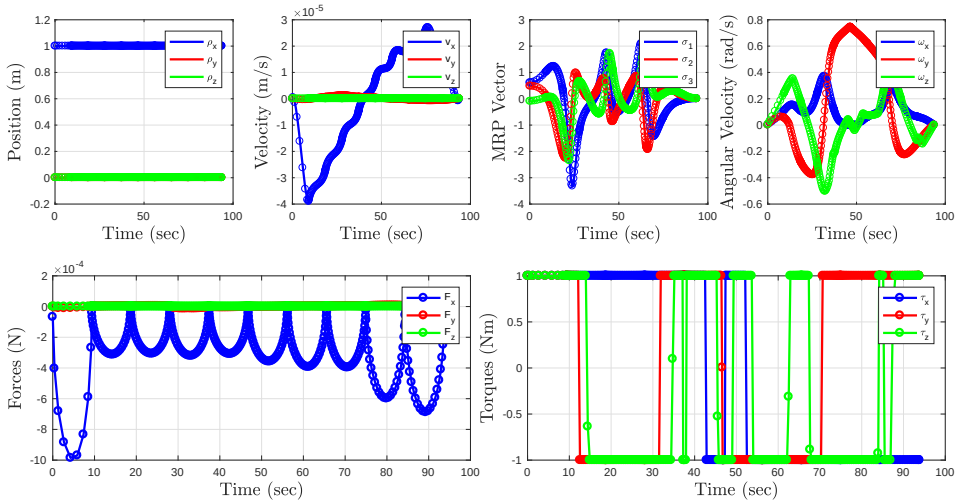

(b) Sample Case #2, Chief not tumbling

Figure 5.19. Sample cases from attitude (zero angular velocity, rendezvous position) subspace with non-tumbling chief.

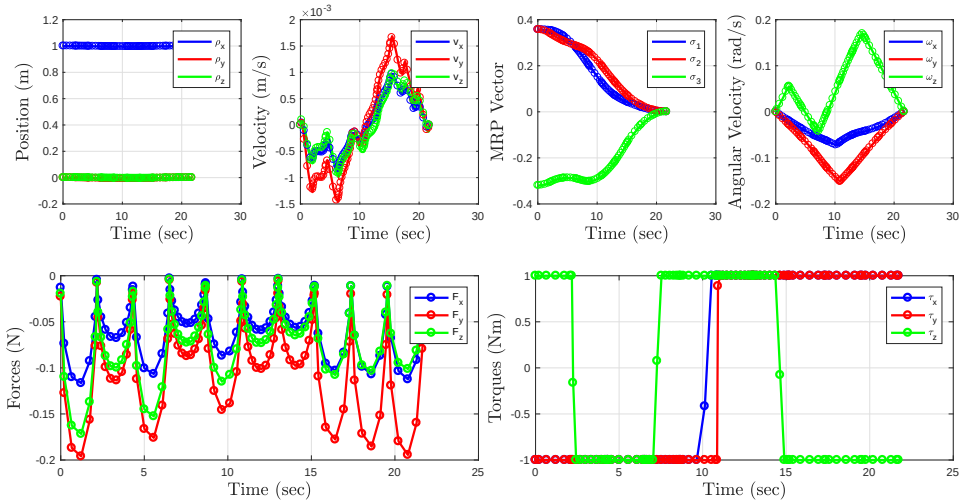

(a) Sample Case #1, Chief tumbling

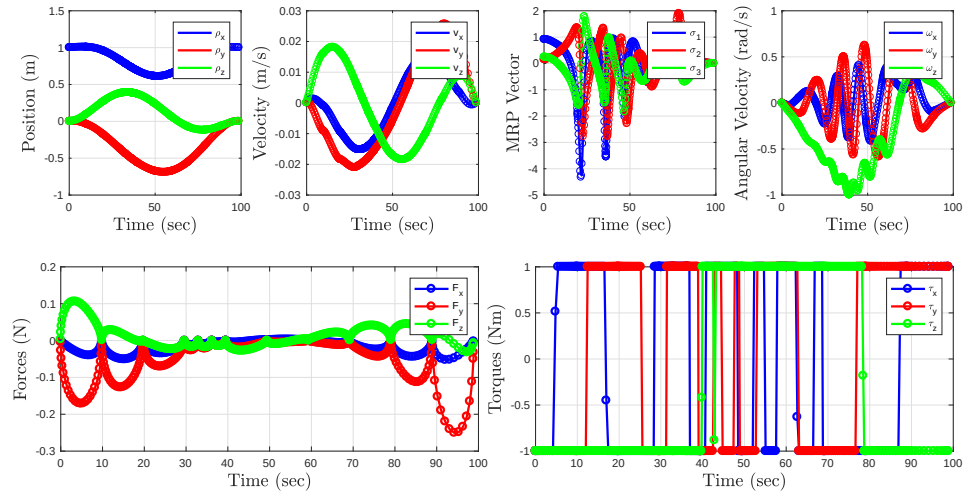

(b) Sample Case #2, Chief tumbling

Figure 5.20. Sample cases from attitude (zero angular velocity, rendezvous position) subspace with tumbling chief.

Table 5.6 reports the percentage of cases that did not solve successfully. The backward reachability analysis of the 6-DOF system provided valuable insight into the feasibility of rendezvous maneuvers from a variety of relative positions and relative attitudes. To the best of the author's knowledge, this is the first time reachability analysis results for the problem of rendezvous with a tumbling chief have been presented.

Table 5.6. Case failures during 6-DOF reachability analysis.

Subspace (Slice)	Chief tumble state	Number of Cases	% failed
Position; NMC velocity	Not tumbling	27000	0.09
Position; NMC velocity	Tumbling	27000	1.37
Attitude; zero ang. velocity	Not Tumbling	8000	5.51
Attitude; zero ang. velocity	Tumbling	8000	5.7

5.2.3 Chief Eccentricity Effect on Reachability Analysis

The scenarios analyzed in the previous sections were for a chief spacecraft in a circular orbit (i.e., eccentricity was exactly $e = 0$). The unsimplified dynamics, however, is valid for orbits of any eccentricity. Practically, even nominal circular orbits have a small nonzero eccentricity value. In this section, the effect of a nonzero eccentricity on the reachability analysis is examined. The translational reachability for the tumbling chief scenario, outlined in Table 5.5, was re-investigated for chief orbital eccentricities of $e = 0.05$ and $e = 0.1$. The set of test points remained the same, as outlined in Section 5.2.1. Figure 5.21 shows the comparison of the relative position backward reachability for the different eccentricity values and a non-tumbling chief. Figure 5.22 shows these results for a tumbling chief. There is no discernible difference in the minimum time contour plots in these figures. This is an expected result since the relative distances considered in these cases are relatively small, and the maneuver times are much smaller than the orbital period. Notably, the solver encountered a slightly larger number of failures with higher eccentricities, as reported in Table 5.7.

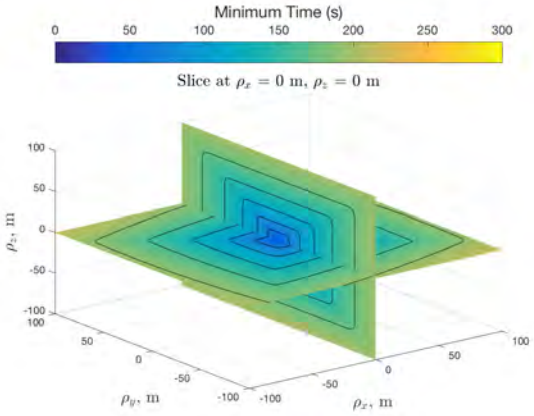

(a) Chief not tumbling, $e = 0$

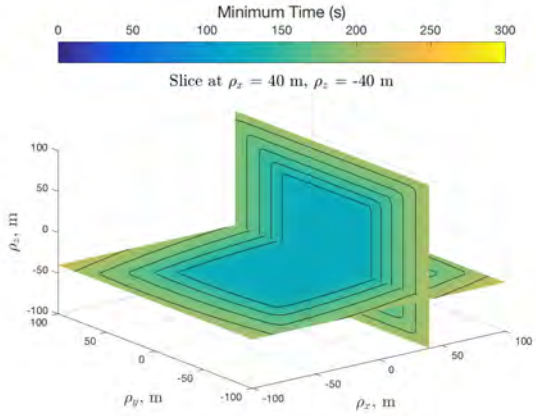

(b) Chief not tumbling, $e = 0$

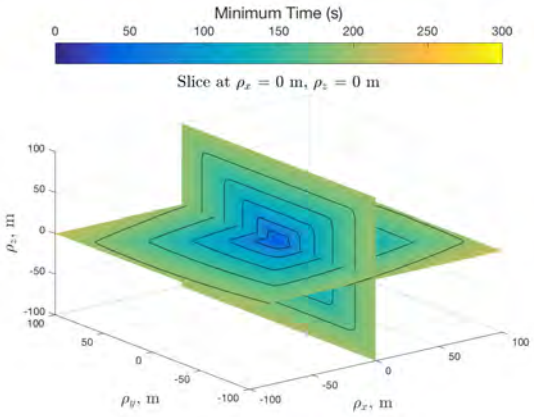

(c) Chief not tumbling, $e = 0.05$

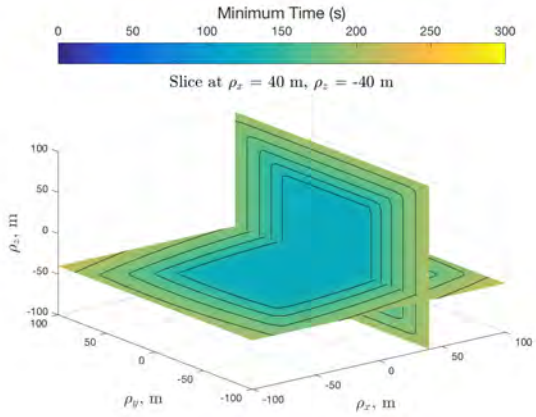

(d) Chief not tumbling, $e = 0.05$

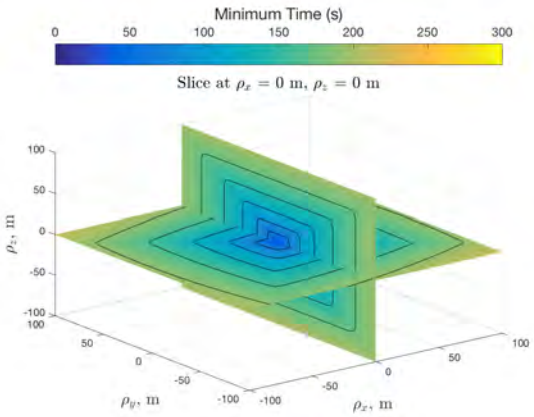

(e) Chief not tumbling, $e = 0.1$

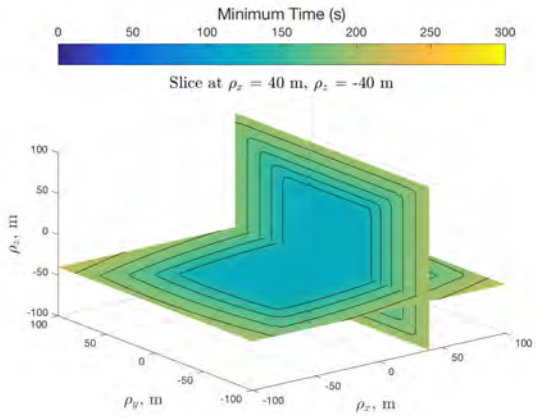

(f) Chief not tumbling, $e = 0.1$

Figure 5.21. Comparison of relative position backward T-reachable sets for chief orbital eccentricities of $e = 0$, $e = 0.05$, and $e = 0.1$.

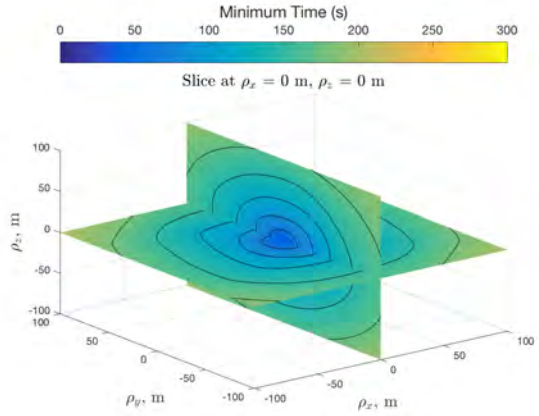

(a) Chief tumbling, $e = 0$

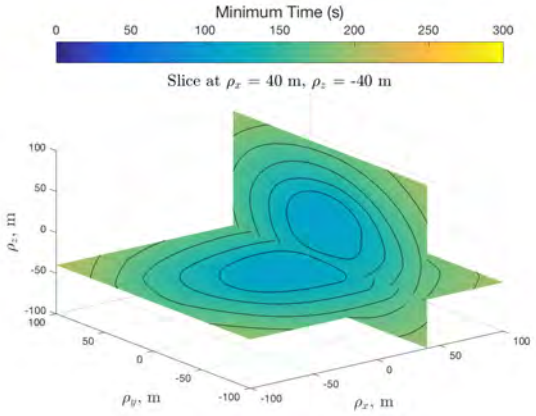

(b) Chief tumbling, $e = 0$

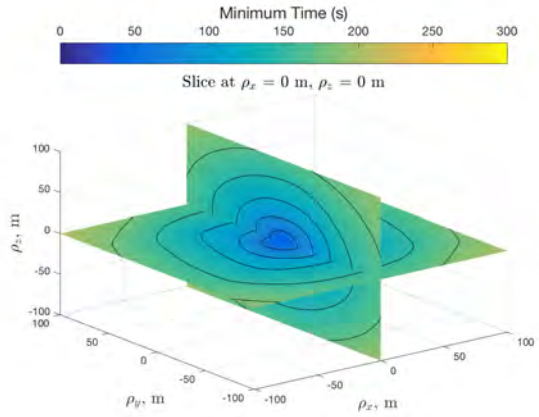

(c) Chief tumbling, $e = 0.05$

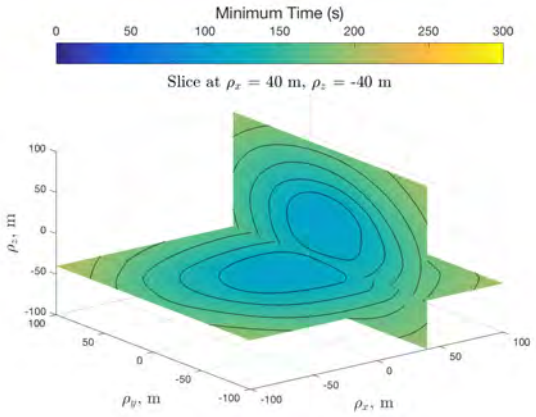

(d) Chief tumbling, $e = 0.05$

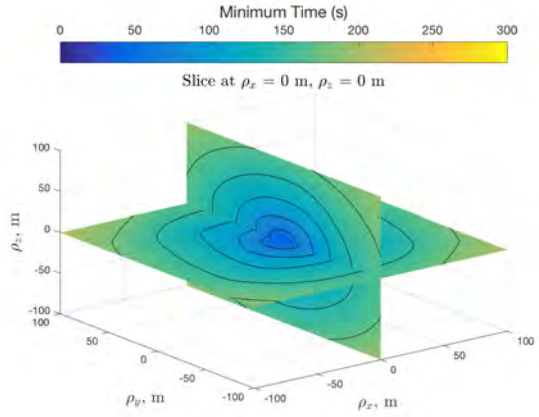

(e) Chief tumbling, $e = 0.1$

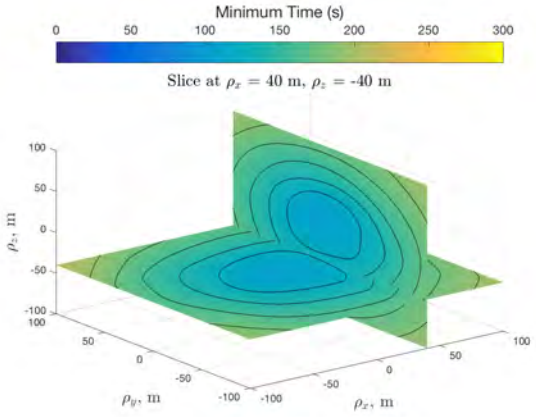

(f) Chief tumbling, $e = 0.1$

Figure 5.22. Comparison of relative position backward T-reachable sets for chief orbital eccentricities of $e = 0$, $e = 0.05$, and $e = 0.1$.

Table 5.7. Case failures during translational 6-DOF reachability analysis for chief orbital eccentricities of $e = 0$, $e = 0.05$, and $e = 0.1$.

Subspace (Slice)	Chief Tumbling Profile	Number of Cases	% failed
Position; NMC velocity	Not Tumbling ($e = 0$)	27000	0.09
Position; NMC velocity	Tumbling ($e = 0$)	27000	1.37
Position; NMC velocity	Not Tumbling ($e = 0.05$)	27000	0.11
Position; NMC velocity	Tumbling ($e = 0.05$)	27000	1.79
Position; NMC velocity	Not Tumbling ($e = 0.1$)	27000	0.41
Position; NMC velocity	Tumbling ($e = 0.1$)	27000	3.21

5.3 Summary

This chapter tackled the problem of analyzing the reachability characteristics of a high-dimensional, nonlinear, coupled dynamical system, representing the spacecraft rendezvous scenario with a tumbling chief. First, the reachability characteristics of the 6-DOF rendezvous problem were examined, assuming the chief is in a circular orbit and rotating on its orbit plane at a constant rate. Backward reachable sets were visualized in predefined subspaces, by computing a sampling of minimum time solutions and plotting minimum time contours on the subspace of interest. This first set of results allowed for comparison with results from Chapter 4, and served to validate the reachability analysis methodology. Additionally, by running a larger population of test cases in these scenarios, the results herein provided additional insight into the problem, especially in the analysis of reachable relative attitudes. To the best of the author's knowledge, this is the first time reachability analysis has been presented for the relative attitude between two rigid bodies.

The 6-DOF rendezvous problem was also examined for a chief, again in circular orbit, in tumbling motion. Backward reachable sets were visualized, as in the previous scenarios, in the predefined relative position and relative attitude subspaces. The results provided valuable insight into the capabilities inherent in this complex dynamical system. The results also brought to light some sensitivities, especially in the relative attitude cases when MRP singularities were encountered. These sensitivities could be alleviated by providing more sophisticated initial guesses to the GPOPS-II solver, or by using a non-singular set of attitude parameters (i.e., unit quaternions).

Lastly, the effect of nonzero chief orbital eccentricity on this reachability analysis was

examined. It was shown that for the relatively small maneuver times and relative distances considered, a nonzero eccentricity did not have a visible effect on the results.

The research contributions offered in this chapter are shown in Table 5.8.

Table 5.8. Research contributions in Chapter 5.

Contribution	**Objective**
6-DOF Reachability analysis of rendezvous with chief rotating on orbit plane	2
6-DOF Reachability analysis of rendezvous with chief in tumbling motion	2
Reachability analysis of relative attitude between two rigid bodies	2
Analysis of chief orbital eccentricity effect on reachability results	2

THIS PAGE INTENTIONALLY LEFT BLANK

Part III

Autonomous Guidance and Control Strategy: Rendezvous with a Tumbling Object

THIS PAGE INTENTIONALLY LEFT BLANK

CHAPTER 6:
Autonomous Guidance via Model Predictive Control

The previous chapters answered the first research objective, showing a family of initial conditions from which a maneuver to rendezvous with a tumbling object is feasible. This chapter focuses on the application of an autonomous guidance and control algorithm to this problem. Specifically, the MPC framework is leveraged to develop an autonomous, optimization-based, stable, algorithm to control the 6-DOF relative motion. First, the MPC framework is described, along with its various applications in control of spacecraft relative motion. Secondly, an applied reachability concept is defined, applicable to the closed-loop 6-DOF system controlled by MPC. Finally, results of the closed-loop reachability analysis are presented and compared to the previous results. Some of the work included in this chapter was published in [89].

6.1 The Model Predictive Control Framework

Recent advancements in computing technology have produced a research trend in the aerospace guidance and control community towards CG&C algorithms [14]. MPC is among the most notable CG&C methods [15]. MPC is a finite horizon, optimization-based control approach that can handle dynamically changing constraints. By limiting the horizon of the optimization problem, MPC reduces the complexity of on-board computations, thus making it an attractive option for autonomous systems. Assume that the system to be controlled is described by the control affine dynamics

$$\dot{x} = f(x,t) + g(x,t)u(t), \tag{6.1}$$

with $x \in \mathbb{R}^n$ and $u \in \mathbb{R}^m$. Discretizing the system with sampling time t_s, and assuming the control input stays constant between sampling instants (i.e., zero-order hold), yields the discrete prediction model

$$x_{k+1} = f_d(x_k, k) + g_d(x_k, k)u_k, \tag{6.2}$$

where k is the discrete step, and functions f_d and g_d are the discretized versions of the continuous vector fields. Given an initial condition, x_k, at time step k, a desired state, x_d, and the prediction horizon, $N \in \mathbb{N}$, the following optimization problem is formulated at every time step [90]:

$$\begin{aligned}
\text{minimize} \quad &: \quad J = \sum_{i=0}^{N-1} l(x_{k+i},\ u_{k+i},\ x_d) + V_f(x_N,\ x_d) && \text{(6.3a)}\\
\text{subject to} \quad &: \quad \text{for } i = 0, \ldots, N-1, \\
&\qquad x_{k+1+i} = f_d(x_{k+i}, k+i) + g_d(x_{k+i}, k+i)u_{k+i} && \text{(6.3b)}\\
&\qquad u_{k+i} \in \mathcal{U}, && \text{(6.3c)}
\end{aligned}$$

where l is the stage cost, V_f is the terminal cost, and $\mathcal{U}$ is the set of admissible controls. Assuming that the optimization problem in (6.3) can be solved at time step k, its solution provides the optimal control sequence,

$$U_k^* = \{u_{0|k}, u_{1|k}, \ldots, u_{N-1|k}\} \subset \mathcal{U}, \tag{6.4}$$

made up of the $N-1$ control inputs predicted at time step k. The first element from the sequence is applied to the system (i.e., $u_k = u_{0|k}$), and the problem is resolved at the next time step. The resulting feedback control law is written as

$$\kappa(k) = \{u_k, u_{k+1}, u_{k+2}, \ldots\}. \tag{6.5}$$

Implementing an autonomous MPC algorithm requires some analysis. First, assuming the optimization problem can be solved on-board, is there a guarantee that the resulting feedback control law will be stabilizing? Then, since the method is dependent on the ability to solve this optimization problem efficiently, is there a guarantee that the optimization problem will remain feasible throughout the process?

Stability

Stability is not an inherent characteristic of MPC. In most cases, stability can be designed into the MPC optimization problem, by including a terminal cost in the cost functional and a terminal set constraint [91]. However, choosing these parameters appropriately can be

challenging. Specifically for constrained regulator problems, analysis exists showing the appropriate selection of these parameters [90].

Typically, the stage cost is chosen as the quadratic regulator function,

$$l(x_k, u_k, x_d) = (x_k - x_d)^T Q(x_k - x_d) + u_k^T R u_k, \tag{6.6}$$

with positive semi-definite $Q \in \mathbb{R}^{n\times n}$ and positive definite $R \in \mathbb{R}^{m\times m}$ [90], [92]. This choice enforces a positive definite stage cost.

The terminal cost term, $V_f(x_N, x_d)$, must be chosen as a global Control Lyapunov Function (CLF) of the system (6.2), meeting the inequality [90]

$$V_f(f_d(x) + g_d(x)u) - V_f(x) + l(x, u) \leq 0, \ \forall x \in \mathbb{R}^n. \tag{6.7}$$

Essentially, this condition ensures that the derivative of V_f is negative semi-definite. Selecting l and V_f with the considerations above, ensures that the MPC cost will be monotonically decreasing and the feedback control will be stabilizing [90].

The terminal set constraint is an additional stabilizing consideration that adds the constraint $x_N \in \mathcal{X}_f$. With this constraint, the final state from the optimization solution is forced to lie within a region from which a known feedback control solution exists. As such, this terminal set should be chosen to be a control invariant set of the system [90], [92]. The terminal set constraint provides theoretical assurance of stability, but is often omitted in practice since it can be hard to compute an appropriate invariant set, and the additional constraint complicates the optimization problem. When omitting the terminal set constraint, stability can be enforced by inflating the terminal cost or using a sufficiently large horizon [90], [92].

Recursive Feasibility

It has been assumed, up to this point, that the MPC optimization problem posed has a solution, and can be solved efficiently enough to allow for on-board implementation. Generally speaking, that is not the case. Suppose that at time step k the solution to the MPC optimization problem, with initial state x_k, provides the optimal control sequence $U_k^* = \{u_{0|k}, u_{1|k}, \ldots, u_{N-1|k}\} \subset \mathcal{U}$, with corresponding predicted trajectory $X_k = \{x_{0|k}, x_{1|k}, \ldots, x_{N|k}\}$. The successor state after applying the first control input is

$x_{k+1} = f_d(x_k, k) + g_d(x_k, k)u_{0|k}$. The successive optimization problem must then be solved at time step $k + 1$, with the initial condition x_{k+1}.

If the application of the first element of U_k^* ensures that a feasible solution to the optimization problem exists at time instant $k + 1$, such formulation of MPC is referred to as recursively feasible [93]. Ensuring recursive feasibility is generally difficult, especially if dynamically reconfigurable constraints are used. From a theoretical standpoint, recursive feasibility can be achieved by enforcing a terminal invariant set constraint [93], [94]. Computing invariant sets, as mentioned earlier, for constrained systems is not a trivial task, and in many cases this approach may not be practical.

A more practical approach is to assess recursive feasibility properties of a specific implementation of MPC, on a case-by-case basis. Utilizing convex formulations of MPC, where the underlying optimization problem is convex [95], offers an advantage in terms of computational efficiency and recursive feasibility [96]. In [89], the recursive feasibility properties of three different convex MPC algorithms are compared for the problem of spacecraft rendezvous with keep-out-zone constraints. The disadvantage of convex methods, of course, is that not all problems have an equivalent convex formulation. In most cases, the convex problem is an approximation of the actual problem. Producing convex approximations of nonconvex optimization problems is an open research topic in the field of CG&C (see for example [97]–[101]).

In this research, the focus is applying the MPC framework to the full 6-DOF spacecraft rendezvous problem, without any further approximations. The understanding is that recursive feasibility, in this case, cannot be guaranteed due to the nonconvex nature of the underlying optimization problem. The algorithm's recursive feasibility properties are only assessed empirically.

6.1.1 Previous MPC Applications to Spacecraft Rendezvous Problems

MPC has a rich history in a variety of applications. A comprehensive survey is presented by Eren et al. [96], offering a review of the impact MPC has had across the industrial and aerospace communities, as well as specifically bringing out the challenges associated with applying this guidance and control framework to an autonomous space system. Undoubtedly, MPC is on the cutting edge of guidance and control technologies that will enable autonomous

spacecraft RPO.

Applications of MPC to the spacecraft relative motion control problem date back to 1999, with an application to spacecraft formation keeping [102]. Richards and How [103] later apply MPC to a spacecraft rendezvous problem while incorporating constraints to ensure feasibility in the presence of disturbances. More recently, literature on this topic has been focused on computationally efficient MPC formulations for spacecraft rendezvous in the presence of control and state constraints (i.e., keep-ot-zones), in order to enable on-board implementation. Park et al. [104] present a Linear Quadratic (LQ) version of MPC for planar spacecraft rendezvous using the linearized CW dynamics model. In their work, they develop the rotating hyperplane method to enforce a convex keep-out-zone constraint. Additionally they take into account line-of-sight, docking velocity, and control constraints. The resulting MPC optimization is a Quadratic Programming (QP) problem, that can be solved efficiently [104]. Their work is extended to 3-D rendezvous problems by Weiss et al. [105], [106], again taking advantage of the LQ-MPC formulation with linearized (convex) constraints. A hardware-in-the loop validation of the LQ-MPC algorithm, with the rotating hyperplane constraint, is offered by Petersen et al. [107] on a wheeled robot emulating a spacecraft relative motion trajectory. Jewison [108], [109] extends the capabilities of MPC to handle multiple and moving obstacles, with an algorithm demonstrated in simulation. Jewison's approach handles the nonconvex keep-out-zone constraints directly, and uses a Sequential Quadratic Programming (SQP) solver to solve the underlying optimization problem. Finally, a set of experimental campaigns have been conducted on the air bearing testbed, Proximity Operations of Spacecraft: Experimental hardware-In-the-loop DYNamic test bed (POSEIDYN), at NPS. POSEIDYN offers quasi-frictionless, planar, dynamic environment for testing autonomous guidance and control algorithms for proximity maneuvers between multiple vehicles, simulating spacecraft on an orbit plane [110]. Many variants of MPC implementations have been successfully demonstrated including LQ-MPC for docking with obstacle avoidance using the rotating hyperplane method [111], LQ-MPC and Nonlinear Model Predictive Control (NMPC) for docking in the presence of multiple obstacles [112], and NMPC for docking with a rotating vehicle [113].

The MPC framework has also been applied to the problem of spacecraft attitude control, dating back to 1997. Crassidis et al. [114] implement NMPC to control a spacecraft's

attitude, using quaternion dynamics, and incorporating control constraints. A similar problem is solved by Myung and Bang [115], with an NMPC approach, but using the minimal MRP attitude parametrization and also incorporating external disturbances into the formulation. Focusing more on on-board applications, Hegranaes et al. [116] present an explicit MPC formulation for spacecraft attitude control. The explicit MPC solves, off-line, a series of linear constrained MPC problems by linearizing the quaternion kinematic and dynamic equations. The set of explicit solutions produces a look-up table that is used on-line to generate an on-board solution. Wood et al. [117] present an LQ-MPC formulation, based on linearized Euler angle kinematics and dynamics, for spacecraft attitude control actuated by magnetic torque rods. Ikeda et al. [118] consider a NMPC algorithm for attitude control of spacecraft with a pyramid Control Moment Gyroscope (CMG) system, while also considering avoidance of singular CMG configurations. Gupta et al. [119] present a geometric mechanics-based NMPC formulation, resulting in an efficient solver that exploits the Lie structure of SO(3). Their formulation incorporates both control and exclusion zone constraints. In extending this work, Lee et al. implement the SO(3)-based NMPC algorithm to a spacecraft with reaction wheels. Guiggianni et al. [120] show a LQ-MPC formulation for a spacecraft attitude control problem, actuated by reaction wheels, using linearized Euler angle kinematic and dynamic equations. In order to improve computational efficiency, they implement a fixed-point QP solver. Petersen et al. [82] show an application of NMPC to an underactuated spacecraft attitude control problem, when the spacecraft has only two functioning reaction wheels.

A vast variety of applications of MPC have been seen related to spacecraft rendezvous and attitude control problems; some focus on the formulation of guidance algorithms for different scenarios and constraints, while others focus on the computational aspects of devising efficient solvers for the underlying optimization problem. However, literature is lacking in the area of 6-DOF guidance and control via MPC. One of the few 6-DOF applications is Lee and Mesbahi's [47], [48] on MPC for a 6-DOF, dual-quaternion based, constrained precision landing problem. To the best of the author's knowledge, the MPC framework has not been applied to the problem of 6-DOF spacecraft rendezvous with a tumbling chief - this is the focus of this chapter.

6.2 Nonlinear MPC Algorithm for Spacecraft Rendezvous with a Tumbling Object

The 6-DOF relative dynamic equations, describing the problem of spacecraft rendezvous with a tumbling chief, were derived in Chapter 2 and are repeated here for completeness:

$$\dot{\boldsymbol{\rho}} = \mathbf{v} \tag{6.8a}$$

$$\begin{aligned}\dot{\mathbf{v}} = & -\frac{\mu}{R_d^3}\boldsymbol{\rho} + \frac{\mu\left(R_d^3 - R_c^3\right)}{R_c^3 R_d^3}\mathbf{r}_c^{\mathsf{C}} + \frac{1}{m_d}\mathbf{F}_d - \left[J_c^{-1}\left(-[\boldsymbol{\omega}_c]^{\times} J_c \boldsymbol{\omega}_c\right)\right]^{\times}\boldsymbol{\rho} \\ & -2[\boldsymbol{\omega}_c]^{\times}\mathbf{v} - [\boldsymbol{\omega}_c]^{\times}\left([\boldsymbol{\omega}_c]^{\times}\boldsymbol{\rho}\right)\end{aligned} \tag{6.8b}$$

$$\dot{\boldsymbol{\sigma}} = \frac{1}{4}\tilde{B}\boldsymbol{\omega}^{\mathsf{D}} \tag{6.8c}$$

$$\begin{aligned}\dot{\boldsymbol{\omega}}^{\mathsf{D}} = & J_d^{-1}\left[\mathbf{M}_d^{\mathsf{D}} - [\boldsymbol{\omega}^{\mathsf{D}} + C_{\mathsf{D/C}}\boldsymbol{\omega}_c]^{\times} J_d(\boldsymbol{\omega}^{\mathsf{D}} + C_{\mathsf{D/C}}\boldsymbol{\omega}_c)\right] \\ & -C_{\mathsf{D/C}}\left[J_c^{-1}\left(-[\boldsymbol{\omega}_c]^{\times} J_c\boldsymbol{\omega}_c\right)\right] - [C_{\mathsf{D/C}}\boldsymbol{\omega}_c]^{\times}\boldsymbol{\omega}^{\mathsf{D}}.\end{aligned} \tag{6.8d}$$

Defining the state vector $x = [\boldsymbol{\rho},\ \mathbf{v},\ \boldsymbol{\sigma},\ \boldsymbol{\omega}^{\mathsf{D}}]^T \in \mathbb{R}^{12}$ and control vector $u = [\mathbf{F}_d,\ \mathbf{M}_d^{\mathsf{D}}]^T \in \mathbb{R}^6$, the system can be written in control-affine form,

$$\dot{x} = f(x,t) + Gu, \tag{6.9}$$

with f and G defined in (2.22) and (2.23) respectively. Now, with sampling time t_s, and assuming zero-order hold on the control input, the system can be written in discrete form

$$x_{k+1} = f_d(x_k, k) + G_d u_k, \tag{6.10}$$

where f_d and G_d are the discrete versions of the vector fields f and G. The discretization of the system is accomplished numerically, within the software tools used to realize this implementation (discussed in Section 6.2.1).

The NMPC algorithm is designed with the stabilizing considerations discussed in Section 6.1. Given the desired rendezvous state, x_d, the stage cost is defined as,

$$l(x_k, u_k, x_d) = (x_k - x_d)^T Q(x_k - x_d) + u_k^T R u_k, \tag{6.11}$$

with $Q \geq 0$, and $R > 0$. The weighting parameter Q is chosen to be inversely proportional to the maximum allowable state error, and R is chosen inversely proportional to the maximum available control effort [121]:

$$Q = \text{diag}\left[\ldots \frac{\alpha_i^2}{x_{i_{max}}^2} \ldots\right] \text{for } i = 1, 2 \ldots, 12, \tag{6.12}$$

$$R = \text{diag}\left[\ldots \frac{\beta_i^2}{u_{i_{max}}^2} \ldots\right] \text{for } i = 1, 2, \ldots, 6, \tag{6.13}$$

where α_i and β_i are constant weights chosen for each state and control variable respectively, $x_{i_{max}}$ is the maximum error in each state variable, and $u_{i_{max}}$ is the maximum control authority for each control variable.

As mentioned earlier, the terminal cost term must be a global CLF of the nonlinear system to guarantee stability. It is generally quite difficult to come up with a global CLF, so often a local CLF, in a neighborhood of the desired state, is used. With a sufficiently long horizon, choosing a local CLF as the terminal weight term produces a stable feedback MPC law [90], [92]. A local CLF can be chosen by linearizing the nonlinear system about the desired state, and solving the infinite horizon, unconstrained, discrete LQR problem. The terminal cost is then set to

$$V_f = (x_N - x_d)^T Q_f (x_N - x_d), \tag{6.14}$$

where $Q_f > 0$ is the stabilizing solution to the Discrete Algebraic Riccati Equation (DARE), corresponding to the discrete LQR. A derivation of the DARE is included in the Appendix. Note that for this scenario, the dynamics is time-varying due to the orbital and tumbling motion of the chief. As a result, the linearized system will become less accurate over time, which will adversely affect closed-loop stability. To alleviate this concern, the DARE solution is recomputed at every iteration of the algorithm, and Q_f is updated.

The control constraints, as with the previous scenarios, are in the form $||u||_\infty \leq u_{max}$. Staring with the initial condition, x_k, and a finite prediction horizon, N, the NMPC Optimal

Control Problem (NMPC-OCP) to be solved at each iteration is:

$$\begin{aligned}
\text{minimize} \quad : \quad & J = \sum_{i=0}^{N-1} (x_{k+i} - x_d)^T Q (x_{k+i} - x_d) + u_{k+i}^T R u_{k+i} + \\
& (x_{k+N} - x_d)^T Q_{f_k} (x_{k+N} - x_d) && \text{(6.15a)} \\
\text{subject to} \quad : \quad & \text{for } i = 0, \ldots, N-1, \\
& x_{k+1+i} = f_d(x_{k+i}, k+i) + G_d u_{k+i} && \text{(6.15b)} \\
& ||u_{k+i}||_\infty \leq u_{max}. && \text{(6.15c)}
\end{aligned}$$

Given a maximum maneuver time, t_{max} (or maximum number of discrete steps), the NMPC algorithm solves the NMPC-OCP at every time step and applies the first control input of the optimal sequence to the system. The process is summarized in Algorithm 1.

Algorithm 1 NMPC algorithm

GIVEN: x_0, x_d, t_{max}, t_s, N, and chief states for $t = [t_0, t_{max}]$
Set $x_k = x_0$, $N_{sim} = {}^{t_{max}}/_{t_s}$
for $k = 1 : N_{sim}$ **do**
    $t_k = (k-1)t_s$ ▷ Time at current iteration
    Compute chief states for $t_k : t_s : t_k + (N-1)t_s \rightarrow$ input into prediction model
    Set $x_c(t_k)$ as the chief state at current time t_k
    Linearize dynamics model at x_d, $x_c(t_k)$
    Solve DARE for infinite horizon problem $\rightarrow$ get value of Q_{f_k}
    Solve corresponding NMPC-OCP $\rightarrow$ get $U_k^* = \{u_{0|k}, u_{1|k}, \ldots, u_{N-1|k}\}$
    Set $\kappa_k = u_{0|k}$
    Propagate dynamics: $x_{k+1} = f_d(x_k, k) + G_d \kappa_k$
    Set $x_k = x_{k+1}$ ▷ Reset initial condition for next iteration
end for

6.2.1 Software Tools Used to Implement NMPC Algorithm

The NMPC algorithm is developed using publicly available MATLAB-based tools. The overarching MPC design toolbox used is "MPCTools" [122], developed at the University

of Wisconsin. The MPCTools package is publicly available and enables users to apply the MPC framework to specific problems. The software offers the necessary tools to formulate and solve the MPC optimization problem, as well as simulate the desired closed-loop system. MPCTools interfaces with "CasADi" [123], [124] to build the NLP problem corresponding to the NMPC-OCP. CasADi, also publicly available, is a symbolic-based toolbox designed for general nonlinear optimization problems. Within the MPC framework, CasADi is used to develop the discretized plant and prediction models, based on the user-defined system dynamics, and constraint functions which are then used to build the NLP to be solved at each iteration. Finally, IPOPT [84] is used to solve the NLP, and obtain the MPC control sequence.

6.3 A Closed-Loop Applied Reachability Concept

The applied reachability analysis presented in Chapters 4 and 5 showed that the rendezvous maneuver to the tumbling chief is feasible. Intuitively, then, a stabilizing feedback control law will cause the system to eventually reach the rendezvous state. Depending on the application, it may be beneficial to conduct applied reachability analysis given a particular feedback control algorithm. In this manner, the behavior of the closed-loop system can be examined. Similar concepts of closed-loop reachability analysis are presented in [125]–[127], but without a formal definition. A definition of a closed-loop, backward T-reachable set is offered here. Let $\kappa(t) \in \mathcal{U}$ be a stabilizing, admissible feedback control law obtained by a user-defined method. The following is defined:

Definition 6.1 *The **closed-loop backward T-reachable set**, $\mathcal{R}_{B_{cl}}(T)$, from the final condition x_f, is the set of states, x_0, from which there exists an admissible feedback control law, $\kappa(t) \in \mathcal{U}$, resulting in an admissible trajectory $\gamma_\Sigma(0,T)$ reaching x_f in time $T > 0$ or less:*

$$\mathcal{R}_{B_{cl}}(T) = \{x(0) |\ \exists\ \kappa(t) \in \mathcal{U} \text{ and } \gamma_\Sigma(0,t),\ x(T) = x_f,\ 0 < t \leq T\}. \tag{6.16}$$

Note that Definition 6.1 does not specify the control law to be used, and applies to any feedback control method.

The closed-loop reachability characteristics can be analyzed using the same methodology used to analyze backward reachability (i.e., plotting contours of equal maneuver time). The boundary of $\mathcal{R}_{B_{cl}}(T)$ will be made up of all initial states from which the closed-loop system reaches the desired state in time T. The minimum time to reach the desired state from these initial conditions will be necessarily smaller or equal to T (i.e., $T^* \leq T$ for each of the points on the boundary of $\mathcal{R}_{B_{cl}}(T)$), meaning that all these states will also be members of the traditional backward reachable set.

6.4 Closed-Loop Reachability Analysis

The reachability analysis conducted in Chapter 5 was repeated, in a closed-loop sense, using the NMPC algorithm. For each scenario the same set of test points was used to analyze the closed-loop reachability on the subspaces defined in Table 5.1. The time to reach the desired state, and roto-translational control effort (see Equation (5.2)), were again used as performance metrics. In this analysis, a failure is defined as a simulation in which the deputy did not achieve the desired state within the allowable state errors. The MPC parameter settings used for these simulations are shown in Table 6.1.

6.4.1 6-DOF Rendezvous with Rotating Chief

The scenario with the chief in circular orbit, rotating about its z body axis at a constant rate, was examined first. The parameters of this scenario are shown in Table 5.3.

Table 6.1. NMPC parameters used for simulation of the 6-DOF system.

Parameter	**Value**
Sampling time, t_s (sec)	5
Horizon, N (steps)	25
Q weights (translational), $\alpha_{1:6}$	1
Q weights (rotational), $\alpha_{7:12}$	10^{-4}
Max position error, $x_{1:3_{max}}$	10^{-1}
Max velocity error, $x_{4:6_{max}}$	10^{-2}
Max rotational state error, $x_{7:12_{max}}$	10^{-4}
R weights, $\beta_{1:6}$	1

Analysis of Relative Position Closed-Loop Backward Reachability

The translational closed-loop reachability was investigated by repeating the analysis in Section 5.1.1 using the NMPC algorithm (27,000 test points with chief rotation rates of $\Omega = 0,\ 2,$ and 4, degrees per second; total of 81,000 runs). Figure 6.1 shows the resulting NMPC contours, at values of $\rho_x = 0\ m$ and $\rho_z = 0\ m$, compared to the minimum time contours presented in Figure 5.1. Figure 6.2 shows the comparison at values of $\rho_x = 40\ m$ and $\rho_z = -40\ m$. It is evident in these two figures that the overall shape of the closed-loop sets is very similar to the shape of the reachable sets. It is also clear that the closed-loop sets show larger maneuver times, which is expected. It is noticeable, in Figures 6.1 and 6.2, that the closed-loop NMPC contours (plots on the right) are not as smooth as the minimum time contours. This is likely due to the discrete nature of NMPC; since the sampling time is 5 sec, all maneuver times are a multiple of that sampling time. As a result, if one of the test points takes one more iteration to converge within the desired tolerance, compared to a nearby test point, the maneuver time difference is 5 sec. Using a smaller sampling time may make the contour lines smoother, but at the cost of increasing the complexity of the on-board optimization problem.

Figure 6.3 shows the correlation between the maneuver time and control effort for the 27,000 cases, for each scenario. The histograms and correlation plots in Figure 6.3 show very similar trends to what was observed in the minimum time cases in Figure 5.3. The two bang-bang lines show the upper and lower bounds on control effort assuming either all six controls are always at maximum value, or only one control is at maximum. The upper bound (all six controls at maximum) is valid, but the lower bound is not a theoretical certainty for the NMPC controller (i.e., there could exist a solution with none of the controls always at maximum). It is evident that in this case, all data falls within these bounds. Notably, there were no failures in these simulations, as reported in Table 6.2; all 81,000 cases were completed successfully. For comparison, Figure 6.4 shows the difference in maneuver time and control effort between the NMPC and MT-OCP simulations. It can be seen that the vast majority of NMPC simulations exhibited longer maneuver times, and larger control effort.

In Section 5.1.1 two sample cases were selected to show an example of the minimum time trajectories. The same two cases were selected again to show the corresponding NMPC trajectories. Figure 6.5 shows the state and control trajectories for the two samples when the chief rotation rate is $\Omega = 0\ deg/s$. Figures 6.6 and 6.7, show the sample trajectories for the

cases with chief rotation rate $\Omega = 2\ deg/s$ and $\Omega = 4\ deg/s$, respectively. Recall that in the minimum time trajectories, in Figures 5.4 - 5.6, the control inputs that were not bang-bang exhibited oscillatory behavior. As a feedback controller, the NMPC control history does not exhibit this behavior. Also, it is evident in Figure 6.6 and 6.7, the translational forces converge to the non-zero values required to maintain the rendezvous condition.

Analysis of Relative Attitude Closed-Loop Backward Reachability

The rotational closed-loop reachability was investigated by repeating the analysis in Section 5.1.2 using the NMPC algorithm (8,000 test points with chief rotation rates of $\Omega = 0,\ 2,$ and 4, degrees per second; total of 24,000 runs). Figure 6.8 shows the NMPC maneuver time surfaces, projected on a sphere representing $\boldsymbol{\sigma}^T\boldsymbol{\sigma} = 0.4$, in comparison to the minimum time surfaces in Figure 5.7. Figure 6.9 shows the comparison of the surfaces projected on a sphere representing $\boldsymbol{\sigma}^T\boldsymbol{\sigma} = 0.7$. From these figures, it is clear that the NMPC maneuvers were much longer than the minimum time maneuvers. Also, the NMPC surfaces do not show color variations (i.e., all maneuvers times were similar). This result is not surprising since the minimum time maneuvers also did not show a large spread of minimum times. In fact, in Figure 5.9, it was seen that most minimum times were between 10 and 15 seconds, meaning that the spread is equal to the NMPC sampling time.

Figure 6.10 shows the correlation between the maneuver time and control effort for the 8,000 cases, for each scenario. The histograms confirm that the vast majority of cases have maneuver times of about 100 seconds. The correlation plots show that the control effort for these cases is below the bang-bang line, indicating that the control inputs are not saturated. It is evident that as the chief's rotation rate increases the NMPC control effort increases, while the maneuver times remained about the same. In comparison to the minimum time solutions, the NMPC solutions for these cases exhibited longer maneuver times but smaller control effort. As reported in Table 6.2, no failures were encountered during these simulations. For comparison, Figure 6.11 shows the difference in maneuver time and control effort between the NMPC and MT-OCP simulations. It can be seen that at lower chief rotation rates the NMPC simulations exhibited longer maneuver times and lower control effort. At a higher chief rotation rate, however, some of the NMPC cases showed higher control effort as well as maneuver time.

In Section 5.1.2 two sample cases were selected to show an example of the minimum time

trajectories. The same two cases were selected again to show the corresponding NMPC trajectories. Figure 6.12 shows the state and control trajectories for the two samples when the chief rotation rate is $\Omega = 0\ deg/s$. Figures 6.13 and 6.14, show the sample trajectories for the cases with chief rotation rate $\Omega = 2\ deg/s$ and $\Omega = 4\ deg/s$, respectively. The sample trajectories show that a constant force is required in the x direction in order to maintain the rendezvous position; a result that was analytically shown in Section 4.3.1. Unlike the minimum time attitude trajectories for the second sample case seen in Figure 5.10 - Figure 5.12, the NMPC trajectories for these cases do not encounter singularities in the MRP trajectories.

Table 6.2. Case failures during 6-DOF closed-loop reachability analysis.

Subspace (Slice)	Chief Rotation Rate, deg/s	Number of Cases	% failed
Position; NMC velocity	0	27000	0
Position; NMC velocity	2	27000	0
Position; NMC velocity	4	27000	0
Attitude; zero ang. velocity	0	8000	0
Attitude; zero ang. velocity	2	8000	0
Attitude; zero ang. velocity	4	8000	0

The above results demonstrated that the 6-DOF NMPC algorithm can successfully reach the desired rendezvous condition. Although, from a theoretical perspective, recursive feasibility of the NMPC algorithm cannot be guaranteed, the fact that no failures were encountered in these cases is a significant demonstration of the algorithm's robustness to different initial conditions.

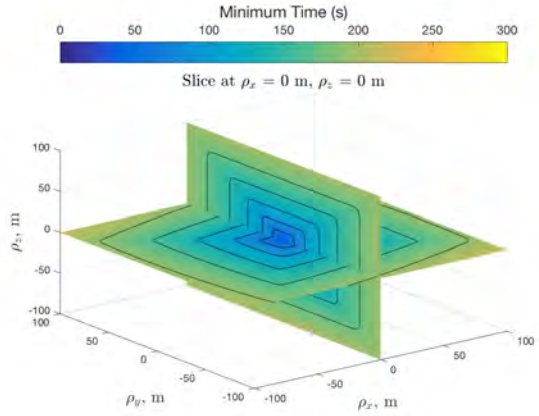

(a) $\Omega = 0\ deg/s$ (MT-OCP)

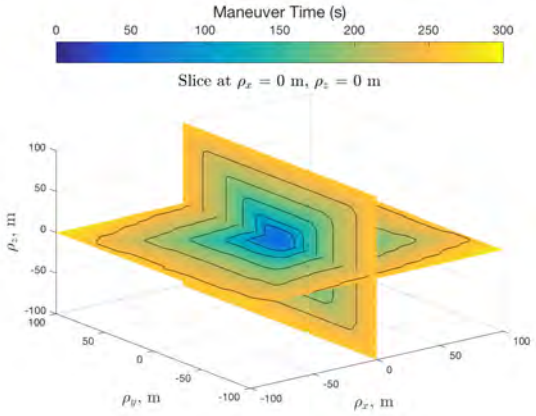

(b) $\Omega = 0\ deg/s$ (NMPC)

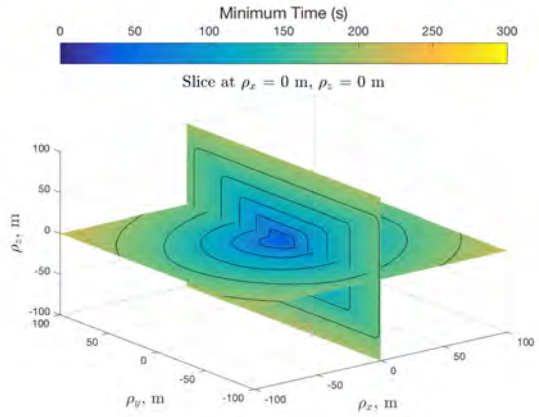

(c) $\Omega = 2\ deg/s$ (MT-OCP)

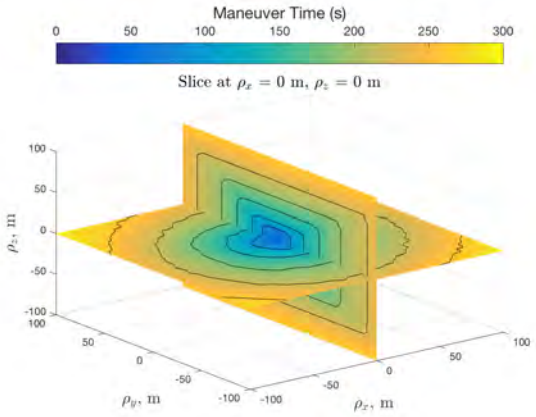

(d) $\Omega = 2\ deg/s$ (NMPC)

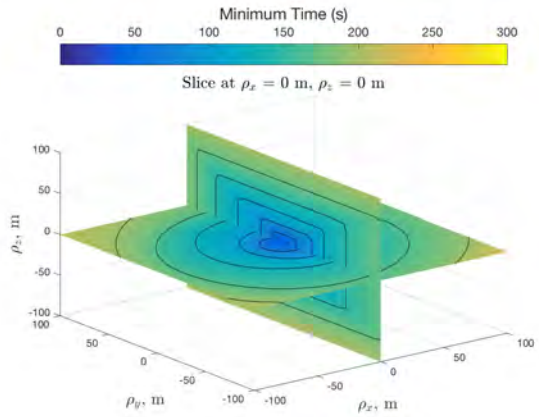

(e) $\Omega = 4\ deg/s$ (MT-OCP)

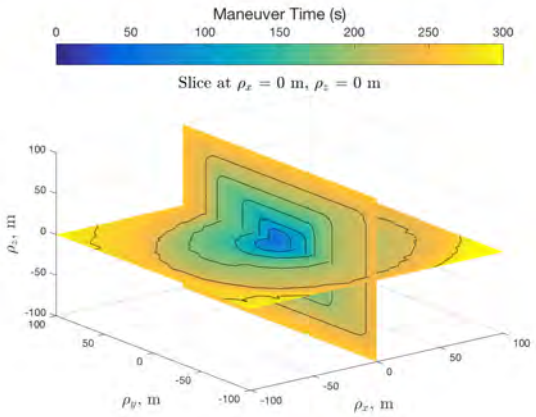

(f) $\Omega = 4\ deg/s$ (NMPC)

Figure 6.1. Relative position closed-loop backward T-reachable sets compared to traditional backward T-reachable sets.

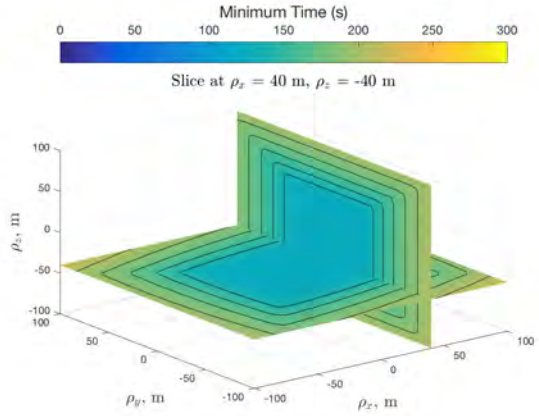

(a) $\Omega = 0\ deg/s$ (MT-OCP)

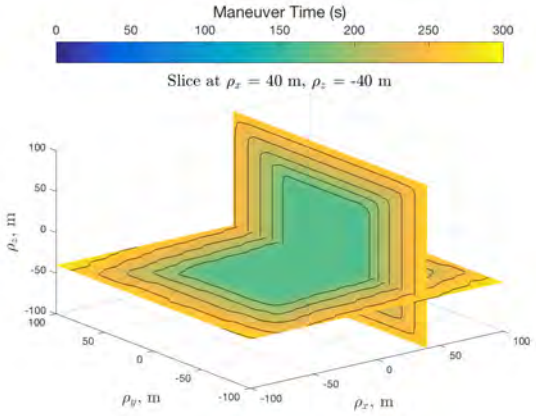

(b) $\Omega = 0\ deg/s$ (NMPC)

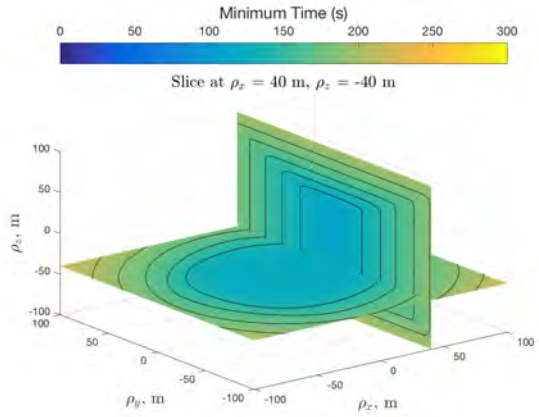

(c) $\Omega = 2\ deg/s$ (MT-OCP)

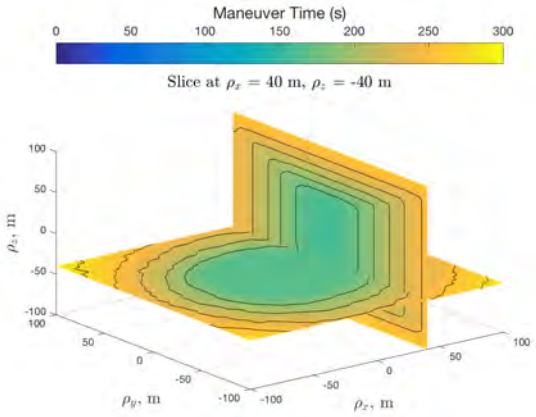

(d) $\Omega = 2\ deg/s$ (NMPC)

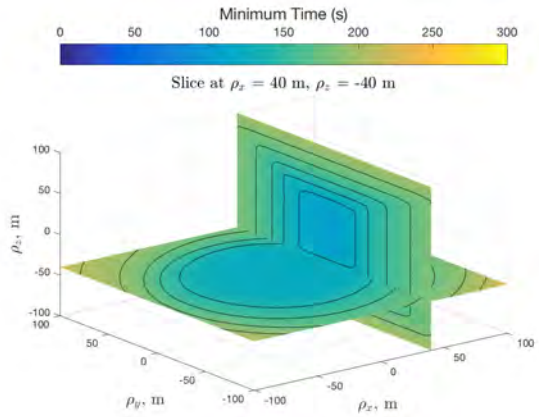

(e) $\Omega = 4\ deg/s$ (MT-OCP)

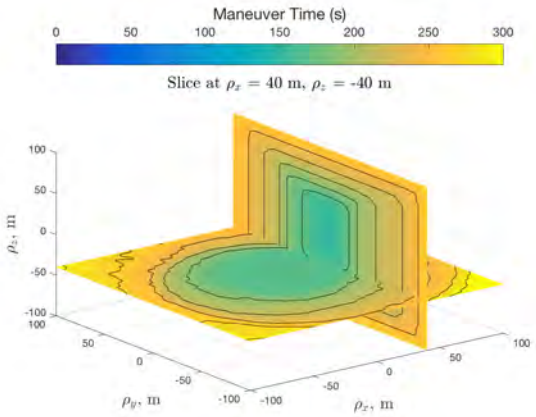

(f) $\Omega = 4\ deg/s$ (NMPC)

Figure 6.2. Relative position closed-loop backward T-reachable sets compared to traditional backward T-reachable sets.

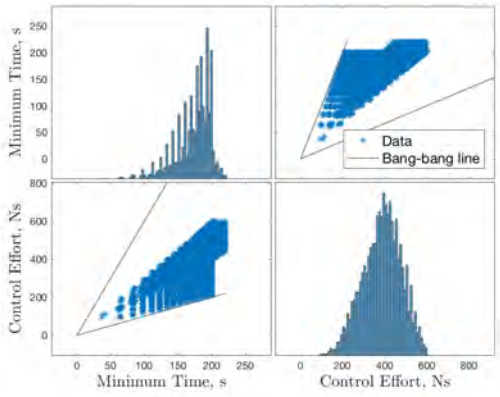

(a) $\Omega = 0\ deg/s$ (MT-OCP)

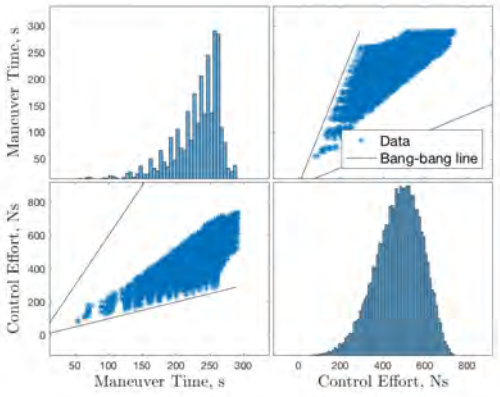

(b) $\Omega = 0\ deg/s$ (NMPC)

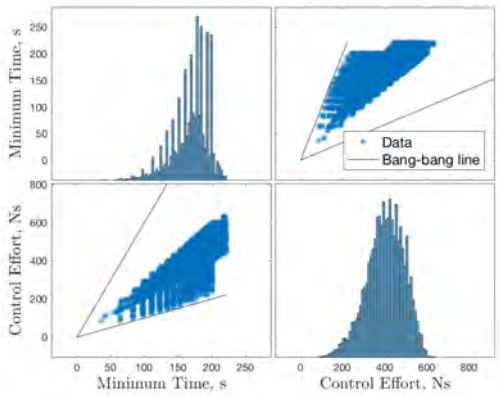

(c) $\Omega = 2\ deg/s$ (MT-OCP)

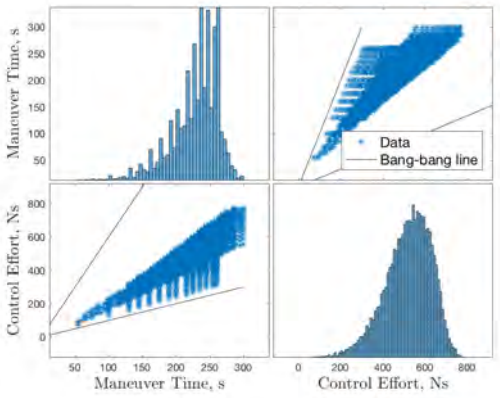

(d) $\Omega = 2\ deg/s$ (NMPC)

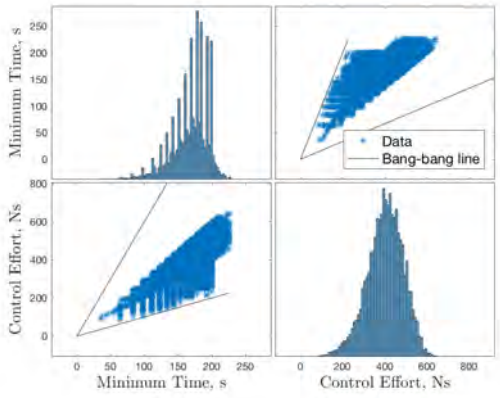

(e) $\Omega = 4\ deg/s$ (MT-OCP)

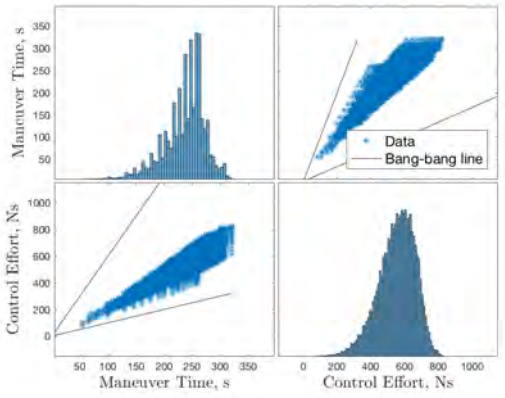

(f) $\Omega = 4\ deg/s$ (NMPC)

Figure 6.3. NMPC maneuver time and control effort histograms and correlation for position (NMC velocity, aligned attitude) subspace.

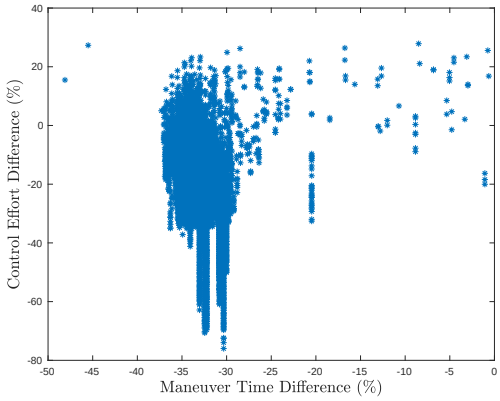

(a) $\Omega = 0\ deg/s$)

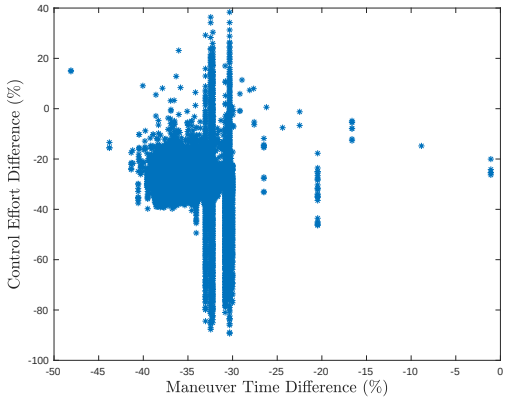

(b) $\Omega = 2\ deg/s$)

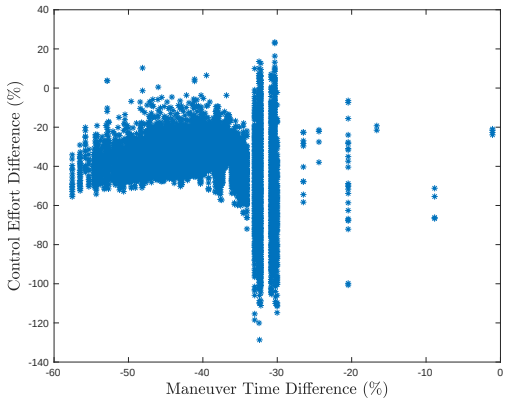

(c) $\Omega = 4\ deg/s$)

Figure 6.4. Comparison of NMPC and MT-OCP maneuver time and control effort results for position (NMC velocity, aligned attitude) subspace.

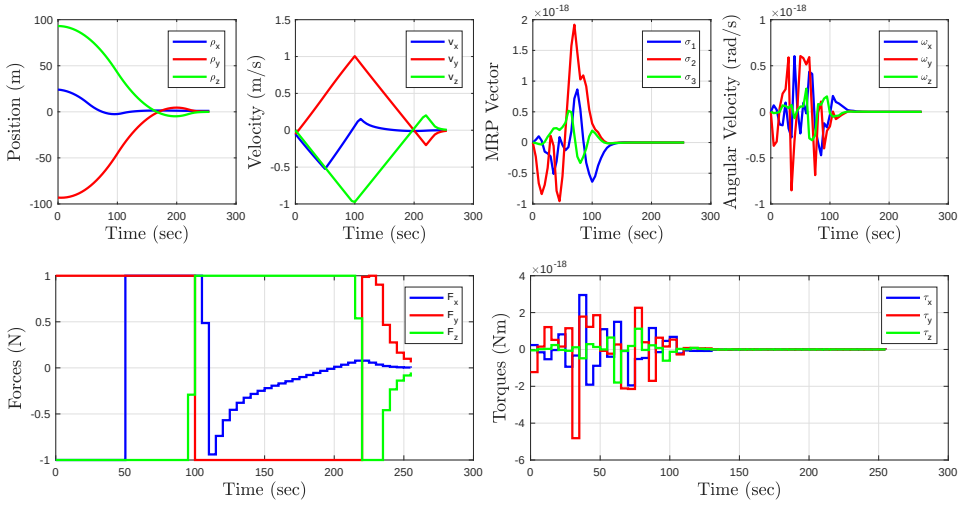

(a) Sample Case #1, $\Omega = 0\ deg/s$

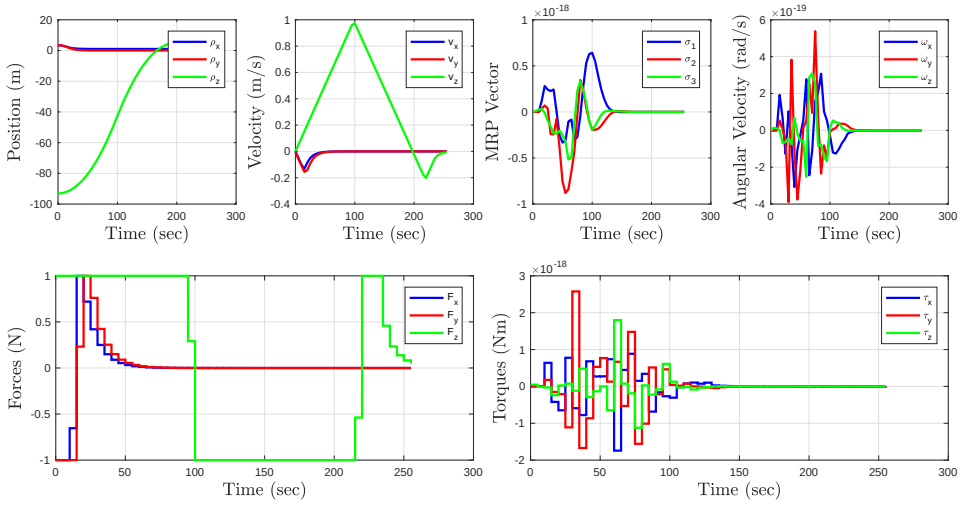

(b) Sample Case #2, $\Omega = 0\ deg/s$

Figure 6.5. Sample NMPC closed-loop cases from position (NMC velocity, aligned attitude) for $\Omega = 0\ deg/s$.

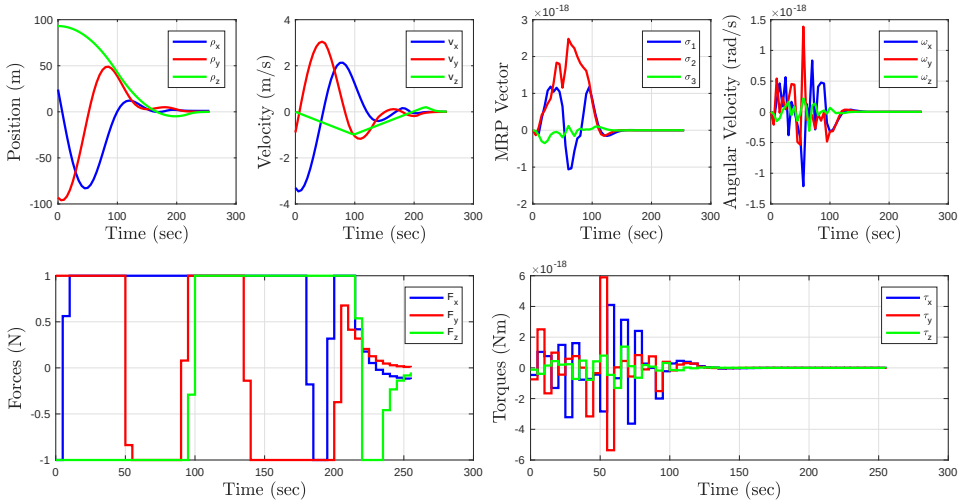

(a) Sample Case #1, $\Omega = 2\ deg/s$

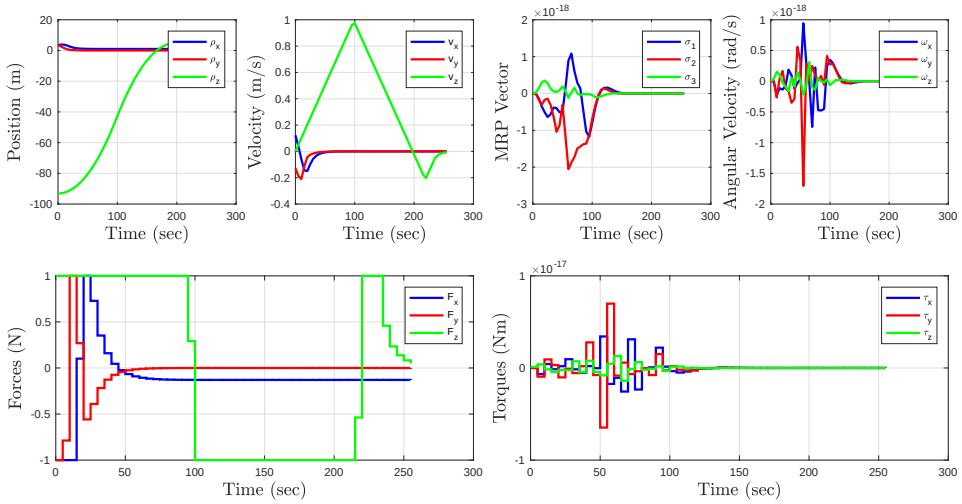

(b) Sample Case #2, $\Omega = 2\ deg/s$

Figure 6.6. Sample NMPC closed-loop cases from position (NMC velocity, aligned attitude) for $\Omega = 2\ deg/s$.

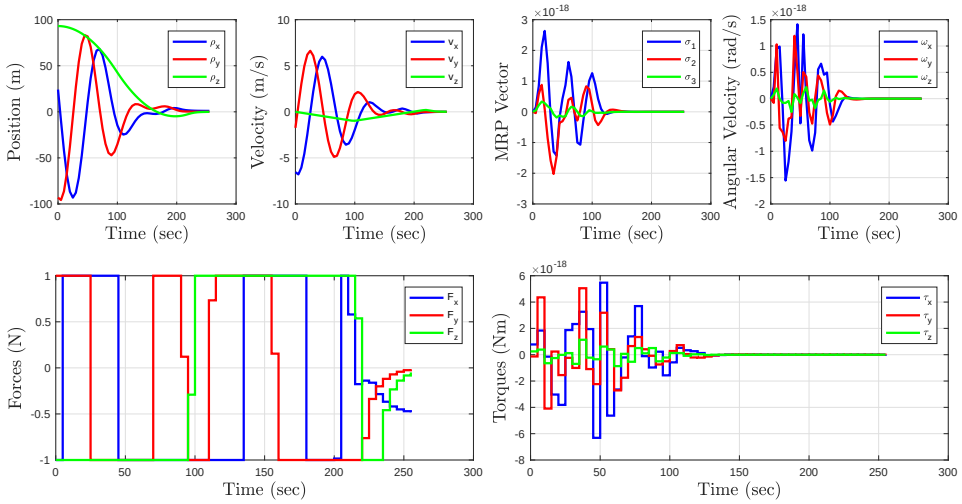

(a) Sample Case #1, $\Omega = 4\ deg/s$

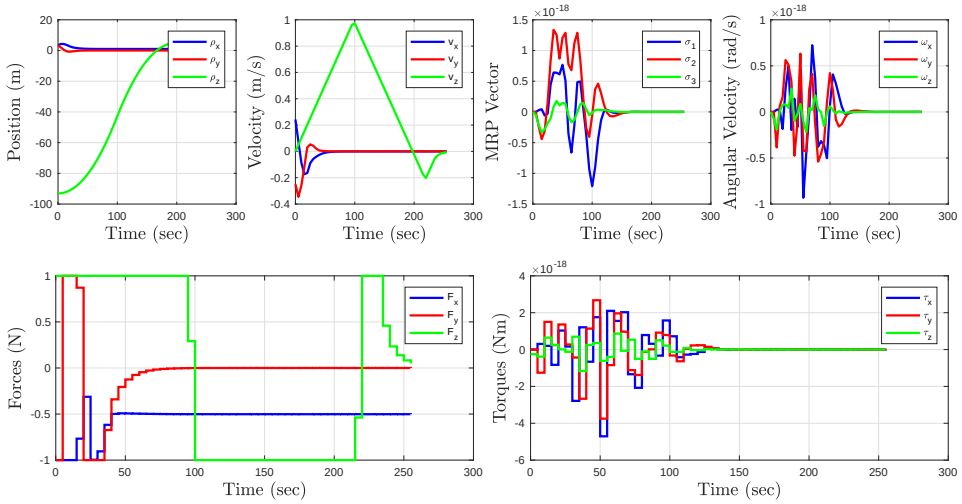

(b) Sample Case #2, $\Omega = 4\ deg/s$

Figure 6.7. Sample NMPC closed-loop cases from position (NMC velocity, aligned attitude) for $\Omega = 4\ deg/s$.

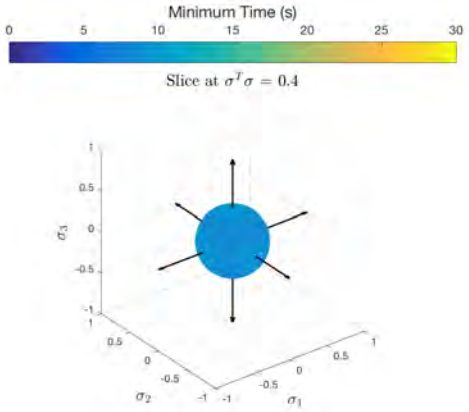

(a) $\Omega = 0\ deg/s$ (MT-OCP)

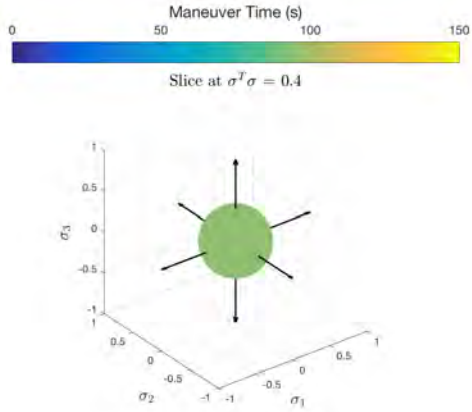

(b) $\Omega = 0\ deg/s$ (NMPC)

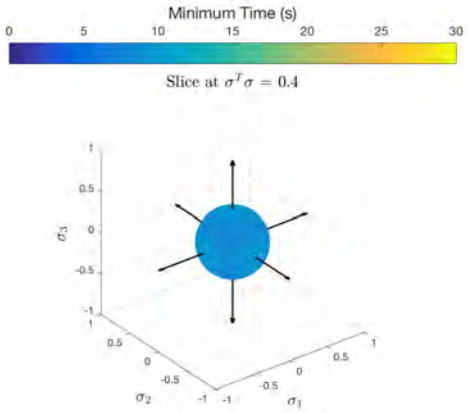

(c) $\Omega = 2\ deg/s$ (MT-OCP)

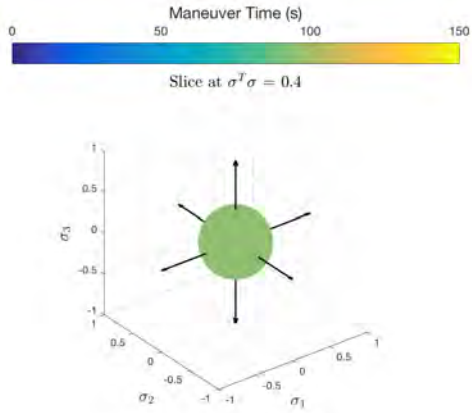

(d) $\Omega = 2\ deg/s$ (NMPC)

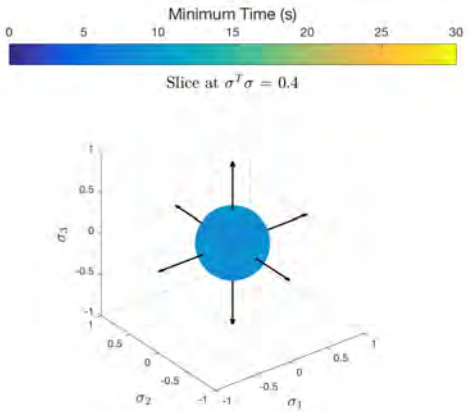

(e) $\Omega = 4\ deg/s$ (MT-OCP)

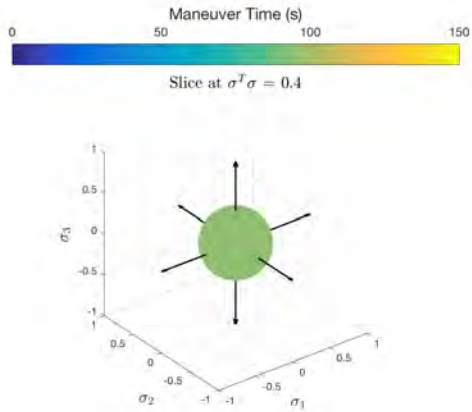

(f) $\Omega = 4\ deg/s$ (NMPC)

Figure 6.8. Relative attitude closed-loop backward T-reachable sets compared to traditional backward T-reachable sets.

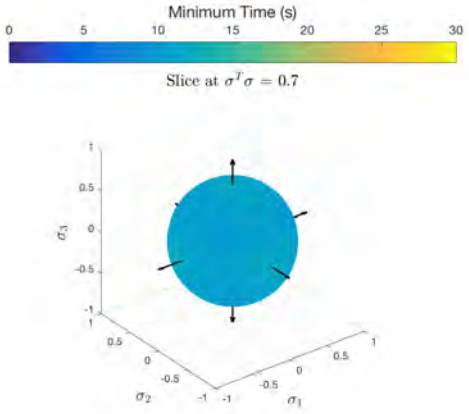

(a) $\Omega = 0\ deg/s$ (MT-OCP)

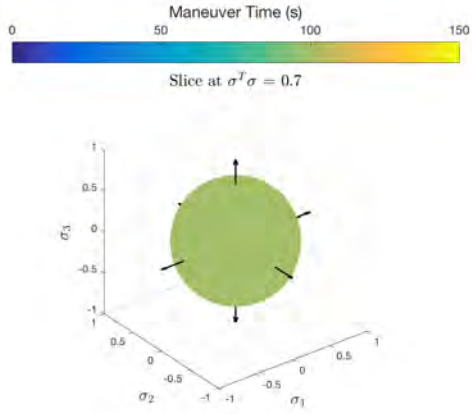

(b) $\Omega = 0\ deg/s$ (NMPC)

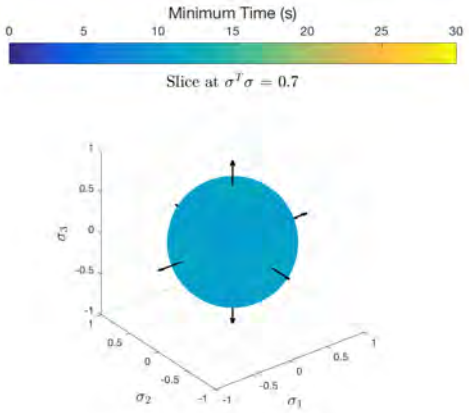

(c) $\Omega = 2\ deg/s$ (MT-OCP)

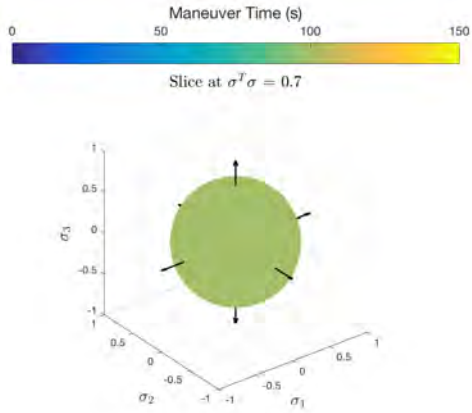

(d) $\Omega = 2\ deg/s$ (NMPC)

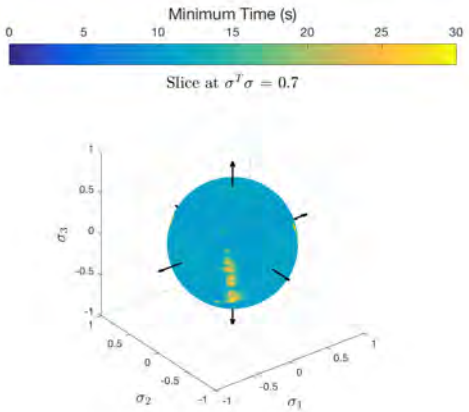

(e) $\Omega = 4\ deg/s$ (MT-OCP)

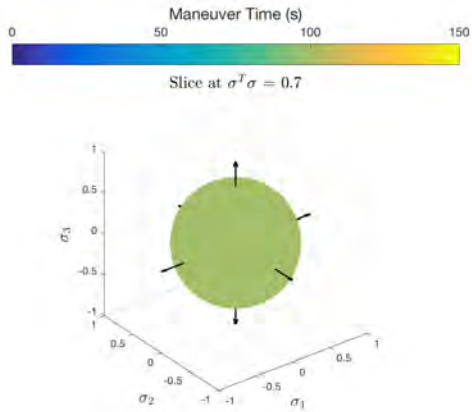

(f) $\Omega = 4\ deg/s$ (NMPC)

Figure 6.9. Relative attitude closed-loop backward T-reachable sets compared to traditional backward T-reachable sets.

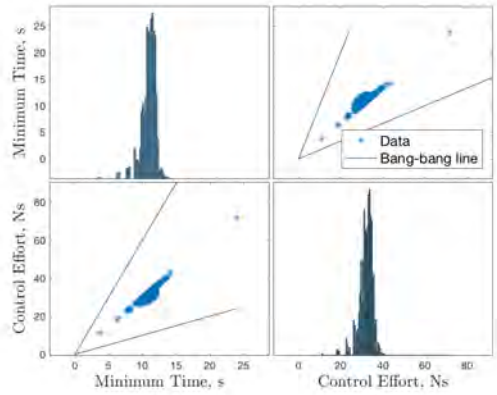

(a) $\Omega = 0\ deg/s$ (MT-OCP)

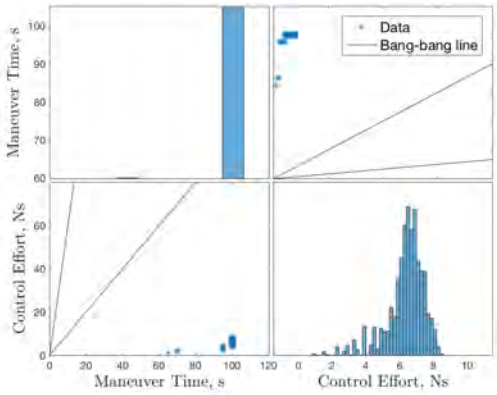

(b) $\Omega = 0\ deg/s$ (NMPC)

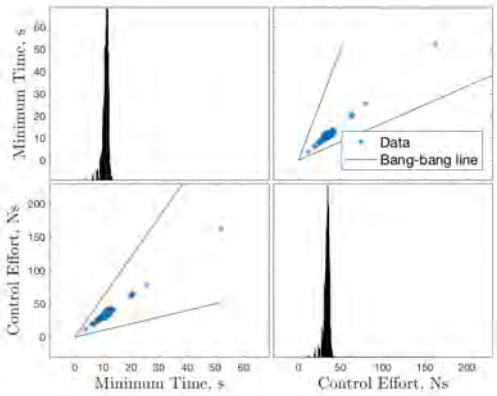

(c) $\Omega = 2\ deg/s$ (MT-OCP)

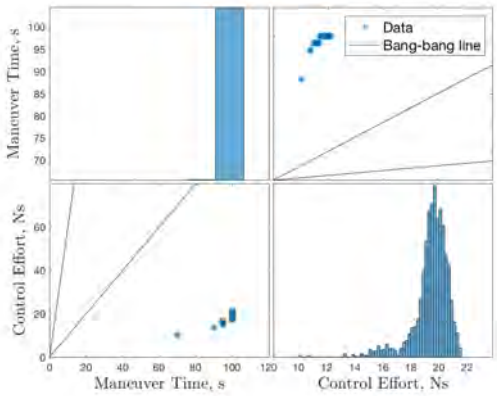

(d) $\Omega = 2\ deg/s$ (NMPC)

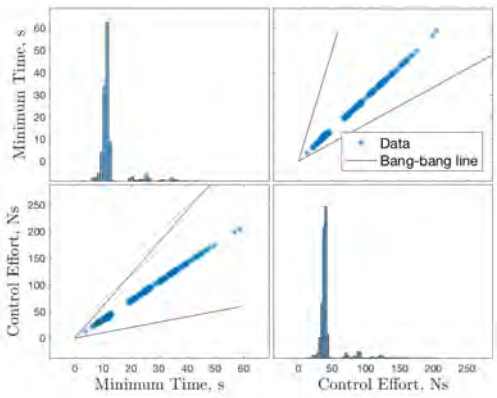

(e) $\Omega = 4\ deg/s$ (MT-OCP)

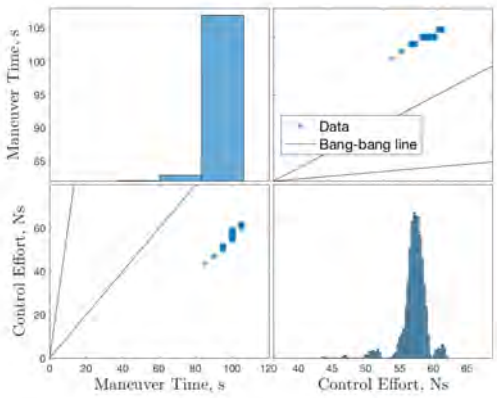

(f) $\Omega = 4\ deg/s$ (NMPC)

Figure 6.10. NMPC maneuver time and control effort histograms and correlation for attitude (zero angular velocity, rendezvous position) subspace.

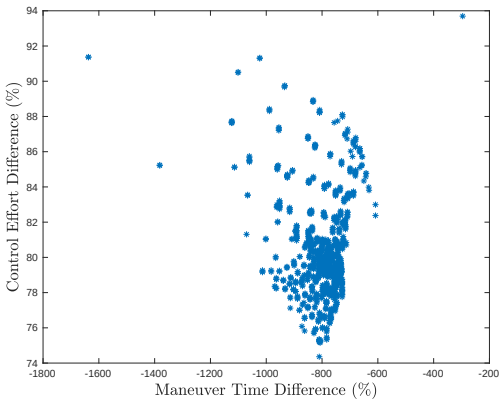

(a) $\Omega = 0\ deg/s$)

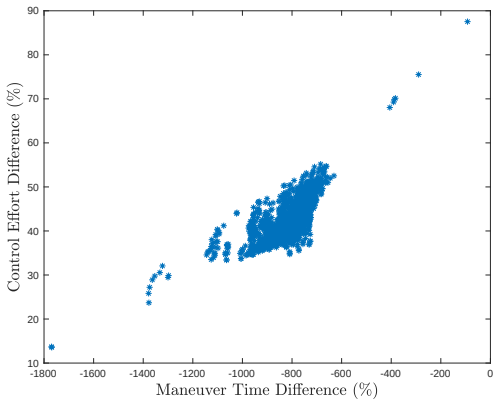

(b) $\Omega = 2\ deg/s$)

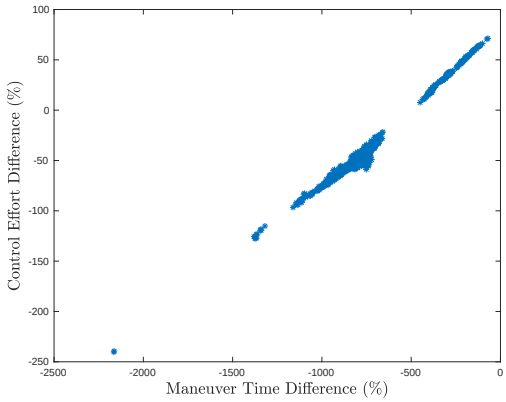

(c) $\Omega = 4\ deg/s$)

Figure 6.11. Comparison of NMPC and MT-OCP maneuver time and control effort results for attitude (zero angular velocity, rendezvous position) subspace.

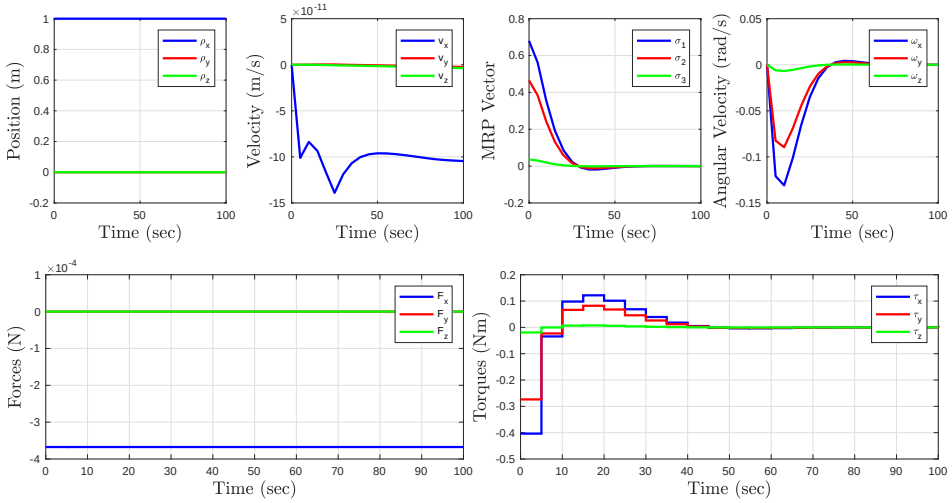

(a) Sample Case #1, $\Omega = 0\ deg/s$

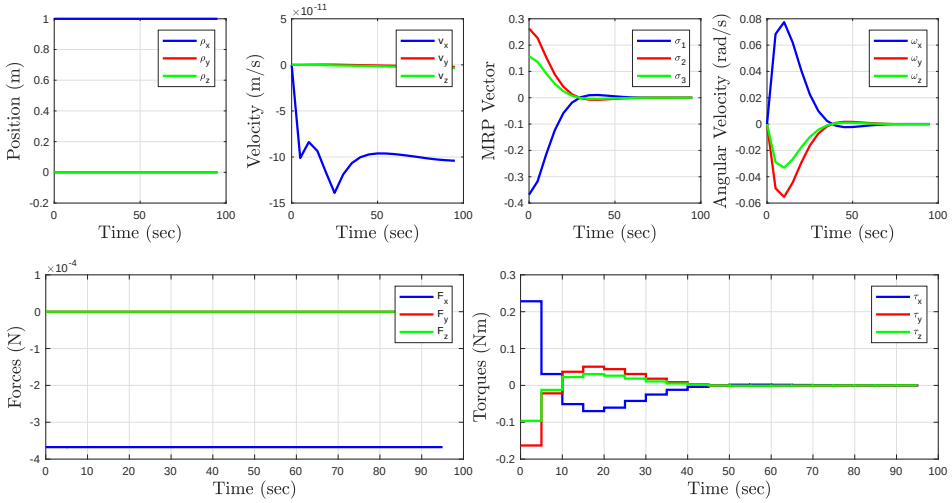

(b) Sample Case #2, $\Omega = 0\ deg/s$

Figure 6.12. Sample NMPC closed-loop cases from attitude (zero angular velocity, rendezvous position) for $\Omega = 0\ deg/s$.

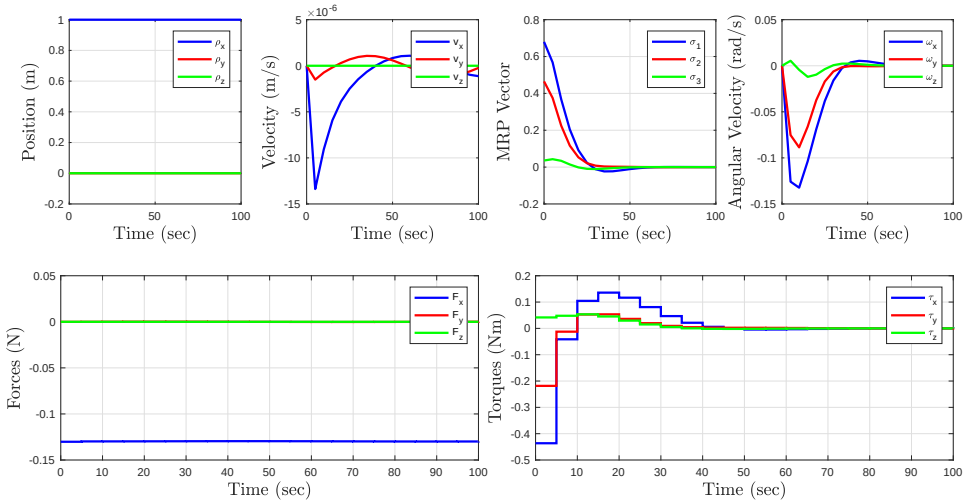

(a) Sample Case #1, $\Omega = 2\ deg/s$

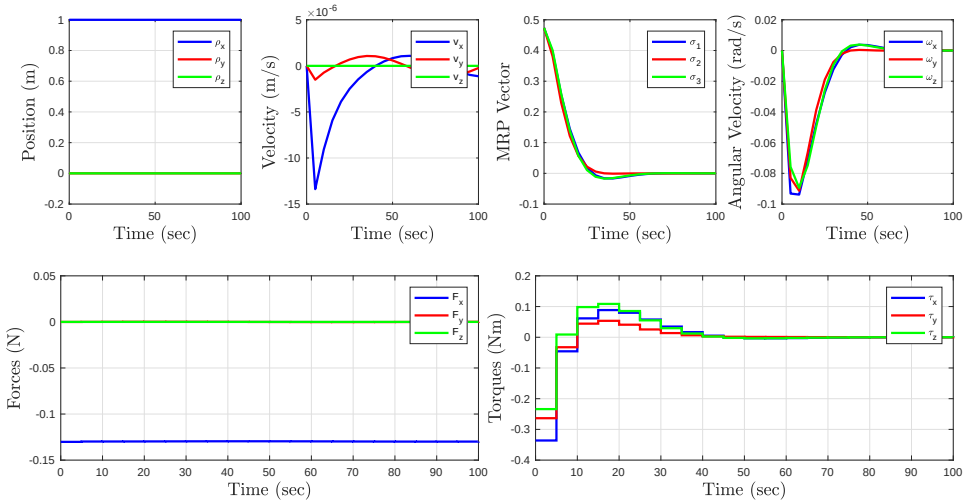

(b) Sample Case #2, $\Omega = 2\ deg/s$

Figure 6.13. Sample NMPC closed-loop cases from attitude (zero angular velocity, rendezvous position) for $\Omega = 2\ deg/s$.

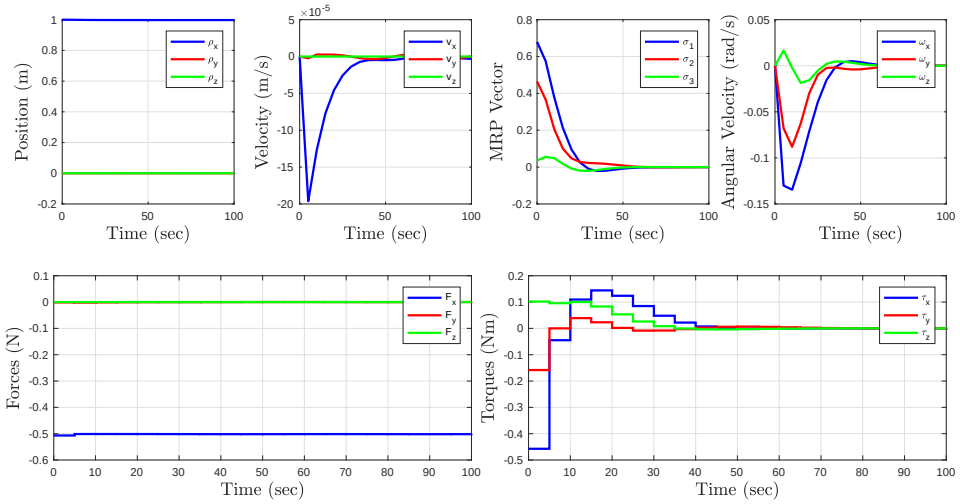

(a) Sample Case #1, $\Omega = 4\ deg/s$

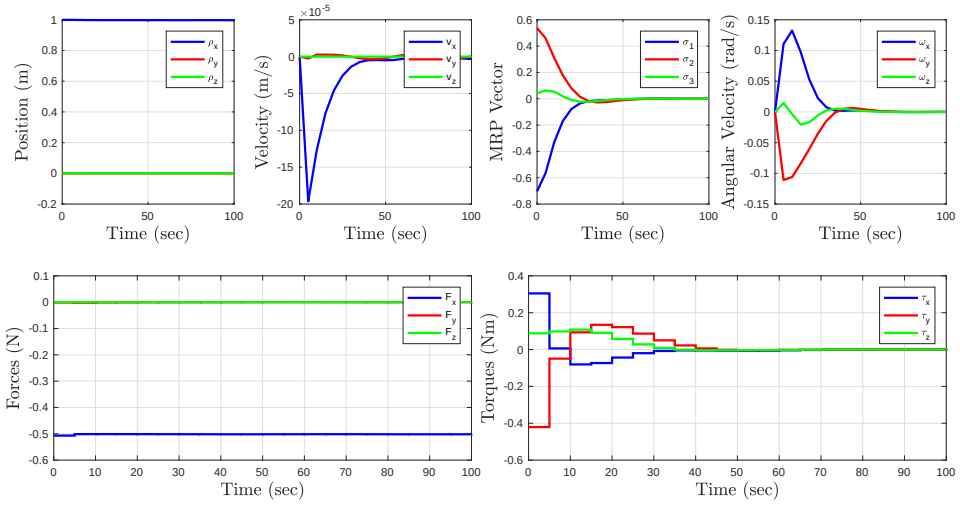

(b) Sample Case #2, $\Omega = 4\ deg/s$

Figure 6.14. Sample NMPC closed-loop cases from attitude (zero angular velocity, rendezvous position) for $\Omega = 4\ deg/s$.

6.4.2 6-DOF Rendezvous with Tumbling Chief

The tumbling chief scenario was considered next, as defined in Table 5.5.

Analysis of Relative Position Closed-Loop Backward Reachability

The translational closed-loop reachability was investigated by repeating the analysis in Section 5.2.1 using the NMPC algorithm (27,000 test points with chief tumble rates of $\boldsymbol{\omega}_{\mathsf{C/L}} = [0, 0, 0]^T$ and $\boldsymbol{\omega}_{\mathsf{C/L}} = [-2, 1, 1]^T$ degrees per second; total of 54,000 runs). Figure 6.15 shows the resulting NMPC contours, at values of $\rho_x = 0\,m$ and $\rho_z = 0\,m$, compared to the minimum time contours presented in Figure 5.13. Figure 6.16 shows the comparison at values of $\rho_x = 40\ m$ and $\rho_z = -40\ m$. As the results in the planar rotation scenario showed, the NMPC contours in Figure 6.15b and 6.15d have a very similar shape to the minimum time contours, but are not as smooth. The closed-loop sets show larger maneuver times, as expected.

Figure 6.17 shows the correlation between the maneuver time and control effort for the 27,000 cases, for each scenario. It can be seen that when the chief is tumbling these maneuvers require more control effort. The histograms and correlation plots show very similar trends to what was observed in the minimum time cases. As with the previous scenario, no failures were encountered in these cases, as reported in Table 6.3. For comparison, Figure 6.18 shows the difference in maneuver time and control effort between the NMPC and MT-OCP simulations. It can be seen that the vast majority of NMPC simulations exhibited longer maneuver times, and larger control effort.

Two sample cases were selected to show an example of the NMPC trajectories. Figure 6.19 shows the state and control trajectories for the two samples when the chief is not tumbling, and Figure 6.20 shows the same trajectories with a tumbling chief. It is evident that the translational control inputs with the tumbling chief are more aggressive, similar to bang-bang behavior, resulting in higher control effort.

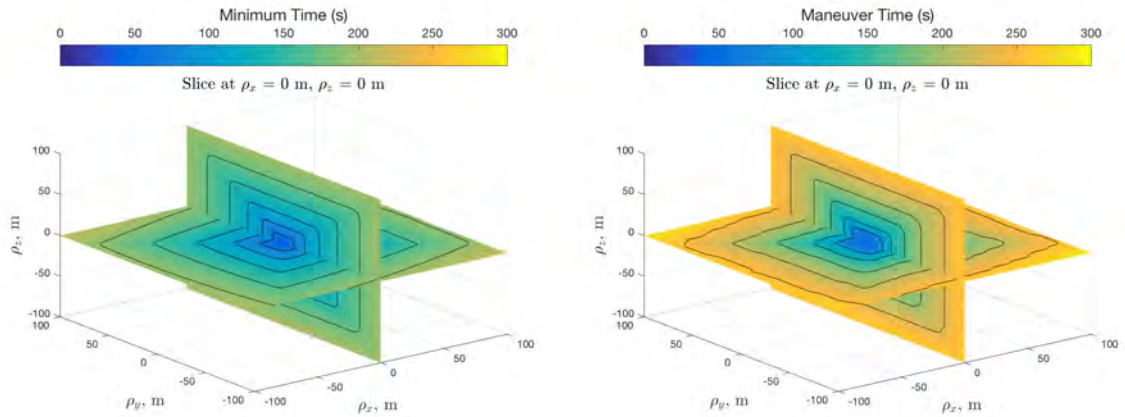

(a) Chief not tumbling (MT-OCP)

(b) Chief not tumbling (NMPC)

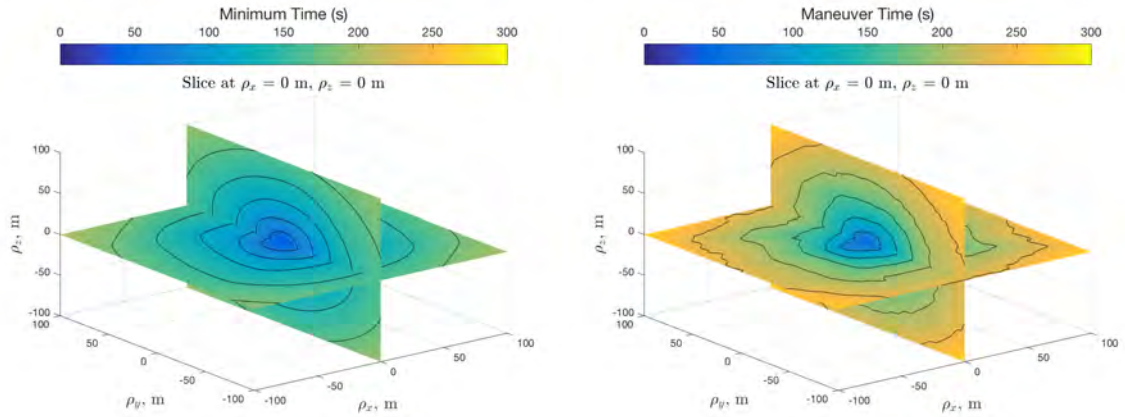

(c) Chief tumbling (MT-OCP)

(d) Chief tumbling (NMPC)

Figure 6.15. Relative position closed-loop backward T-reachable sets compared to traditional backward T-reachable sets.

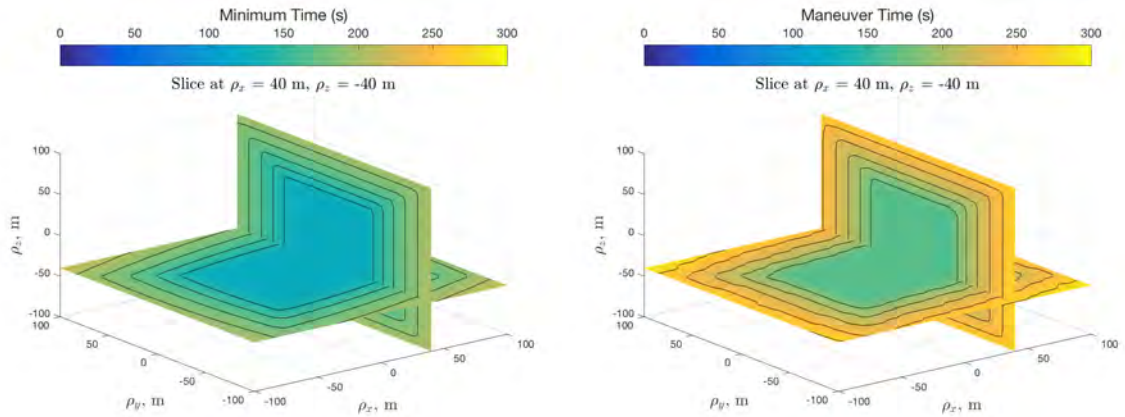

(a) Chief not tumbling (MT-OCP)

(b) Chief not tumbling (NMPC)

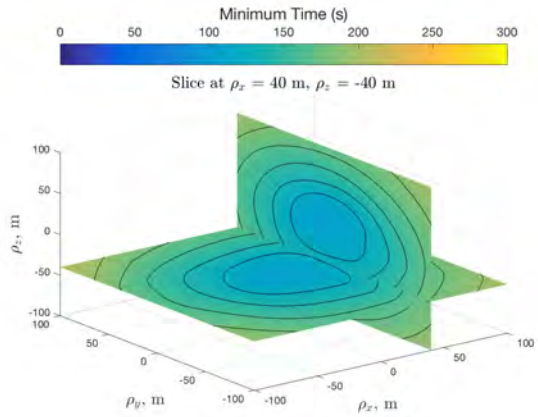

(c) Chief tumbling (MT-OCP)

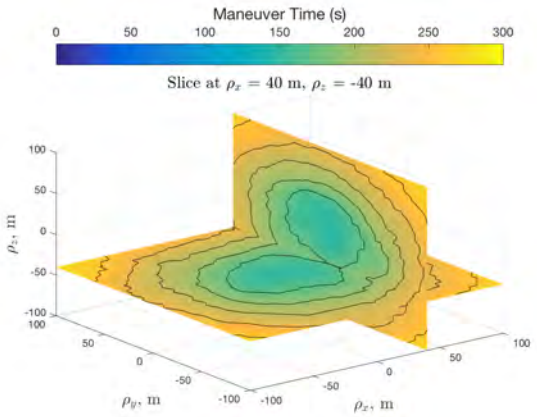

(d) Chief tumbling (NMPC)

Figure 6.16. Relative position closed-loop backward T-reachable sets compared to traditional backward T-reachable sets.

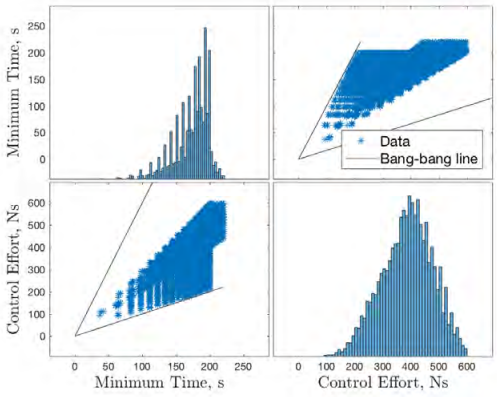

(a) Chief not tumbling (MT-OCP)

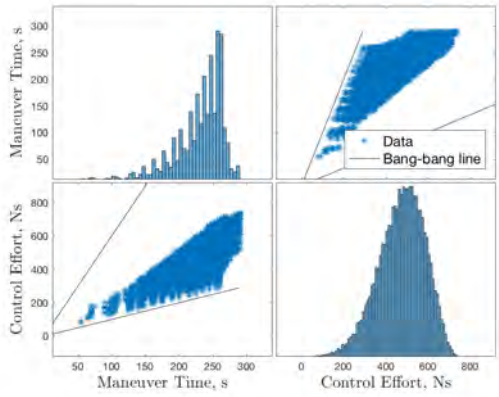

(b) Chief not tumbling (NMPC)

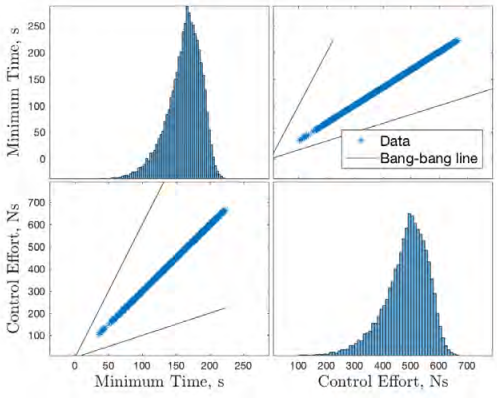

(c) Chief tumbling (MT-OCP)

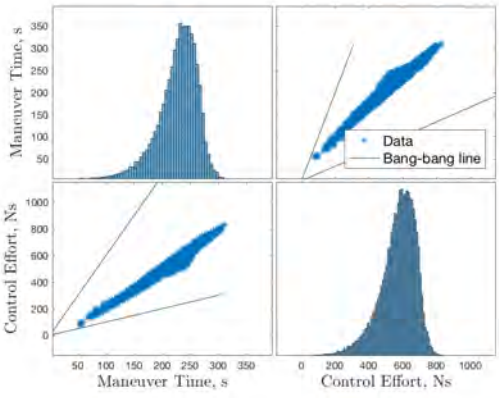

(d) Chief tumbling (NMPC)

Figure 6.17. NMPC maneuver time and control effort histograms and correlation for position (NMC velocity, aligned attitude) subspace.

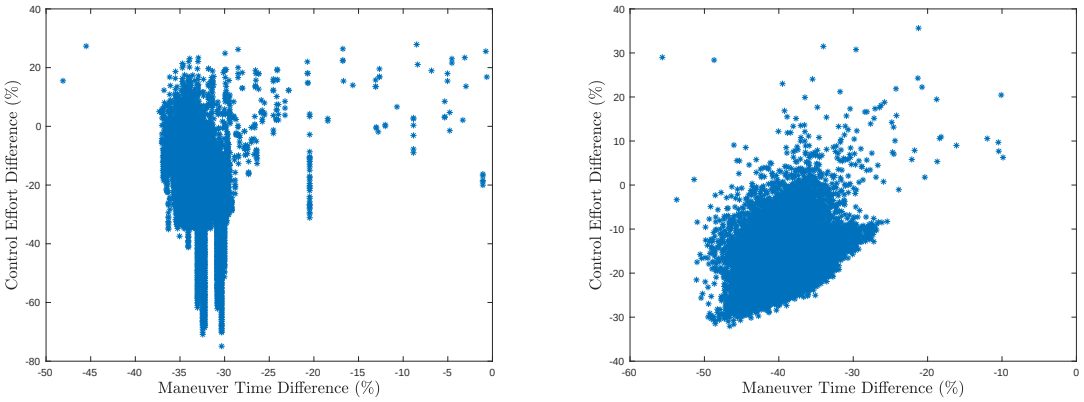

(a) Chief not tumbling

(b) Chief tumbling

Figure 6.18. Comparison of NMPC and MT-OCP maneuver time and control effort results for position (NMC velocity, aligned attitude) subspace.

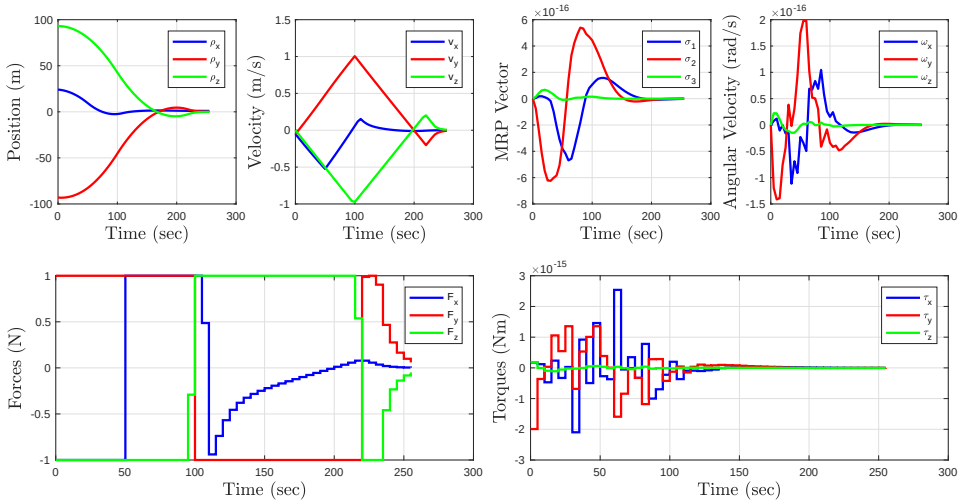

(a) Sample Case #1, Chief not tumbling

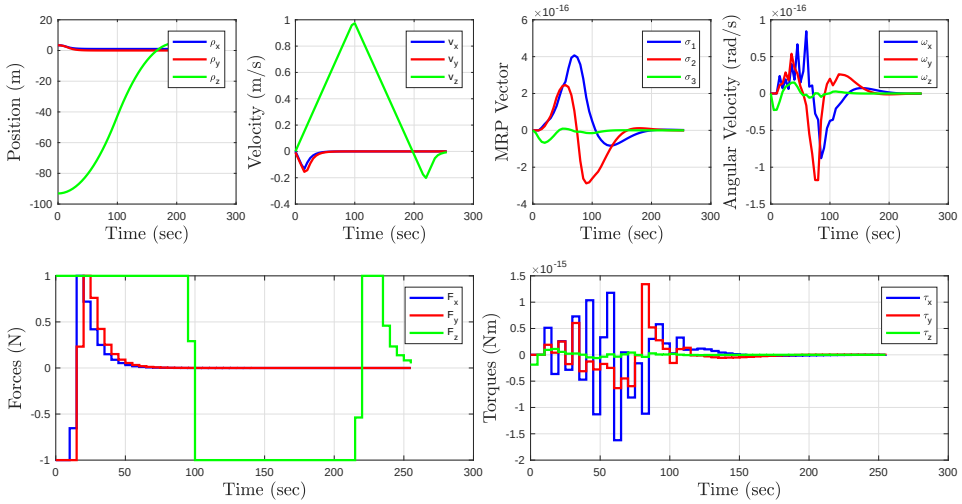

(b) Sample Case #2, Chief not tumbling

Figure 6.19. Sample NMPC closed-loop cases from position (NMC velocity, aligned attitude) with non-tumbling chief.

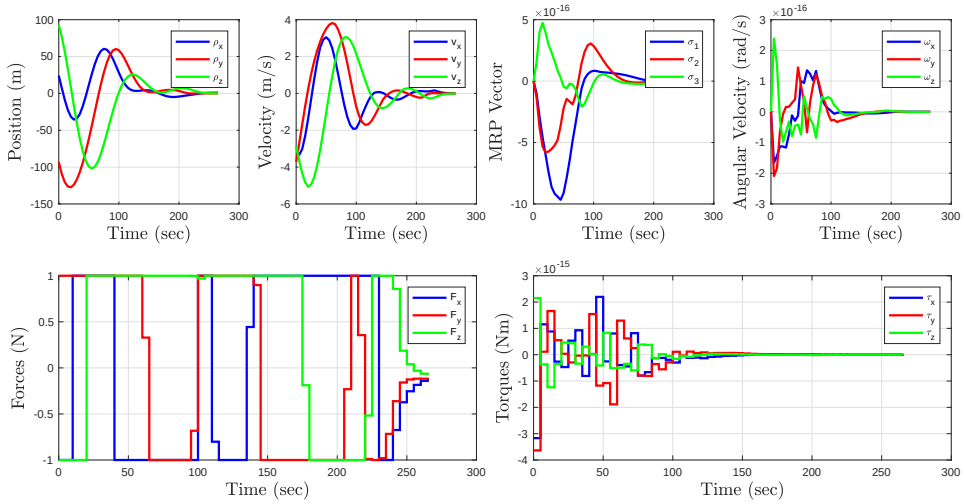

(a) Sample Case #1, Chief tumbling

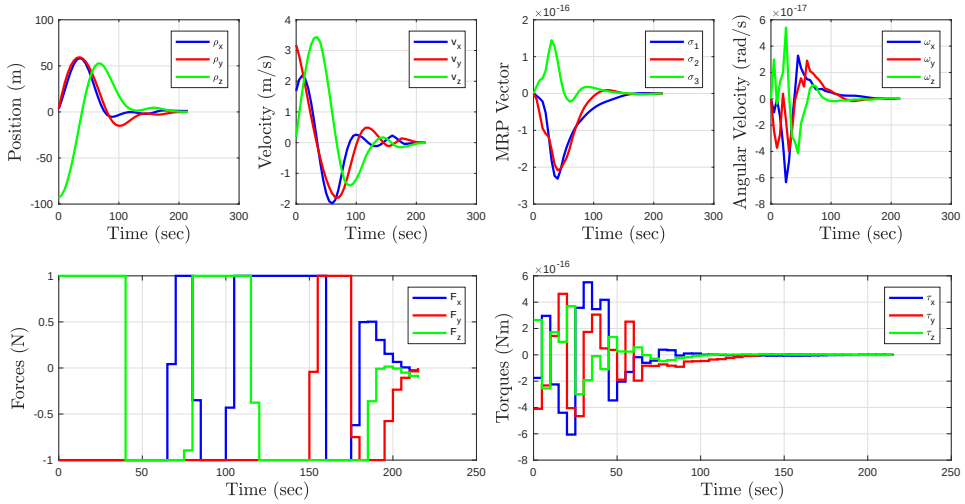

(b) Sample Case #2, Chief tumbling

Figure 6.20. Sample NMPC closed-loop cases from position (NMC velocity, aligned attitude) with tumbling chief.

Analysis of Relative Attitude Closed-Loop Backward Reachability

The rotational closed-loop reachability was investigated by repeating the analysis in Section 5.2.2 using the NMPC algorithm (8,000 test points with chief tumble rates of $\boldsymbol{\omega}_{\mathsf{C/L}} = [0, 0, 0]^T$ and $\boldsymbol{\omega}_{\mathsf{C/L}} = [-2, 1, 1]^T$ degrees per second; total of 16,000 runs). Figure 6.21 shows the NMPC maneuver time surfaces, projected on a sphere representing $\boldsymbol{\sigma}^T\boldsymbol{\sigma} = 0.4$, in comparison to the minimum time surfaces in Figure 5.17. Figure 6.22 shows the comparison of the surfaces projected on a sphere representing $\boldsymbol{\sigma}^T\boldsymbol{\sigma} = 0.7$. From these Figures, it is clear that the NMPC maneuvers are much longer than the minimum time maneuvers. Notably, the singularity areas, seen on the minimum time spheres as bright yellow spots, are not visible on the NMPC spheres.

Figure 6.23 shows the correlation between the maneuver time and control effort for the 8,000 cases, for each scenario. These cases showed a larger spread of maneuver times, as opposed to the planar rotation scenario results shown in Figure 6.10. The correlation plots show that the control effort for these cases is below the bang-bang line, indicating that the control inputs are not saturated. It is also evident that, with the tumbling chief, the control effort is higher than the non-tumbling case, while the spread of maneuver times are pretty similar. In comparison to the minimum time solutions, the NMPC solutions for these cases exhibited longer maneuver times but smaller control effort. As reported in Table 6.3, there were no failures in these cases. For comparison, Figure 6.24 shows the difference in maneuver time and control effort between the NMPC and MT-OCP simulations. It can be seen that for the non-tumbling chief the NMPC simulations exhibited longer maneuver times and lower control effort. With the tumbling chief, however, some of the NMPC cases showed higher control effort as well as maneuver time.

Two sample cases were selected to show an example of the NMPC trajectories. Figure 6.25 shows the state and control trajectories for the two samples when the chief is not tumbling, and Figure 6.26 shows the same trajectories with a tumbling chief. It is clear, in Figure 6.26, that when the chief is tumbling a time-varying translational control input is required to maintain the rendezvous condition. As with the planar rotation sample cases, the NMPC attitude trajectories in Figure 6.25 and Figure 6.26 do not exhibit singularities.

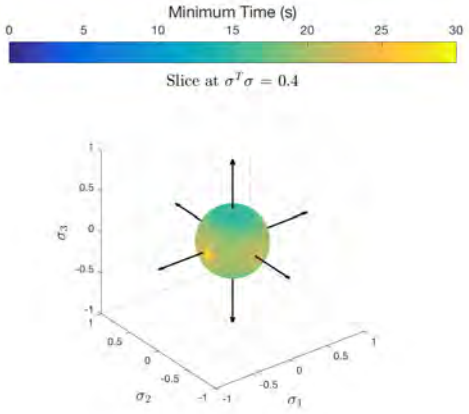

(a) Chief not tumbling (MT-OCP)

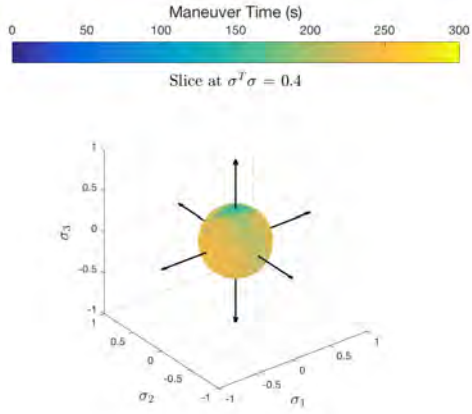

(b) Chief not tumbling (NMPC)

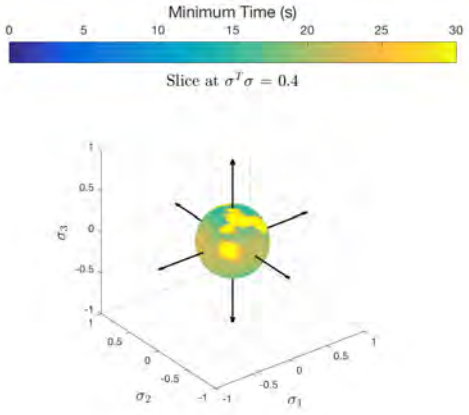

(c) Chief tumbling (MT-OCP)

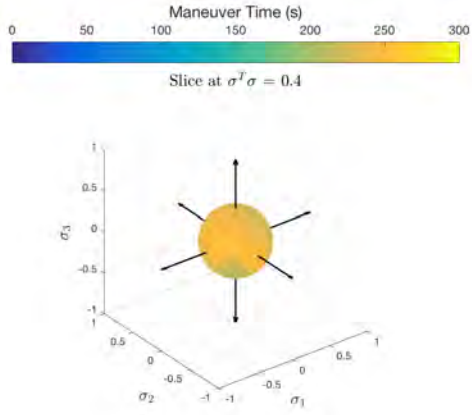

(d) Chief tumbling (NMPC)

Figure 6.21. Relative attitude closed-loop backward T-reachable sets compared to traditional backward T-reachable sets.

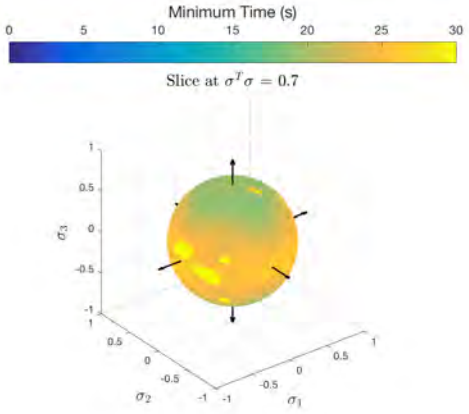

(a) Chief not tumbling (MT-OCP)

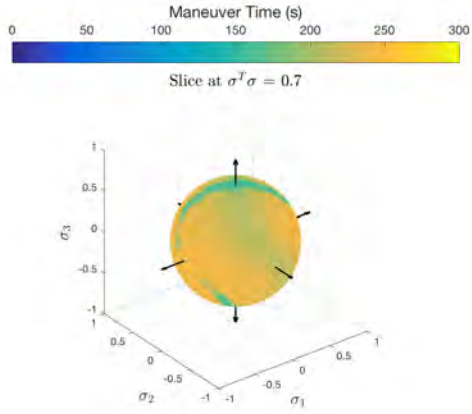

(b) Chief not tumbling (NMPC)

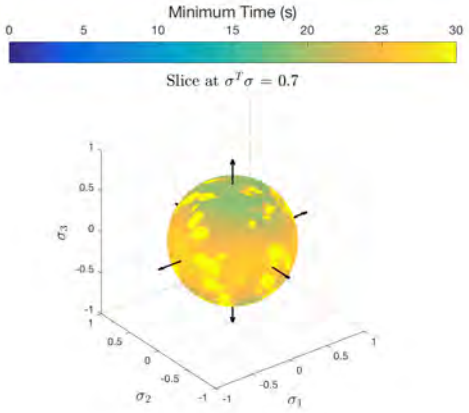

(c) Chief tumbling (MT-OCP)

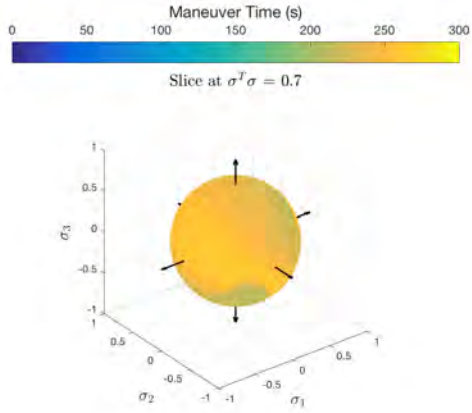

(d) Chief tumbling (NMPC)

Figure 6.22. Relative attitude closed-loop backward T-reachable sets compared to traditional backward T-reachable sets.

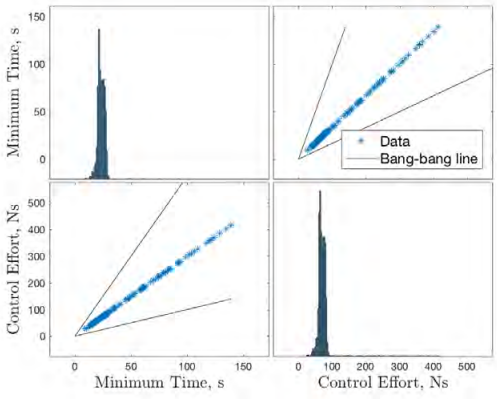

(a) Chief not tumbling (MT-OCP)

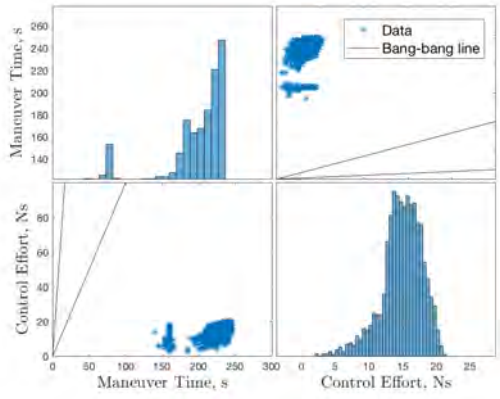

(b) Chief not tumbling (NMPC)

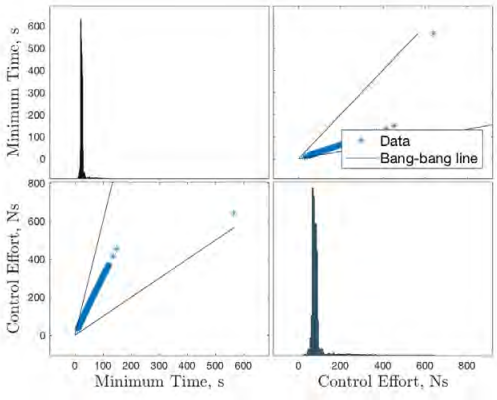

(c) Chief tumbling (MT-OCP)

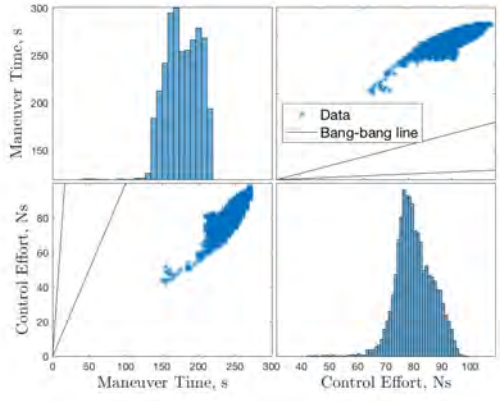

(d) Chief tumbling (NMPC)

Figure 6.23. NMPC maneuver time and control effort histograms and correlation for attitude (zero angular velocity, rendezvous position) subspace.

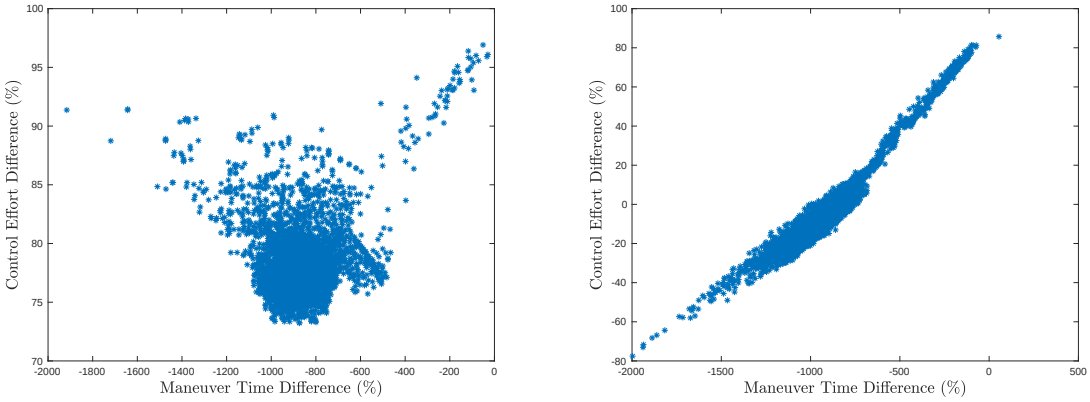

(a) Chief not tumbling

(b) Chief tumbling

Figure 6.24. Comparison of NMPC and MT-OCP maneuver time and control effort results, for attitude (zero angular velocity, rendezvous position) subspace.

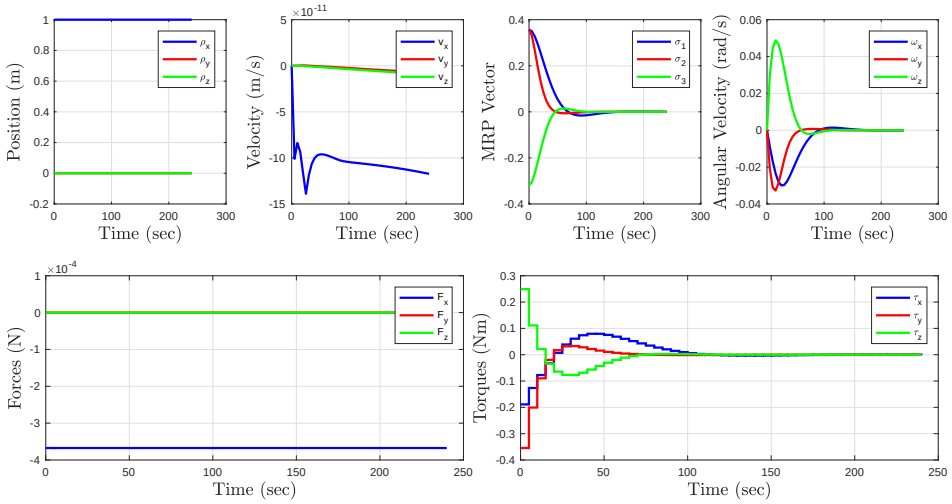

(a) Sample Case #1, Chief not tumbling

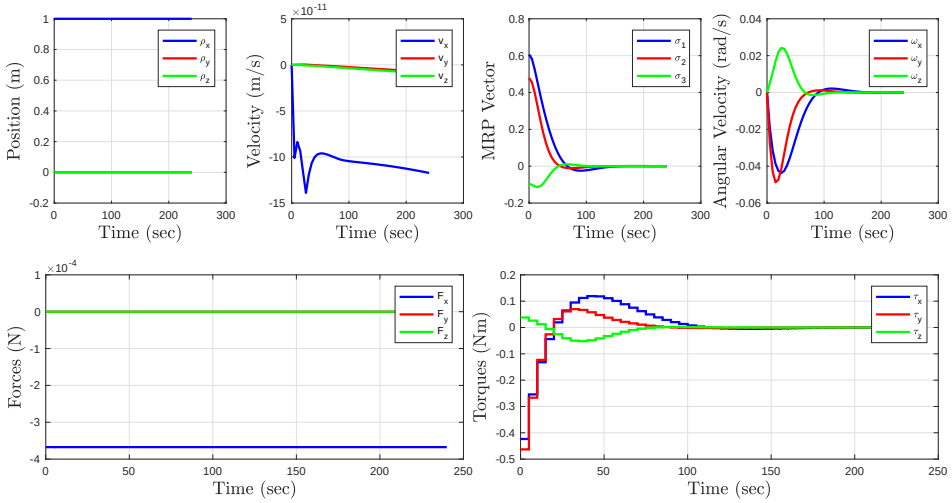

(b) Sample Case #2, Chief not tumbling

Figure 6.25. Sample NMPC closed-loop cases from attitude (zero angular velocity, rendezvous position) with non-tumbling chief.

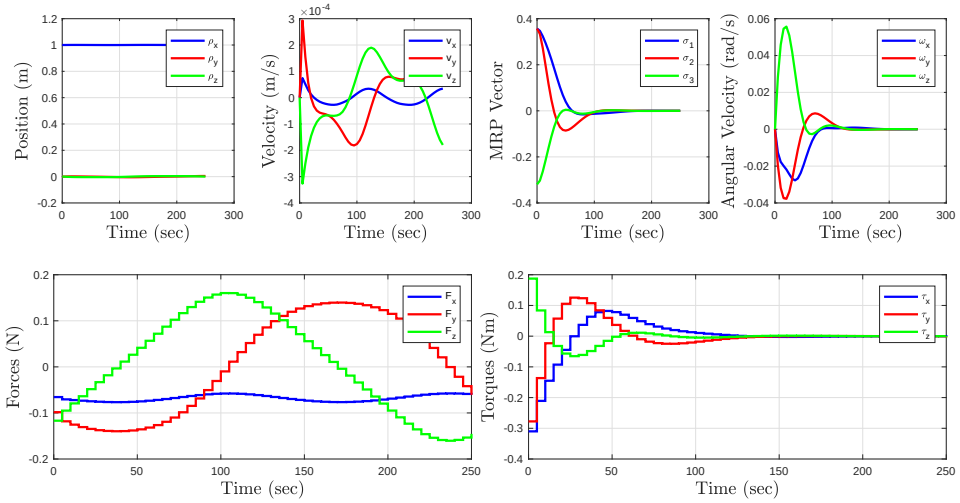

(a) Sample Case #1, Chief tumbling

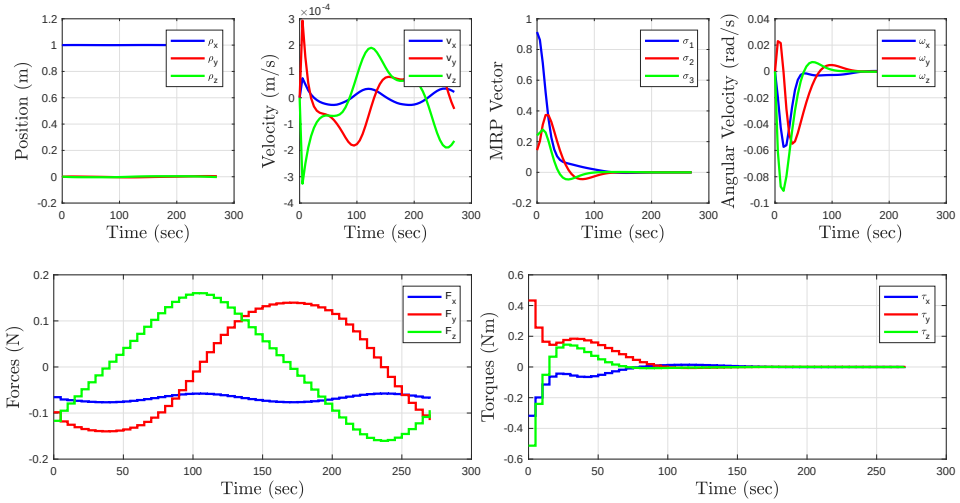

(b) Sample Case #2, Chief tumbling

Figure 6.26. Sample NMPC closed-loop cases from attitude (zero angular velocity, rendezvous position) with tumbling chief.

As in the planar rotation scenario, Table 6.3 shows that no failures were encountered with the NMPC algorithm. The closed-loop backward reachability analysis provided valuable insight into the feasibility of rendezvous maneuvers, using the NMPC algorithm, from a variety of relative positions and relative attitudes, for the scenario when the chief spacecraft is in a circular orbit and tumbling.

Table 6.3. Case failures during 6-DOF closed-loop reachability analysis.

Subspace (Slice)	Chief tumbling state	Number of Cases	% failed
Position; NMC velocity	Not Tumbling	27000	0
Position; NMC velocity	Tumbling	27000	0
Attitude; zero ang. velocity	Not Tumbling	8000	0
Attitude; zero ang. velocity	Tumbling	8000	0

6.4.3 Chief Eccentricity Effect on Closed-Loop Reachability Analysis

In this section, the effect of a nonzero eccentricity on the closed-loop reachability analysis is examined. The translational closed-loop reachability for the tumbling chief scenario, presented in Section 6.4.2, was re-investigated for chief orbital eccentricities of $e = 0.05$ and $e = 0.1$. Figure 6.27 shows the comparison of the relative position backward reachability for the different eccentricity values and a non-tumbling chief. Figure 6.28 shows these results for a tumbling chief. In these plots, there is no discernible difference in the NMPC maneuver time contours as eccentricity increases. Additionally, no failures were encountered during these simulations, as reported in Table 6.4.

Table 6.4. Case failures during translational 6-DOF closed-loop reachability analysis for chief orbital eccentricities of $e = 0$, $e = 0.05$, and $e = 0.1$.

Subspace (Slice)	Chief Tumbling Profile	Number of Cases	% failed
Position; NMC velocity	Not Tumbling ($e = 0$)	27000	0
Position; NMC velocity	Tumbling ($e = 0$)	27000	0
Position; NMC velocity	Not Tumbling ($e = 0.05$)	27000	0
Position; NMC velocity	Tumbling ($e = 0.05$)	27000	0
Position; NMC velocity	Not Tumbling ($e = 0.1$)	27000	0
Position; NMC velocity	Tumbling ($e = 0.1$)	27000	0

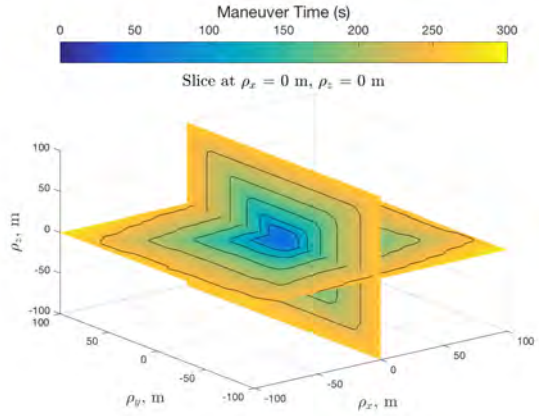

(a) Chief not tumbling, $e = 0$

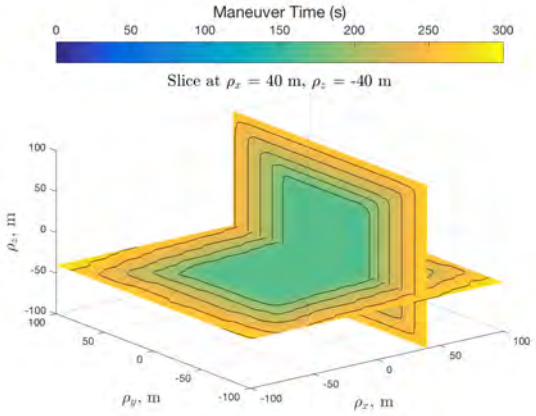

(b) Chief not tumbling, $e = 0$

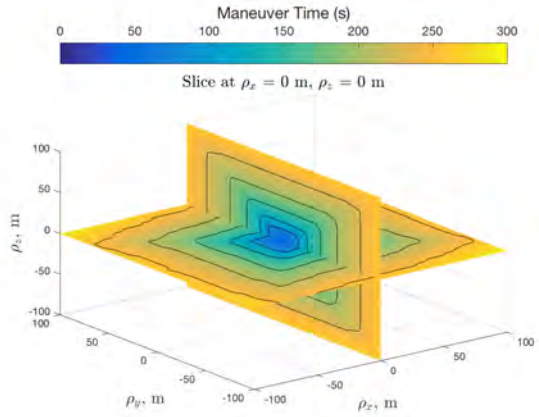

(c) Chief not tumbling, $e = 0.05$

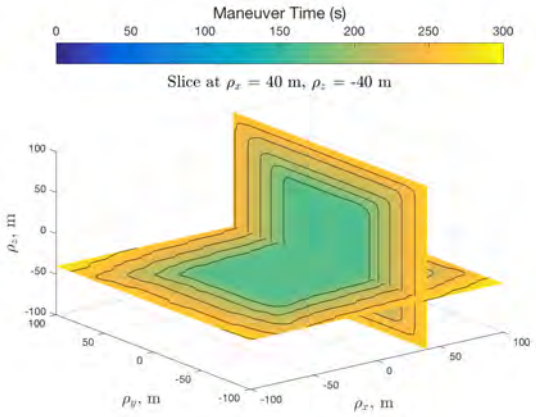

(d) Chief not tumbling, $e = 0.05$

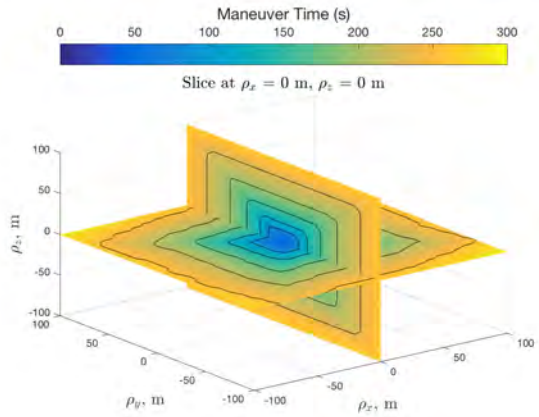

(e) Chief not tumbling, $e = 0.1$

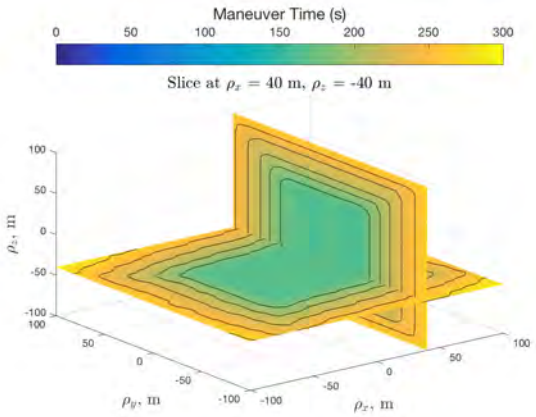

(f) Chief not tumbling, $e = 0.1$

Figure 6.27. Comparison of relative position closed-loop backward T-reachable sets for chief orbital eccentricities of $e = 0$, $e = 0.05$, and $e = 0.1$.

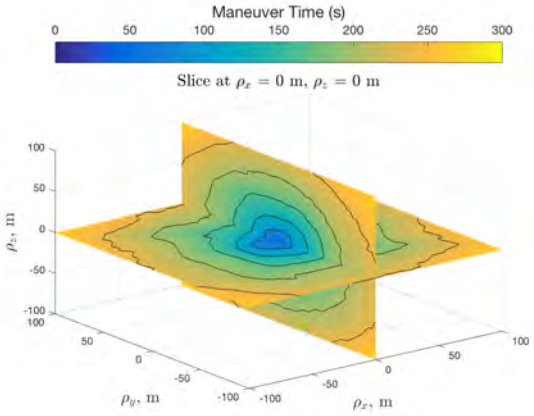

(a) Chief tumbling, $e = 0$

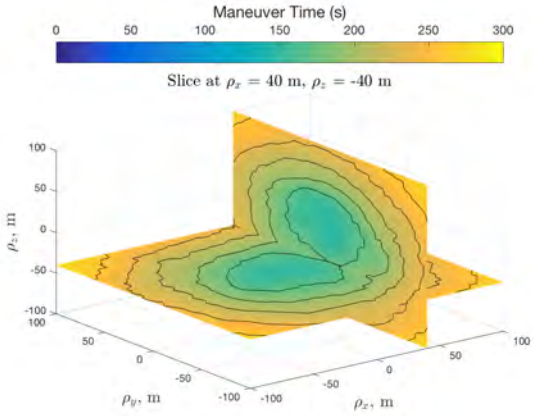

(b) Chief tumbling, $e = 0$

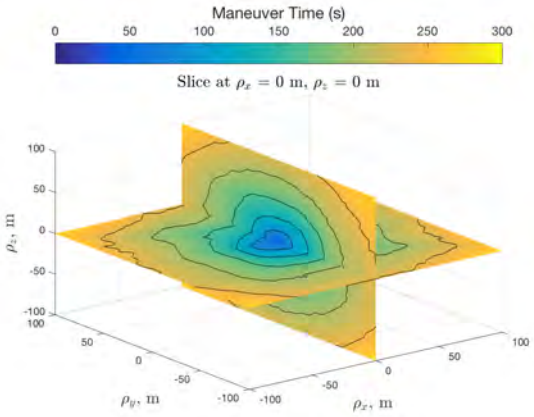

(c) Chief tumbling, $e = 0.05$

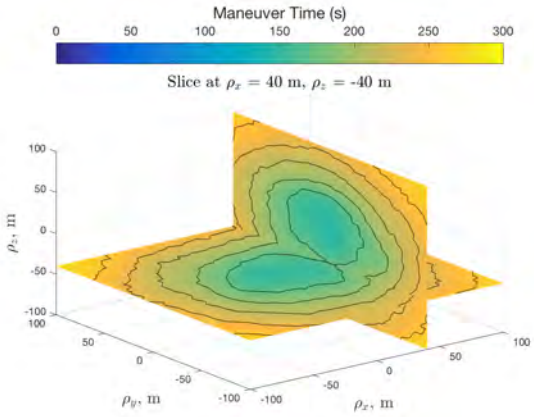

(d) Chief tumbling, $e = 0.05$

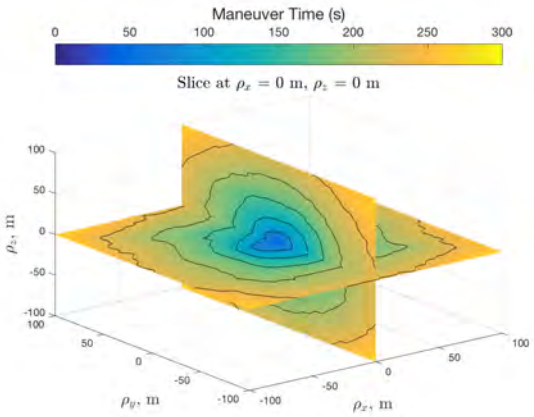

(e) Chief tumbling, $e = 0.1$

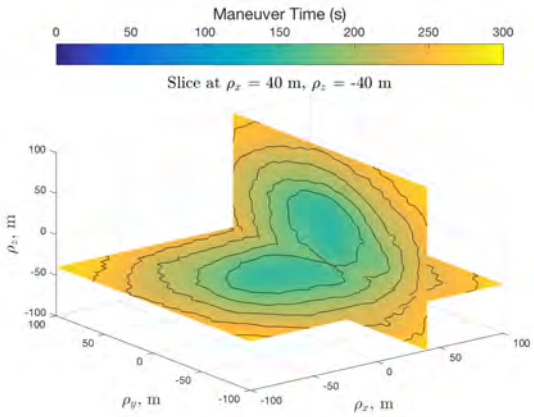

(f) Chief tumbling, $e = 0.1$

Figure 6.28. Comparison of relative position closed-loop backward T-reachable sets for chief orbital eccentricities of $e = 0$, $e = 0.05$, and $e = 0.1$.

6.5 Summary

This chapter introduced the MPC framework, applied to the problem of autonomous rendezvous with a tumbling object. An algorithm was designed, using the NMPC approach, that results in a stabilizing feedback control law. A closed-loop reachability analysis concept was then defined, as inspired by recent literature. Closed-loop reachability analysis allows designers to examine the behavior of a particular control law, to determine initial conditions from which feasible feedback solutions exist.

Closed-loop reachability analysis was conducted for the 6-DOF rendezvous problem with the chief spacecraft rotating on the orbit plane, and in a tumbling motion. The closed-loop backward reachable sets were visualized in the predefined relative position and relative attitude subspaces. These results were compared to the reachability analysis presented in Chapter 5. It was observed that the overall shape of the closed-loop backward T-reachable sets matched the shape of the backward T-reachable sets, presented in Chapter 5. As expected, maneuver times for the closed-loop system were longer than the minimum time maneuvers. Notably, the sensitivity issues encountered in solving the MT-OCP for this applied reachability analysis, were not encountered during the NMPC simulations.

Recursive feasibility of the NMPC algorithm could not be guaranteed due to the nonconvex nature of the underlying optimization problem. During this phase of research, the NMPC algorithm was run for hundreds of thousands of simulations, varying initial conditions and orbital eccentricities, without a single failure. This empirical evidence provides confidence that this implementation of NMPC is recursively feasible.

The research contributions offered in this chapter are shown in Table 6.5.

Table 6.5. Research contributions in Chapter 6.

Contribution	**Objective**
Design of NMPC algorithm for 6-DOF autonomous rendezvous with tumbling object	3
Definition of closed-loop backward reachable sets	2, 3
6-DOF Closed-loop reachability analysis of rendezvous with tumbling chief	2, 3

CHAPTER 7:
Test Cases: Safe Autonomous Rendezvous with a Tumbling Object

This chapter validates the NMPC algorithm, developed in Chapter 6, through further simulations of specific spacecraft rendezvous test cases with the additional safety consideration of avoiding collision between the two spacecraft. The collision avoidance constraint is important in order to ensure safety during the execution of the maneuver. A closer look at a subset of the simulations conducted in Chapters 5 and 6 reveals that for the non-rotating chief scenario ($\Omega = 0\ deg/s$ as presented in Figure 6.1a and 6.1b), approximately 51% of the MT-OCP trajectories and 41% of the NMPC trajectories resulted in a collision with the chief. In the simulations considered in this chapter, the collision avoidance constraint is added to ensure the trajectory remains safe. The performance of the autonomous guidance algorithm, in terms of maneuver time, control effort, and computation time, is compared to the time optimal solution.

7.1 Definition of Test Cases

The test cases are designed with the motivation of autonomous on-orbit assembly or servicing missions. The chief and deputy spacecraft are chosen to have the same mass and inertia properties (e.g., modular components of a larger structure). Seven test cases are defined as shown in Table 7.1. It is assumed that the chief spacecraft body CCS is initially aligned with the LVLH CCS. The chief is in a circular LEO. The initial relative position puts the deputy in an off-plane NMC, and an initial relative attitude defined by a 90 degree rotation about an off-principal axis. The desired rendezvous condition, as in the reachability analysis scenarios, is one meter off the chief's center of mass along the x direction. Two different spacecraft geometries are examined, as depicted in Figure 7.1. For the first set of cases, the chief and deputy are defined as spherically symmetric spacecraft with inertia properties shown in Table 5.3 (Figure 7.1a). For the second set of cases, the chief and deputy are defined as triaxial spacecraft with inertia properties shown in Table 5.5 (Figure 7.1b). According to the dimensions of the chief, an ellipsoidal Keep-Out-Zone (KOZ) is enforced, centered at the chief's center-of-mass, with semi-axes equal to the chief's length, width,

and height, in order to avoid collisions.

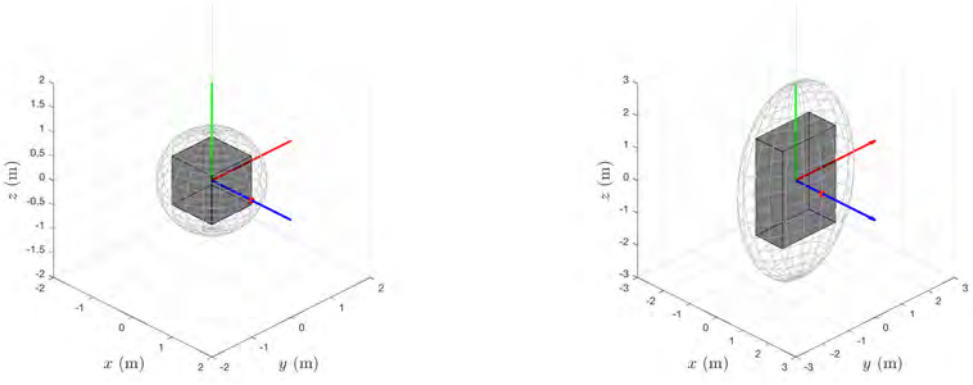

(a) Symmetric Spacecraft (b) Triaxial Spacecraft

Figure 7.1. Spacecraft geometries considered; body axes shown as blue (x), red (y), and green (z); red dot shows desired rendezvous point.

Cases 1 and 4 are the baseline cases for spherical and triaxial spacecraft geometry, respectively, with a non-tumbling chief. Cases 2 and 3 examine constant rotations about a principal axis for spherically symmetric geometries. Finally, Cases 5-7 examine three different tumbling profiles. These cases are summarized in Table 7.1.

An unreachable test case is also designed in order to investigate the behavior of NMPC with an initial relative state outside of the backward reachable set.

7.2 NMPC Algorithm

The NMPC algorithm described in 6.2 is modified to include the ellipsoidal KOZ constraint, generally written as

$$\boldsymbol{\rho}^T P \boldsymbol{\rho} \geq 1, \tag{7.1}$$

where P is the positive-definite matrix defining the size and shape of the ellipsoid and $\boldsymbol{\rho}$ is the relative position of the deputy with respect to the chief. Starting with the initial condition, x_0, and a finite prediction horizon, N, the NMPC-OCP to be solved at each

Table 7.1. Test cases for validation of NMPC algorithm

Chief Orbital Elements	$a = 6878.137$ km, $e = 0$, $i = 50$ deg
	$RAAN = 0$ deg, $\omega_p = 0$ deg, $f_0 = 0$ deg
Chief & Dep Mass (kg)	100
Chief & Dep Inertia (kg-m^2)	$diag(16.67,\ 16.67,\ 16.67)$ (Symmetric)
	$diag(108.33,\ 83.33,\ 41.67)$ (Triaxial)
F_{max} (N)	1
M_{max} $(N$-$m)$	1
T_{max} (s)	1000
Desired final condition	$\boldsymbol{\rho}_d = [1, 0, 0]^T\ m$
	$\boldsymbol{v}_d = [0, 0, 0]^T\ m/s$
	$\boldsymbol{\sigma}_d = [0, 0, 0]^T$
	$\boldsymbol{\omega}_d = [0, 0, 0]^T\ rad/s$
Initial condition	$\boldsymbol{\rho}_0 = [0, 100, 20]^T\ m$
	$\boldsymbol{v}_0 = [0.0553, 0, 0]^T\ m/s$
	$\boldsymbol{\sigma}_0 = [0.1107, 0.2214, 03321]^T$
	$\boldsymbol{\omega}_0 = [0.05, -0.03, 0.01]^T\ rad/s$
Case 1	Symmetric Spacecraft; No Tumble ($\boldsymbol{\omega}_{\mathsf{C/L}} = [0,\ 0,\ 0]^T\ deg/s$)
Case 2	Symmetric Spacecraft; $\boldsymbol{\omega}_{\mathsf{C/L}} = [0,\ 0,\ 4]^T\ deg/s$
Case 3	Symmetric Spacecraft; $\boldsymbol{\omega}_{\mathsf{C/L}} = [0,\ 4,\ 0]^T\ deg/s$
Case 4	Triaxial Spacecraft; No Tumble ($\boldsymbol{\omega}_{\mathsf{C/L}} = [0,\ 0,\ 0]^T\ deg/s$)
Case 5	Triaxial Spacecraft; $\boldsymbol{\omega}_{\mathsf{C/L}} = [-2,\ 1,\ 1]^T\ deg/s$
Case 6	Triaxial Spacecraft; $\boldsymbol{\omega}_{\mathsf{C/L}} = [1,\ -2,\ 1]^T\ deg/s$
Case 7	Triaxial Spacecraft; $\boldsymbol{\omega}_{\mathsf{C/L}} = [1,\ 1,\ -2]^T\ deg/s$

iteration is:

$$\text{minimize} \quad : \quad J = \sum_{i=0}^{N-1} (x_{k+i} - x_d)^T Q (x_{k+i} - x_d) + u_{k+i}^T R u_{k+i} + (x_{k+N} - x_d)^T Q_{f_k} (x_{k+N} - x_d) \tag{7.2a}$$

$$\text{subject to} \quad : \quad \text{for } i = 0, \ldots, N-1,$$

$$x_{k+1+i} = f_d(x_{k+i}, k+i) + G_d u_{k+i} \tag{7.2b}$$

$$||u_{k+i}||_\infty \leq u_{max} \tag{7.2c}$$

$$-\boldsymbol{\rho}_{k+i}^T P \boldsymbol{\rho}_{k+1} + 1 \leq 0. \tag{7.2d}$$

The addition of the nonconvex KOZ constraint complicates the on-board optimization problem. In order to avoid recursive feasibility issues, the KOZ is relaxed to a soft constraint by introducing the slack variable, s. The slack variable is appended to the cost functional in (7.2a), with a scalar weight. It has been shown that an appropriate weight to ensure constraint satisfaction is larger than the Lagrange multiplier corresponding to the constraint [99]. Without prior knowledge of the Lagrange multiplier, a large weight must be selected to ensure constraints are met. However, a weight that is too large may sacrifice the stabilizing terminal cost. This becomes a tradeoff between constraint satisfaction and stability, which must be examined for autonomous applications.

Choosing Q_f as the solution to the DARE, as described in 6.2, ensures that the terminal cost is a local CLF of the system. Then, any positive scalar multiple of this function is also a local CLF. A weighting scalar is incorporated in the terminal cost to tradeoff with the slack variable. The relaxed NMPC-OCP to be solved at each iteration is:

$$\begin{aligned}
\text{minimize} \quad : \quad & J = \epsilon s + \sum_{i=0}^{N-1} (x_{k+i} - x_d)^T Q (x_{k+i} - x_d) + u_{k+i}^T R u_{k+i} + \\
& \eta (x_{k+N} - x_d)^T Q_{f_k} (x_{k+N} - x_d) && (7.3a) \\
\text{subject to} \quad : \quad & \text{for } i = 0, \ldots, N-1, \\
& x_{k+1+i} = f_d(x_{k+i}, k+i) + G_d u_{k+i} && (7.3b) \\
& ||u_{k+i}||_\infty \leq u_{max} && (7.3c) \\
& -\boldsymbol{\rho}_{k+i}^T P \boldsymbol{\rho}_{k+1} + 1 \leq s, && (7.3d)
\end{aligned}$$

where $\epsilon > 0$ is the weighting parameter on the slack variable, and $\eta > 0$ is the weighting parameter on the terminal cost. The parameters used for these simulations are shown in Table 7.2.

7.3 Results

All seven test cases were run, using MATLAB 2016b, on a Macbook Pro, with a 2.2 GHz Intel Core i7 processor. The MT-OCP for each test case was solved using GPOPS-II [83]. The GPOPS-II settings used for these test cases are shown in Table 7.3. The NMPC

Table 7.2. NMPC parameters used for simulation of the autonomous rendezvous test cases.

Parameter	Value
Sampling time, t_s (sec)	5
Horizon, N (steps)	25
Q weights (translational), $\alpha_{1:6}$	1
Q weights (rotational), $\alpha_{7:12}$	10^{-4}
Max position error, $x_{1:3_{max}}$	10^{-1}
Max velocity error, $x_{4:6_{max}}$	10^{-2}
Max rotational state error, $x_{7:12_{max}}$	10^{-4}
R weights, $\beta_{1:6}$	1
Slack variable weight, ϵ	10^{8}
Terminal cost weight, η	10^{-3}

Table 7.3. GPOPS-II parameters used to solve the MT-OCP for the rendezvous test cases.

Parameter	Value
Mesh tolerance	$1e$-5
Max mesh refinements	20
Min collocation points	25
Max collocation points	50
Max NLP iterations	1000
Initial Guess	Endpoints (zero control)

was implemented using MPCTools and CasADi [122]–[124]. For both algorithms, IPOPT was used as the NLP solver and the solutions were validated by propagating the optimal controls through the 6-DOF dynamics. The following metrics were used to compare the two algorithms:

1. Rendezvous Time (s): final time when the rendezvous condition is reached.
2. Control Effort (Ns): amount of control usage during the maneuver, computed by

$$ce = \int_0^{t_f} \left(||u_T||_1 + \frac{1}{b}||u_R||_1 \right) dt, \tag{7.4}$$

   with $b = 1$.
3. Computation Time (s): for the MT-OCP this is the amount of time GPOPS-II took to solve the problem; for NMPC this is reported as an average of how long it took to

solve the NMPC-OCP during each iteration of the algorithm, along with the standard deviation.

4. Maximum Computation Time (s): this metric only applies to NMPC and shows the largest amount of time spent in solving the NMPC-OCP throughout the simulation.
5. State Error: difference in the final state reached and the desired state. This is computed as the norm of the vector difference for relative position, relative velocity, and relative angular velocity, and the magnitude of the MRP error vector for the relative attitude [50].

The test cases were first examined with respect to the deputy's ability to maintain the rendezvous condition. The MT-OCP and NMPC solutions for each test case are then discussed individually. The final results are tabulated Table 7.4.

7.3.1 Maintaining the Rendezvous Condition

The deputy's ability to maintain the rendezvous condition for each case was assessed by determining the required translational forces, and ensuring they are within the 1 N limit. This analysis was accomplished by initializing the simulations at the desired rendezvous condition, propagating the motion forward in time, and computing the steady-state control input, u_s, per (2.25). Figure 7.2 shows that the resulting translational control forces required to maintain the rendezvous point are well below the limit. For Cases 1 and 4, when the chief is not tumbling, the answer is the same. As shown in Figure 7.2a only a small constant force is required in order to account for the chief's motion along its orbital path. For Cases 2 and 3 the required force is more substantial, but constant, since the chief is now rotating about one of its principal axes at a constant rate. For Cases 5, 6, and 7, when the chief is tumbling, the required forces become periodic.

7.3.2 Case 1 Results

The MT-OCP and NMPC solutions for Case 1 are presented in Figures 7.3 - 7.10.

MT-OCP Solution

Figure 7.3 shows the relative trajectory and the deputy and chief's orientations with respect to the LVLH CCS. The plots show four screenshots of the trajectory as the simulation

Table 7.4. Results on performance of MT-OCP and NMPC algorithms for the autonomous rendezvous test cases.

Case #	**Alg.**	**Rend. Time** (s)	**Control Eff.** (Ns)	**Comp. Time** (s)	**Max Comp. Time** (s)	**State Error**			
						$\boldsymbol{\rho}$ (m)	$\boldsymbol{v}$ (m/s)	$\boldsymbol{\sigma}$	$\boldsymbol{\omega}$ (rad/s)
1	MT-OCP	194.27	425.48	15.16	N/A	0.214	0.002	3.8e-6	3.7e-5
	NMPC	265	453.57	1.41 ± 0.66	4.36	0.057	0.006	3.1e-8	2.8e-6
2	MT-OCP	182.81	406.98	119.73	N/A	0.025	0.001	6.2e-7	6.0e-5
	NMPC	260	595.04	1.59 ± 0.72	6.92	0.07	0.007	9.5e-8	1.1e-5
3	MT-OCP	198.24	597.32	162.48	N/A	0.665	0.039	3.5e-7	4.1e-5
	NMPC	265	548.89	1.44 ± 0.76	5.04	0.064	0.006	1.6e-10	3.5e-6
4	MT-OCP	194.27	433.79	15.38	N/A	0.155	0.002	6.4e-6	6.0e-5
	NMPC	310	605.62	1.9 ± 0.42	4.33	0.096	0.01	5.5e-9	2.3e-6
5	MT-OCP	170.34	522.65	34.17	N/A	0.008	0.0003	1.4e-6	7.7e-5
	NMPC	250	624.78	1.95 ± 0.41	3.86	0.014	0.001	1.7e-8	1.4e-5
6	MT-OCP	168.82	506.03	25.88	N/A	0.022	0.0006	3.0e-5	1.2e-4
	NMPC	365	926.35	1.3 ± 0.52	4.04	0.083	0.007	1.6e-8	1.2e-5
7	MT-OCP	175.49	538.85	32.72	N/A	0.01	0.0002	1.9e-6	1.6e-4
	NMPC	245	620.88	1.32 ± 0.45	3.99	0.068	0.007	5.6e-9	9.3e-6

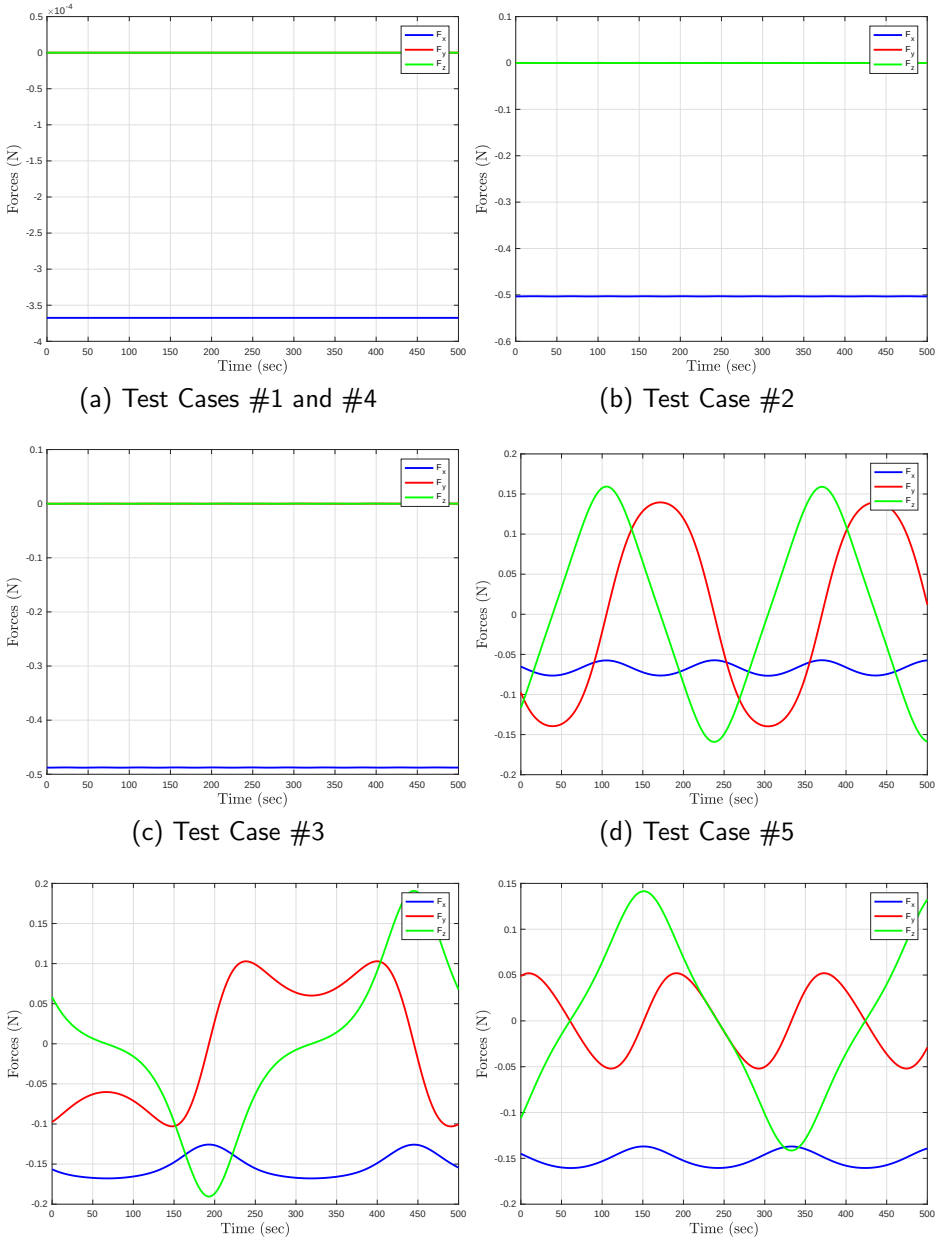

(a) Test Cases #1 and #4

(b) Test Case #2

(c) Test Case #3

(d) Test Case #5

(e) Test Case #6

(f) Test Case #7

Figure 7.2. Translational control forces required to maintain the rendezvous condition for each test case.

progresses. A close-up view around the chief is included in each of the four plots. The minimum time to rendezvous was 194.27 *sec* with control effort 425.48 Ns. The MT-OCP was solved in 15.16 *sec*.

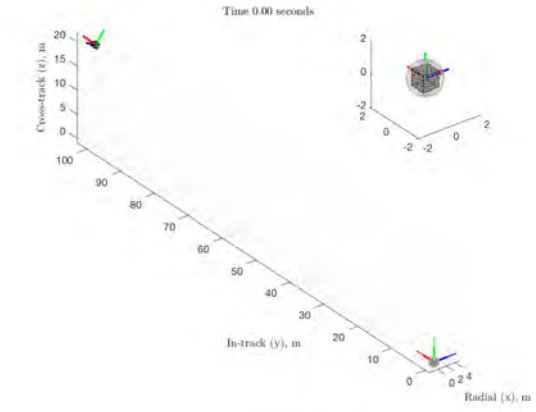

(a) Starting Condition

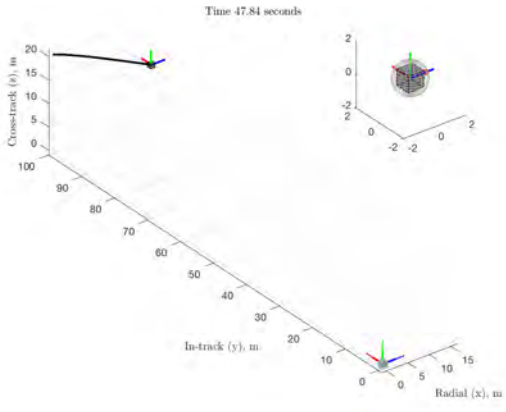

(b) Mid-Maneuver Screenshot #1

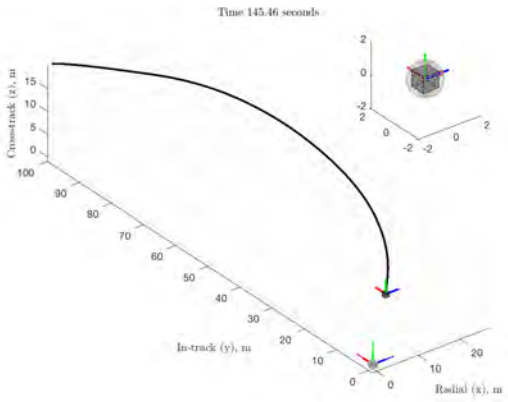

(c) Mid-Maneuver Screenshot #2

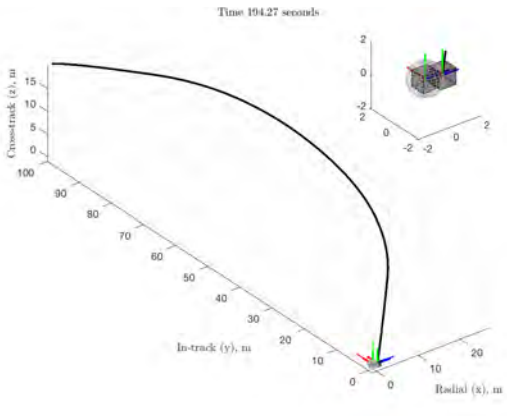

(d) Final Condition

Figure 7.3. Case 1–relative trajectory for minimum time maneuver.

Figure 7.4 shows the state history. The circles on these plots indicate the MT-OCP solution given by GPOPS-II, while the lines indicate the state trajectories propagated independently with the optimal control values. The propagated trajectory is used to calculate the state error at the end of the maneuver. The relative position was off by $0.214/m$, while the relative velocity, attitude, and angular velocity errors were much smaller. The state error could likely be improved by decreasing the solver tolerance, or increasing the number of nodes, at the cost of increasing the computational load. Figure 7.5 shows the optimal controls. The forces in the x and y direction exhibited bang-bang behavior, while the z force and the torques were oscillatory. Figure 7.6 shows the evaluation of the KOZ constraint, as shown in (7.1), and the Hamiltonian for the MT-OCP trajectory. It is clear that collisions

were successfully avoided since the value of the path constraint remains above 1. For this particular case the system is time-invariant since the chief is not tumbling. As a result, the Hamiltonian evaluated on the time optimal trajectory is expected to be equal to 0, and constant [58]. The plot of the Hamiltonian in Figure 7.6 shows some variation but is on the order of 10^{-3}, so the Hamiltonian does remain fairly close to 0. This result verifies that this solution is optimal.

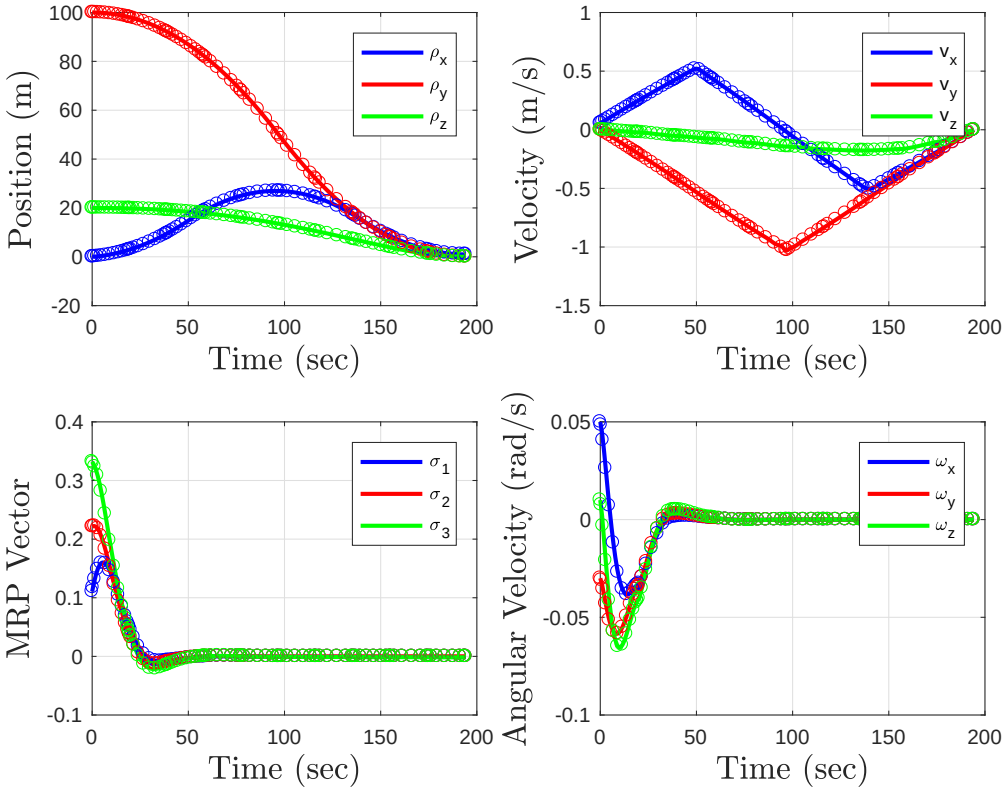

Figure 7.4. Case 1–state history for minimum time maneuver.

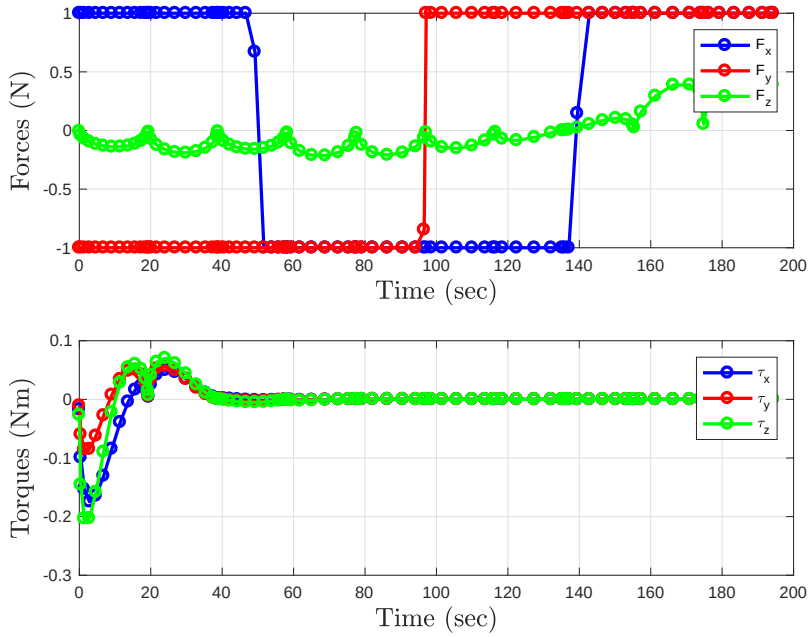

Figure 7.5. Case 1–control history for minimum time maneuver.

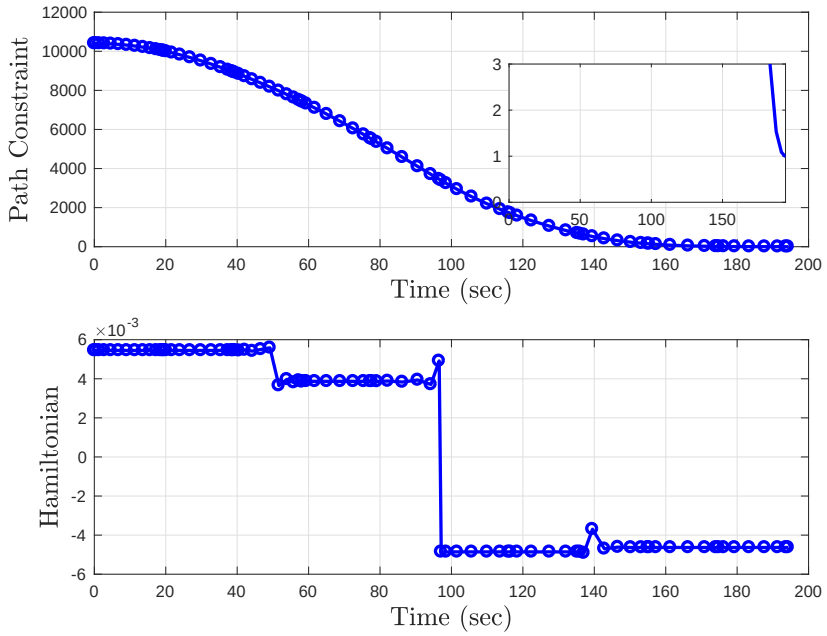

Figure 7.6. Case 1–verification of KOZ constraint satisfaction and time history of Hamiltonian.

NMPC Solution

Figure 7.7 shows the relative trajectory and the deputy and chief's orientations with respect to the LVLH CCS. The plots show four screenshots of the trajectory as the simulation progresses. A close-up view around the chief is included in each of the four plots. The time to rendezvous was 265 sec with control effort 453.57 Ns. The average time to solve the NMPC-OCP was 1.41 sec, with standard deviation of 0.66 sec. The maximum computation time was 4.36 sec.

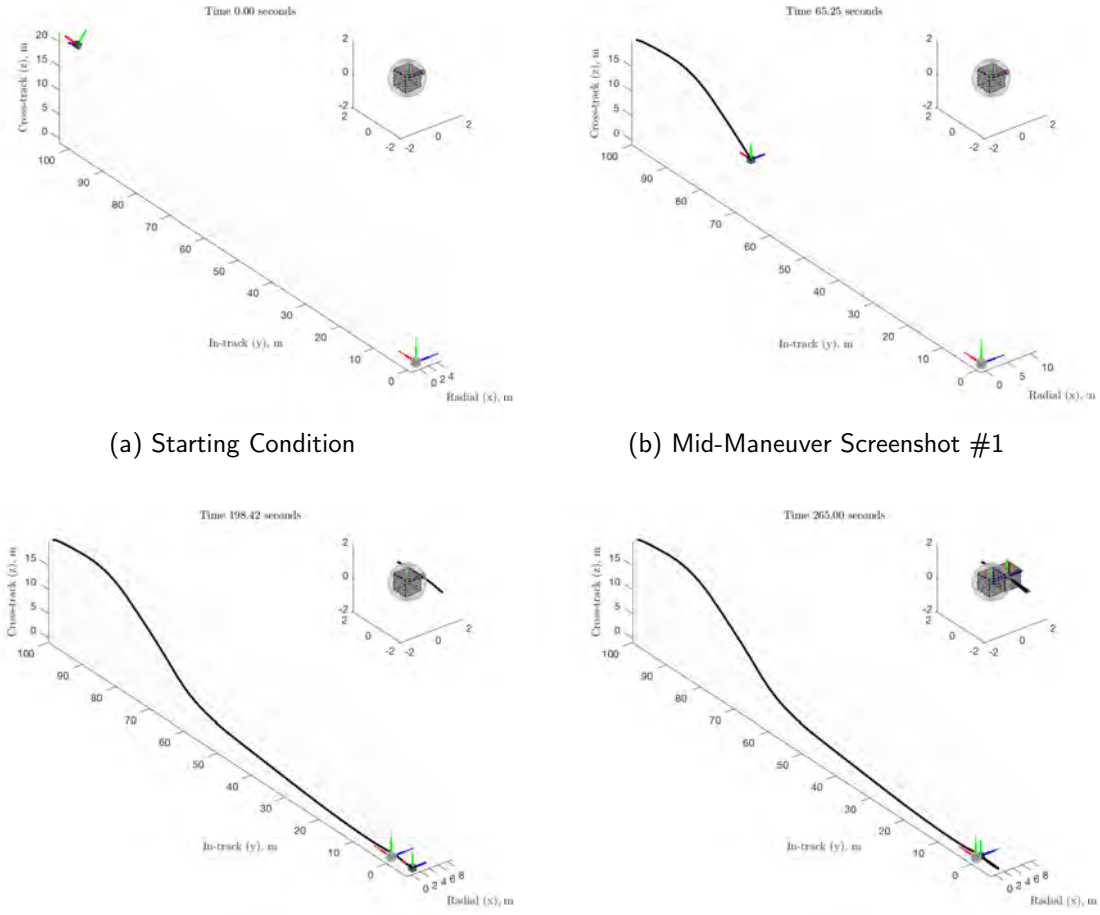

(a) Starting Condition

(b) Mid-Maneuver Screenshot #1

(c) Mid-Maneuver Screenshot #2

(d) Final Condition

Figure 7.7. Case 1–relative trajectory for NMPC maneuver.

Figure 7.8 shows the state history. The circles on these plots indicate the NMPC solution, while the lines indicate the state trajectories propagated independently with the NMPC

control values. The propagated trajectory is used to calculate the state error at the end of the maneuver. Since the state error tolerance is explicitly designed into the Q weighting matrix of the NMPC algorithm, the state errors were within the desired tolerances. Figure 7.9 shows the NMPC controls. Unlike the MT-OCP controls, in Figure 7.5, the NMPC solution shows all three forces at maximum values for a certain amount of time, which caused a slighlty higher control effort in this case. Further tuning of the NMPC algorithm could decrease the control effort, at the cost of increasing the maneuver time. Figure 7.10 shows the evaluation of the KOZ constraint, as shown in (7.1), and the value of the NMPC cost functional throughout the trajectory. It is clear that collisions were successfully avoided since the value of the path constraint remains above 1. The trend of the value function is monotonically decreasing, which is the desired result for a stabilizing NMPC feedback controller.

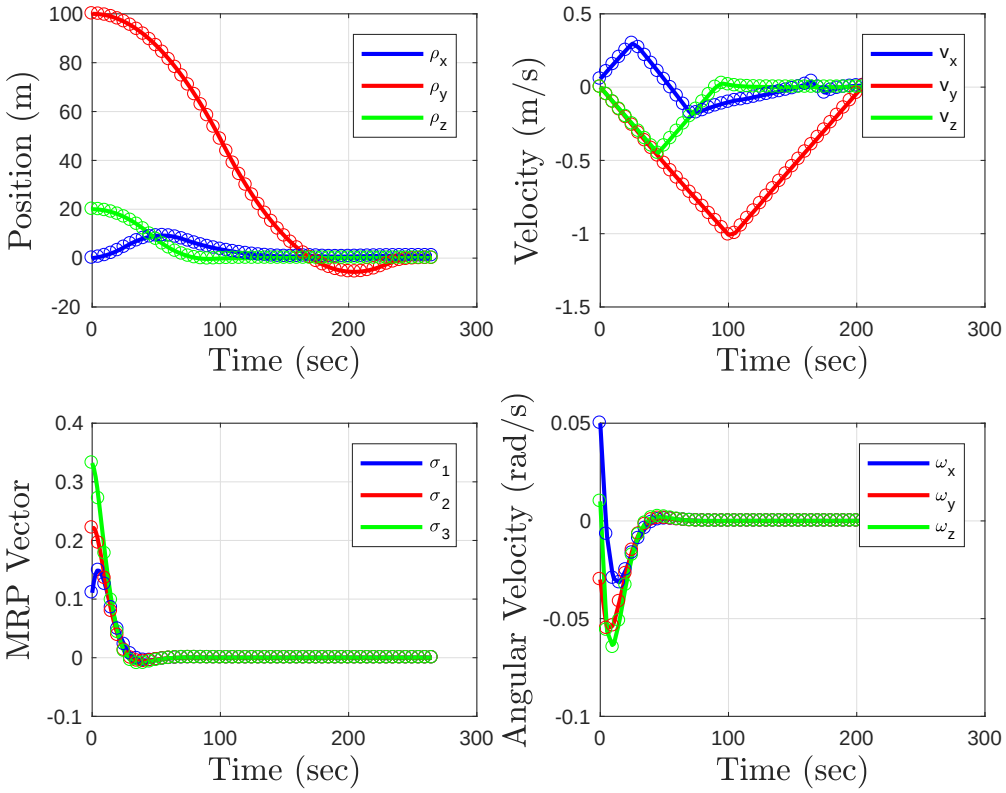

Figure 7.8. Case 1–state history for NMPC maneuver.

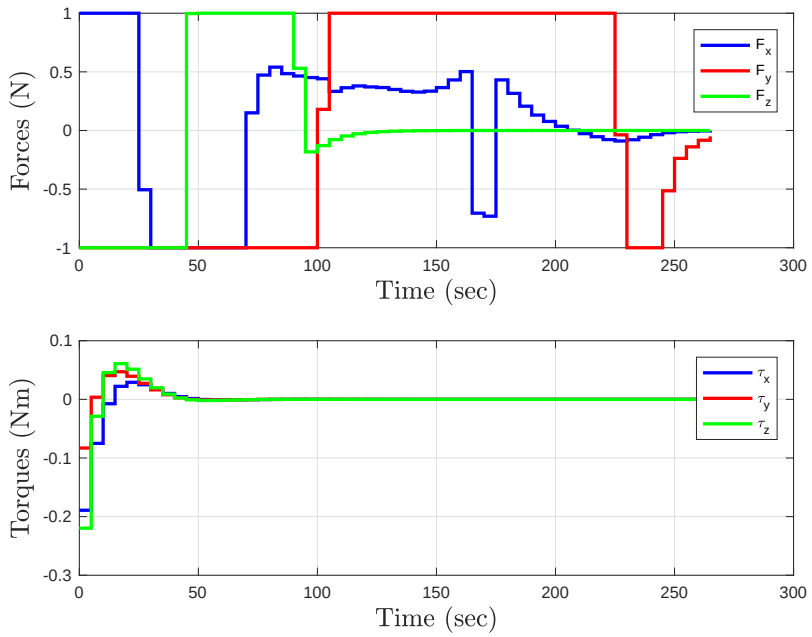

Figure 7.9. Case 1–control history for NMPC maneuver.

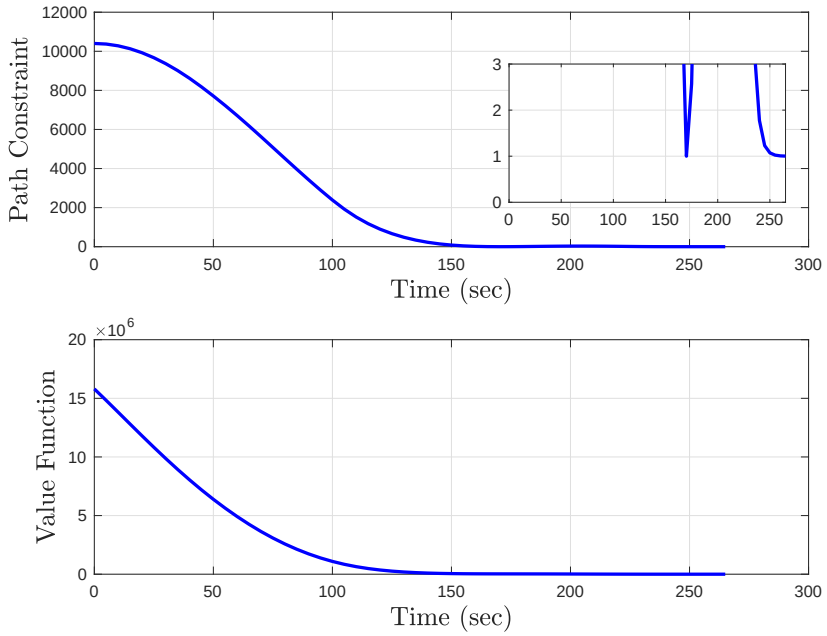

Figure 7.10. Case 1–verification of KOZ constraint satisfaction and time history of NMPC value function.

7.3.3 Case 2 Results

The MT-OCP and NMPC solutions for Case 2 are presented in Figures 7.11 - 7.18.

MT-OCP Solution

Figure 7.11 shows the relative trajectory and the deputy and chief's orientations with respect to the LVLH CCS. The plots show four screenshots of the trajectory as the simulation progresses. A close-up view around the chief is included in each of the four plots. The minimum time to rendezvous was 182.81 sec with control effort 406.98 Ns. The MT-OCP was solved in 119.73 sec.

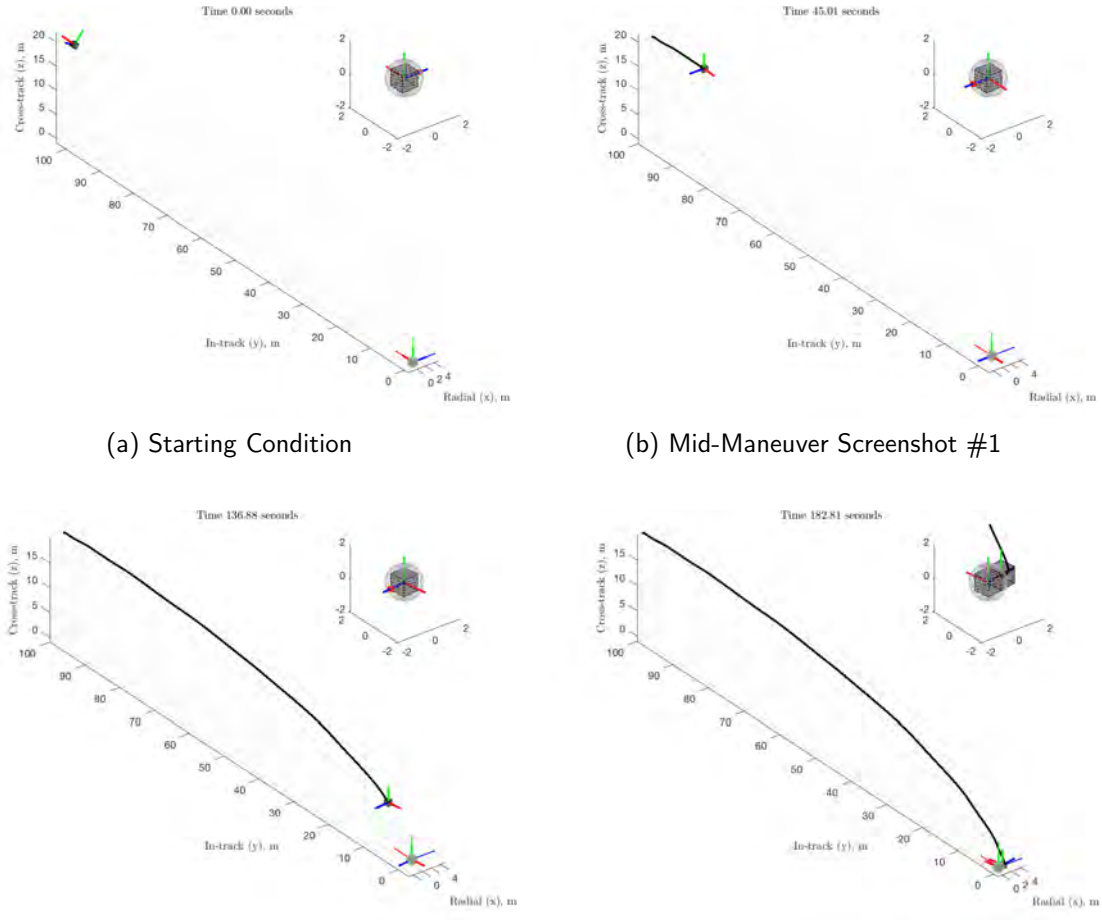

(a) Starting Condition

(b) Mid-Maneuver Screenshot #1

(c) Mid-Maneuver Screenshot #2

(d) Final Condition

Figure 7.11. Case 2–relative trajectory for minimum time maneuver.

Figure 7.12 shows the state history. The circles on these plots indicate the MT-OCP solution given by GPOPS-II, while the lines indicate the state trajectories propagated independently with the optimal control values. The propagated trajectory is used to calculate the state error at the end of the maneuver. The state errors in this case were small. Figure 7.13 shows the optimal controls. The forces in the x and y direction exhibited bang-bang behavior with multiple switches, while the z force and the torques were oscillatory. Figure 7.14 shows the evaluation of the KOZ constraint, and the Hamiltonian for the MT-OCP trajectory. It is clear that collisions were successfully avoided. Due to the time-varying nature of the dynamics, there is no expectation on the value of the Hamiltonian.

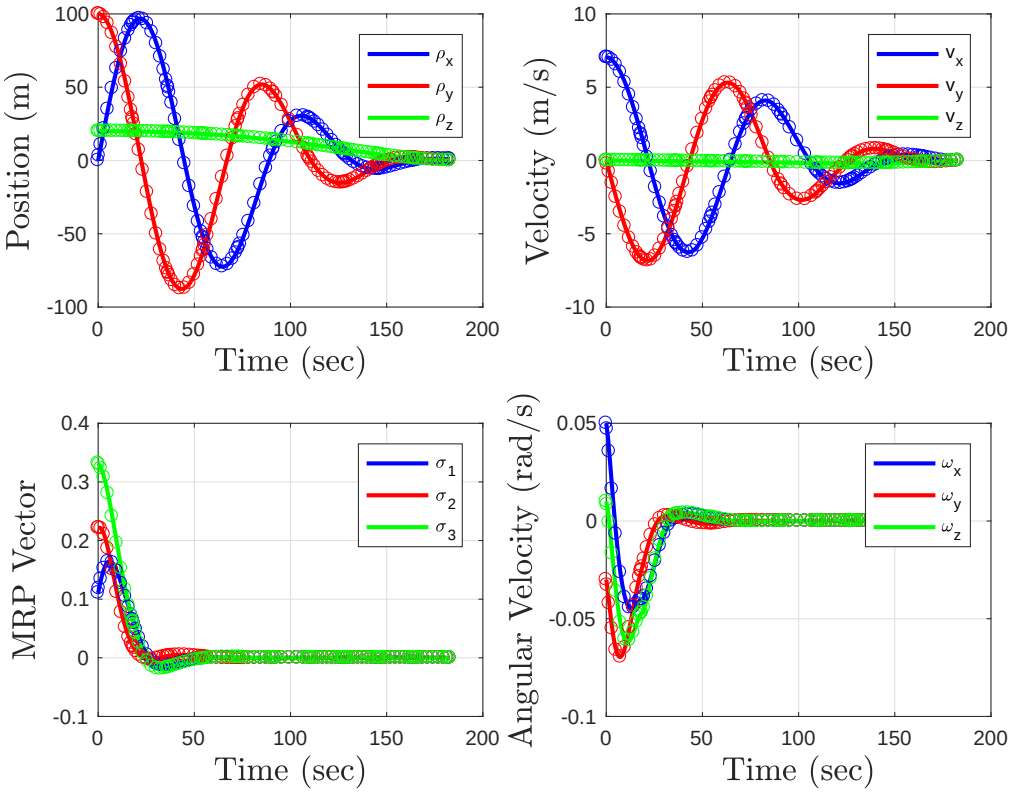

Figure 7.12. Case 2–state history for minimum time maneuver.

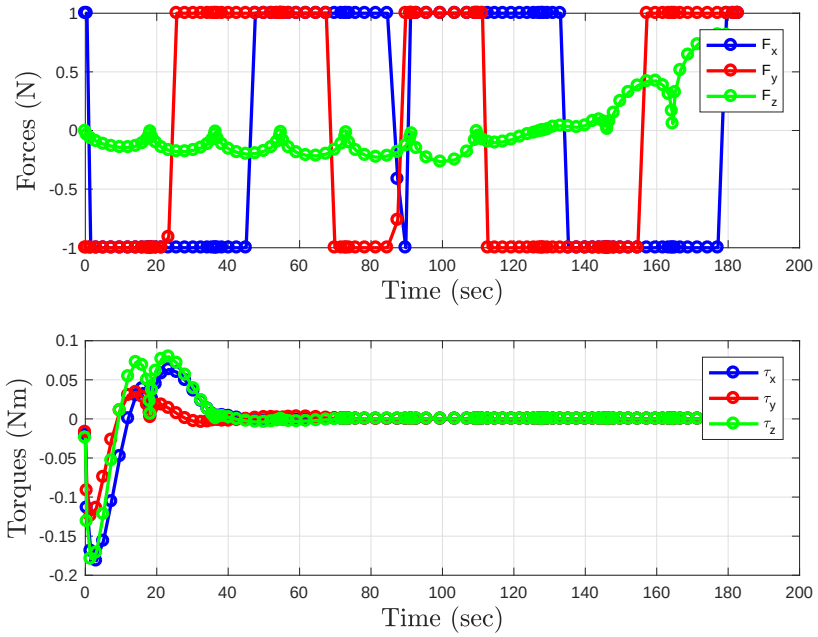

Figure 7.13. Case 2–control history for minimum time maneuver.

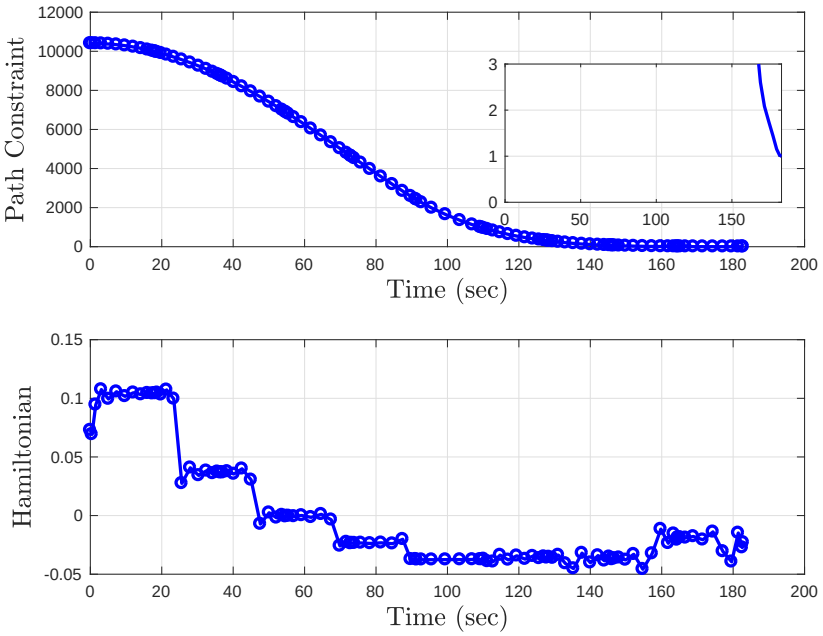

Figure 7.14. Case 2–verification of KOZ constraint satisfaction and time history of Hamiltonian.

NMPC Solution

Figure 7.15 shows the relative trajectory and the deputy and chief's orientations with respect to the LVLH CCS. The plots show four screenshots of the trajectory as the simulation progresses. A close-up view around the chief is included in each of the four plots. The time to rendezvous was 260 sec with control effort 595.04 Ns. The average time to solve the NMPC-OCP was 1.59 sec, with standard deviation of 0.72 sec. The maximum computation time was 6.92 sec.

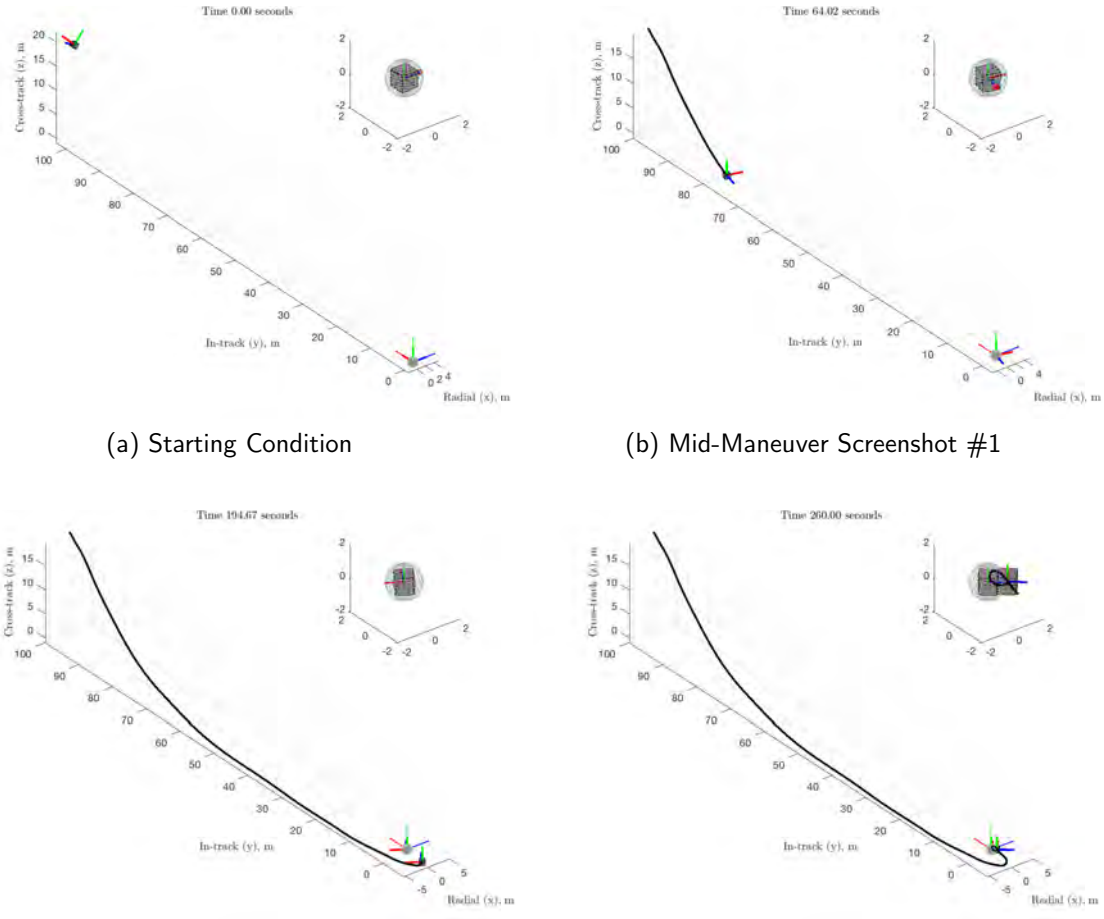

(a) Starting Condition

(b) Mid-Maneuver Screenshot #1

(c) Mid-Maneuver Screenshot #2

(d) Final Condition

Figure 7.15. Case 2–relative trajectory for NMPC maneuver.

Figure 7.16 shows the state history. The circles on these plots indicate the NMPC solution, while the lines indicate the state trajectories propagated independently with the NMPC

control values. The propagated trajectory is used to calculate the state error at the end of the maneuver. Since the state error tolerance is explicitly designed into the Q weighting matrix of the NMPC algorithm, the state errors were within the desired tolerances. Figure 7.17 shows the NMPC controls. As in Case 1, the NMPC solution shows more aggressive control force in the z direction in comparison to the MT-OCP solution. As a result, the NMPC control effort is higher. Further tuning of the NMPC algorithm could decrease the control effort, at the cost of increasing the maneuver time. In Figure 7.17 it can be seen that at the end of the maneuver the control forces converge to the values required to maintain the rendezvous condition; as a feedback controller, the NMPC algorithm is able to reach and maintain the rendezvous state. Figure 7.18 shows the evaluation of the KOZ constraint, and the value of the NMPC cost functional throughout the trajectory. It is clear that collisions were successfully avoided and the NMPC feedback control law is stabilizing.

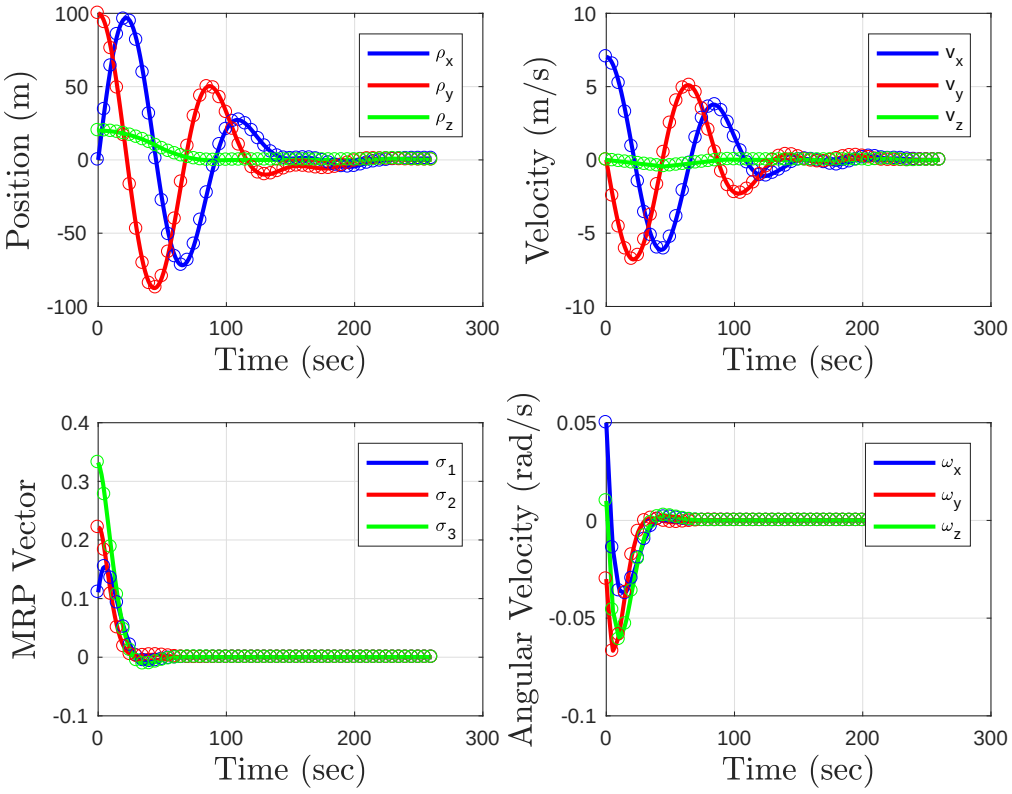

Figure 7.16. Case 2–state history for NMPC maneuver.

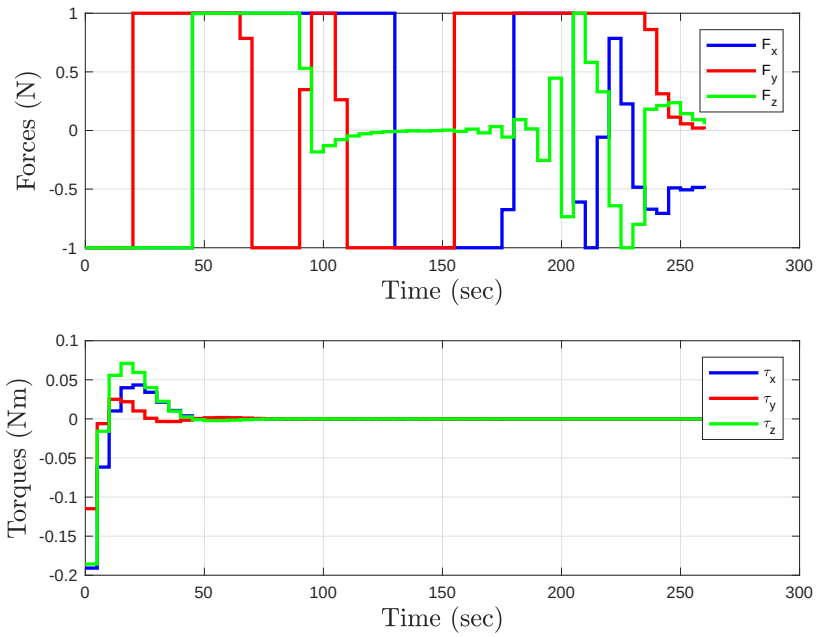

Figure 7.17. Case 2–control history for NMPC maneuver.

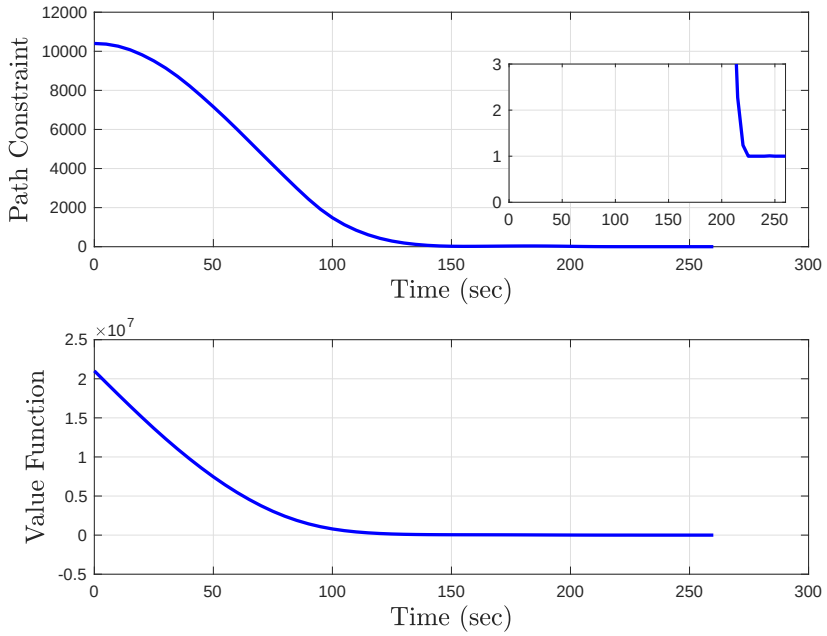

Figure 7.18. Case 2–verification of KOZ constraint satisfaction and time history of NMPC value function.

7.3.4 Case 3 Results

The MT-OCP and NMPC solutions for Case 3 are presented in Figures 7.19 - 7.26.

MT-OCP Solution

Figure 7.19 shows the relative trajectory and the deputy and chief's orientations with respect to the LVLH CCS. The plots show four screenshots of the trajectory as the simulation progresses. A close-up view around the chief is included in each of the four plots. The minimum time to rendezvous was 198.24 sec with control effort 597.32 Ns. The MT-OCP was solved in 162.48 sec.

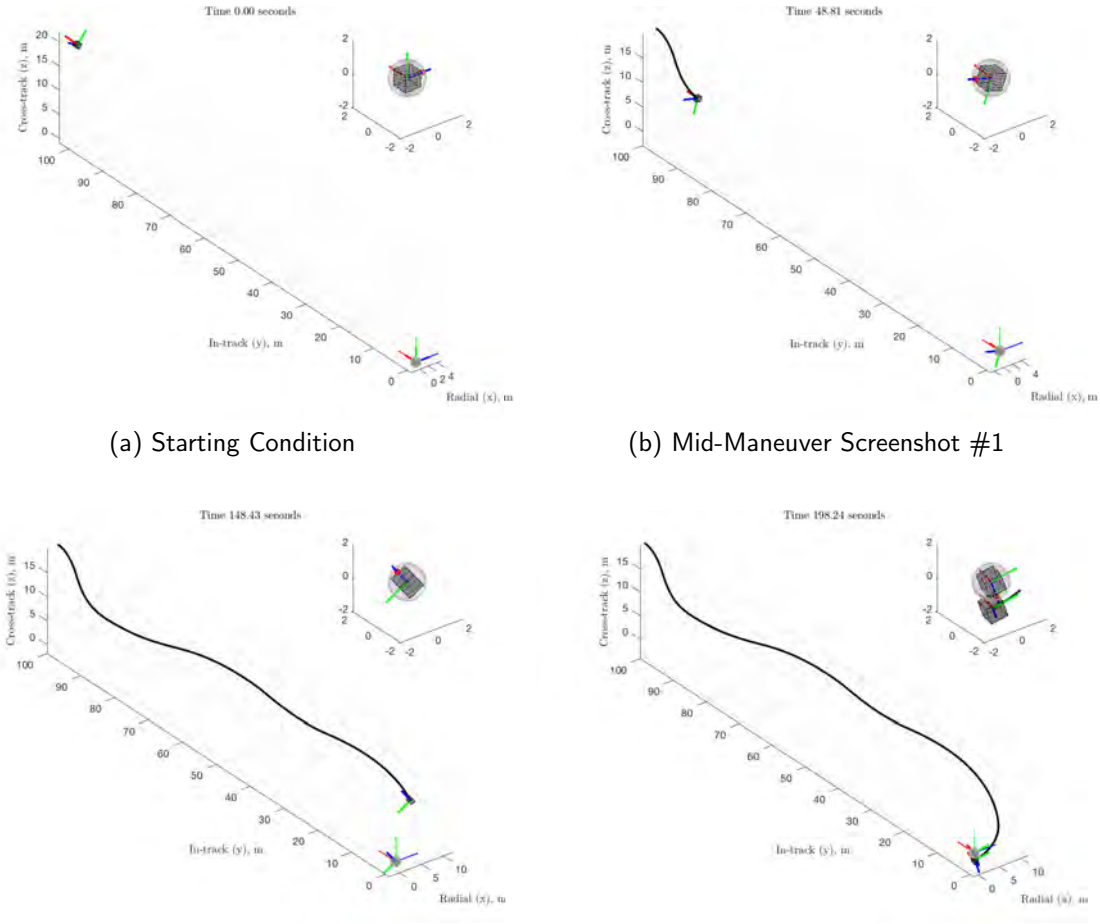

(a) Starting Condition

(b) Mid-Maneuver Screenshot #1

(c) Mid-Maneuver Screenshot #2

(d) Final Condition

Figure 7.19. Case 3–relative trajectory for minimum time maneuver.

Figure 7.20 shows the state history. The circles on these plots indicate the MT-OCP solution given by GPOPS-II, while the lines indicate the state trajectories propagated independently with the optimal control values. It is noticeable in Figure 7.19d that the deputy did not quite reach the desired relative position. This case exhibited the largest relative position error of 0.665 m. The state error could likely be improved by using a tighter solver tolerance, or increasing the number of nodes, at the cost of increasing the computational load. Figure 7.21 shows the optimal controls. All three control forces exhibited bang-bang behavior in this case, while the torques were oscillatory. Figure 7.22 shows the evaluation of the KOZ constraint, and the Hamiltonian for the MT-OCP trajectory. It is clear that collisions were successfully avoided. Due to the time-varying nature of the dynamics, there is no expectation on the value of the Hamiltonian.

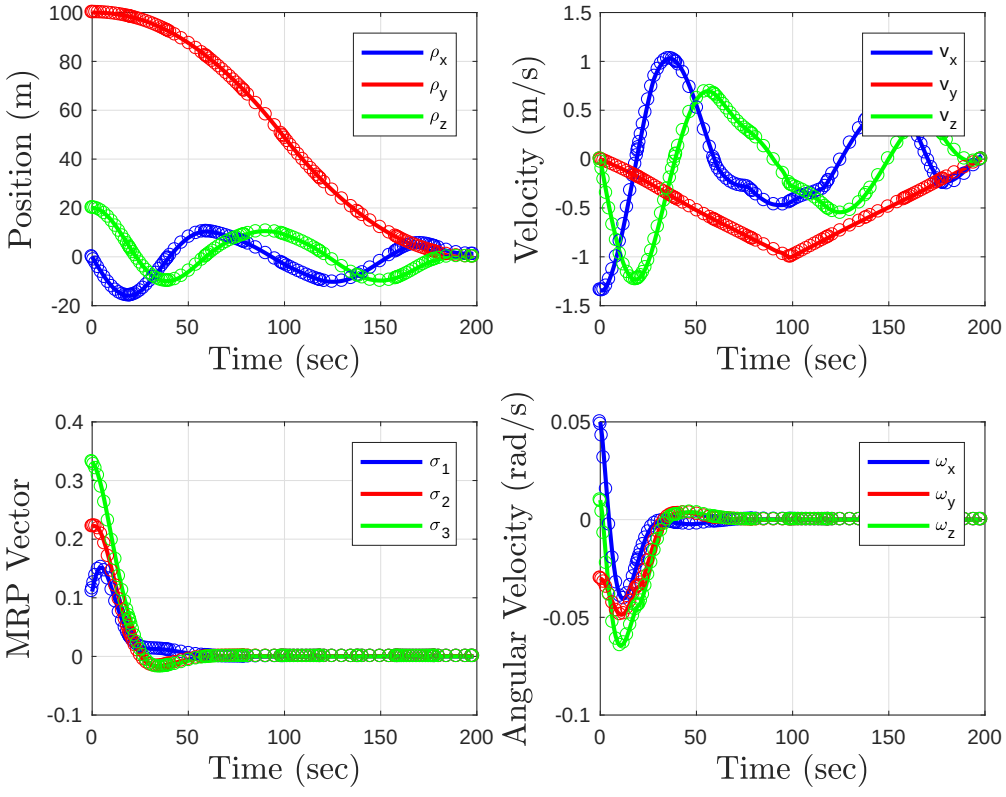

Figure 7.20. Case 3–state history for minimum time maneuver.

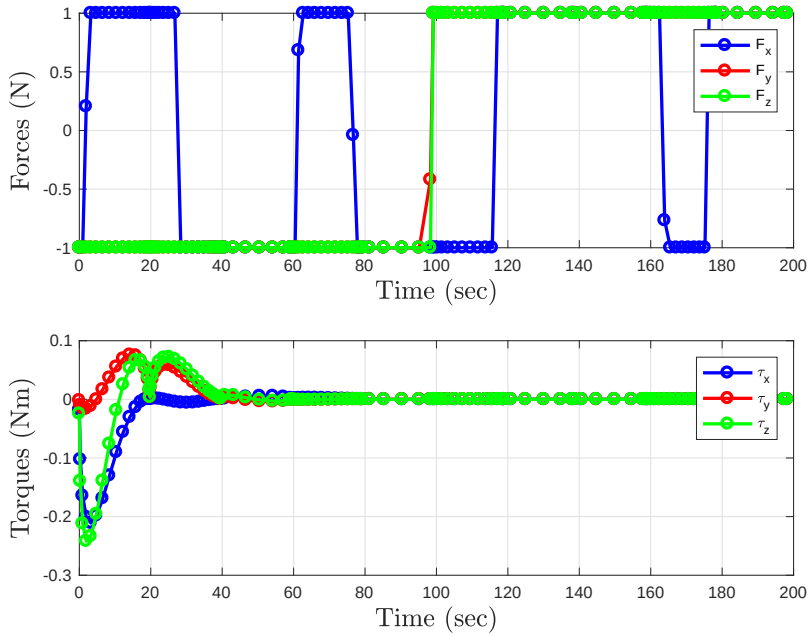

Figure 7.21. Case 3–control history for minimum time maneuver.

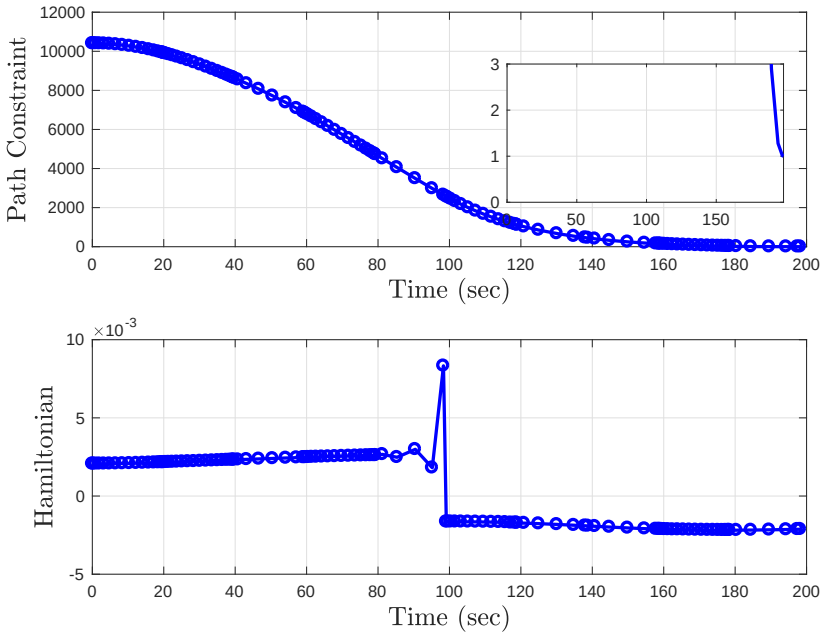

Figure 7.22. Case 3–verification of KOZ constraint satisfaction and time history of Hamiltonian.

NMPC Solution

Figure 7.23 shows the relative trajectory and the deputy and chief's orientations with respect to the LVLH CCS. The plots show four screenshots of the trajectory as the simulation progresses. A close-up view around the chief is included in each of the four plots. The time to rendezvous was 265 sec with control effort 548.89 Ns. The average time to solve the NMPC-OCP was 1.44 sec, with standard deviation of 0.76 sec. The maximum computation time was 5.04 sec.

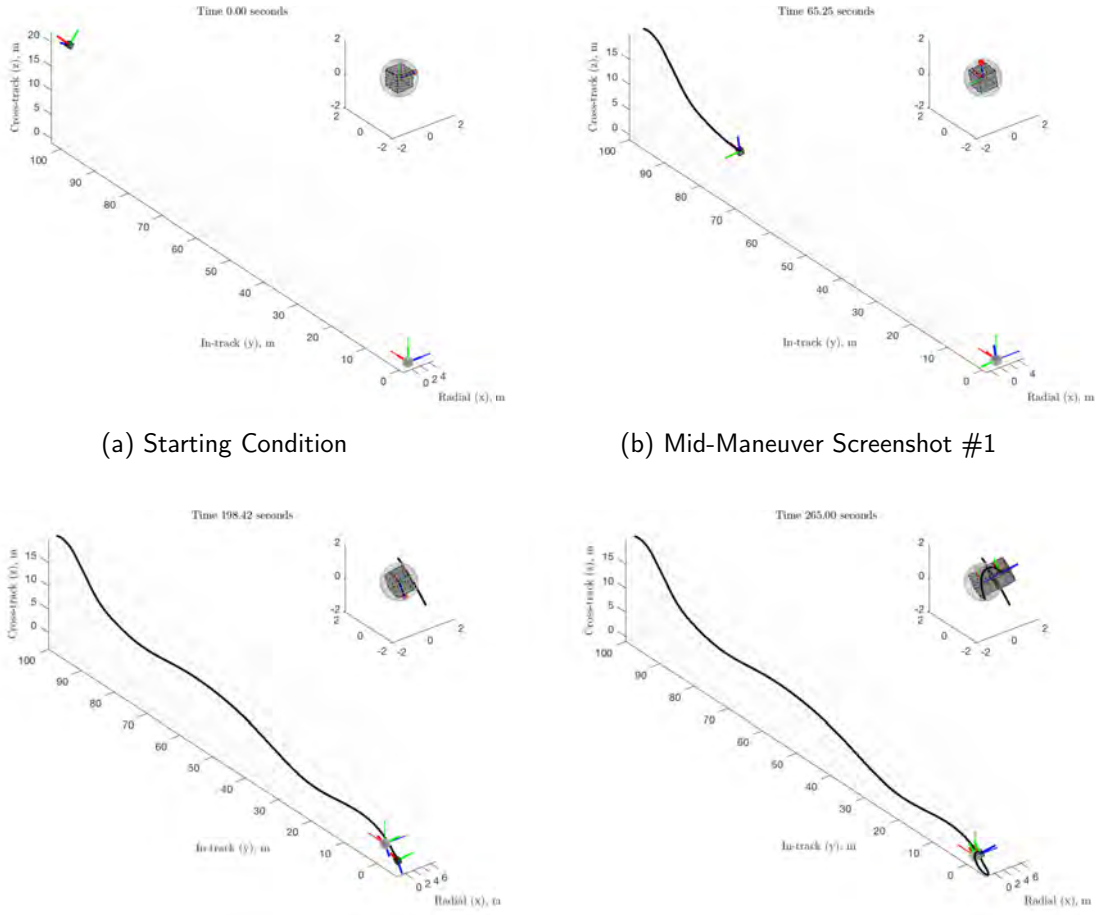

(a) Starting Condition

(b) Mid-Maneuver Screenshot #1

(c) Mid-Maneuver Screenshot #2

(d) Final Condition

Figure 7.23. Case 3–relative trajectory for NMPC maneuver.

Figure 7.24 shows the state history. The circles on these plots indicate the NMPC solution, while the lines indicate the state trajectories propagated independently with the NMPC

control values. The state errors were within the desired tolerances, as designed into the algorithm. Figure 7.25 shows the NMPC controls. In this case, the x and z control forces were less aggressive than the MT-OCP bang-bang solutions which resulted in a lower overall control effort. It can be seen that the control forces converge to the values required to maintain the rendezvous condition. Figure 7.26 shows the evaluation of the KOZ constraint, and the value of the NMPC cost functional throughout the trajectory. It is clear that collisions were successfully avoided and the NMPC feedback control law is stabilizing.

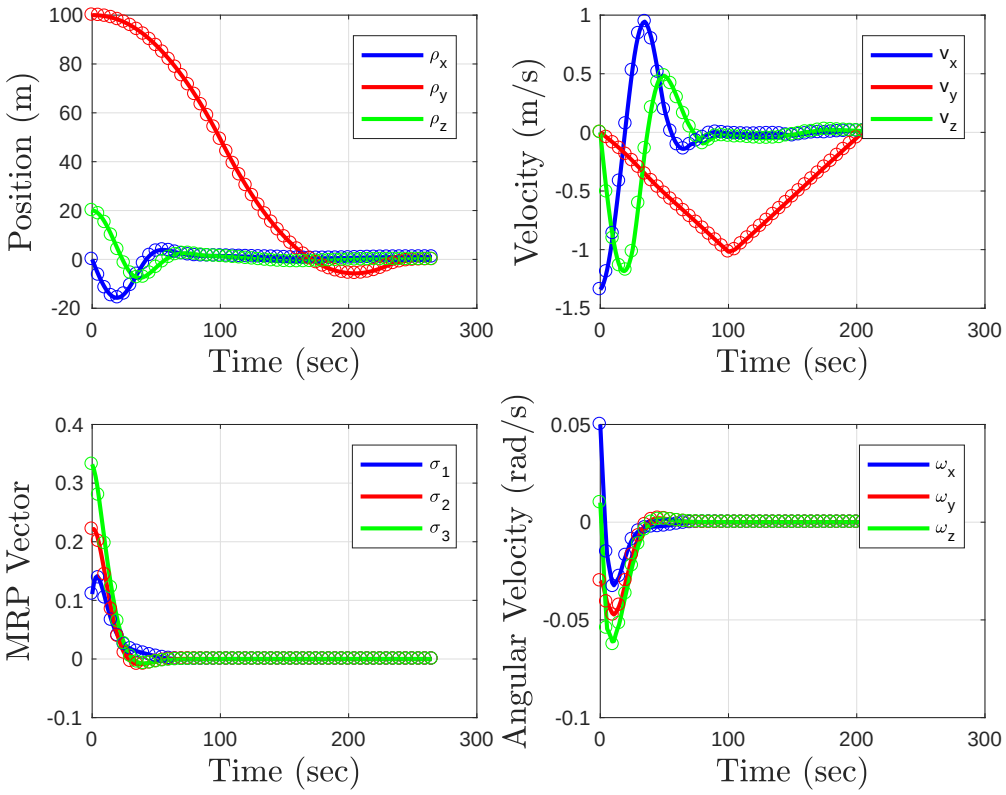

Figure 7.24. Case 3–state history for NMPC maneuver.

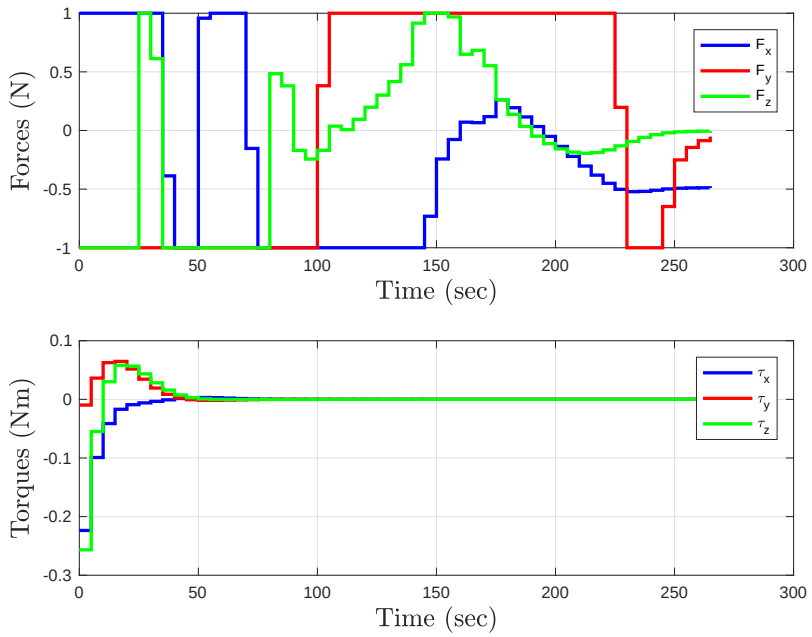

Figure 7.25. Case 3–control history for NMPC maneuver.

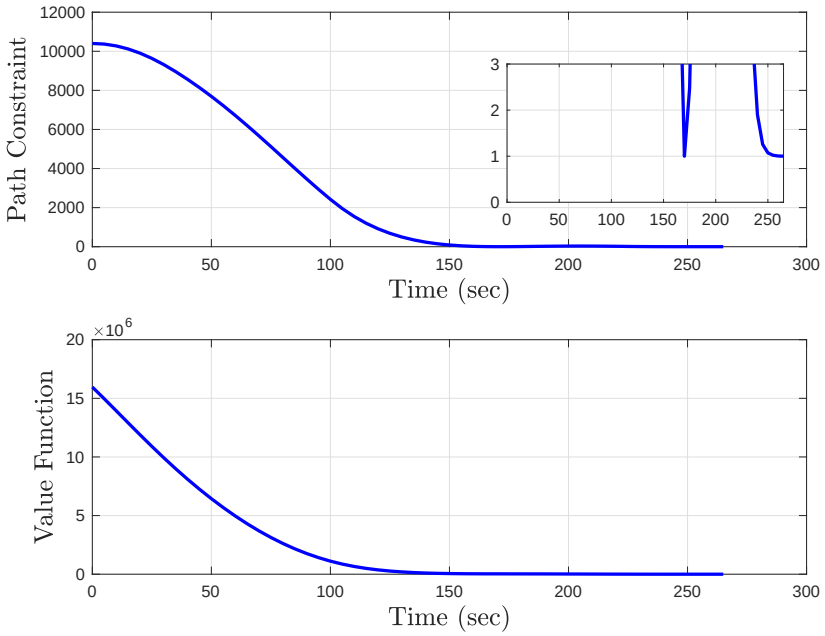

Figure 7.26. Case 3–verification of KOZ constraint satisfaction and time history of NMPC value function.

7.3.5 Case 4 Results

The MT-OCP and NMPC solutions for Case 4 are presented in Figures 7.27 - 7.34.

MT-OCP Solution

Figure 7.27 shows the relative trajectory and the deputy and chief's orientations with respect to the LVLH CCS. The plots show four screenshots of the trajectory as the simulation progresses. A close-up view around the chief is included in each of the four plots. The minimum time to rendezvous was 194.27 sec with control effort 433.79 Ns. The MT-OCP was solved in 15.38 sec.

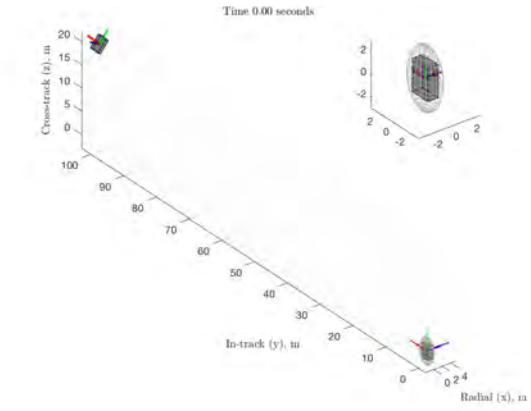

(a) Starting Condition

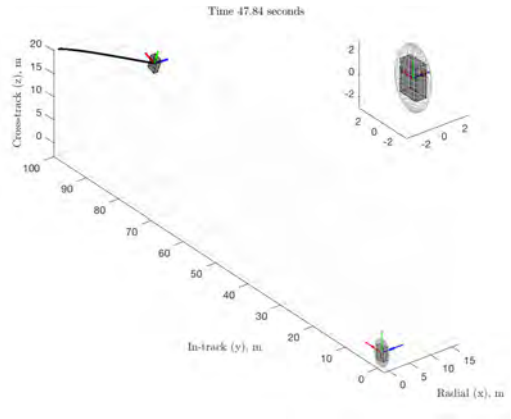

(b) Mid-Maneuver Screenshot #1

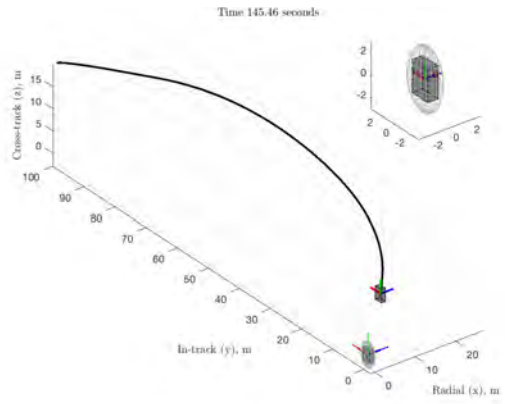

(c) Mid-Maneuver Screenshot #2

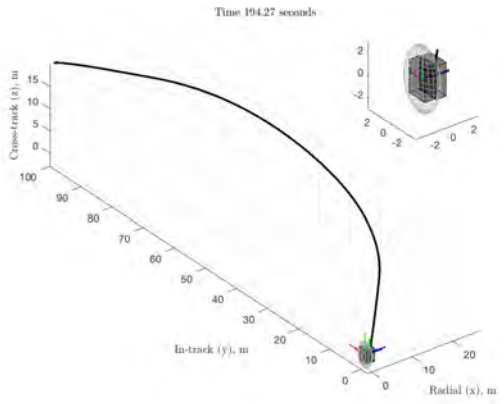

(d) Final Condition

Figure 7.27. Case 4–relative trajectory for minimum time maneuver.

Figure 7.28 shows the state history. The circles on these plots indicate the MT-OCP solution given by GPOPS-II, while the lines indicate the state trajectories propagated independently with the optimal control values. The relative position error at the end of the maneuver was 0.155 m, while the errors in other states were smaller. Figure 7.29 shows the optimal controls. The MT-OCP solution in this case is very similar to the solution of Case 1; the only difference between these two scenarios is the deputy and chief inertia properties. The MT-OCP solution for this case shows almost identical forces and slightly higher torques, in comparison to Figure 7.5, in order to compensate for the larger inertia values. As a result the expended control effort for Case 4 is slightly higher than in Case 1. Figure 7.30 shows the evaluation of the KOZ constraint, and the Hamiltonian for the MT-OCP trajectory. It is clear that collisions were successfully avoided.

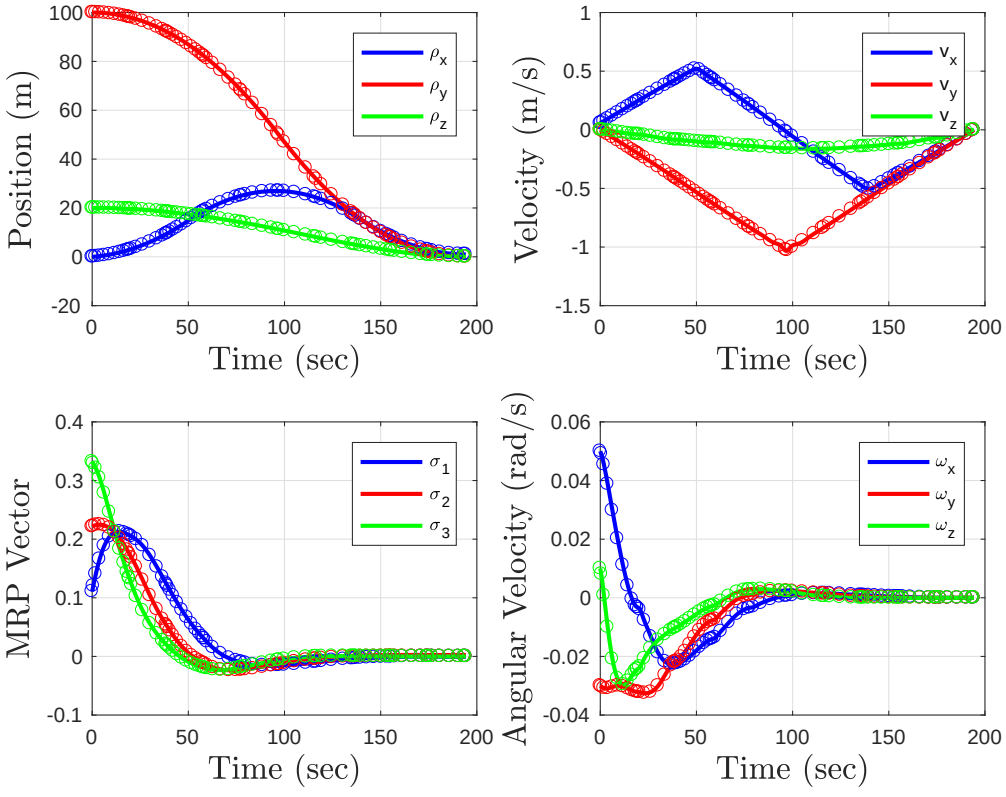

Figure 7.28. Case 4–state history for minimum time maneuver.

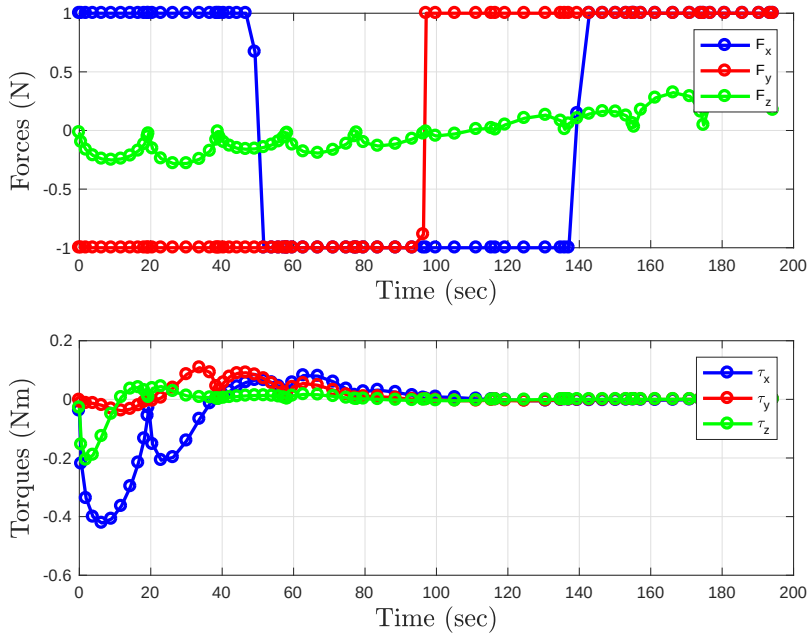

Figure 7.29. Case 4–control history for minimum time maneuver.

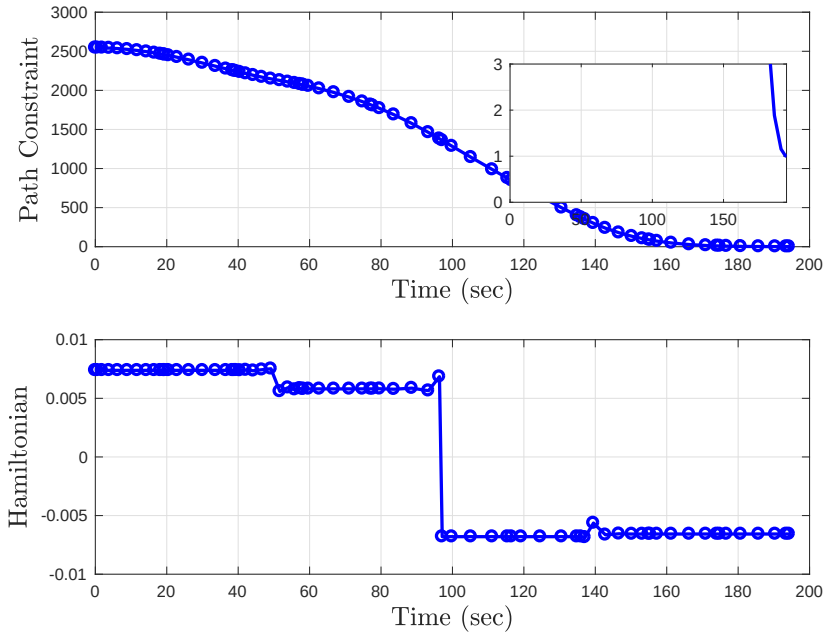

Figure 7.30. Case 4–verification of KOZ constraint satisfaction and time history of Hamiltonian.

NMPC Solution

Figure 7.31 shows the relative trajectory and the deputy and chief's orientations with respect to the LVLH CCS. The plots show four screenshots of the trajectory as the simulation progresses. A close-up view around the chief is included in each of the four plots. The time to rendezvous was 310 sec with control effort 605.62 Ns. The average time to solve the NMPC-OCP was 1.9 sec, with standard deviation of 0.42 sec. The maximum computation time was 4.33 sec.

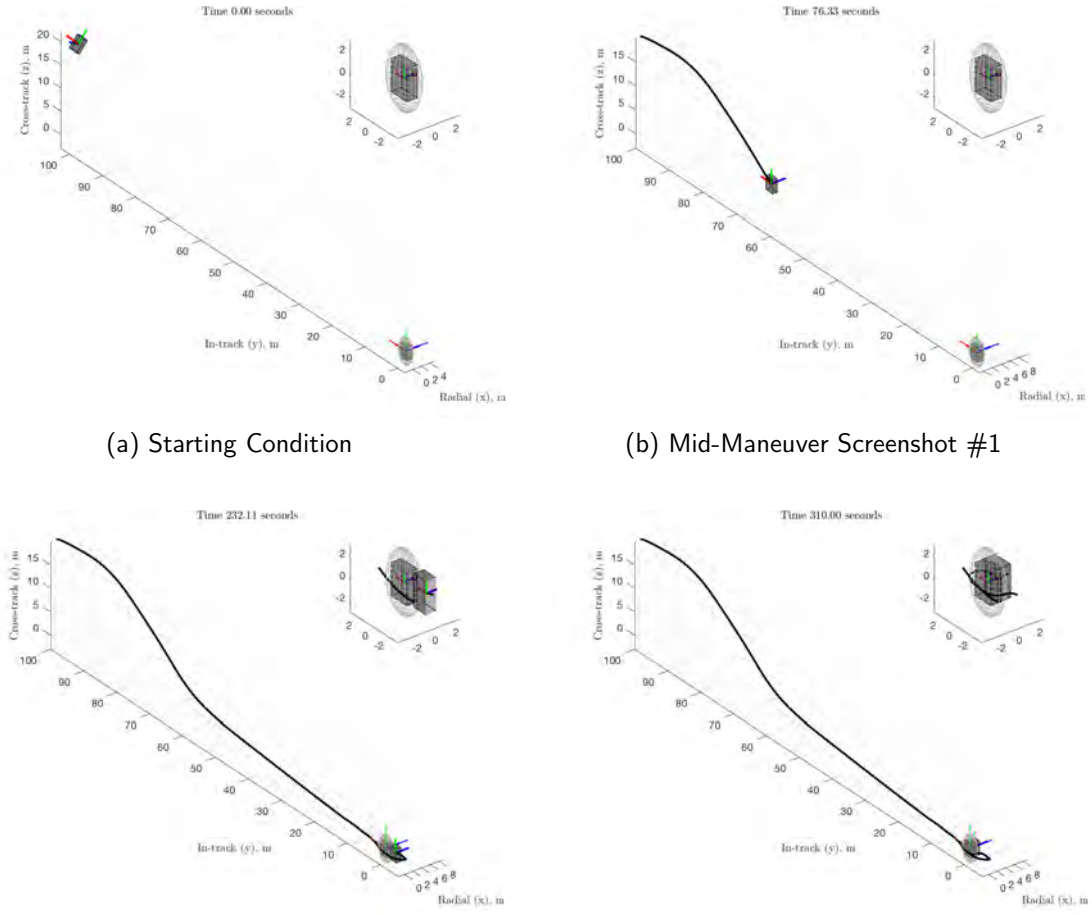

(a) Starting Condition

(b) Mid-Maneuver Screenshot #1

(c) Mid-Maneuver Screenshot #2

(d) Final Condition

Figure 7.31. Case 4–relative trajectory for NMPC maneuver.

Figure 7.32 shows the state history. The circles on these plots indicate the NMPC solution, while the lines indicate the state trajectories propagated independently with the NMPC

control values. The state errors were within the desired tolerances, as designed into the algorithm. Figure 7.33 shows the NMPC controls. In comparison the NMPC solution for Case 1, the NMPC solution in this case showed more aggressive control forces in the x direction, resulting in a higher control effort. From the trajectory in Figure 7.31d it can be seen that the solution in this case takes deputy behind and around the KOZ, where in Case 1 the trajectory remained in front of the KOZ (see Figure 7.7d). This result could be due to the ellipsoidal KOZ shape, as opposed to the spherical shape in Case 1. Due to the nonconvexity of the KOZ constraint, however, there exist multiple feasible solutions to this problem, and the algorithm in this case converged to a different, but still feasible, solution. As shown in Figure 7.34, constraint satisfaction and stability were maintained.

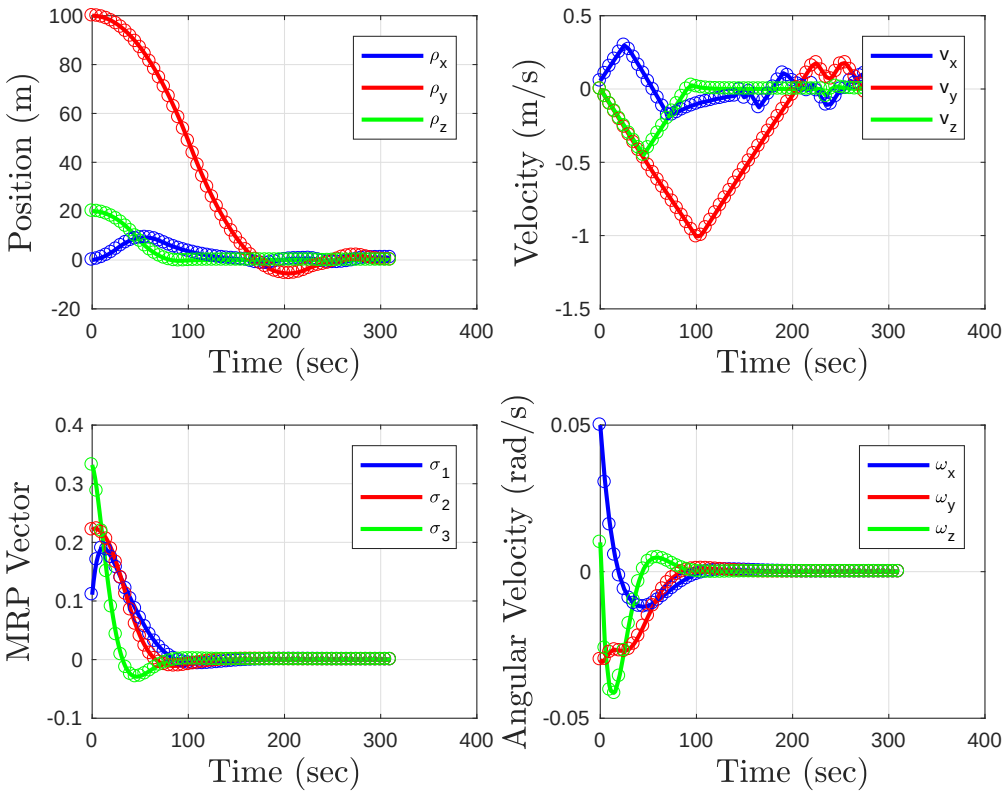

Figure 7.32. Case 4–state history for NMPC maneuver.

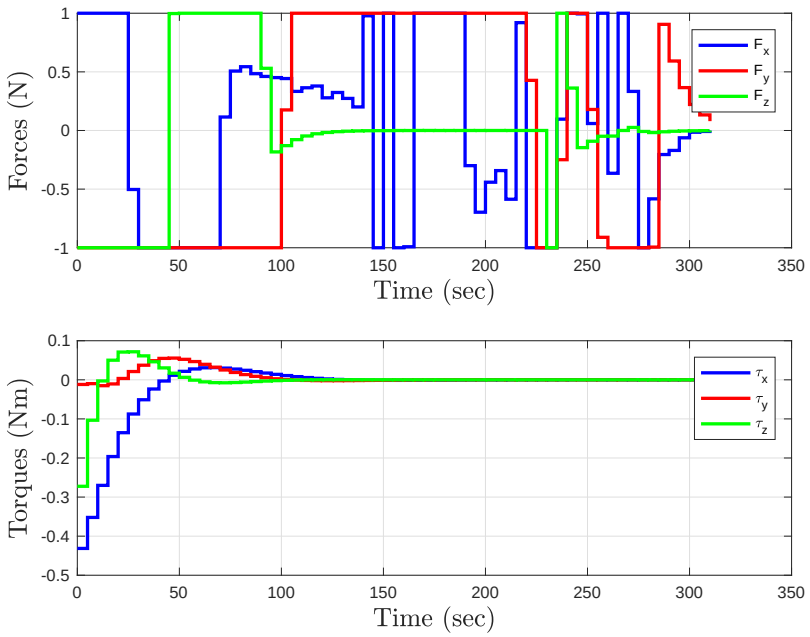

Figure 7.33. Case 4–control history for NMPC maneuver.

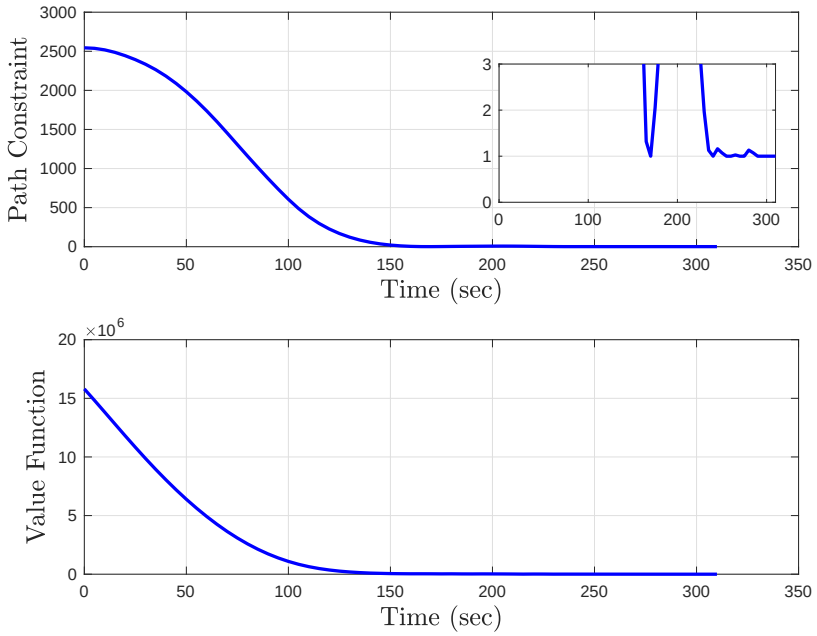

Figure 7.34. Case 4–verification of KOZ constraint satisfaction and time history of NMPC value function.

7.3.6 Case 5 Results

The MT-OCP and NMPC solutions for Case 5 are presented in Figures 7.35 - 7.42.

MT-OCP Solution

Figure 7.35 shows the relative trajectory and the deputy and chief's orientations with respect to the LVLH CCS. The plots show four screenshots of the trajectory as the simulation progresses. A close-up view around the chief is included in each of the four plots. The minimum time to rendezvous was 170.34 sec with control effort 522.65 Ns. The MT-OCP was solved in 34.17 sec.

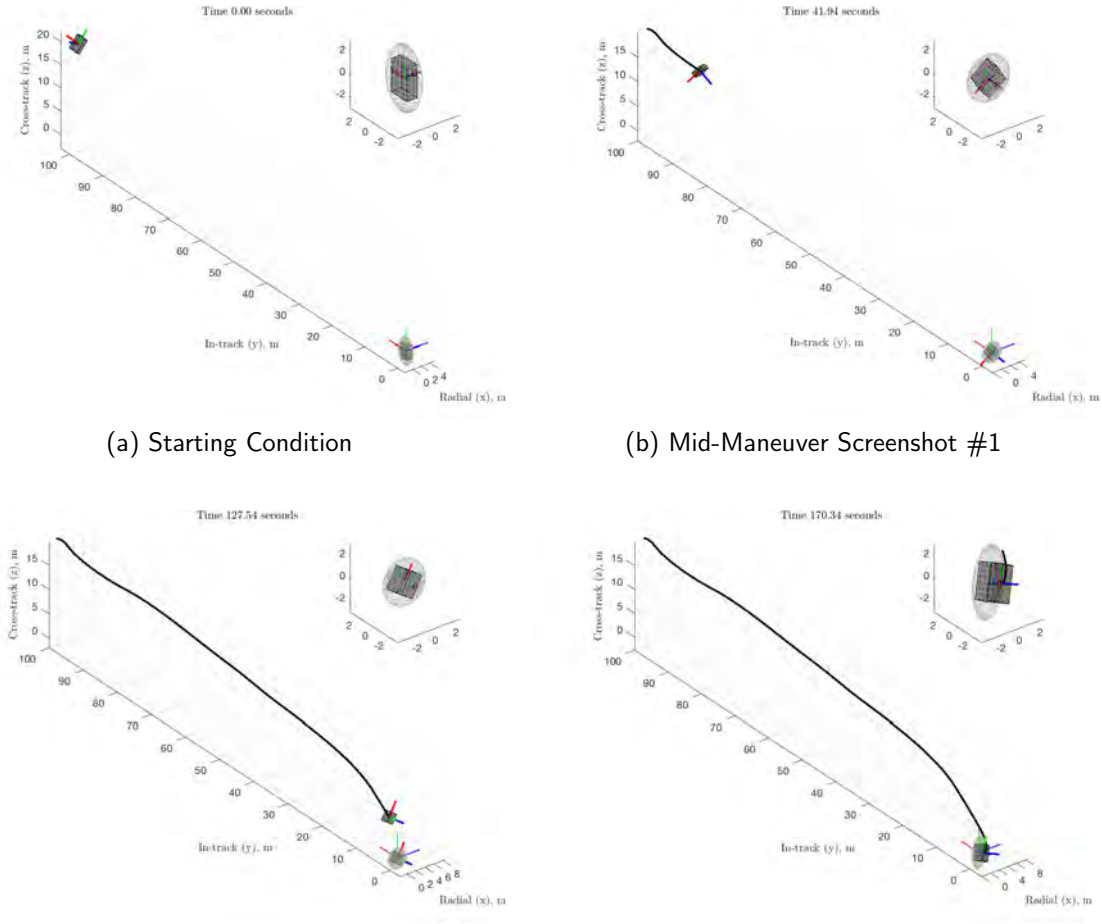

(a) Starting Condition

(b) Mid-Maneuver Screenshot #1

(c) Mid-Maneuver Screenshot #2

(d) Final Condition

Figure 7.35. Case 5–relative trajectory for minimum time maneuver.

Figure 7.36 shows the state history. The circles on these plots indicate the MT-OCP solution given by GPOPS-II, while the lines indicate the state trajectories propagated independently with the optimal control values. All state errors at the end of the maneuver in this case were small. Figure 7.37 shows the optimal controls. All three control forces exhibited bang-bang behavior, while the torques were oscillatory. Figure 7.38 shows the evaluation of the KOZ constraint, and the Hamiltonian for the MT-OCP trajectory. It is clear that collisions were successfully avoided. As with previous cases, there was no expectation on the Hamiltonian due to the time-varying nature of the dynamics.

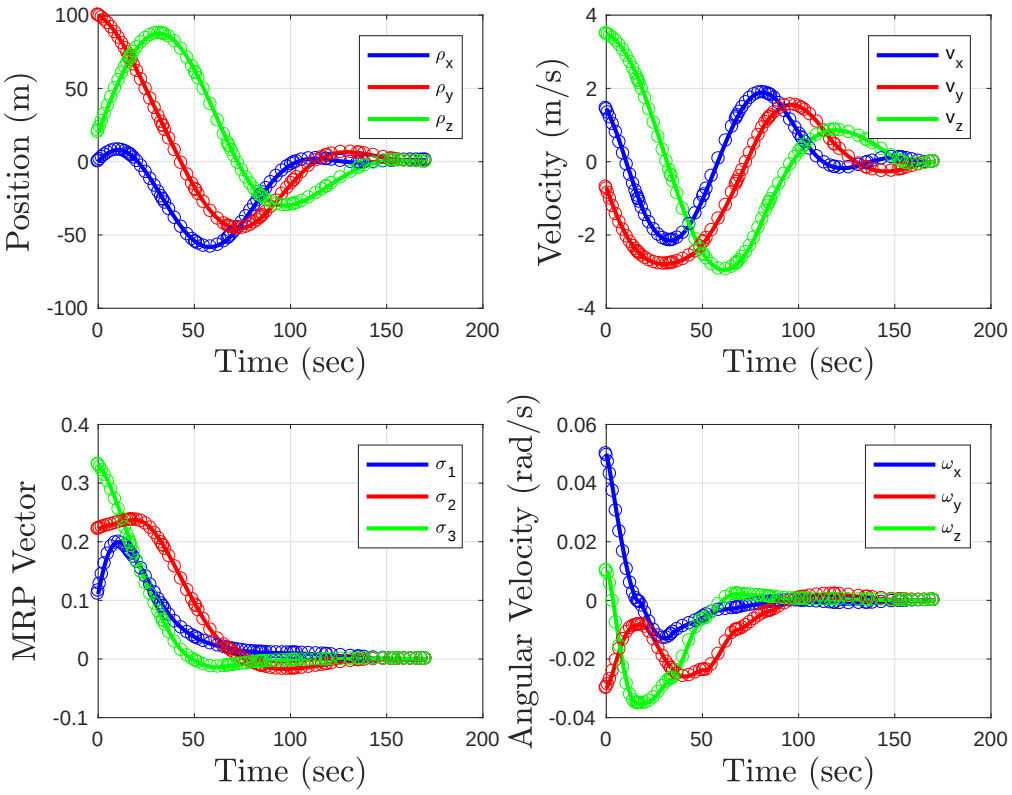

Figure 7.36. Case 5–state history for minimum time maneuver.

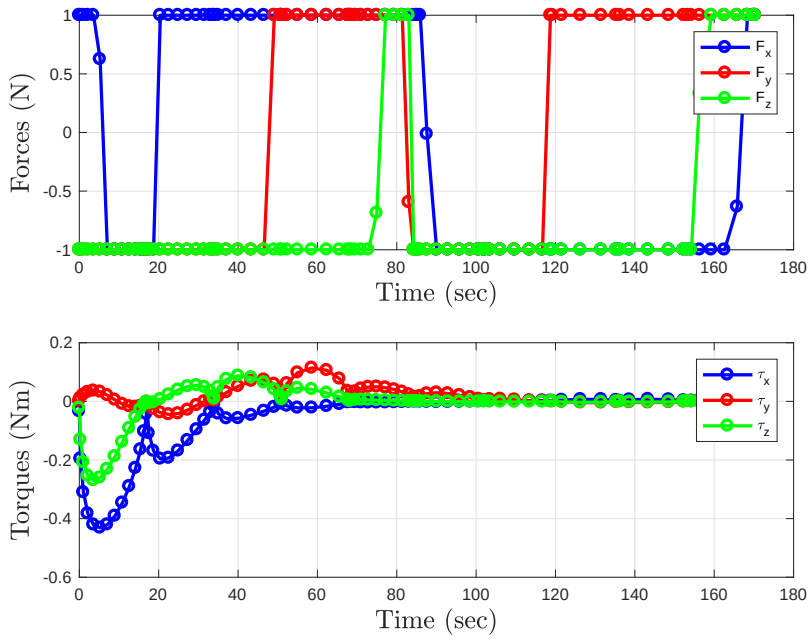

Figure 7.37. Case 5–control history for minimum time maneuver.

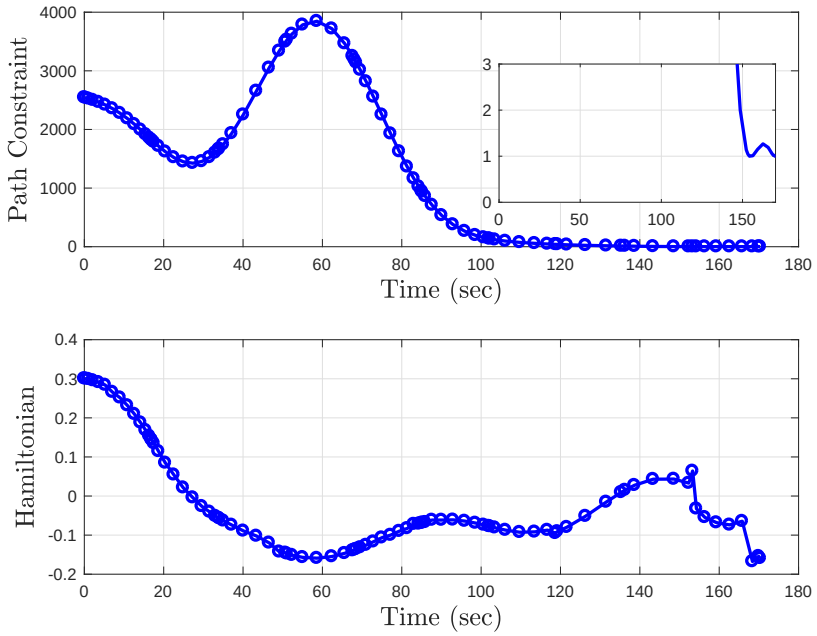

Figure 7.38. Case 5–verification of KOZ constraint satisfaction and time history of Hamiltonian.

NMPC Solution

Figure 7.39 shows the relative trajectory and the deputy and chief's orientations with respect to the LVLH CCS. The plots show four screenshots of the trajectory as the simulation progresses. A close-up view around the chief is included in each of the four plots. The time to rendezvous was 250 sec with control effort 624.78 Ns. The average time to solve the NMPC-OCP was 1.95 sec, with standard deviation of 0.41 sec. The maximum computation time was 3.86 sec.

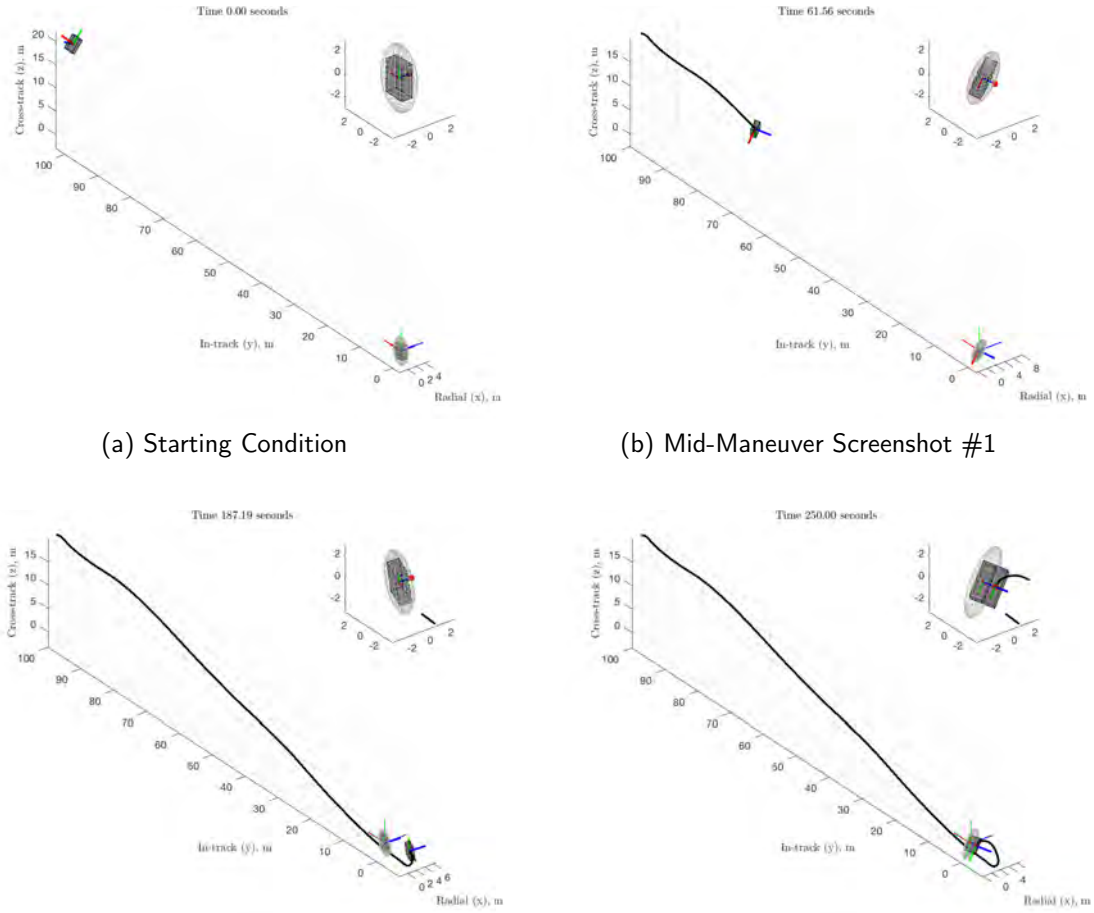

(a) Starting Condition

(b) Mid-Maneuver Screenshot #1

(c) Mid-Maneuver Screenshot #2

(d) Final Condition

Figure 7.39. Case 5–relative trajectory for NMPC maneuver.

Figure 7.40 shows the state history. The circles on these plots indicate the NMPC solution, while the lines indicate the state trajectories propagated independently with the NMPC

control values. The state errors were within the desired tolerances, as designed into the algorithm. Figure 7.41 shows the NMPC controls. As with the MT-OCP solution, the control forces in this case were at maximum values for the majority of the maneuver. As a result, the NMPC control effort is larger since the maneuver was longer than the minimum time maneuver. Further tuning of the NMPC algorithm could decrease the control effort, at the cost of increasing the maneuver time. As shown in Figure 7.42, constraint satisfaction and stability were maintained.

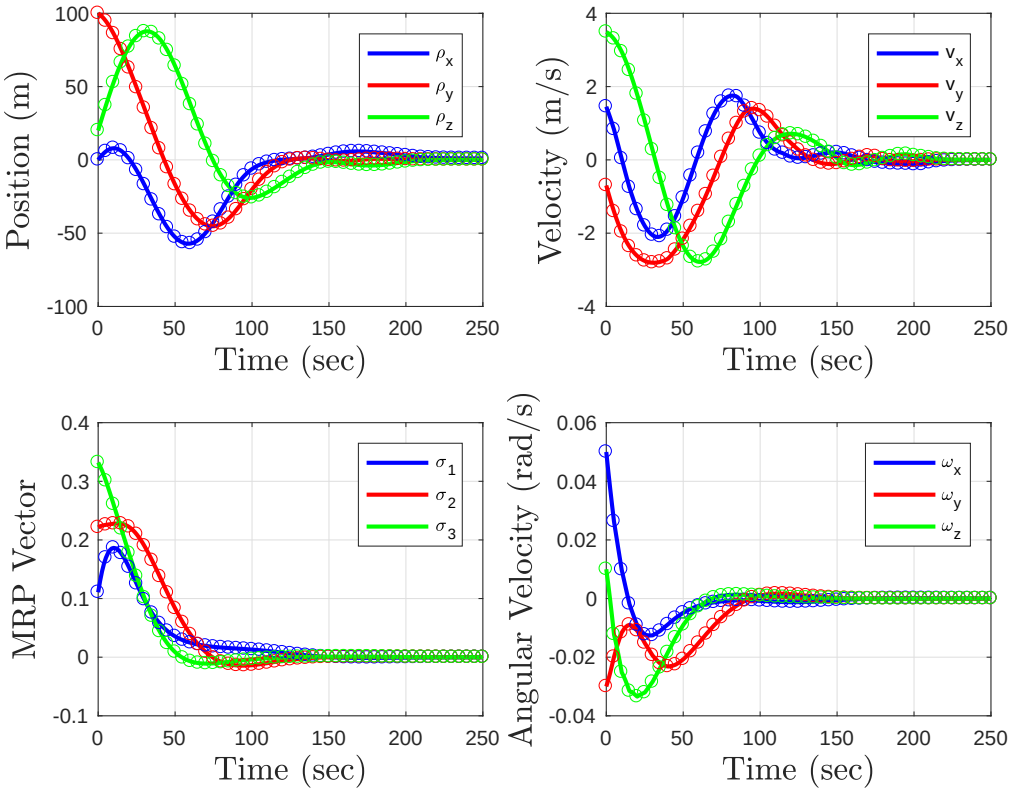

Figure 7.40. Case 5–state history for NMPC maneuver.

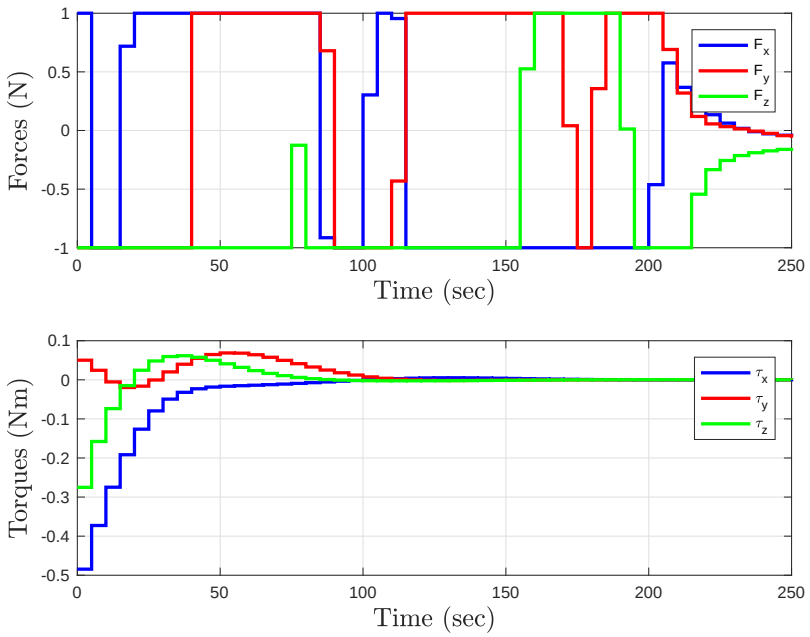

Figure 7.41. Case 5–control history for NMPC maneuver.

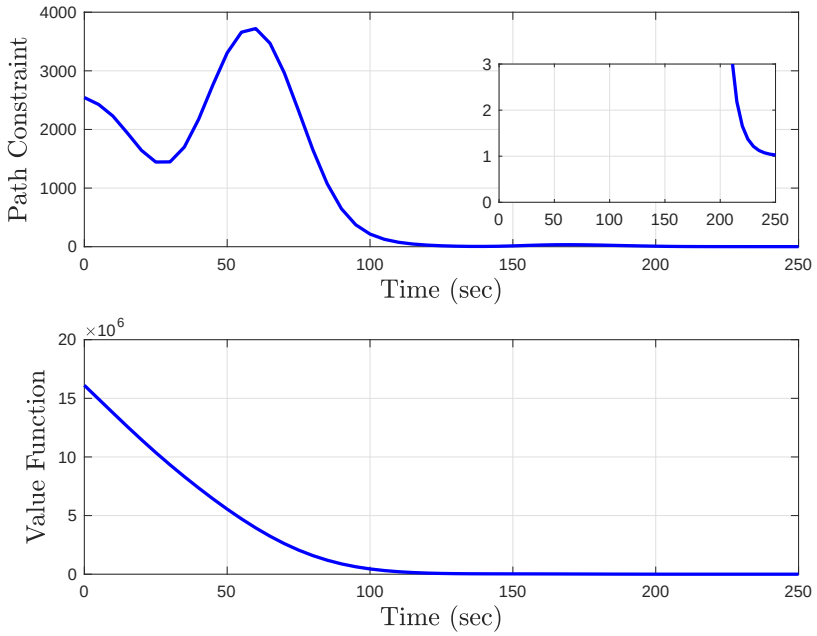

Figure 7.42. Case 5–verification of KOZ constraint satisfaction and time history of NMPC value function.

7.3.7 Case 6 Results

The MT-OCP and NMPC solutions for Case 6 are presented in Figures 7.43 - 7.50.

MT-OCP Solution

Figure 7.43 shows the relative trajectory and the deputy and chief's orientations with respect to the LVLH CCS. The plots show four screenshots of the trajectory as the simulation progresses. A close-up view around the chief is included in each of the four plots. The minimum time to rendezvous was 168.82 sec with control effort 506.03 Ns. The MT-OCP was solved in 25.88 sec.

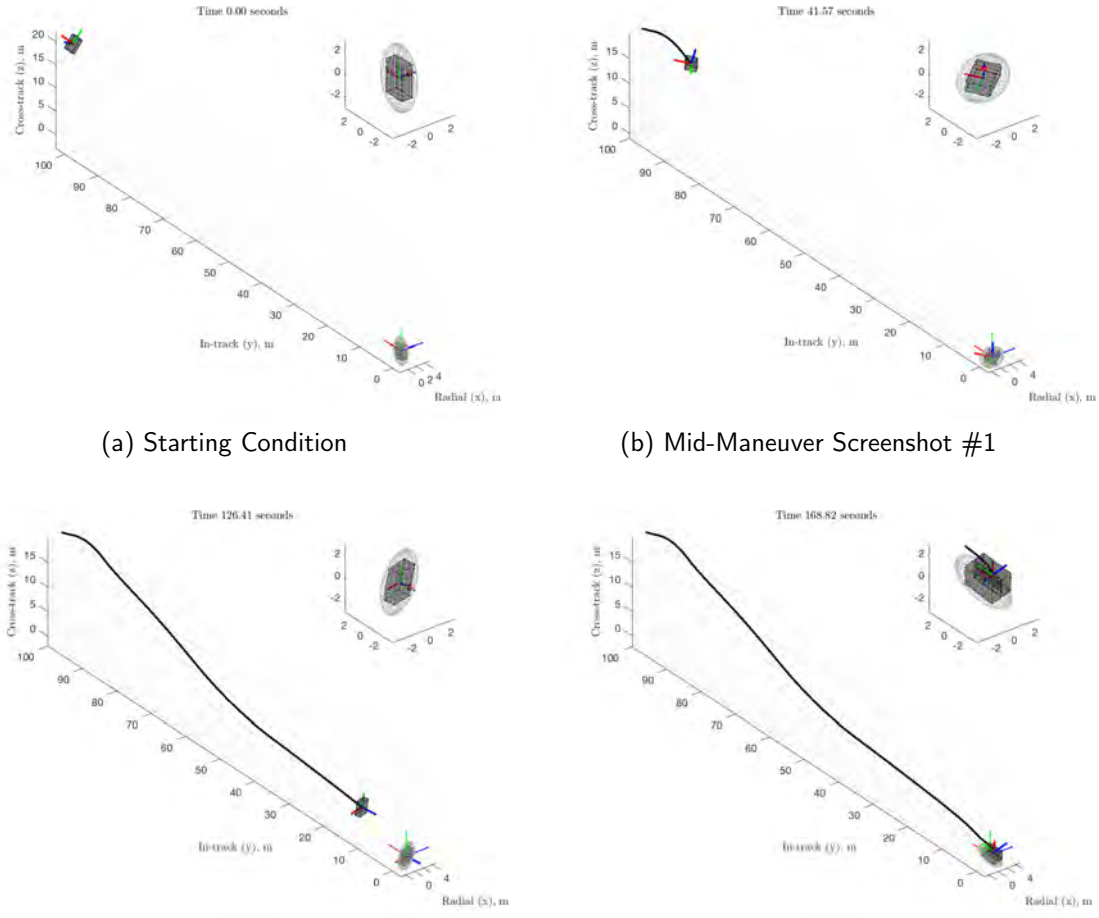

(a) Starting Condition

(b) Mid-Maneuver Screenshot #1

(c) Mid-Maneuver Screenshot #2

(d) Final Condition

Figure 7.43. Case 6–relative trajectory for minimum time maneuver.

Figure 7.44 shows the state history. The circles on these plots indicate the MT-OCP solution given by GPOPS-II, while the lines indicate the state trajectories propagated independently with the optimal control values. All state errors at the end of the maneuver in this case were small. Figure 7.45 shows the optimal controls. All three control forces exhibited bang-bang behavior, while the torques were oscillatory. Figure 7.46 shows the evaluation of the KOZ constraint, and the Hamiltonian for the MT-OCP trajectory. It is clear that collisions were successfully avoided. As with previous cases, there was no expectation on the Hamiltonian due to the time-varying nature of the dynamics.

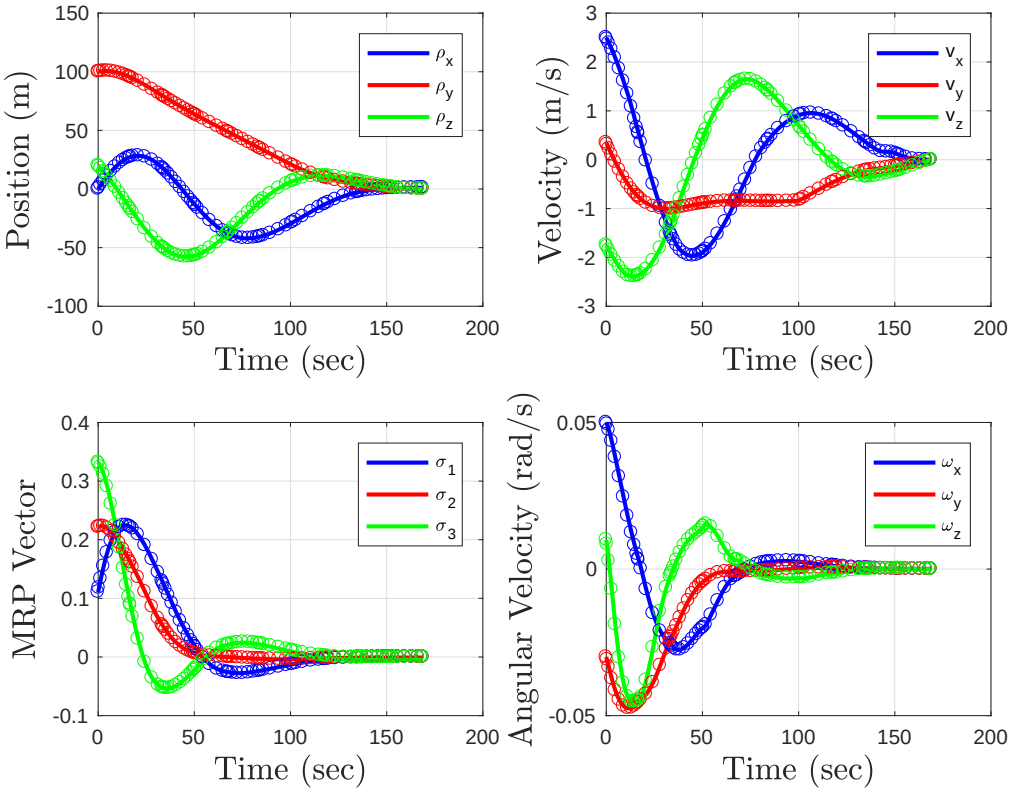

Figure 7.44. Case 6–state history for minimum time maneuver.

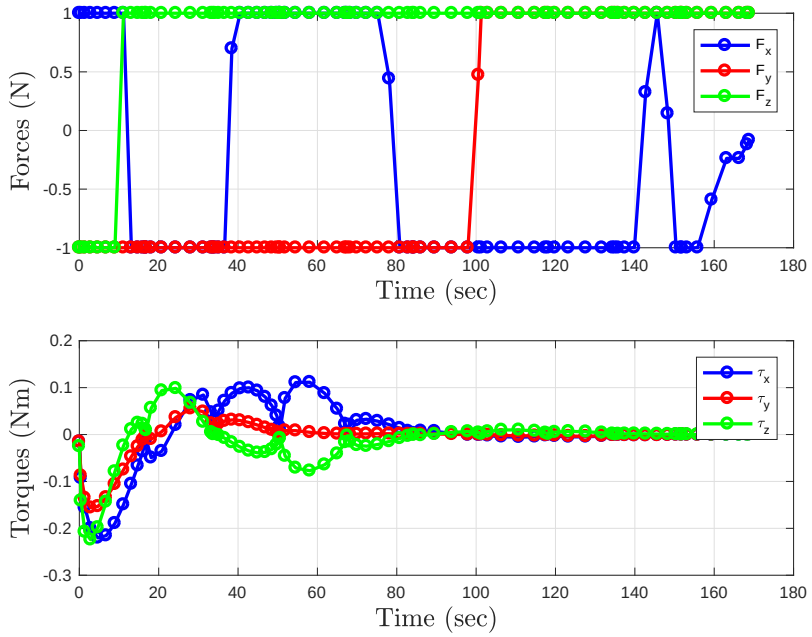

Figure 7.45. Case 6–control history for minimum time maneuver.

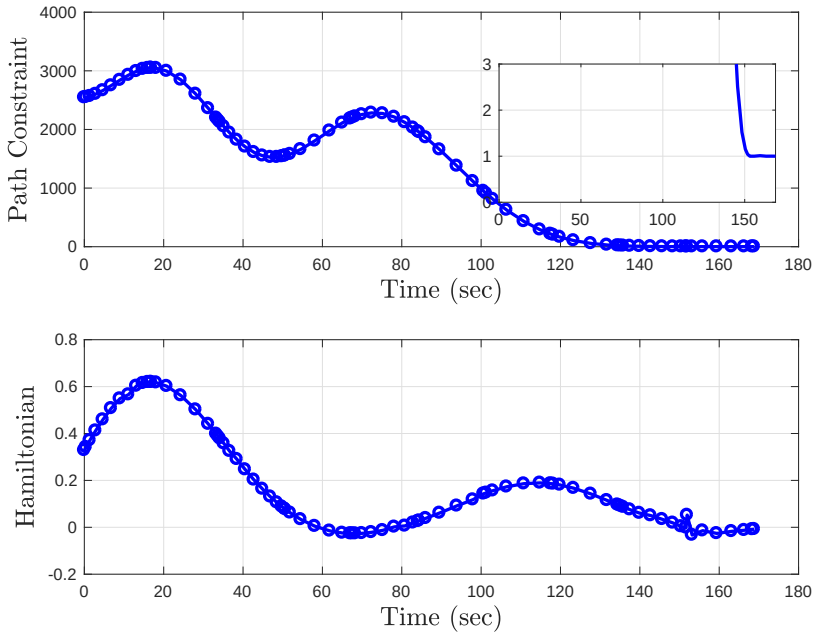

Figure 7.46. Case 6–verification of KOZ constraint satisfaction and time history of Hamiltonian.

NMPC Solution

Figure 7.47 shows the relative trajectory and the deputy and chief's orientations with respect to the LVLH CCS. The plots show four screenshots of the trajectory as the simulation progresses. A close-up view around the chief is included in each of the four plots. The time to rendezvous was 365 sec with control effort 926.35 Ns. The average time to solve the NMPC-OCP was 1.3 sec, with standard deviation of 0.52 sec. The maximum computation time was 4.04 sec.

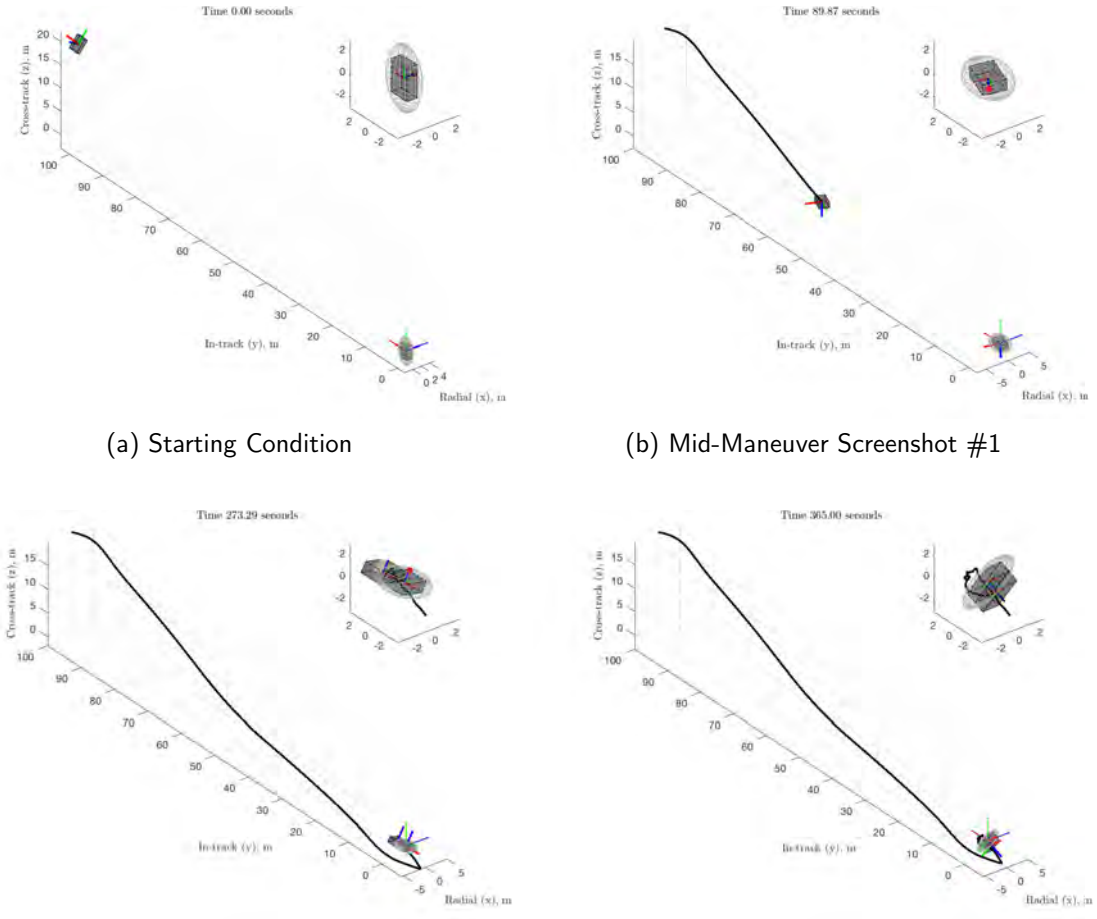

(a) Starting Condition

(b) Mid-Maneuver Screenshot #1

(c) Mid-Maneuver Screenshot #2

(d) Final Condition

Figure 7.47. Case 6–relative trajectory for NMPC maneuver.

Figure 7.48 shows the state history. The circles on these plots indicate the NMPC solution, while the lines indicate the state trajectories propagated independently with the NMPC

control values. The state errors were within the desired tolerances, as designed into the algorithm. Figure 7.49 shows the NMPC controls. The NMPC solution for this case exhibited the largest control effort. In Figure 7.49 the control force in the z direction shows some chattering starting at about 200 *sec*. Examining the path constraint in Figure 7.50 reveals that at 200 *sec* the deputy is at the edge of the KOZ constraint, and stays along the edge for the remainder of the maneuver. This can also be seen in Figure 7.47c where the deputy and chief are shown side-by-side. The chattering in the control input is likely due to the deputy trying to achieve the rendezvous condition while on the edge of the KOZ constraint.

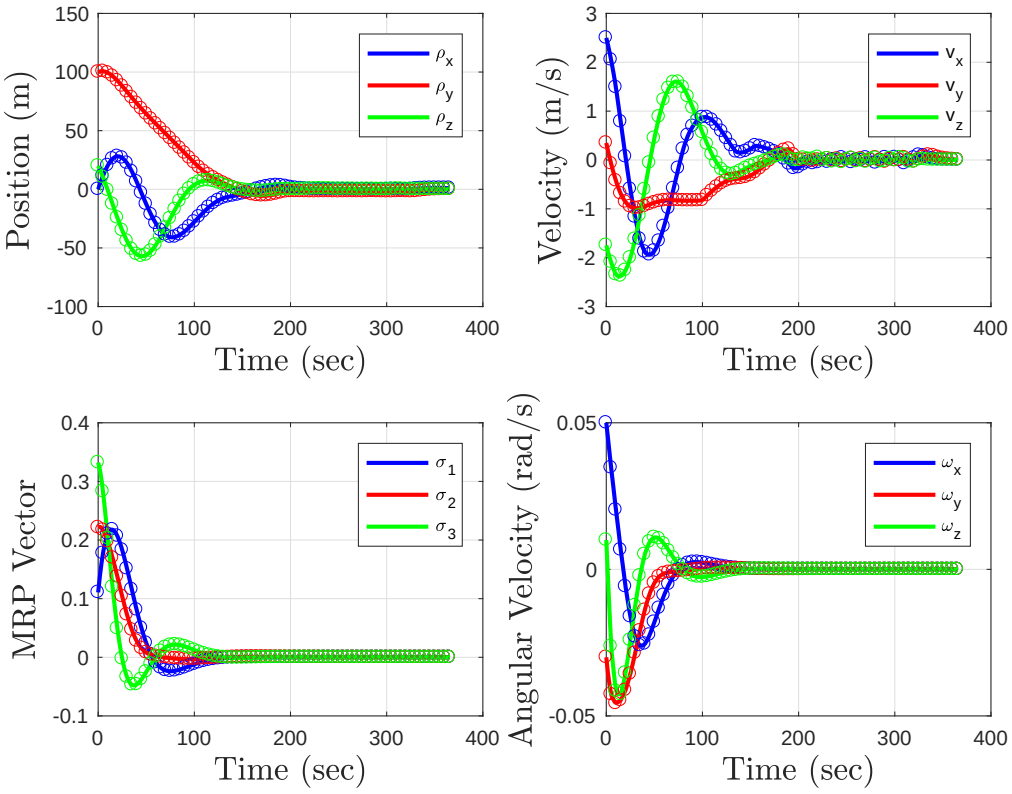

Figure 7.48. Case 6–state history for NMPC maneuver.

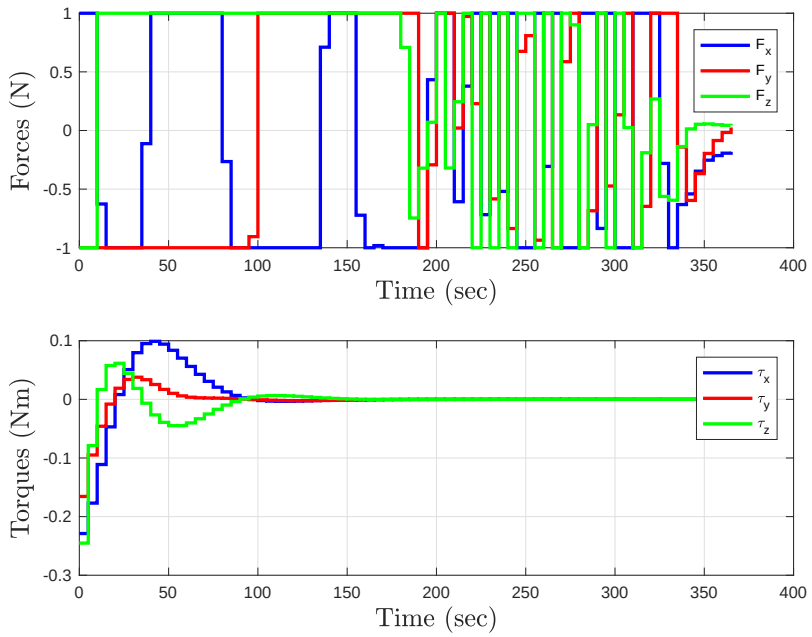

Figure 7.49. Case 6–control history for NMPC maneuver.

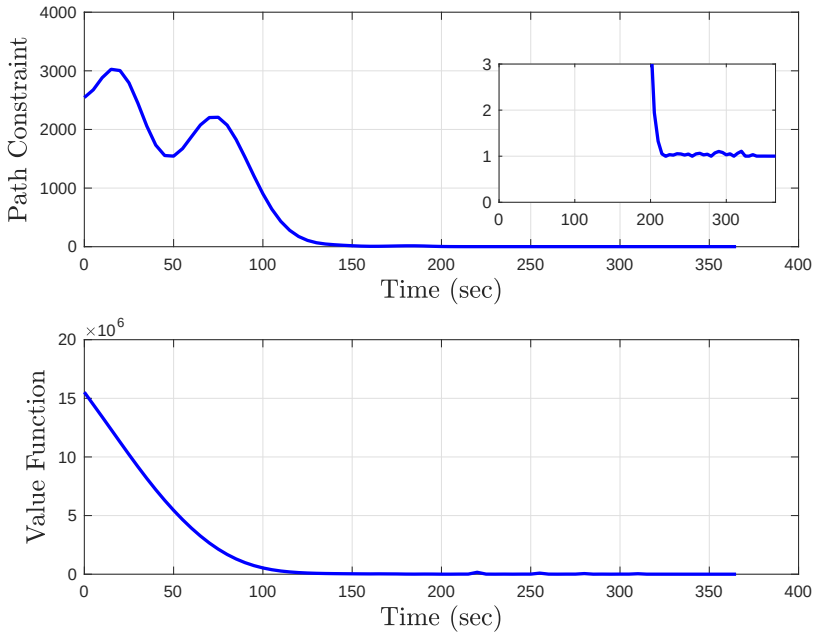

Figure 7.50. Case 6–verification of KOZ constraint satisfaction and time history of NMPC value function.

7.3.8 Case 7 Results

The MT-OCP and NMPC solutions for Case 7 are presented in Figures 7.51 - 7.58.

MT-OCP Solution

Figure 7.51 shows the relative trajectory and the deputy and chief's orientations with respect to the LVLH CCS. The plots show four screenshots of the trajectory as the simulation progresses. A close-up view around the chief is included in each of the four plots. The minimum time to rendezvous was 175.49 sec with control effort 538.85 Ns. The MT-OCP was solved in 32.72 sec.

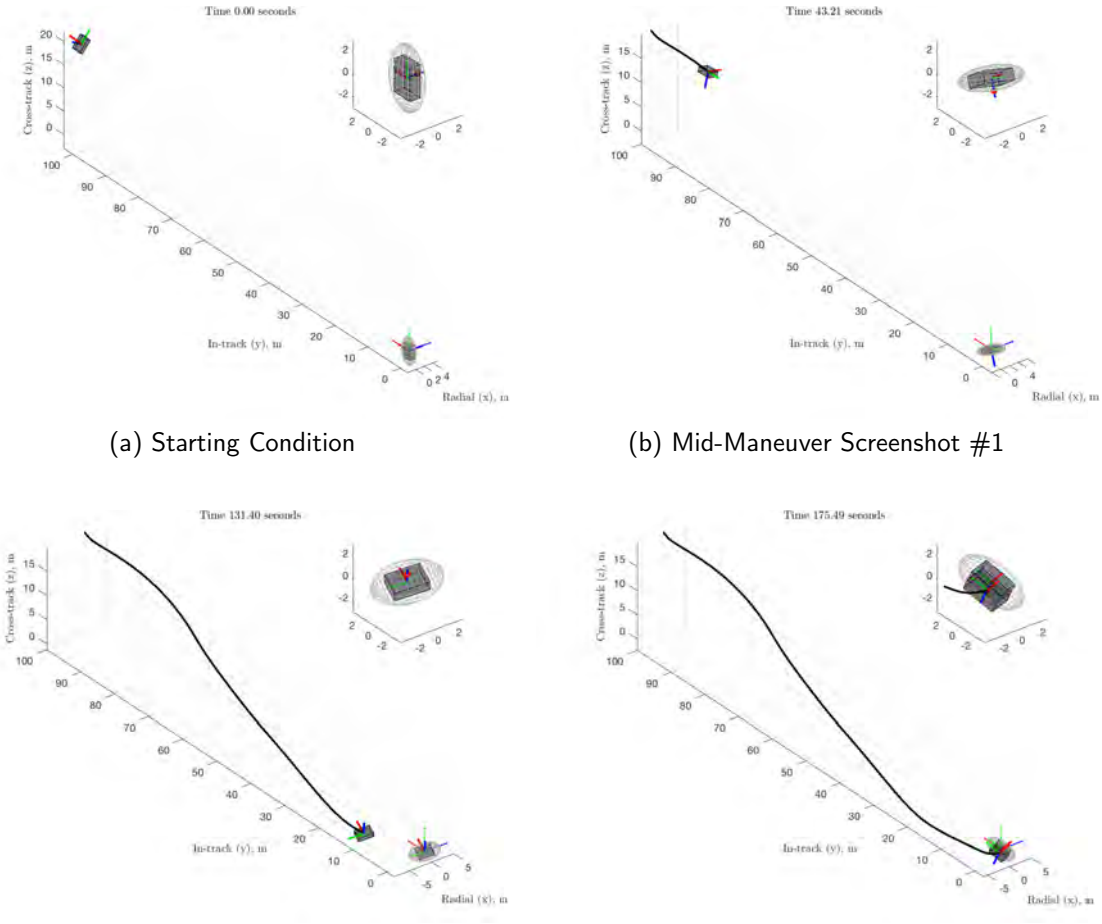

(a) Starting Condition

(b) Mid-Maneuver Screenshot #1

(c) Mid-Maneuver Screenshot #2

(d) Final Condition

Figure 7.51. Case 7–relative trajectory for minimum time maneuver.

Figure 7.52 shows the state history. The circles on these plots indicate the MT-OCP solution given by GPOPS-II, while the lines indicate the state trajectories propagated independently with the optimal control values. All state errors at the end of the maneuver in this case were small. Figure 7.53 shows the optimal controls. All three control forces exhibited bang-bang behavior, while the torques were oscillatory. Figure 7.54 shows the evaluation of the KOZ constraint, and the Hamiltonian for the MT-OCP trajectory. It is clear that collisions were successfully avoided. As with previous cases, there was no expectation on the Hamiltonian due to the time-varying nature of the dynamics.

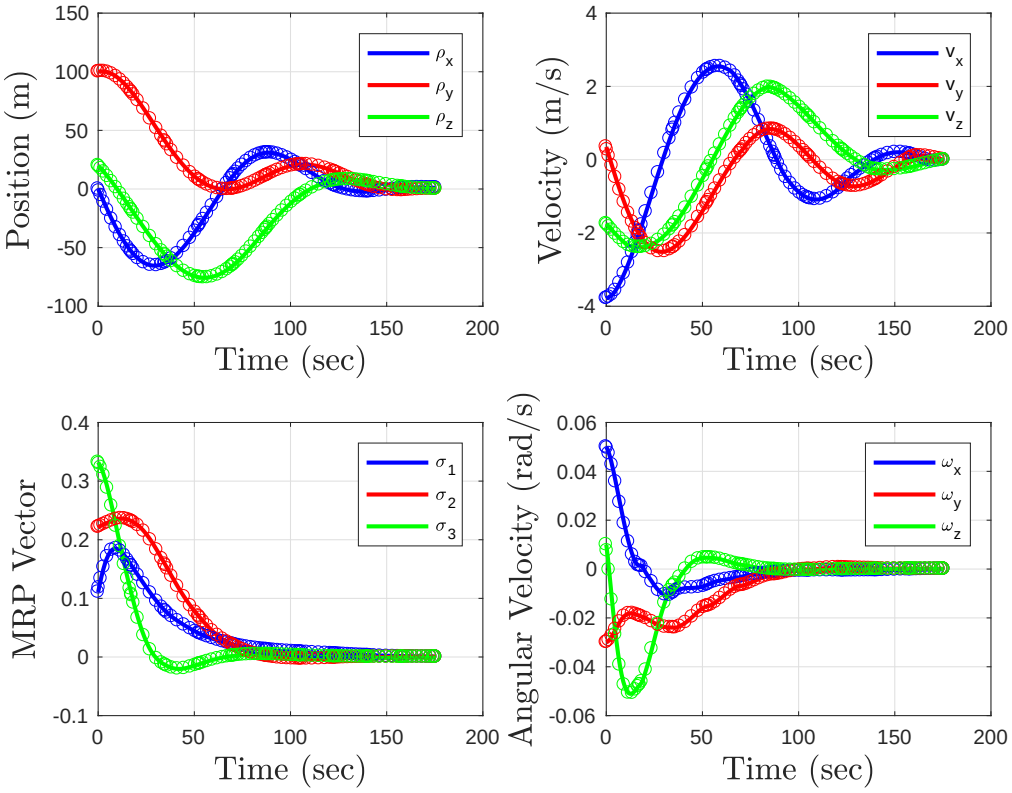

Figure 7.52. Case 7–state history for minimum time maneuver.

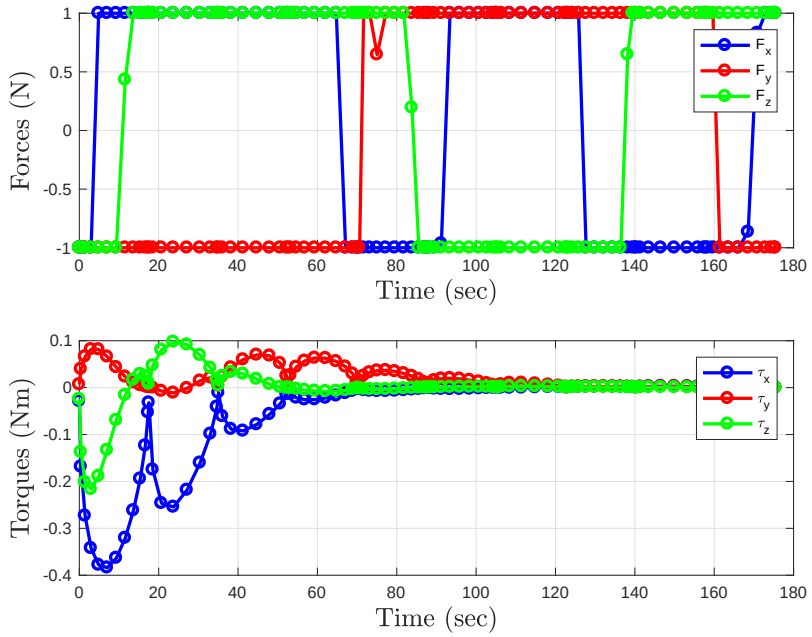

Figure 7.53. Case 7–control history for minimum time maneuver.

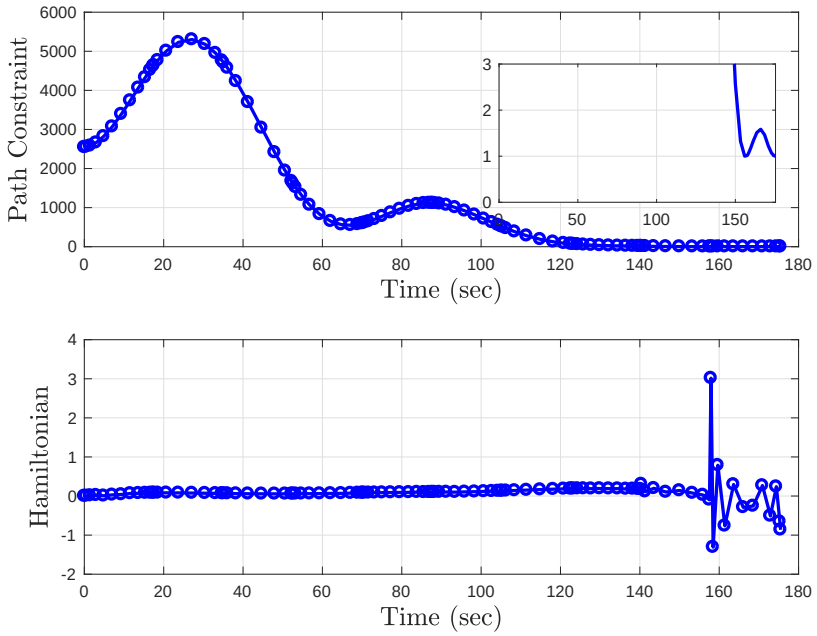

Figure 7.54. Case 7–verification of KOZ constraint satisfaction and time history of Hamiltonian.

NMPC Solution

Figure 7.55 shows the relative trajectory and the deputy and chief's orientations with respect to the LVLH CCS. The plots show four screenshots of the trajectory as the simulation progresses. A close-up view around the chief is included in each of the four plots. The time to rendezvous was 245 sec with control effort 620.88 Ns. The average time to solve the NMPC-OCP was 1.32 sec, with standard deviation of 0.45 sec. The maximum computation time was 3.99 sec.

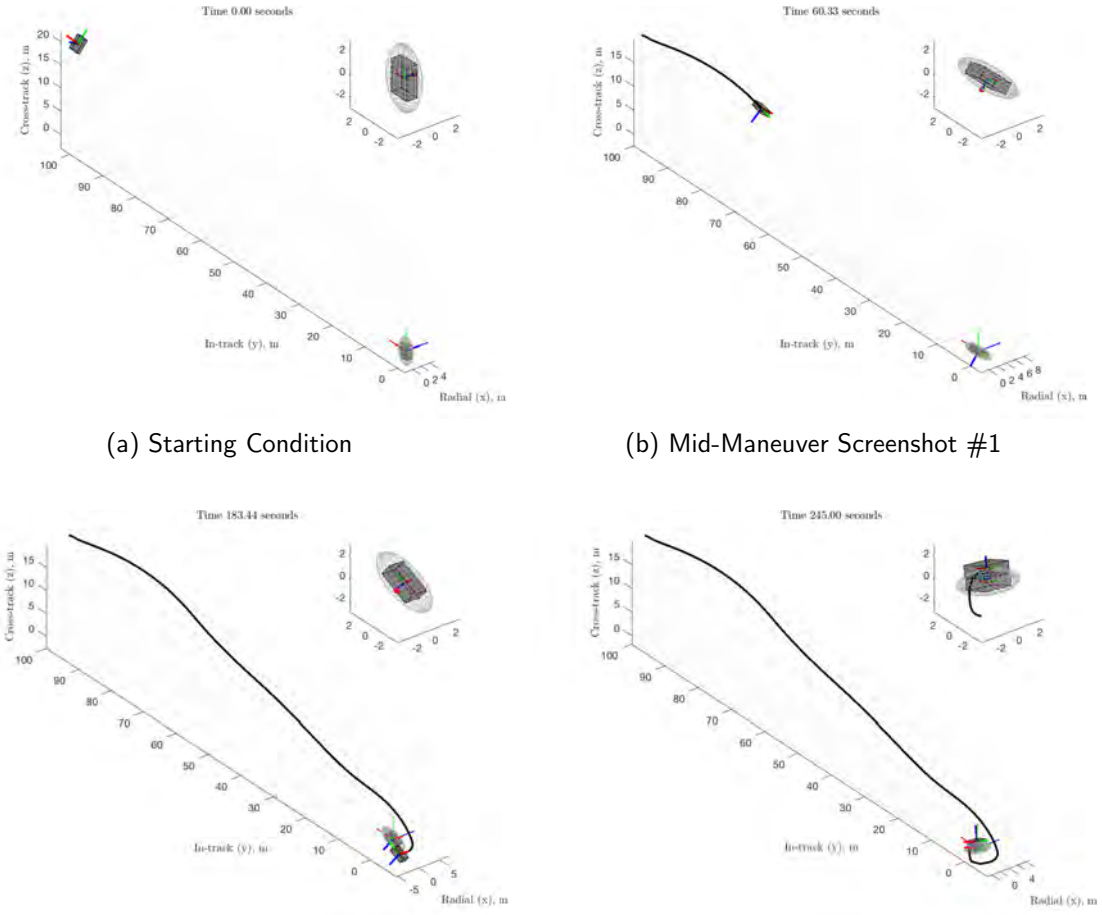

(a) Starting Condition

(b) Mid-Maneuver Screenshot #1

(c) Mid-Maneuver Screenshot #2

(d) Final Condition

Figure 7.55. Case 7–relative trajectory for NMPC maneuver.

Figure 7.56 shows the state history. The circles on these plots indicate the NMPC solution, while the lines indicate the state trajectories propagated independently with the NMPC

control values. The state errors were within the desired tolerances, as designed into the algorithm. Figure 7.57 shows the NMPC controls. As with the MT-OCP solution, the control forces in this case were at maximum values for the majority of the maneuver. As a result, the NMPC control effort is larger since the maneuver was longer than the minimum time maneuver. Further tuning of the NMPC algorithm could decrease the control effort, at the cost of increasing the maneuver time. As shown in Figure 7.58, constraint satisfaction and stability were maintained.

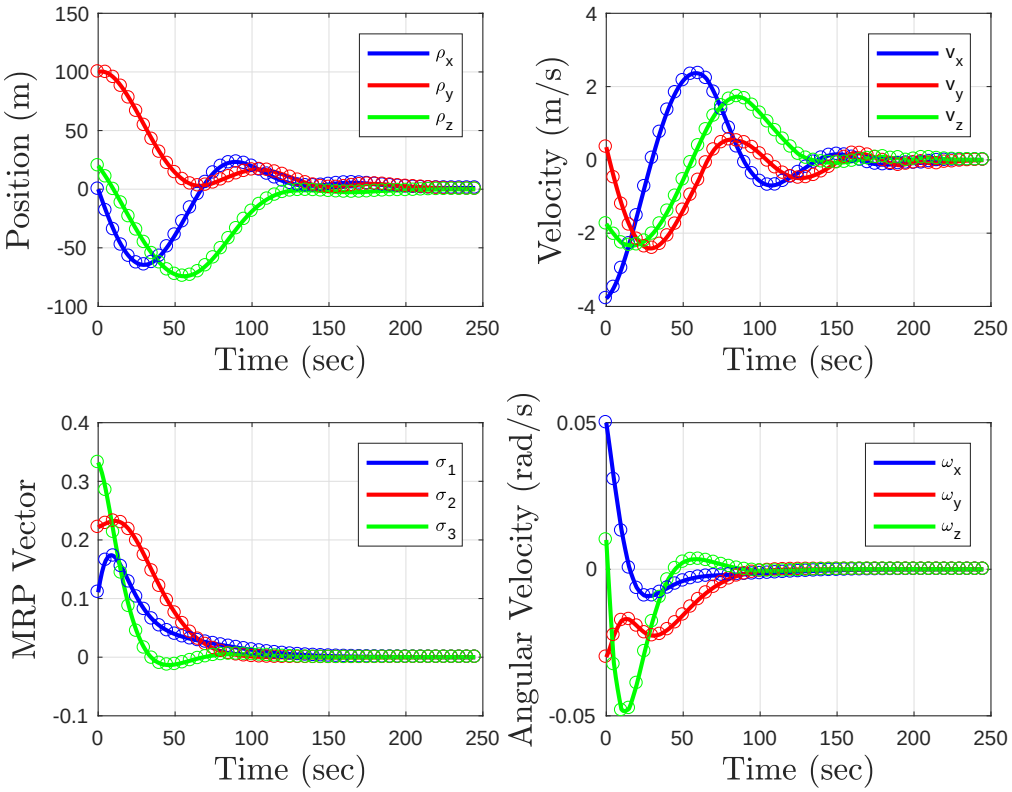

Figure 7.56. Case 7–state history for NMPC maneuver.

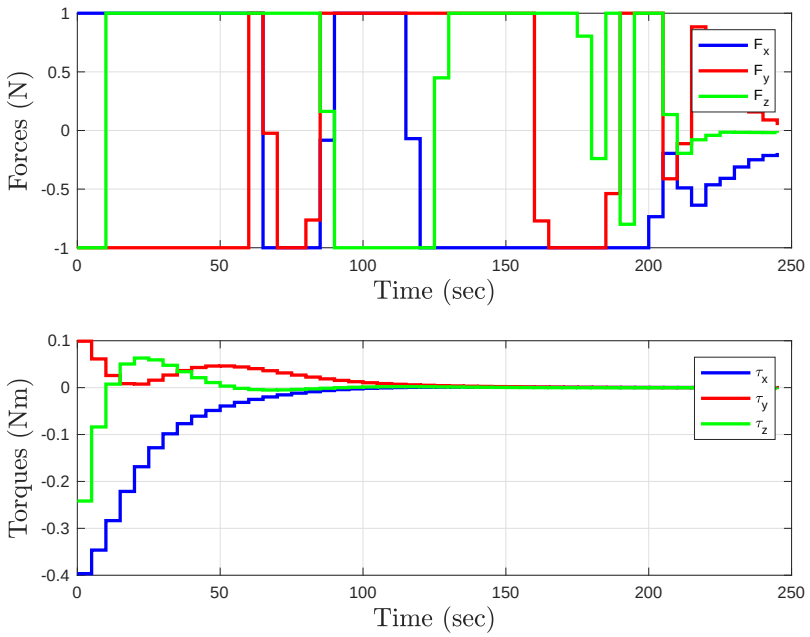

Figure 7.57. Case 7–control history for NMPC maneuver.

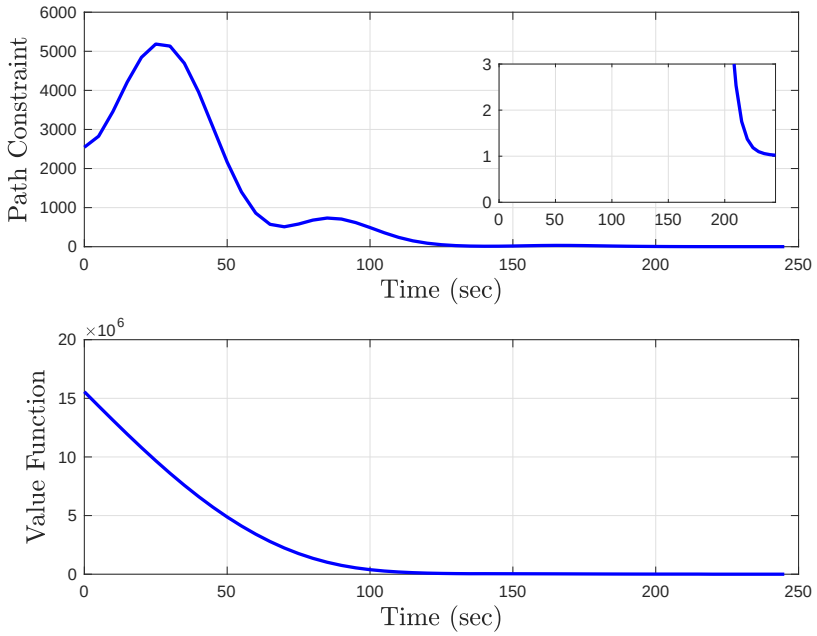

Figure 7.58. Case 7–verification of KOZ constraint satisfaction and time history of NMPC value function.

7.4 Unreachable Case

The test cases presented in the previous section showed examples of successful rendezvous maneuvers maneuvers. In a situation where the initial relative state is not within the backward T-reachable set, for the allowed 1000 sec, the maneuver is by definition infeasible. In this case it would be expected that the NMPC algorithm would not succeed. In order to illustrate this point, a case was selected from the previous applied reachability analysis that is outside of the backward reachable set.

The unreachable case was selected from the analysis conducted in Chapter 4. The initial condition is set as $\boldsymbol{\rho}_0 = [100, 100, 0]^T\ m$, $\boldsymbol{v}_0 = [0, 0, 0]^T\ m/s$, $\boldsymbol{\sigma}_0 = [0.1107, 0.2214, 03321]^T$, and $\boldsymbol{\omega}_0 = [0.05, -0.03, 0.01]^T\ rad/s$. The chief and deputy spacecraft are spherically symmetric, and the chief is rotating on the orbit plane with $\boldsymbol{\omega}_{\mathsf{C/L}} = [0,\ 0,\ 4]^T\ deg/s$. The applied reachability analysis presented in Figure 4.11c shows that from this relative position, with zero relative velocity, the rendezvous state is not reachable.

The GPOPS-II solver for this case reported that the MT-OCP is infeasible, as expected. Without any knowledge of the inherent infeasibility of this scenario, the NMPC algorithm attempted the maneuver. Figure 7.59 shows the resulting state history, Figure 7.60 shows the control history, and Figure 7.61 shows the path constraint and NMPC cost functional history. It is clear that the deputy was not able to reach the rendezvous condition, even though the algorithm solved successfully throughout the $1,000\ sec$ simulation. The NMPC cost functional history in Figure 7.61 reveals a stability issue in this case since the value is not monotonically decreasing. This result highlights the importance of reachability analysis before the application of an autonomous guidance algorithm.

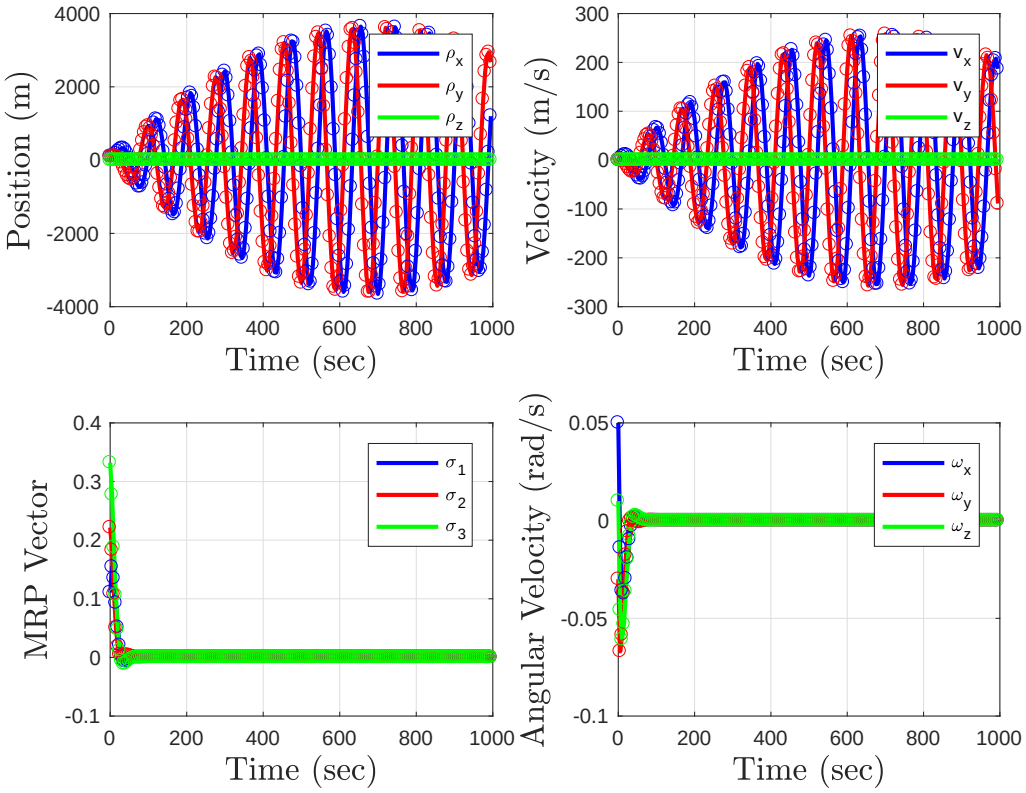

Figure 7.59. Unreachable case–state history for NMPC maneuver.

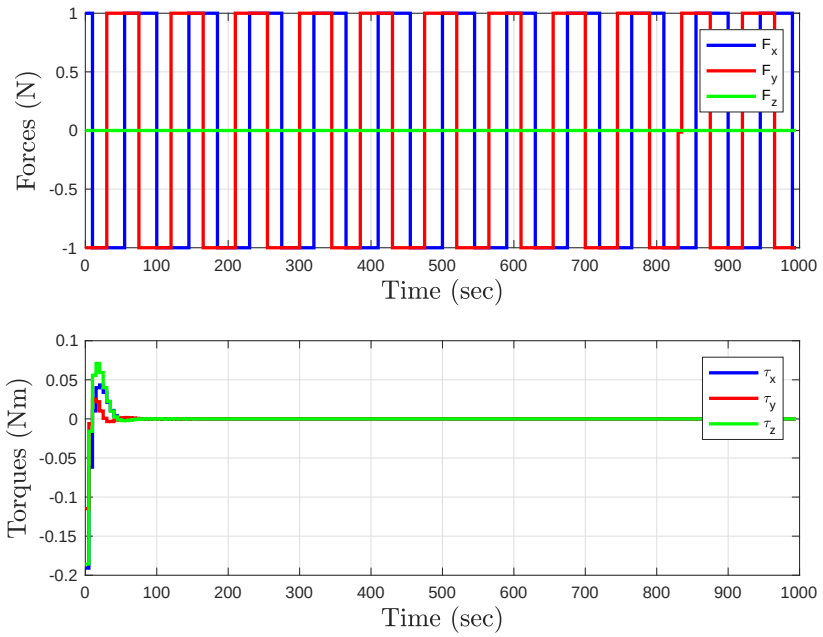

Figure 7.60. Unreachable case–control history for NMPC maneuver.

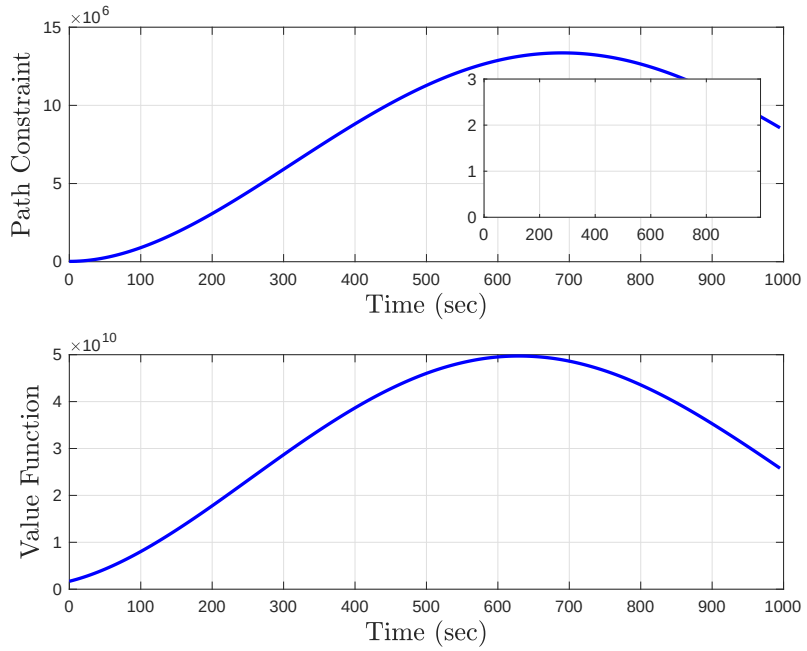

Figure 7.61. Unreachable case–verification of KOZ constraint satisfaction and time history of NMPC value function.

7.5 Summary

This chapter applied the MPC framework to the problem of spacecraft rendezvous with a tumbling chief, in the presence of control and collision avoidance constraints. Seven test cases were developed to validate the NMPC control algorithm in simulation and compare performance to the MT-OCP in terms of maneuver time, control effort, computation time, and state error at the time of rendezvous. The general trend of the results was that the NMPC solution exhibited higher control effort than the MT-OCP, which was attributed to the tuning parameters within the NMPC algorithm. As a feedback controller, the algorithm focuses on minimizing the state error along the trajectory (tuned through the Q matrix) which resulted in some aggressive control behavior in order to drive the state to the desired values. Minimization of the expended control effort is tuned through the R matrix. Further tuning of the algorithm could result in decreased control effort, at the cost of a longer duration maneuver.

Results showed that the NMPC computation time was, on average, about the same for all cases and under 2 sec. With a sampling time of 5 sec, solving this problem on-board, in real time, would be feasible. In a couple of cases, specifically Cases 2 and 3, the maximum NMPC computation time was higher than 5 sec. From a practical standpoint, if a solution is not available after 5 sec, the algorithm could use the next control from the previous optimal control sequence. Another advantage offered by the NMPC algorithm is that the state errors for all cases were fairly consistent, since a tolerance on the state error is designed into the selection of the Q weighting parameters. All cases showed that this implementation of MPC was stabilizing since the value function was monotonically decreasing.

Finally, an unreachable case was attempted to illustrate that the NMPC algorithm would be unsuccessful, and highlight the importance of applied reachability analysis before implementation of an autonomous guidance algorithm. The research contributions offered in this chapter are shown in Table 7.5.

Table 7.5. Research contributions in Chapter 7.

Contribution	Objective
Validation of NMPC algorithm for 6-DOF autonomous rendezvous with tumbling object	3

Part IV

Concluding Material

THIS PAGE INTENTIONALLY LEFT BLANK

CHAPTER 8:
Conclusion

This chapter closes the dissertation by summarizing the research that was accomplished and the contributions to the field. Additionally, some future research directions are discussed as a potential extension to the work herein.

8.1 Research Summary

The problem of autonomous spacecraft rendezvous with a tumbling object was studied. Although GNC algorithms for this type of mission have been presented in previous publications, a research gap was identified in the fundamental analysis of the relative spacecraft dynamics under the consideration of a tumbling chief spacecraft.

Recent advancements in computing technologies enable the use of more sophisticated CG&C algorithms, instead of traditional control methods. These algorithms are desirable for autonomous applications due to their ability to optimize performance and explicitly handle constraints (e.g., safety, control limits). In an autonomous setting, however, some important questions must be answered before an algorithm implementation can be realized. These questions were the focus of this research.

The first research question addressed the feasibility of a maneuver by analyzing the spacecraft relative dynamics. Specifically, a backward reachability analysis was conducted in order to find a set of initial conditions from which rendezvous maneuvers are possible. This analysis is important as it provides insight into the inherent capabilities of the dynamic system. With these capabilities well understood, an autonomous, computation-based, guidance algorithm can be applied to the rendezvous problem, with confidence that a solution exists. Due to the complexity of the 6-DOF relative dynamics, reachability computations are intractable with current tools. In this research, a method was proposed to conduct reachability analysis on user-defined subspaces by exploiting the relationship between reachability and time optimal control. It was shown that boundaries of backward reachable sets can be visualized as minimum time contours over the subspace of interest. Utilizing this methodology, reachability analysis of the 6-DOF system became tractable.

The second research question addressed the autonomous guidance problem by utilizing the MPC framework. MPC is a finite horizon, optimization-based, control approach that can handle dynamically changing constraints. The underlying MPC optimization problem solves for the sequence of optimal control inputs for a subinterval of the problem (i.e., the prediction horizon), while taking into account the system dynamics and constraints. In a feedback framework, the first control value from the sequence is applied to the system and the problem is solved again at the next iteration. The recursive feasibility, and stability properties of MPC were discussed, culminating in the development of a stabilizing MPC algorithm for the 6-DOF autonomous spacecraft rendezvous problem.

8.1.1 List of Considered Rendezvous Scenarios

This section provides a list of rendezvous scenarios considered throughout this research in Table 8.1. The scenarios are separated in two categories: reachability analysis, and guidance test cases. Note that for reachability analysis, each scenario included thousands of simulations for different initial conditions (see Chapters 4-6). The guidance test cases, however, were single simulations with the MT-OCP and NMPC algorithms (see Chapter 7).

8.1.2 Results

Traditional relative motion models do not account for the chief's tumbling motion, and usually treat translational and rotational components separately. In order to accomplish the research objectives in this dissertation, a 6-DOF relative motion model was derived that incorporates the chief's tumbling motion (see Chapter 2). Reachability analysis was then conducted using the derived relative motion model. A stand-alone list of spacecraft rendezvous scenarios considered throughout this dissertation is included in Table 8.1.

Reachability analysis was first conducted for a simplified rendezvous scenario, where the chief is assumed to be rotating on the orbit plane about its z body axis at a constant rate (see Chapter 4). By simplifying the relative dynamics to only consider motion on the orbit plane, the dimensionality of the problem was significantly reduced. Furthermore, making an assumption that the deputy was in very close proximity to the chief, and maneuvers were of short duration, led to the derivation of a LTI system describing the relative dynamics. Backward reachability of the LTI system was studied using polytopic approximation methods. Next, the chief's orbital motion was re-incorporated into the relative dynamics. It was

Table 8.1. List of spacecraft rendezvous scenarios considered in this research.

Tumbling Profile	**Spacecraft Geometry**	**Chief Orbit Eccentricity**	**Chief Rotation** (deg/sec)	**Relative Dynamics**
Reachability Analysis				
Constant Rotation	Spherically symmetric	Neglected	z principal axis $\Omega = 0,\ 5,\ 10,\ 15,\ 20$	Planar, 3-DOF, LTI
Constant Rotation	Spherically symmetric	$e = 0$	z principal axis $\Omega = 0,\ 2,\ 4,\ 6$	Uncoupled, 3-DOF, LTV translational, Nonlinear rotational
Constant Rotation	Spherically symmetric	$e = 0$	z principal axis $\Omega = 0,\ 2,\ 4$	Unsimplified, 6-DOF, Nonlinear
Tumbling	Triaxial	$e = 0,\ 0.05,\ 0.1$	Off-principal axis $\boldsymbol{\omega}_c = [0,\ 0,\ 0]^T$ $\boldsymbol{\omega}_c = [-2,\ 1,\ 1]^T$	Unsimplified, 6-DOF, Nonlinear
Guidance Test Cases				
Constant Rotation	Spherically symmetric	$e = 0$	Principal axis $\boldsymbol{\omega}_c = [0,\ 0,\ 0]^T$ $\boldsymbol{\omega}_c = [0,\ 0,\ 4]^T$ $\boldsymbol{\omega}_c = [0,\ 4,\ 0]^T$	Unsimplified, 6-DOF, Nonlinear
Tumbling	Triaxial	$e = 0$	Off-principal axis $\boldsymbol{\omega}_c = [0,\ 0,\ 0]^T$ $\boldsymbol{\omega}_c = [-2,\ 1,\ 1]^T$ $\boldsymbol{\omega}_c = [1,\ -2,\ 1]^T$ $\boldsymbol{\omega}_c = [1,\ 1,\ -2]^T$	Unsimplified, 6-DOF, Nonlinear

assumed that the chief was in a circular orbit, relative distances were small in comparison to the chief's orbit radius, and the chief and deputy were spherically symmetric rigid bodies. This resulted in a simplified 6-DOF dynamic system which was decomposed into a LTV translational subsystem and a nonlinear rotational subsystem. The backward reachability characteristics of the two subsystems were studied independently, using the minimum time contour methodology described in Chapter 3. It was also shown, in Section 4.3.1, that there exists an analytical maximum chief rotation rate for which the deputy is able to maintain the rendezvous condition given limited control authority.

After investigating the backward reachability characteristics of a simplified scenario, the reachability of the generalized 6-DOF rendezvous problem was analyzed (see Chapter 5).

In this scenario, the chief and deputy were assumed to be triaxial rigid bodies, and the chief was tumbling (i.e., initial angular velocity component in all three body axes). The full 6-DOF relative motion model, derived in Chapter 2, was used to analyze the backward reachability characteristics for this scenario. Using the minimum time contour methodology described in Chapter 3, the backward reachability characteristics of the 6-DOF system were studied on two subspaces: a relative position subspace, and a relative attitude subspace.

The reachability analysis that was conducted provided valuable insight into this complex scenario. Results successfully answered the first research question by depicting sets of initial states from which rendezvous maneuvers were feasible, within a given amount of time.

Drawing from the applied reachability analysis conducted in the first phase of research, a closed-loop reachability concept was formally defined to assess the reachability characteristics of a particular feedback control law. This concept was applied to the problem of rendezvous with a tumbling object in order to analyze the closed-loop backward reachability of the MPC algorithm (see Chapter 6). It was observed that the overall shape of the closed-loop backward reachable sets matched the shape of the sets presented in Chapter 5. As expected, maneuver times for the closed-loop system were longer than the minimum time maneuvers. Notably, during the thousands of simulations ran with the MPC algorithm, there were no failures. This fact served as empirical evidence to demonstrate the recursive feasibility of the MPC implementation.

Finally, the autonomous guidance algorithm was validated using a set of rendezvous scenarios, with different spacecraft geometries and chief tumbling profiles (see Chapter 7). Performance of the NMPC algorithm was compared to the MT-OCP solution, in terms of maneuver time, control effort, computation time, and state error. Results showed that the NMPC algorithm, as tuned for these simulations, tended to converge to solutions with longer maneuver durations and larger control effort. On the other hand, a significant advantage was offered by consistently low computation times and state errors. NMPC computation times were, on average, under 2 sec, while the algorithm sampling time was 5 sec. Therefore, an on-board implementation of NMPC would be feasible.

8.1.3 Contributions

The contributions of this research are listed in Table 8.2. Notably, to the best of the author's knowledge, this was the first time reachability analysis results were presented for a 6-DOF spacecraft rendezvous problem and, more specifically, for rendezvous with a tumbling object. Additionally, reachability analysis for spacecraft attitude control problems has not been seen in literature. The technique proposed during this research for the visualization of a set of relative attitudes is another contribution to the field. Finally, although MPC has a rich history, this work was the first application of MPC to a 6-DOF spacecraft rendezvous problem.

8.2 Future Work

Embarking on a research journey often results in more questions than answers. Unfortunately, not all of these questions can be answered in the limited amount of time available to complete an academic degree. Even when the end of a research project is declared, there is bound to be more work that could be done.

An obvious next step to progress the reachability analysis that was presented in this dissertation is to expand the spectrum of scenarios that are investigated; look at different chief tumbling motions, different types of orbits, the inclusion of perturbing forces and torques, or state constraints. Investigating the sensitivity of the MT-OCP solver to user-defined parameters would be beneficial. Also, the generation of more appropriate initial guesses to seed the solver for these types of maneuvers is an open research topic. From a space operations perspective, it would be interesting to assess the operational applicability of this type of reachability analysis. How would reachability analysis affect how space systems are operated?

On the topic of autonomous guidance, a robustness analysis of the NMPC algorithm is a logical next step. Given that the algorithm uses a deterministic prediction model, how well would it respond in an uncertain environment? How sensitive is the algorithm to the tuning parameters? What kind of state estimation technique could be used in conjunction with NMPC? Additionally, from a computational efficiency standpoint, could a convex MPC formulation be applied to this problem successfully? If so, what are the computational advantages, and how does performance compare to the NMPC? Finally, it would be

beneficial to explore some options in scenarios that are inherently infeasible (i.e., conditions outside of the reachable set). Does this scenario necessitate the use of a different guidance strategy? Could the NMPC be tuned, in real time, with the objective of placing the spacecraft with a reachable set?

Table 8.2. List of research contributions.

Contribution	Task	Chapter
Derivation of chief perspective 6-DOF relative dynamics model	1, 2	2
Methodology for applied reachability analysis via minimum time contours	2	3
Method for visualization of reachable attitudes on the MRP subspace	2	3
Derivation of simplified models suitable for reachability analysis	1, 2	4
Analytical upper bound on chief rotation rate for maintaining rendezvous	1, 2	4
Reachability analysis of planar docking maneuver in close proximity	2	4
Reachability analysis of rendezvous with circular chief rotating on orbit plane	2	4
6-DOF Reachability analysis of rendezvous with chief rotating on orbit plane	2	5
6-DOF Reachability analysis of rendezvous with chief in tumbling motion	2	5
Reachability analysis of relative attitude between two rigid bodies	2	5
Analysis of chief orbital eccentricity effect on reachability results	2	5
Design of NMPC algorithm for 6-DOF autonomous rendezvous with tumbling object	3	6
Definition of closed-loop backward reachable sets	2, 3	6
6-DOF Closed-loop reachability analysis of rendezvous with tumbling chief	2, 3	6
Validation of NMPC algorithm for 6-DOF autonomous rendezvous with tumbling object	3	7

THIS PAGE INTENTIONALLY LEFT BLANK

APPENDIX: Discrete-Time LQR

In this section, the Discrete-time LQR problem is reviewed, and the corresponding DARE is derived. The solution to the DARE is an important result used to incorporate stabilizing considerations into the design of a MPC algorithm. The material in this appendix is adapted from the derivations seen in [58], [128].

The goal of the LQR controller is to drive a controllable (or stabilizable) linear system to the origin from an arbitrary initial state, using state feedback. The steady-state (or infinite horizon), discrete-time, LQR problem is written as follows:

$$\text{minimize} \quad : \quad J = \frac{1}{2}\sum_{i=0}^{\infty} x_{k+i}^T Q x_{k+i} + u_{k+i}^T R u_{k+i} \tag{A.1a}$$

$$\text{subject to} \quad : \quad x_{k+1} = A_d x_k + B_d u_k. \tag{A.1b}$$

The system Hamiltonian is,

$$H = \frac{1}{2}\left(x_{k+i}^T Q x_{k+i} + u_{k+i}^T R u_{k+i}\right) + \lambda_k^T \left(A_d x_k + B_d u_k\right). \tag{A.2}$$

Applying the necessary conditions for optimal control yields the following:

$$x_{k+1} \quad = \quad \frac{\partial H}{\partial \lambda_k} = A_d x_k + B_d u_k \tag{A.3a}$$

$$\lambda_{k+1} \quad = \quad -\frac{\partial H}{\partial x_k} = -Q x_k - A_d^T \lambda_k \tag{A.3b}$$

$$0 \quad = \quad \frac{\partial H}{\partial u_k} = R u_k + B_d^T \lambda_k \tag{A.3c}$$

$$\implies \quad u_k^* = -R^{-1} B_d^T \lambda_k. \tag{A.3d}$$

Combining (A.3d) and (A.3a) yields,

$$x_{k+1} = A_d x_k - B_d R^{-1} B_d^T \lambda_k. \tag{A.4}$$

Now it is assumed that the control is a state feedback of the form $u_k = -K x_k$, and the costate has the form $\lambda_k = Q_f x_k$, where K and Q_f are constant matrices. The optimal feedback

gain can be derived as follows:

$$\begin{aligned} u_k &= -Kx_k = -R^{-1}B_d^T Q_f x_k \implies \\ K &= R^{-1}B_d^T Q_f. \end{aligned} \tag{A.5}$$

Since $\lambda_k = Q_f x_k$, it follows that $\lambda_{k+1} = Q_f x_{k+1}$. Then plugging in (A.3b) and (A.4) yields the following equality:

$$\begin{aligned} -Qx_k - A_d^T \lambda_k &= Q_f \left(A_d x_k - B_d R^{-1} B_d^T \lambda_k \right) \implies \\ -Qx_k - A_d^T Q_f x_k &= Q_f \left(A_d x_k - B_d R^{-1} B_d^T Q_f x_k \right) \implies \\ \left(-Q - A_d^T Q_f - Q_f A_d + Q_f B_d R^{-1} B_d^T Q_f \right) x_k &= 0. \end{aligned} \tag{A.6}$$

In order for (A.6) to hold, it must be true that,

$$-Q - A_d^T Q_f - Q_f A_d + Q_f B_d R^{-1} B_d^T Q_f = 0. \tag{A.7}$$

Equation A.7 is known as the DARE. The DARE can be solved by the eigenvalues and eigenvectors of the corresponding Hamiltonian system, as shown in [128]. As a quadratic equation, more than one solution exists. The stabilizing solution is the positive-definite matrix, Q_f, which provides the appropriate feedback gain matrix for the discrete LQR problem. In this research, the DARE was solved using MATLAB's built-in *dlqr* command.

List of References

[1] S. Segal and P. Gurfil, "Effect of kinematic rotation-translation coupling on relative spacecraft translational dynamics," *Journal of Guidance, Control, and Dynamics*, vol. 32, no. 3, pp. 1045–1050, 2009.

[2] K. T. Alfriend, S. R. Vadali, P. Gurfil, J. P. How, and L. S. Breger, *Spacecraft Formation Flying: Dynamics, Control, and Navigation* (Elsevier Astrodynamics Series). Oxford, UK: Butterworth-Heinmann, 2010, ch. 4, 5, 9.

[3] W. Fehse, *Automated Rendezvous and Docking of Spacecraft*. Cambridge University Press, 2003.

[4] On-Orbit Satellite Servicing Study: Project Report. (2010). [Online]. Available: https://sspd.gsfc.nasa.gov/images/nasa_satellite%20servicing_project_report_0511.pdf. Accessed: 13 August 2018.

[5] R. Alfred. (2011, April). April 11, 1984: Shuttle Makes House Call, Repairs Satellite. [Online]. Available: https://www.wired.com/2011/04/0411space-shuttle-astronauts-repair-solar-max-satellite/. Accessed: 20 September 2017.

[6] S. Nolet, "Development of a guidance, navigation and control architecture and validation process enabling autonomous docking to a tumbling satellite," Ph.D. dissertation, Massachusetts Institute of Technology, 2007.

[7] G. A. Boyarko, "Spacecraft guidance strategies for proximity maneuvering and close approach with a tumbling object," Ph.D. dissertation, Naval Postgraduate School, Monterey, CA, 2010. Available: http://hdl.handle.net/10945/10539

[8] D. C. Woffinden and D. K. Geller, "Navigating the road to autonomous orbital rendezvous," *Journal of Spacecraft and Rockets*, vol. 44, no. 4, pp. 898–909, 2007.

[9] M. B. Quadrelli, L. J. Wood, J. E. Riedel, M. C. McHenry, M. Aung, L. A. Cangahuala, R. A. Volpe, P. M. Beauchamp, and J. A. Cutts, "Guidance, navigation, and control technology assessment for future planetary science missions," *Journal of Guidance, Control, and Dynamics*, vol. 38, no. 7, pp. 1165–1186, 2015.

[10] P. M. Beauchamp, J. A. Cutts, M. B. Quadrelli, L. J. Wood, J. E. Riedel, M. C. McHenry, M. Aung, L. A. Cangahuala, and R. A. Volpe, "Guidance, navigation, and control technology assessment for future planetary science missions," in *2013 AIAA Space Forum*. San Diego, CA: AIAA, 2013.

[11] The Collision of Iridium 33 and Cosmos 2251. (2015). [Online]. Available: http://www.aerospace.org/crosslinkmag/fall-2015/the-collision-of-iridium-33-and-cosmos-2251/. Accessed: 19 April 2017.

[12] Summary of DART Accident Report. [Online]. Available: https://www.nasa.gov/mission_pages/dart/main/. Accessed: 19 April 2017.

[13] G. Di Mauro, M. Lawn, and R. Bevilacqua, "Survey on guidance navigation and control requirements for spacecraft formation-flying missions," *Journal of Guidance, Control, and Dynamics*, vol. 41, no. 3, pp. 581–602, 2018.

[14] P. Lu, "Introducing computational guidance and control," *Journal of Guidance, Control, and Dynamics*, vol. 40, no. 2, p. 193, February 2017.

[15] P. Tsiotras and M. Mesbahi, "Toward an algorithmic control theory," *Journal of Guidance, Control, and Dynamics*, vol. 40, no. 2, pp. 194–196, February 2017.

[16] C. G. Henshaw, "A variational technique for spacecraft trajectory planning," Ph.D. dissertation, University of Maryland, College Park, Maryland, 2003.

[17] Z. Ma, O. Ma, and B. N. Shashikanth, "Optimal control for spacecraft to rendezvous with a tumbling satellite in a close range," in *Proceedings of the 2006 IEEE/RSJ International Conference on Intelligent Robots and Systems*. Beijing, China: IEEE, 2006, pp. 4109–4114.

[18] A. Fejzić, "Development of control and autonomy algorithms for docking to complex tumbling satellites," Master's thesis, Massachusetts Institute of Technology, Sept 2008.

[19] S. McCamish, "Distributed autonomous control of multiple spacecraft during close proximity operations," Ph.D. dissertation, Naval Postgraduate School, Monterey, CA, 2007.

[20] G. A. Boyarko, O. Yakimenko, and M. Romano, "Optimal rendezvous trajectories of a controlled spacecraft and a tumbling object," *Journal of Guidance, Control, and Dynamics*, vol. 34, no. 4, pp. 1239–1252, 2011.

[21] J. Ventura, M. Ciarcià, M. Romano, and U. Walter, "An inverse dynamics-based trajectory planner for autonomous docking to a tumbling target," in *AIAA SciTech Forum: AIAA Guidance, Navigation, and Control Conference*, no. AIAA 2016-0876. San Diego, CA: AIAA, 2016.

[22] M. Wilde, M. Ciarcià, A. Grompone, and M. Romano, "Experimental characterization of inverse dynamics guidance in docking with a rotating target," *Journal of Guidance, Control, and Dynamics*, vol. 39, no. 6, pp. 1173–1187, 2016.

[23] J. Michael, K. Chudej, and J. Pannek, "Modelling and optimal control of a docking maneuver with an uncontrolled satellite," in *IFAC Proceedings Volumes 45.2*, 2012, pp. 1135–1140.

[24] D. C. Sternberg and D. Miller, "Parametrization of fuel-optimal synchronous approach trajectories to tumbling targets," *Frontiers in Robotics and AI*, vol. 5, no. 33, pp. 1–11, 2018.

[25] W. Lu, Y. Geng, X. Chen, and F. Zhang, "Relative position and attitude coupled control for autonomous docking with a tumbling target," *International Journal of Control and Automation*, vol. 4, no. 4, pp. 1–22, 2011.

[26] A. Xueyan, R. Zhang, and W. Lu, "Terminal sliding mode control of attitude synchronization for autonomous docking to a tumbling satellite," in *Proceedings of the 2013 International Conference on Mechatronic Sciences, Electric Engineering and Computer (MEC)*. Shenyang, China: IEEE, 2013, pp. 2760–2763.

[27] L. Sun and W. Huo, "Nonlinear robust adaptive control for spacecraft proximity operations," in *Proceedings of the 19th World Congress of the International Federation of Automatic Control (IFAC)*. Cape Town, South Africa: IFAC, 2014, pp. 2219–2224.

[28] D. A. Vallado, *Fundamentals of Astrodynamics and Applications*, 3rd ed. Hawthorne, CA: Microcosm Press, 2007, ch. 1-3.

[29] L. Guarnaccia, R. Bevilacqua, and S. Pastorelli, "Suboptimal LQR-based spacecraft full motion control: Theory and experimantation," *Acta Astronautica*, vol. 122, pp. 114–136, 2016.

[30] Y.-H. Wu, X.-B. Cao, Y.-J. Xing, P.-F. Zheng, and S.-J. Zhang, "Relative motion coupled control for formation flying spacecraft via convex optimization," *Aerospace Science and Technology*, vol. 14, pp. 415–428, 2010.

[31] K.-Y. Lian, L.-S. Wang, and L.-C. Fu, "Controllability of spacecraft systems in a central gravitational field," *IEEE Transactions on Automatic Control*, vol. 39, no. 12, pp. 2426–2441, 1994.

[32] H. Pan and V. Kapila, "Adaptive nonlinear control for spacecraft formation flying with coupled translational and attitude dynamics," in *Proceedings of the 40th Conference on Decision and Control*. Orlando, FL: IEEE, 2001, pp. 2057–2062.

[33] D. Lee and G. Vukovich, "Kinematically coupled spacecraft relative motion without attitude synchronization assumption," *Aerospace Science and Technology*, vol. 45, pp. 316–323, 2015.

[34] C. Petersen and I. Kolmanovsky, "Coupled translational and rotational dynamics for precise constrained rendezvous and docking with periodic reference governors," in *26th AAS/AIAA Spaceflight Mechanics Meeting*. Napa Valley, CA: AAS, 2016.

[35] B. Wie, *Space Vehicles Dynamics and Control*, 2nd ed. (AIAA Education Series). American Institute of Aeronautics and Astronautics, Inc., 2008, ch. 4, pp. 299–303.

[36] J. Rooney, "A comparison of representations of general spatial screw displacement," *Environment & Planning B*, vol. 5, no. 1, pp. 45–88, 1978.

[37] J. Funda and R. P. Paul, "A computational analysis of screw transformations in robotics," *IEEE Transactions on Robotics and Automation*, vol. 6, no. 3, pp. 348–356, June 1990.

[38] L. Holguin, S. P. Viswanathan, and A. Sanyal, "Guidance and control for spacecraft autonomous rendezvous and proximity maneuvers using a geometric mechanics framework," in *AIAA Guidance, Navigation, and Control Conference*, no. AIAA 2012-4921. Minneapolis, MN: AIAA, 2012.

[39] D. Lee and G. Vukovich, "Robust adaptive terminal sliding mode control on SE(3) for autonomous spacecraft rendezvous and docking," *Nonlinear Dyncamics*, vol. 83, pp. 2263–2279, 2016.

[40] T. Lee, "Computational geometric mechanics and control of rigid bodies," Ph.D. dissertation, The University of Michigan, 2008.

[41] T. Lee, M. Leok, and N. H. McClamroch, "Lie group variational integrators for the full body problem," *Computer Methods in Applied Mechanics and Engineering*, vol. 196, 2007.

[42] G. Misra, A. Sanyal, and E. Samiei, "Asteroid landing guidance design in the framework of coupled orbit-attitude spacecraft dynamics," in *Proceedings of the 25th AAS/AIAA Spaceflight Mechanics Meeting*, no. AAS 15-430. Williamsburg, VA: AAS, 2015, pp. 1969–1980.

[43] W. D. Price, "Nonlinear control for dual quaternion systems," Ph.D. dissertation, Embry-Riddle Aeronautical University, Daytona Beach, FL, 2013.

[44] N. Filipe, "Nonlinear pose control and estimation for space proximity operations: An approach based on dual quaternions," Ph.D. dissertation, Georgia Institute of Technology, December 2014.

[45] J.-Y. Wang, H.-Z. Liang, Z.-W. Sun, S.-N. Wu, and S.-J. Zhang, "Relative motion coupled control based on dual quaternion," *Aerospace Science and Technology*, vol. 25, pp. 102–113, 2013.

[46] N. Filipe and P. Tsiotras, "Adaptive postition and attitude-tracking controller for satellite proximity operations using dual quaternions," *Journal of Guidance, Control, and Dynamics*, vol. 38, no. 4, pp. 566–577, April 2015.

[47] U. Lee and M. Mesbahi, "Constrained autonomous precision landing via dual quaternions and model predictive control," *Journal of Guidance, Control, and Dynamics*, vol. 40, no. 2, pp. 292–308, February 2017.

[48] U. Lee and M. Mesbahi, "Optimal powered descent guidance with 6-DOF line of sight constraints via unit dual quaternions," in *2015 AIAA SciTech Forum: AIAA Guidance, Navigation, and Control Conference*, no. AIAA 2015-0319. Kissimmee, FL: AIAA, 2015.

[49] C. Zagaris and M. Romano, "Applied reachability analysis for spacecraft rendezvous and docking with a tumbling object," in *SciTech Forum (28th Spaceflight Mechanics Meeting)*, no. 2018-2220. Reston, VA: AIAA, Jan 2018.

[50] H. Schaub and J. L. Junkins, *Analytical Mechanics of Space Systems*. American Institute of Aeronautics and Astronautics, Inc., 2003, ch. 1-3.

[51] C. Zagaris and M. Romano, "Analysis of spacecraft planar docking with rotating body in close proximity," in *27th AAS/AIAA Spaceflight Mechanics Meeting*, no. AAS 17-419. San Antonio, TX: AAS, 2017, pp. 1047–1060. Available: http://hdl.handle.net/10945/51980

[52] C. Zagaris and M. Romano, "Reachability analysis of planar spacecraft docking with rotating body in close proximity," *Journal of Guidance, Control, and Dynamics*, vol. 41, no. 6, pp. 1413–1419, 2018.

[53] O. Maler, "Computing reachable sets: An introduction," CNRS-VERIMAG, Tech. Rep., 2008.

[54] F. Bullo and A. D. Lewis, *Geometric Control of Mechanical Systems: Modeling, Analysis, and Design for Simple Mechanical Control Systems* (Texts in Applied Mathematics). New York, NY: Springer, 2005, no. 49.

[55] D. R. Snow, "Determining reachable regions and optimal controls," in *Advances in Control Systems: Theory and Applications*, vol. 5, C. T. Leondes, Ed. New York, NY: Academic Press Inc., 1967, pp. 133–196.

[56] J. Lygeros, "On reachability and minimum cost optimal control," *Automatica*, vol. 40, no. 6, pp. 917–927, 2004.

[57] I. M. Mitchell, A. M. Bayen, and C. J. Tomlin, "A time-dependent Hamilton-Jacobi formulation of reachable sets for continuous dynamic games," *IEEE Transactions on Automatic Control*, vol. 50, no. 7, pp. 947–957, July 2005.

[58] D. E. Kirk, *Optimal Control Theory: An Intoduction*. Dover, 2004, ch. 3, 5, pp. 259–260.

[59] I. M. Mitchell and C. J. Tomlin, "Level set methods for computation in hybrid systems," in *Lecture Notes in Computer Science (LNCS)* (International Workshop on Hybrid Systems: Computation and Control (HSCC '00)). Berlin Heidelberg, Germany: Springer-Verlag, 2000, vol. 1790, pp. 310–323.

[60] I. M. Mitchell, "A toolbox of level set methods (version 1.1)," http://www.cs.ubc.ca/~mitchell/ToolboxLS, Department of Computer Science, University of British Columbia, Vancouver, BC, Canada, 2007.

[61] M. Chen and C. J. Tomlin, "Hamilton-jacobi reachability: Some recent theoretical advances and applications in unmanned airspace management," *The Annual Review of Control, Robotics, and Autonomous Systems*, vol. 1, pp. 333–358, 2018.

[62] M. Oishi, I. M. Mitchell, C. J. Tomlin, and P. Saint-Pierre, "Computing viable sets and reachable sets to design feedback linearizing control laws under saturation," in *Proceedings of the 45th IEEE Conference on Decision and Control*, 2006.

[63] J. Ding, J. Sprinkle, C. J. Tomlin, S. S. Sastry, and J. L. Paunicka, "Reachability calculations for vehicle safety during manned/unmanned vehicle interaction," *Journal of Guidance, Control, and Dynamics*, vol. 35, no. 1, pp. 138–152, 2012.

[64] D. M. Stipanović, I. Hwang, and C. J. Tomlin, "Computation of an over-approximation of the backwards reachable set using subsystem level set functions," in *Proceedings of the 2003 European Control Conference*. Cambridge, United Kingdom: IEEE, 2003, pp. 300–305.

[65] M. Chen, S. Herbert, and C. J. Tomlin, "Fast reachable set approximations via state decoupling disturbances," in *Proceedings of the IEEE 55th Conference on Decision and Control*, December 2016, pp. 191–196.

[66] I. B. Makhlouf, P. Hansch, and S. Kowalewski, "Comparison of reachability methods for uncertain linear time-invariant systems," in *Proceedings of the 2013 European Control Conference*. New York, NY: IEEE, 2013, pp. 1101–1106.

[67] A. Girard, C. Le Guernic, and O. Maler, "Efficient computation of reachable sets of linear time-invariant systems with inputs," in *Lecture Notes in Computer Science (LNCS)* (International Workshop on Hybrid Systems: Computation and Control (HSCC '06)), 2006, vol. 3927.

[68] M. R. Greenstreet and I. M. Mitchell, "Reachability analysis using polygonal projections," in *Lecture Notes in Computer Science (LNCS)* (International Workshop on Hybrid Systems: Computation and Control (HSCC '99)). Springer-Verlag, 1999, vol. 1569, pp. 103–116.

[69] A. Kurzhanskiy and P. Varaiya, "Ellipsoidal techniques for reachability analysis of discrete-time linear systems," *IEEE Transactions on Automatic Control*, vol. 52, no. 1, pp. 26–38, 2007.

[70] M. Herceg, M. Kvasnica, C. Jones, and M. Morari, "Multi-parametric toolbox 3.0," in *Proceedings of the European Control Conference*. New York, NY: IEEE, July 17-19 2013, pp. 502–510, http://control.ee.ethz.ch/~mpt.

[71] P. Varaiya, "Reach set computation using optimal control," in *Verification of Digital and Hybrid Systems*. Springer-Verlag, 2000, pp. 323–331.

[72] I. Hwang, D. M. Stipanović, and C. J. Tomlin, "Polytopic approximations of reachable sets applied to linear dynamic games and a class of nonlinear systems," in *Advances in Control, Communication Networks, and Transportation Systems: In Honor of Pravin Varaiya*. Birkhauser Boston, 2005, pp. 3–19.

[73] M. Holzinger and D. Scheeres, "Applied reachability for space situational awareness and safety in spacecraft proximity operations," in *AIAA Guidance, Navigation, and Control Conference*. Chicago, IL: AIAA, August 2009.

[74] D. Dueri, B. Acikmese, M. Baldwin, and R. S. Erwin, "Finite-horizon controllability and reachability for deterministic and stochastic linear control systems with convex constraints," in *Proceedings of the 2014 American Control Conference*. New York, NY: IEEE, June 2014, pp. 5016–5023.

[75] U. Eren, D. Dueri, and B. Açıkmeşe, "Constrained reachability and controllability sets for planetary precision landing via convex optimization," *Journal of Guidance, Control, and Dynamics*, vol. 38, no. 11, pp. 2067–2083, 2015.

[76] B. HomChaudhuri, M. Oishi, M. Shubert, M. Baldwin, and R. S. Erwin, "Computing reach-avoid sets for space vehicle docking under continuous thrust," in *Proceedings of the 55th Conference on Decision and Control*. Las Vegas, NV: IEEE, 2016, pp. 3312–3318.

[77] M. Athans and P. L. Falb, *Optimal Control: An Introduction to the Theory and Its Applications*. New York, NY: McGraw-Hill Book Company, 1966, ch. 4-6.

[78] E. Sontag and H. Sussmann, "Time-optimal control of manipulators," in *Proceedings of IEEE International Conference of Robotics and Automation*. New York, NY: IEEE, 1986, pp. 1692–1697.

[79] J.-J. E. Slotine and W. Li, *Applied Nonlinear Control*. Upper Saddle River, NJ: Prentice Hall International Inc., 1991.

[80] R. Hermann and A. J. Krenner, "Nonlinear controllability and observability," *IEEE Transactions on Automatic Control*, vol. 22, no. 5, pp. 728–740, 1977.

[81] P. E. Crouch, "Spacecraft attitude control and stabilization: Applications of geometric control theory to rigid body models," *IEEE Transactions on Automatic Control*, vol. 29, no. 4, pp. 321–331, 1984.

[82] C. Petersen, F. Leve, and I. Kolmanovsky, "Model predictive control of an underactuated spacecraft with two reaction wheels," *Journal of Guidance, Control, and Dynamics*, vol. 40, no. 2, pp. 320–332, Feb 2016.

[83] M. A. Patterson and A. V. Rao, *GPOPS-II: A General Purpose MATLAB Software for Multiple-Phase Optimal Control Problems, Version 2.1*, July 2016. Available: http://www.gpops2.com/

[84] A. Wächter and L. T. Biegler, "On the implementation of an interior-point filter line-search algorithm for large-scale nonlinear programming," *Mathematical Programming*, vol. 106, no. 1, pp. 25–57, 2006.

[85] J. E. Gayek, "A survey of techniques for approximating reachable and controllable sets," in *Proceedings of the 30th Conference on Decision and Control*. Brighton, England: IEEE, 1991, pp. 1724–1729.

[86] J. T. Betts, "Survey of numerical methods for trajectory optimization," *Journal of Guidance, Control, and Dynamics*, vol. 21, no. 2, pp. 193–207, 1998.

[87] K. Shoemake, "Uniform random rotations," in *Graphics Gems III*, D. Kirk, Ed. Academic Press, Inc., 1995, pp. 124–132.

[88] R. Zappulla II, "Experimental evaluation methodology for spacecraft proximity maneuvers in a dynamic environment," Ph.D. dissertation, Naval Postgraduate School, Monterey, CA, June 2017.

[89] C. Zagaris, H. Park, J. Virgili-Llop, R. Zappulla II, M. Romano, and I. Kolmanovsky, "Model predictive control of spacecraft relative motion with convexified keep-out-zone constraints," *Journal of Guidance, Control, and Dynamics*, 2018, article in advance.

[90] J. B. Rawlings and D. Q. Mayne, *Model Predictive Control: Theory and Design*. Madison, Wisconsin: Nob Hill Publishing, 2015, ch. 2, pp. 112–153.

[91] D. Q. Mayne, J. B. Rawlings, C. V. Rao, and P. O. M. Scokaert, "Constrained model predictive control: Stability and optimality," *Automatica*, vol. 36, pp. 798–814, 2000.

[92] L. Grune and J. Pannek, *Nonlinear Model Predictive Control: Theory and Algorithms*. New York, NY: Springer, 2011, ch. 6, pp. 113–161.

[93] J. Löfberg, "Oops! I cannot do it again: Testing for recursive feasibility in MPC," *Automatica*, vol. 48, pp. 550–555, 2012.

[94] E. C. Kerrigan, "Robust constraint satisfaction: Invariant sets and predictive control," Ph.D. dissertation, University of Cambridge, Nov 2000.

[95] S. Boyd and L. Vandenberghe, *Convex Optimization*. New York, NY: Cambridge University Press, 2004, ch. 1, 4, 11.

[96] U. Eren, A. Prach, B. B. Koçer, S. V. Raković, E. Kayacan, and B. Açikmeşe, "Model predictive control in aerospace systems: Current state and opportunities," *Journal of Guidance, Control, and Dynamics*, vol. 40, no. 7, pp. 1541–1566, 2017.

[97] P. Lu and X. Liu, "Autonomous trajectory planning for rendezvous and proximity operations by conic optimization," *Journal of Guidance, Control, and Dynamics*, vol. 36, no. 2, pp. 375–389, 2013.

[98] X. Liu and P. Lu, "Solving nonconvex optimal control problems by convex optimization," *Journal of Guidance, Control, and Dynamics*, vol. 37, no. 3, pp. 750–765, 2014.

[99] Y. Mao, M. Szmuk, and B. Açıkmeşe, "Successive convexification of non-convex optimal control problems with state constraints," in *Proceedings of the 55th Conference on Decision and Control*. Las Vegas, NV: IEEE, 2016, pp. 3636–3641.

[100] J. Virgili-Llop, C. Zagaris, R. Zappulla II, A. Bradstreet, and M. Romano, "Convex optimization for proximity maneuvering of a spacecraft with a robotic manipulator," in *27th AAS/AIAA Spaceflight Mechanics Meeting*, no. AAS 17-418. Springfield, VA: AAS, 2017.

[101] J. Virgili-Llop, C. Zagaris, R. Zappulla II, A. Bradstreet, and M. Romano, "Laboratory experiments on the capture of a tumbling object by a spacecraft-manipulator system using a convex-programming-based guidance," in *AAS/AIAA Astrodynamics Specialist Conference*. Stevenson, WA: AAS, 2017.

[102] V. Manikonda, P. O. Arambel, M. Gopinathan, R. K. Mehra, and F. Y. Hadaegh, "A model predictive control-based approach for spacecraft formation keeping and

attitude control," in *Proceedings of the 1999 American Control Conference*. IEEE, 1999, pp. 4258–4262.

[103] A. Richards and J. P. How, "Model predictive control of vehicle maneuvers with guaranteed completion time and robust feasibility," in *Proceedings of the 2003 American Control Conference*. Denver, CO: IEEE, 2003, pp. 4034–4040.

[104] H. Park, S. Di Cairano, and I. Kolmanovsky, "Model predictive control for spacecraft rendezvous and docking with a rotating/tumbling platform and for debris avoidance," in *Proceedings of the 2011 American Control Conference*. New York, NY: IEEE, 2011, pp. 1922–1927.

[105] A. Weiss, I. Kolmanovsky, M. Baldwin, and R. S. Erwin, "Model predictive control of three dimensional spacecraft relative motion," in *Proceedings of the 2012 American Control Conference*. IEEE, 2012, pp. 173–178.

[106] A. Weiss, M. Baldwin, R. S. Erwin, and I. Kolmanovsky, "Model predictive control for spacecraft rendezvous and docking: Strategies for handling constraints and case studies," *IEEE Transactions on Control Systems Technology*, vol. 23, no. 4, pp. 1638–1647, 2015.

[107] C. Petersen, A. Jaunzemis, M. Baldwin, M. Holzinger, and I. Kolmanovsky, "Model predictive control and extended command governor for improving robustness of relative motion guidance and control," in *24th AAS/AIAA Spaceflight Mechanics Meeting*, no. AAS 14-249. Santa Fe, NM: AAS, 2014.

[108] C. Jewison, R. S. Erwin, and A. Saenz-Otero, "Model predictive control with ellipsoid obstacle constraints for spacecraft rendezvous," in *IFAC-PapersOnLine 48-9*. IFAC, 2015, pp. 257–262.

[109] C. Jewison, "Guidance and control for multi-stage rendezvous and docking operations in the presence of uncertainty," Ph.D. dissertation, Massachusetts Institute of Technology, Cambridge, MA, June 2017.

[110] R. Zappulla II, J. Virgili-Llop, C. Zagaris, H. Park, A. Sharp, and M. Romano, "Floating spacecraft simulator test bed for the experimental testing of autonomous guidance, navigation, and control of spacecraft proximity maneuvers and operations," in *2016 AIAA SPACE Forum: AIAA/AAS Astrodynamics Specialist Conference*. Long Beach, CA: AIAA, 2016.

[111] J. Virgili-Llop, C. Zagaris, H. Park, and M. Romano, "Experimental evaluation of model predictive control and inverse dynamics control for spacecraft proximity and docking maneuvers," *CEAS Space Journal*, pp. 1–13, 2016.

[112] H. Park, C. Zagaris, J. Virgili-Llop, R. Zappulla II, I. Kolmanovsky, and M. Romano, "Analysis and experimentation of model predictive control for spacecraft rendezvous and proximity operations with multiple obstacle avoidance," in *2016 AIAA SPACE Forum: AIAA/AAS Astrodynamics Specialist Conference*, no. AIAA 2016-5273. Long Beach, CA: AIAA, 2016.

[113] H. Park, R. Zappulla II, C. Zagaris, J. Virgili-Llop, and M. Romano, "Nonlinear model predictive control for spacecraft rendezvous and docking with a rotating target," in *Proceedings of the 27th AAS/AIAA Spaceflight Mechanics Meeting*, San Antonio, TX, 2017. Available: http://hdl.handle.net/10945/51984

[114] J. L. Crassidis, F. L. Markley, T. C. Anthony, and S. F. Andrews, "Nonlinear predictive control of spacecraft," *Journal of Guidance, Control, and Dynamics*, vol. 20, no. 6, pp. 1096–1103, 1997.

[115] H.-S. Myung and H. Bang, "Nonlinear predictive attitude control of spacecraft under external disturbances," *Journal of Spacecraft*, vol. 40, no. 5, pp. 696–699, 2003.

[116] O. Hegrenaes, J. T. Gravdahl, and P. Tondel, "Spacecraft attitude control using explicit model predictive control," *Automatica*, vol. 41, pp. 2107–2114, 2005.

[117] M. Wood, W.-H. Chen, and D. Fertin, "Model predictive control of low earth orbiting spacecraft with magneto-torquers," in *Proceedings of the 2006 IEEE Intrnational Conference on Control Applications*. Munich, Germany: IEEE, October 2006, pp. 2908–2913.

[118] Y. Ikeda, T. Nakajima, and Y. Chida, "Attitude control of spacecraft by nmpc with consideration of singularity avoidance of cmg," in *Proceeding of the 51st Conference on Decision and Control*. Maui, HI: IEEE, 2012, pp. 1733–1739.

[119] R. Gupta, U. Kalabic, S. Di Cairano, A. Bloch, and I. Kolmanovsky, "Constrained spacecraft attitude control on SO(3) using fast nonlinear model predictive control," in *Proceedings of the 2015 American Control Conference*. Chicago, IL: AACC, 2015, pp. 2980–2986.

[120] A. Guiggiani, I. Kolmanovsky, P. Patrinos, and A. Bemporad, "Fixed-point contrained model prodictive control of spacecraft attitude," in *Proceedings of the 2015 American Control Conference*. Chicago, IL: AACC, 2015, pp. 2317–2322.

[121] A. E. Bryson, *Applied Linear Optimal Control: Examples and Algorithms*. Cambridge, United Kingdom: Cambridge University Press, 2002, ch. 5, 9.

[122] M. J. Risbeck and J. B. Rawlings, *MPCTools: Nonlinear Model Predictive Control Tools for CasADi (Octave Interface)*, University of Wisconsin, Madison, Wisconsin, 2016, accessed: July 2017. Available: https://bitbucket.org/rawlings-group/octave-mpctools

[123] J. A. E. Anderson, J. Gillis, G. Horn, J. B. Rawlings, and M. Diehl, "Casadi – a software framework for nonlinear optimization and optimal control," *Mathematical Programming Computation*, 2018, in Press.

[124] CasADi. [Online]. Available: https://github.com/casadi/casadi/wiki. Accessed: July 2017.

[125] R. Kianfar, P. Falcone, and J. Fredriksson, "Reachability analysis of cooperative adaptive cruise controller," in *15th International IEEE Conference on Intelligent Transportation Systems*. New York, NY: IEEE, 2012, pp. 1537–4542.

[126] S. Hossain, S. Dhople, and T. T. Johnson, "Reachability analysis of closed-loop switching power converters," in *IEEE Power and Energy Conference at Illinois (PECI)*. New York, NY: IEEE, 2013, pp. 130–134.

[127] A. Zutshi, S. Sankaranarayanan, D. J. V., and X. Jin, "Symbolic-numeric reachability analysis of closed-loop control software," in *Proceedings of the 19th International Conference on Hybrid Systems: Computation and Control*. New York, NY: ACM, 2016, pp. 135–144.

[128] J. B. Burl, *Linear Optimal Control: H_2 and H_∞ Methods*. Menlo Park, CA: Addison Wesley Longman, Inc., 1999, ch. 6.

Initial Distribution List

1. Defense Technical Information Center
   Ft. Belvoir, Virginia

2. Dudley Knox Library
   Naval Postgraduate School
   Monterey, California